NANYANG TECHNOLOGICAL UNIVERSITY
SINGAPORE

TARGETING PRO-TUMORIGENIC SIGNALING PATHWAYS IN HEMATOLYMPHOID MALIGNANCIES

KIZHAKEYIL ATISH

LEE KONG CHIAN SCHOOL OF MEDICINE

2020

TARGETING PRO-TUMORIGENIC SIGNALING PATHWAYS IN HEMATOLYMPHOID MALIGNANCIES

KIZHAKEYIL ATISH

LEE KONG CHIAN SCHOOL OF MEDICINE

A thesis submitted to the Nanyang Technological University in partial fulfilment of the requirement for the degree of Doctor of Philosophy

2020

Statement of Originality

I hereby certify that the work embodied in this thesis is the result of original research, is free of plagiarised materials, and has not been submitted for a higher degree to any other University or Institution.

09-01-2020

....

Date Kizhakeyil Atish

Supervisor Declaration Statement

I have reviewed the content and presentation style of this thesis and declare it is free of plagiarism and of sufficient grammatical clarity to be examined. To the best of my knowledge, the research and writing are those of the candidate except as acknowledged in the Author Attribution Statement. I confirm that the investigations were conducted in accord with the ethics policies and integrity standards of Nanyang Technological University Singapore and that the research data are presented honestly and without prejudice.

09-01-2020

.....
Date

Navin Kumar Verma
.....
Asst Prof Navin Kumar Verma

Authorship Attribution Statement

This thesis contains materials from the following five papers published in the following peer-reviewed journals in which I am listed as an author.

1. Chapter 2, Section 2.1 was published as **Kizhakeyil A**, Fazil MHUT, Ong ST, Chalasani MLS, Low JH, Kottaisamy A, Praseetha P, Verma NK (2019) Isolation of human peripheral T cell lymphocytes. ***Methods Mol Biol*** 1930:11-18.
The contribution of the co-authors are as follows:

- I performed isolation of T-cells.
- I, Fazil MHUT, Ong ST and Chalasani MLS, drafted the manuscript.
- Verma NK revised and edited the manuscript.
- Low JH, Kottaisamy A and Praseetha P assisted in maintaining T-cell culture.

2. Chapter 2, Section 2.3.2 was published as Fazil MHUT, Ong ST, Chalasani MLS, **Kizhakeyil A**, Verma NK (2019) GapmeR-mediated gene silencing in motile T-cells. ***Methods Mol Biol*** 1930:67-73.
The contribution of the co-authors are as follows:

- I performed the isolation of T-cells.
- I, Fazil MHUT, Ong ST and Chalasani MLS drafted the manuscript.
- Verma NK revised and edited the manuscript.

3. Chapter 2, Section 2.14 was published as **Kizhakeyil A**, Verma NK (2019) Quantitative real-time PCR for transcriptional changes in T-lymphocytes. ***Methods Mol Biol*** 1930:59-68.
The contribution of the co-authors are as follows:

- I performed the experiments and drafted the manuscript.
- Verma NK revised and edited the manuscript.

4. Chapter 5, Sections 5.1 & 5.6 were included in the research article, which was published as Song TL, Nairismägi ML, Laurensia Y, Lim JQ, Tan J, Li ZM, Pang WL, **Kizhakeyil A**, Wijaya GC, Huang DC, Nagarajan S, Chia BK, Cheah D, Liu YH, Zhang F, Rao HL, Tang T, Wong EK, Bei JX, Iqbal J, Grigoropoulos NF, Ng SB, Chng WJ, Teh BT, Tan SY, Verma NK, Fan H, Lim ST, Ong CK (2018) Oncogenic activation of

the STAT3 pathway drives PD-L1 expression in natural killer/T-cell lymphoma. ***Blood*** 132 (11):1146-1158.

The contribution of the co-authors are as follows:

- I, Song TL, Nairismägi ML, Tan J, Laurensia Y, Li ZM, Pang WL, Wijaya GC and Verma NK provided development of methodology and execution of experiments.
- Song TL, Nairismägi ML, Teh BT and Ong CK provided conception and design.
- Song TL, Lim JQ, Chia BK, Nagarajan S, Grigoropoulos NF, Fan H, and Ong CK provided analysis and interpretation of data.
- Song TL, Lim JQ, Huang DC, Fan H and Ong CK provided writing, review, and revision of manuscript; Lim ST and Ong CK provided study supervision.
- Liu YH, Zhang F, Rao HL, Tang T, Bei JX, Ng SB, and Chng WJ provided samples.
- Chia BK and Cheah D provided material and technical support; and Iqbal J, Ng SB and Tan SY supplied pathologic diagnosis.

5. Chapter 5, Sections 5.2 & 5.3 were published in Fazil MHUT, Ong ST, Chalasani MLS, Low JH, **Kizhakeyil A**, Mamidi A, Carey FHL, Lakshminarayanan R, Kelleher D, Verma NK (2016) GapmeR cellular internalization by macropinocytosis induces sequence-specific gene silencing in human primary T-cells. ***Sci Rep*** 6:37721.

The contribution of the co-authors are as follows:

- I, Fazil MHUT, Ong ST, Chalasani MLS, Low JH, Mamidi A and Carey FHL performed the experiments.
- Verma NK and Kelleher D conceptualized and designed the project and interpreted the data.
- Lakshminarayanan R assisted in data analysis.
- Verma NK and Lakshminarayanan R wrote the manuscript with critical input from Kelleher D.

09-01-2020

. . . . . .
Date

. . . . . .
Kizhakeyil Atish

Acknowledgments

Finishing a PhD Thesis is an individual's achievement but comes with efforts and blessing of many mentors, collaborators, friends and family.

I would like to convey my sincerest gratitude to my supervisor Asst. Prof. Navin Kumar Verma for his unceasing support for my PhD voyage. He has patiently nurtured and guided me irrespective of my flaws and most importantly helped me correct it. I sincerely hope that I will inherit his excellent writing and problem-solving qualities.

I would like to thank my co-supervisor Prof. Tan Suat Hoon for her critical suggestions and recommendations for during thesis writing. I would like to thank the Thesis Advisory Committee (TAC) members: Assoc. Prof. Kevin Pethe, Assoc. Prof. Karen Crasta and Assoc. Prof. Timothy Tan who have provided suggestions and ultimately helped shape this thesis. Without their guidance and continuous assistance, this thesis would not have been possible. I also thank Prof. David Becker for his comments during PhD qualification examination.

I convey my gratitude to Prof. Dermot Kelleher, University of British Columbia, Vancouver, who has provided me with crucial insights on research work.

I thank Dr. Ong Choon Kiat and his group at the National Cancer Centre Singapore (NCCS) and Dr. Nicholas Grigoropoulos and his group at the Singapore General Hospital (SGH) for their crucial insights and directions for research work. I would like to thank Dr. Tammy Song, Dr. Dachaun Huang, Jane Pang and Nur Mahirah for their help provided for conducting experiments at the NCCS. I extend my sincere gratitude to Dr. Bi Xuezhi and Dr. Kok Yee Jiun from Bioprocessing Technology Institute, A*STAR, Singapore for assistance in proteomics analysis and providing theirs comments on the thesis.

I thank Dr. Rajamani Lakshminarayanan and Dr. Madhavi Chalasani for their comments and suggestions during the progress of the research work.

I acknowledge Edwin Lim and LKCMedicine Graduate programme team for their continuous support during the course of the PhD. My sincere thanks Dr. Sini Matthew and safety team as well as RASS, LKCMedicine for the ensuring safe environment and providing excellent research facilities for the study conducted during the PhD.

I acknowledge PhD research fellowship and support provided by Lee Kong Chian School of Medicine, Nanyang Technological University Singapore.

My deepest appreciation to my laboratory colleagues (past and present): Dr. Ong Seow Theng, Dr. Turabe Fazil, Mrs. Praseetha Rajesh, Jian Hui, Jun Cheng, Aik Seng, Xinpeng, Zhi Sheng, Brandon, Eric Foo, James Chen and Aditya Ashok. Thank you all for the encouragement and guidance that allowed me to complete my project with minimal obstacles.

I like to dedicate this work to my parents Mr. Vasu and Mrs. Sushila, my sister Archana and brother in-law Jineesh who have supported and provided me all help during tough times of my life. My sincere thanks to my loving wife Neha and her parents who have been supportive and motived me for the completion of the thesis.

Table of Contents

List of Figures

List of Tables

Abbreviations

ABC	Activated B-cell
ALCL	Anaplastic Large cell lymphoma
ATCC	American Type Cell Culture
ASIR	Age standardized Incidence Rate
Bcl-2, -XL	B-cell lymphoma 2, extra large
BL	Burkitt Lymphoma
BSA	Bovine serum albumin
CCR4	C-C chemokine receptor type 4
CCR7	C-C chemokine receptor type 7
CDKNA1	Cyclin dependent kinase A inhibitor 1
CML	Chronic myeloid leukemia
CLA	Cutaneous Lymphocyte-associated Antigen
CTCL	Cutaneous T-cell lymphoma
DAVID	Database for Annotation, Visualization and Integrated Discovery
DBD	DNA Binding Domain
DDX3X	Dead Box Helicase X linked
DEG	Differentially Expressed Genes
DEP	Differentially Expressed Proteins
DMEM	Dulbecco's Modified Eagle medium
DLBCL	Diffused Large B cell lymphoma
DMSO	Dimethyl sulfoxide
DNase	Deoxyribonuclease
ECM	Extracellular matrix
ELISA	Enzyme-Linked Immunosorbent Assay
epAON	End protected antisense oligonucleotide
ERK	Extracellular Signal-Regulated Kinase
FAM	Fluorescein Amidite
FBS	Fetal bovine serum
FDA	Food and Drug Administration
FDR	False Discovery Rate
GCB	Germinal center B-cell
HDAC	Histone Deacetylase
HRP	Horseradish peroxidase
IC_{50}	Half maximal inhibitory concentration

ICAM	Intercellular Adhesion Molecule
IFNG	Interferon gamma
IL2-R	Interleukin-2 receptor
IL-6	Interleukin-6
IPA	Ingenuity Pathway Analysis
JAK	Janus Kinase
KD	Knockdown
mAb	Monoclonal antibody
MAPK	Mitogen-Activated Protein Kinase
MDR	Multi Drug Resistance
MF	Mycosis Fungoides
miR	Micro RNA
MMP-9	Matrix Metalloproteinase-9
mRNA	Messenger Ribonucleic Acid
MRP1	Multidrug Resistance-Associated Protein 1
mTOR	Mammalian Target of Rapamycin
NCCS	National Cancer Centre Singapore
NF-kB	Nuclear factor kB
NHL	Non-Hodgkin's lymphoma
NKTCL	Natural Killer-T-cell lymphoma
NS	Non-specific
NTD	N Terminal Domain
PARP	poly ADP- ribose polymerase
PBMC	Peripheral Blood Mononuclear Cells
P-gp	P-glycoprotein
PHA	Phytohaemagglutinin
PD-L1	Programmed Death- ligand 1
pSTAT3	Phospho-STAT3
PTCL	Peripheral T cell-lymphoma
qRT-PCR	Quantitative Reverse Transcription Polymerase Chain Reaction
RF	Resistance Factor
RNase	Ribonuclease
RPMI	Rosewell Park Memorial Institute
SGH	Singapore General Hospital
SH2	Src homology-2

shRNA	Short hairpin RNA
siRNA	Small interfering RNA
SILAC	Stable Isotope Labeling of Amino acids in Cell culture
SS	Sézary Syndrome
STAT3	Signal Transducer and Activator of Transcription
VEGF	Vascular endothelial growth factor
WHO	World Health Organization
WT	Wild-type
WES	Whole exome sequencing

Summary

Hematolymphoid malignancies constitute diverse forms of cancers derived from hematopoietic and lymphoid tissues. This group of diseases is prevalent worldwide and accounts for ~5% of all cancers, being the 6th most frequently diagnosed cancer in both men and women. These diseases are broadly categorized into two groups - Hodgkin's Lymphoma (HL) and Non-Hodgkin's Lymphoma (NHL), which include Diffuse Large B-cell Lymphoma (DLBCL), Cutaneous T-cell lymphoma (CTCL) and Natural Killer T-cell Lymphoma (NKTCL). Multiple strategies are in place to manage the disease, but intrinsic and acquired drug resistance remain major impediments for the clinical effectiveness of molecularly targeted therapies in hematolymphoid malignancies. Determining molecular alterations driving resistance to commonly used chemotherapies and defining disease mechanisms are therefore of considerable relevance for understanding the pathogenesis of hematolymphoid malignancies.

In the first part of this thesis, we developed a vorinostat-resistant CTCL cell line (HuT78$_{VR}$). The developed drug-resistant cell culture model can serve as potential clinical tools for screening drugs and investigating vorinostat resistance. We performed RNA-seq and proteomics analyses followed by bioinformatics and identified several pro-tumorigenic pathways, including STAT3 and ERK signaling, to be involved in drug resistance in hematolymphoid malignancies. This dataset expands the list of molecular networks associated with drug resistance that will be extremely useful in the study of their specific roles in hematolymphoid malignancies. Identification of proteins previously not reported in the context of drug resistance may provide new insights into the understanding of hematologic cancer, aid in the search for new potential therapeutic targets, and has implications in precision medicine for treating vorinostat resistant cases.

In the following part of the thesis, we examined the functional involvement of the X-linked *DDX3X* in hematolymphoid malignancies. Using data from clinical analysis and molecular assays, we demonstrated an association between *DDX3X* somatic mutation and poor prognosis. We confirmed *DDX3X* loss-of-function as a key contributing factor to cancer progression in hematolymphoid malignancies. Using CTCL and DLBCL patient-derived cell lines, we showed that DDX3X knockdown in these cells caused significant up-regulation of cytokine signaling pathways (IL-2, IL-4,

IL-10), and increased phosphorylation of STAT3 and p42/44. DDX3X loss increased resistance to doxorubicin and histone deacetylase targeting drugs, including romidepsin and vorinostat, in DLBCL and CTCL cells, respectively. Importantly, both B- and T-cell lineage DDX3X-depleted cells remained sensitive to pharmacological STAT3 inhibition. These findings provide new insight into the molecular mechanisms of chemoresistance in NHLs and identify *DDX3X* mutations as a biomarker for both resistance to standard chemotherapy as well as sensitivity to STAT3 inhibition.

Finally, we elucidated novel mechanisms by which STAT3 activation upregulates PD-L1 expression in hematolymphoid malignancies. These findings strongly indicate that STAT3 is critically vital for hematologic cancer and greatly enhances the understanding of fundamental intracellular mechanisms involved in malignancies. We optimized the "GapmeR" technology and developed a new gene silencer "epAON" that were effective in knocking down STAT3 in cells of hematolymphoid malignancies and successful in inducing apoptosis in these cells.

Taken together, we were able for the first time to obtain insights into vorinostat resistance in CTCL. We demonstrate that the X-linked *DDX3X* is a crucial determinant in NHL aggressiveness. We established that STAT3 activation upregulates PD-L1 expression in cells of hematolymphoid malignancies, which may promote tumor immune evasion. We developed a novel STAT3 inhibitory epAON molecule with promising results *in vitro*, which can be exploited for therapeutic applications.

Chapter 1

General Introduction

1.1 Hematolymphoid malignancies

Hematolymphoid malignancies constitute diverse forms of cancers derived from hematopoietic and lymphoid tissues. Lymphocytes such as T-cells, B-cells, and Natural Killer/T-cell, which are involved in regulating immune functions, often become malignant and transform into lymphoma cells. These cancerous cells multiply over time and accumulate into the lymphoid system and other tissues, such as the skin. This group of diseases is prevalent worldwide and accounts for ~5% of all cancers and are frequently diagnosed in both men and women (Siegel et al., 2019). They contribute to approximately 38% of childhood cancer and cause 44.6% of total cancer deaths in the young population within the age group of fewer than 15 years (Siegel et al., 2019). According to recent data from the USA, approximately one person is diagnosed with blood cancer in every 3 minutes, and 156 people decease every day due to hematolymphoid malignancies, which accounts for 9.4 % of total cancer mortality (Bray et al., 2018; Siegel et al., 2019).

Hematolymphoid malignancies are broadly categorized into two main groups: Hodgkin's lymphoma and non-Hodgkin's lymphoma (NHL). Hodgkin lymphomas affect a relatively smaller number of people (about 12% of all lymphoma cases), and this group of patients can be cured with proper treatments. NHLs comprise a broad category of hematolymphoid neoplasms, in which the Diffuse Large B-Cell Lymphoma (DLBCL) is the most frequently diagnosed. Other NHLs include T-cell lymphomas [e.g. Cutaneous T-Cell Lymphoma (CTCL)], Natural Killer T-Cell Lymphoma (NKTCL), and Burkitt Lymphoma (BL) (Swerdlow et al., 2016). Selected subtypes of hematolymphoid malignancies and their broad classification are summarized in **Figure 1.1**.

NHLs exemplify various forms of lymphoid neoplasms, which arise from lymphocytes that are at multiple stages of hematopoiesis and retains the characteristics of the originated cell types. According to the "International Agency for Research on Cancer," in 2018, age-standardized incidence rate (ASIR) per 100,000 for incidence and mortality for NHL is 5.7 and 2.6, respectively (Bray et al., 2018). In Asia, Singapore has the highest ASIR of 10.1 for NHL (Bray et al., 2018). In Singapore, NHL belongs to the top ten cancer killers, with 398 deaths recorded in 2018. According to the Singapore Cancer Registry, while ASIR for highly prevalent cancers (such as lung and

stomach cancer) has decreased, NHL incidences have steadily increased from 6.8 to 17.8 over the last five decades (Bray et al., 2018).

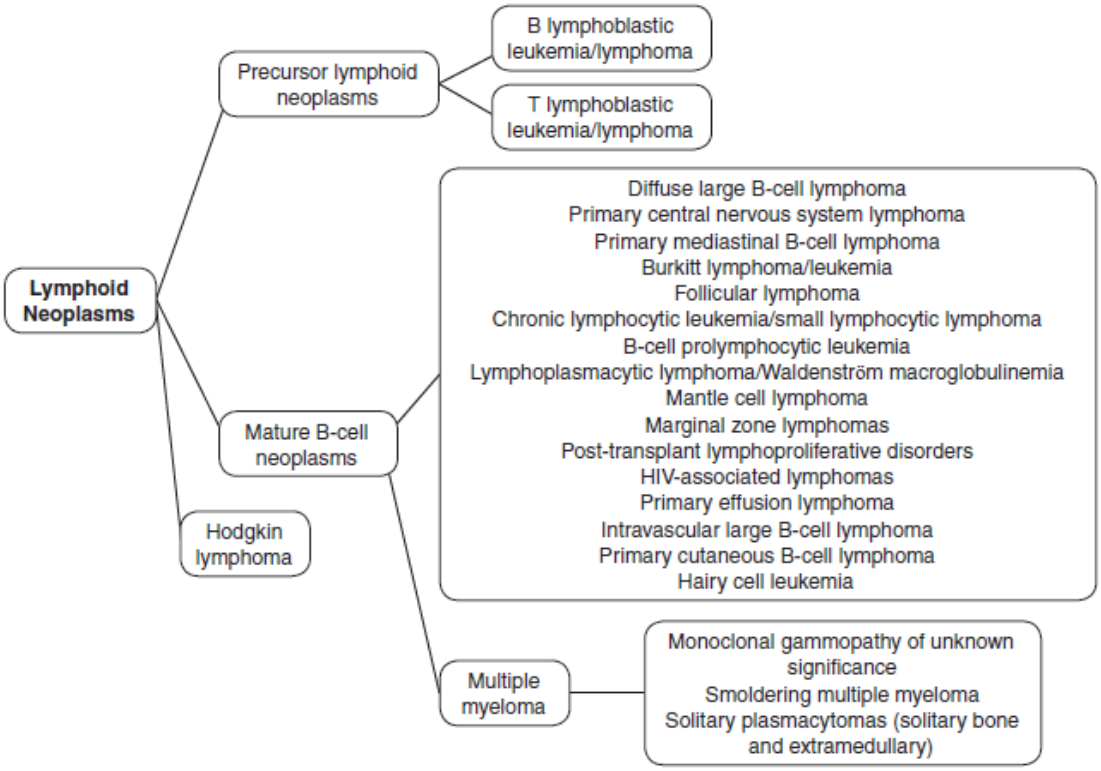

Figure 1.1. Major subtypes of hematolymphoid malignancies as per the 2008 World Health Organization (WHO) classification. It was adapted from the information provided by Jaffe, 2009 (Jaffe, 2009).

The following sections describe the three subtypes of NHLs- CTCL, DLBCL, and NKTCL, in more detail, as my thesis focuses on these NHL subtypes.

1.1.1 Cutaneous T-cell Lymphoma (CTCL)

CTCL is a rare subtype of NHL caused by malignant T-lymphocytes with predominant skin manifestations (Burg et al., 2005). Epidemiological data shows that the incidence of CTCL is continuously increasing (Dalal et al., 2017). Mycosis Fungoides (MF) is the indolent form of CTCL, while Sézary Syndrome (SS) is characterized by a leukemic form of CTCL (Willemze et al., 2005). SS cells are marked with surface expression of L-selectin and C-C chemokine receptor type 7 (CCR7). In contrast, MF cells display skin-homing molecules such as C-C chemokine receptor type 4 (CCR4) and Cutaneous lymphocyte-associated Antigen (CLA) (Clark et al., 2012).

MF is derived from effector memory T-cells and diagnosed as isolated patches of tumors in the skin. Typically, MF steadily progresses from small spots to more infiltrated plaques, a small proportion of which may eventually develop into tumors (Campbell et al., 2010). Even though rare, SS aggressive subtype of CTCL characterized by early systemic dissemination of malignant T-cells (Sézary cells) into the skin, peripheral blood, and lymph nodes (Clark et al., 2012). The course of CTCL is chronic and recurring with survival depending on age at presentation, type of the disease variant, and stage. The survival rate of patients with Stage I and Stage IIA may survive more than 12 years, and while patients with Stage IIB to IV survive less than two years (Wilcox, 2016). Skin directed therapies are effective in early stages; however, advanced stages of the disease require systemic chemotherapies (Aggarwal et al., 2015). Currently, there is no conventional standard of treatment for CTCL (Leuchte et al., 2017).

1.1.2 Natural Killer/T-cell Lymphoma (NKTCL)

NKTCL is rare, but aggressive malignancy of NK cells (Tse and Kwong, 2016). There is a strong predilection about the incidence of NKTCL in Latin American and Asian population. In Asian countries, NKTCL contributes to 6% of lymphoma incidences (Al-Hakeem et al., 2007).

The NKTCL cells are characterized by the expression of $CD56^{+}$on cell surface and possess a repertoire of enzymes involved in cytotoxic activities (Tse and Kwong, 2017). Malignant cells affect multiple tissues, including nose, skin, digestive tract and the testis (Au et al., 1998; Chim et al., 2001; Kwong and Khong, 2011; Takata et al., 2015). Radiation therapy is the first-line treatment for stage I/II patients with an overall response rate of 60%. For NKTCL patients at phase III/IV, chemotherapy is the mainstay therapy, but the relapse rate is very high up to 60% (Cheung et al., 2003; Egashira et al., 1999). NKTCL often poses a risk of high mortality, and patients with aggressive NKTCL involving leukemic form often have meagre survival (< 6 months) (Suzuki et al., 2010).

1.1.3 Diffuse large B-cell Lymphoma (DLBCL)

DLBCL is the most prevalent and aggressive form of NHL and originates from B-cells (Kubuschok et al., 2015). The disease accounts for 30-40% of all NHL cases,

and the overall incidence of DLBCL is 5.6/1,000,000 and with 5- year survival rate of 63.2% (Howlader et al., 2017; Noone et al., 2017).

There are two significant forms of DLBCL- Germinal center B-cell (GCB) and Activated B-cell (ABC) (Nowakowski and Czuczman, 2015). CD10 is one the essential differential marker which classifies DLBCL into GCB ($CD10^{+}$) and ACB ($CD10^{-}$). Oncogenic activation of BCL6, NOTCH2, and deletion of TP53 are common in both sub-groups (Hans et al., 2004).

Generally, old age population (Age>60 years) have a higher incidence than other age groups. Treatment of DLBCL is strategized based on the stage of the disease (localized or advanced). Despite progress in the chemotherapy treatment of DLBCL, patients still experience relapses (Sehn, 2010). The exact reasons for the high rate of relapse and poor prognosis of DLBCL patients are yet to be uncovered and require more research to understand the underpinning characteristics of DLBCL.

1.2 Commonly used chemotherapies for hematolymphoid malignancies

Multiple strategies have been applied to manage hematolymphoid malignancies. These include chemotherapies, radiation therapies, autologous blood transplants, stem cell transplants and immunotherapies. In pure CTCL, skin-directed therapies such as phototherapy are commonly used in treatment.

The following sections describe the commonly used chemotherapies, which constitute the core drug intervention for the treatment of patients with hematolymphoid malignancies.

1.2.1 CHOP

CHOP is combination of four drugs namely, **C**yclophosphamide, doxorubicin hydrochloride (**H**ydroxy daunomycin), vincristine (**O**ncovin) and **P**rednisone. It is the front line of treatment for most NHL subtypes (Coiffier, 2004). Rituximab-CHOP is the standard therapy for DLBCL (Coiffier et al., 2002). Third generation chemotherapy regimens include mBACOD (combination of low dose of methotrexate, bleomycin, doxorubicin, cyclophosphamide, vincristine and dexamethasone), and MACOP-B (combination of leucovorin rescue, doxorubicin, cyclophosphamide, vincristine, prednisone and bleomycin); however, they are associated with high cost and toxicity limiting the success of these therapies (Fisher et al., 1993).

1.2.2 Antibodies and conjugated antibodies

Single antibody agents are currently used in clinics to treat a range of lymphoid neoplasms. Rituximab, a CD20 targeting humanized antibody, is one of the most effective single-agent treatments for DLBCL. A combination of rituximab and CHOP (R-CHOP) enhances the survival rate of patients with DLBCL (Coiffier et al., 2010). Another antibody-drug mogamulizumab, which targets C-C chemokine receptor type 4 (CCR-4), has recently been approved for CTCL patients (Makita and Tobinai, 2017). Antibodies targeting immune checkpoint proteins, such as pembrolizumab (anti-PD-1) (Kwok et al., 2016) and alemtuzumab (anti-CTLA-4), have shown successful outcomes in NKTCL patients (Moreton and Hillmen, 2003).

Anti-CD30 conjugate brentuximab-vedotin (Vonasek et al., 2019) and anti-CD20 antibody conjugate Ibritumomab-tiuxetan have been successful in clinics against CTCL (Mondello et al., 2016).

1.2.3 HDAC (Histone Deacetylase) inhibitors

HDAC inhibitors have shown striking anti-cancer activities in hematolymphoid malignancies (Johnstone, 2002). These inhibitors induce transcription and non-transcriptional effects on cells through the inhibition of de-acetylation of histone complex proteins. Anti-cancer activities of HDAC inhibitors are executed through multifactorial fashions, which include induction of apoptosis, cell cycle arrest, and anti-angiogenic effects (Eckschlager et al., 2017). One of the HDAC inhibitors, vorinostat, gained FDA approval for the treatment of CTCL in 2006 (Mann et al., 2007). Romidepsin, another potent HDAC inhibitors with potency at nanomolar concentrations, was approved for CTCL in 2009 (Furumai et al., 2002; Piekarz et al., 2011).

Other therapeutic agents against lymphoid neoplasms include asparaginase, which is effective against NKTCL (Yong et al., 2009). Small molecule inhibitors, such as Bruton kinase inhibitors **(**ibrutinib) (Deeks, 2017) and PI3K inhibitors (idelalisib & copanlisib) (Markham, 2017; Ramanathan et al., 2016) are used to treat hematolymphoid malignancies. Interferon-gamma and retinoic acid are also used for the treatment of CTCL (Jawed et al., 2014). However, responses to these clinical

interventions are dependent on multiple factors, such as the stage of cancer, genomic heterogeneity, tumor relapse, and occurrence of drug resistance.

1.3 Drug resistance in hematolymphoid malignancies

Intrinsic and acquired drug resistance remain major impediments for the clinical effectiveness of molecularly targeted therapies in hematolymphoid malignancies. Intrinsic resistance is the consequence of pre-existing, stochastic events such as mutations/ amplification/deletion that contributes to chemoresistance. Contrastingly, acquired resistance is the aftermath of adaptation and selection processes in response to therapy.

While the majority of patients respond to standard therapies, the development of acquired resistance is nearly universal, and the majority of patients fail to achieve complete recovery. For example, acquired rituximab-resistance in DLBCL patients confers them being non-responsive to the R-CHOP treatment regimens (Friedberg, 2011; Wilson, 2006). Similarly, both acquired, and de novo resistance to HDAC inhibitors has been described in CTCL patients (Olsen et al., 2007; Piekarz et al., 2009). Thus, the development of resistance to currently approved chemotherapeutics substantially reduces overall survival benefits in these patients. Determining molecular alterations driving resistance to commonly used chemotherapies is, therefore, the first step toward improving their potencies and clinical effectiveness in hematolymphoid malignancies.

1.4 Pro-tumorigenic pathways associated with drug resistance in hematolymphoid malignancies

Genomic alterations, including somatic mutations, amplification, deletion of genes, overexpression and activation of various proteins have been implicated in drug resistance and poor prognosis in hematolymphoid malignancies (Mansoori et al., 2017; Marie, 2001; Xu et al., 2017). Genomic alteration often enhances the proliferative activity of cancer cells (Hanahan and Weinberg, 2011). Genomic lesions in upstream regulators such as JAK/STAT, ERK, and Notch alter the expression of apoptotic genes and subsequently causes defective apoptosis signaling in cancer cells (Catlett-Falcone et al., 1999; Dang, 2012; Mebratu and Tesfaigzi, 2009). Cells with defective apoptosis pathways were resistant to cell death (Tsujimoto, 1998). The down-stream effects of

tumorigenic pathways drive drug resistance and often cause refractory drug response in patients (Mansoori et al., 2017).

The following paragraphs describe some examples of defective signaling pathways associated with chemoresistance in hematolymphoid malignancies, in particular DLBCL, NKTCL, and CTCL.

In DLBCL patients, resistance to R-CHOP therapy is often attributed to the alteration in CD20 expression, and aberrant downstream signaling pathways are major contributors to drug resistance. Other mechanisms include resistance to antibody-mediated cytotoxicity, Fc-receptors polymorphisms (Rezvani and Maloney, 2011), and hyper-activation of NF-κB (Vega et al., 2008) and STAT3 signaling pathways (Huang et al., 2013). A recent study has identified defective B-cell receptor (BCR) signaling pathway (CD79B) and tumor metabolism (Hexokinase 3) and aberrant cell proliferation, migration, invasion and tumor microenvironment (Indoleamine 2,3-dioxygenase (IDO1), chemokine (C-X-C motif) ligand 13 [CXCL13] in chemo-resistant DLBCL (Fornecker et al., 2019), highlighting the molecular complexity of drug resistance in hematologic malignancies.

Traditional chemotherapy and radiotherapy often fail in the treatment of NKTCL (Suzuki et al., 2010). IL-2Rα up-regulation promotes tumor cell proliferation, progression, and chemoresistance in NKTCL (Wang et al., 2013). MAPK/NF-κB pathway mediates high expression of the cytokine IL-2 and an inhibitory protein Programmed Death Ligand 1 (PD-L1), which positively correlates with chemoresistance (Bi et al., 2016; Wang et al., 2018). The oncogenic activation of the Wnt pathway often leads to poor response to chemotherapy in NKTCL patients (Qin et al., 2019a).

Previous reports suggest that the constitutive expression of STAT3 predicts therapy resistance to vorinostat in CTCL patients (Fantin et al., 2008). Another pro-survival pathway, p42/44 MAPK signaling, plays a critical role in HDAC resistance in CTCL (Chakraborty et al., 2013). As compared to DLBCL and NKTCL, limited studies have investigated on the role of tumorigenic pathways in mechanisms of drug resistance in CTCL.

In the past few years, many studies have shown that transporters genes such as ABCB1, ABCC1, and ABCG2 are critical components in chemotherapy resistance (Gottesman et al., 2002; Robey et al., 2018; Sharom, 2008; Tamaki et al., 2011). These genes are involved in the efflux of chemotherapy agents and subsequently protecting cells from cytotoxic effects (Sharom, 2008). Previous studies have shown that de novo expression of MDR genes, impedes the success of cytotoxic chemotherapy in DLBCL (Yagi et al., 2013). ABCB1 expression is induced in DLBCL patients upon chemotherapy treatment (Shen et al., 2011). Similarly, in NKTCL, neoplasms are relatively chemoresistant because of the high basal level expression of P-glycoprotein (P-gp) (Yamaguchi et al., 1995). Hence, CHOP therapy has been replaced by non-anthracycline regimens (Tse and Kwong, 2013). However, in CTCL, MDR genes expression is not associated with drug resistance (Jillella et al., 2000; Robey et al., 2006).

Many groups have shown that ion channels play a critical role in cancer drug resistance. Overexpression of K+, Na+, Ca2+, and Cl- ion channels are often implicated in abnormal proliferation and drug resistance of cancer cells (Duvvuri et al., 2012; Li and Xiong, 2011). These channels are crucially involved in modulation of pro-survival pathways (MAPK signaling), ROS generation, the decay of membrane potential, and caspase activity (Hoffmann and Lambert, 2014; Kischel et al., 2019).

Even though gene profiling studies suggest that ion channels are implicated in disease progression of CTCL and DLBCL, no direct evidence is available on its role in drug resistance (Hu et al., 2019; Magi et al., 2019).

Next-Generation Sequencing (NGS) technologies have accelerated sequencing efforts to decipher gene variants linked to human diseases (Singleton, 2011). Recent studies have identified mutations/alterations in several genes associated with dysregulated apoptotic pathways in lymphoid neoplasms (Manso et al., 2017; Peng et al., 2019). Also, Whole Exome Sequencing (WES) has brought in a radical shift in the identification and characterization of genomic lesions involved in malignant transformation. Major clinical studies on lymphoma using advanced genomic tools in the past few years have shown pivotal roles played by DDX3X and STAT3 in the progression of lymphoid malignancies (Jiang et al., 2015; Kucuk et al., 2015). We hypothesize that these genes may directly or indirectly influence the efficiency of the

cellular apoptotic machinery. Even though these mutations have been identified, but very few are validated.

1.4.1 DDX3X, DEAD-box helicase 3 X-linked

DDX3X is a member of the RNA helicase protein family and performs multiple cellular activities such as transcription, splicing, RNA transport, and translation. DDX3X plays a crucial role in processes, including cell cycle control, stress response, apoptosis, virus infection, and tumorigenesis (Snijders Blok et al., 2015).

DDX3X protein is composed of 662 amino acids and comprises 12 conserved motifs, which are distributed in 2 recA-like domains –the helicase ATP-binding domain and the helicase C-terminal domain (Hogbom et al., 2007). Each motif is attributed to physiological functions of interacting with ATP and RNA for the execution of helicase activities (**Figure 1.2**).

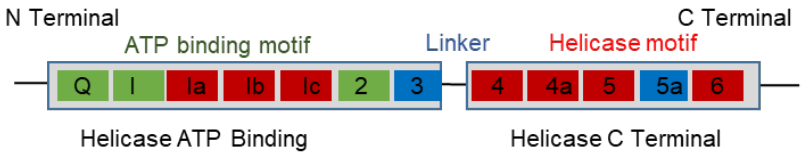

Figure 1.2 An illustration depicting the linear structure of the DDX3X protein. Two domains i) Helicase ATP Binding domain ii) Helicase C terminal domain of DDX3X have a different physiological role and composed of 12 motifs.

Multifunctional roles of DDX3X have been studied in various tumor models. Altered expressions of DDX3X or DDX3X somatic mutations are involved in the pathogenesis and progression of several cancer types, depending on specific tissue/tumor types. DDX3X is considered as a double-edged sword in cancer, as it can either play a role of oncogene or tumor suppressor gene in a context-dependent manner (He et al., 2018). For example, in breast cancer cell lines, DDX3X overexpression promotes proliferation and epithelial-mesenchymal like transformation correlating with tumor progression (Bol et al., 2013).

DDX3X can also function as a tumor-suppressive gene. It enhances the promoter activities of the p21waf1/cip1 gene and increases p21waf1/cip1 expression and thus exerts growth-suppressive effects in hepatocellular carcinoma (Chao et al., 2006). DDX3X loss causes an increase in cyclin D1 in hepatitis virus-associated hepatocellular carcinoma (Chang et al., 2006). In lung cancer, DDX3X loss promotes cancer

progression through the concealment of the MDM2/slug axis (Wang et al., 2009). Similarly, DDX3X depletion promotes colorectal cancer progression through the Snail/E cadherin pathway (Su et al., 2015). DDX3X plays a crucial role in the formation of an anti-apoptotic complex, which inhibits apoptotic signals by interfering with the death receptors (Sun et al., 2008). DDX3X down-regulation promotes tumorigenesis by depleting the miRNAs involved in cancer progression (Chen et al., 2012). DDX3X is involved in the regulation of tumor-suppressive miRNA such as miR-122, miR-200b, miR-145, and miR-200c involved in tumorigenesis in liver cells (Li et al., 2016) (**Figure 1.3**).

DDX3X is the eminently mutated tumor suppressive gene in NK-cell leukemia (Dufva et al., 2018). *DDX3X* mutations were prominently found in Epstein Barr virus^{+} NKTCL (Cai et al., 2019). Recurrent truncated forms of DDX3X have been identified in chronic lymphocytic leukemia (CLL) patients (Landau et al., 2015; Ojha et al., 2015). In another study using 28 Burkitt lymphoma (BL) patients' samples, 9 out of 28 patients were identified with *DDX3X* mutations (Schmitz et al., 2012; Zhou et al., 2019). Somatic mutations of *DDX3X* are prevalent in NKTCL, as Jiang et al. showed that 21 out of 105 NKTCL patients have alterations in *the DDX3X* gene (Jiang et al., 2015). However, the mechanisms and the pathways through which DDX3X is involved in hematolymphoid malignancies remain to be uncovered.

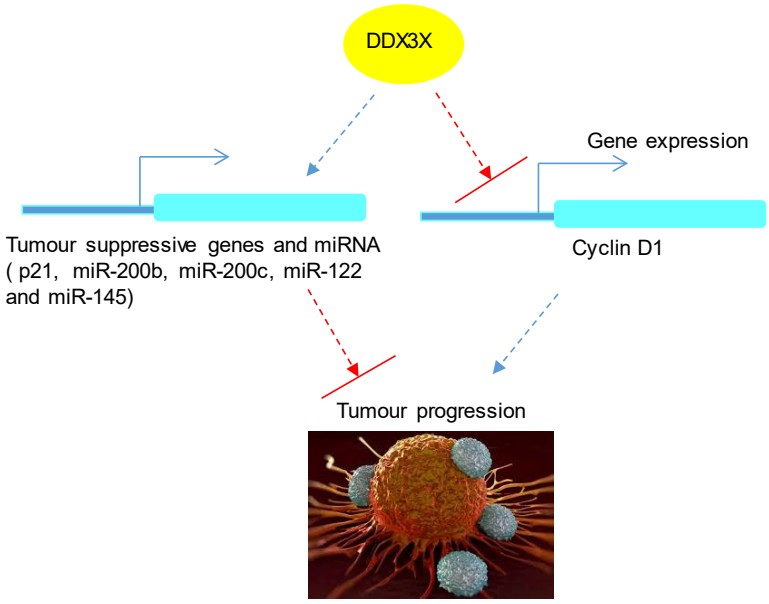

Figure 1.3 An illustration summarizing the tumor-suppressive roles of DDX3X. In liver carcinoma, DDX3X increases the promoter activities of p21 and downregulates cyclin D1 to inhibit tumor growth. In addition, DDX3X controls tumor-suppressive miRNAs (miR-200b, miR-122, miR-145) and suppressing tumorigenesis.

1.4.2 STAT3 (**S**ignal **T**ransducer and **A**ctivator of **T**ranscription **3**)

STAT3 is a transcriptional factor that regulates cell proliferation, differentiation, apoptosis, angiogenesis, inflammation, and Th1/anti-tumor immune responses (Bromberg et al., 1999; Darnell et al., 1994). It has been established that aberrant STAT3 activation causes tumor progression through its influence on the transcription of oncogenes involved in cancer progression. STAT3 is often activated by genetic alterations or triggered by environmental factors, such as carcinogenic chemicals, UV light exposure, infection, and smoking (Liu et al., 2018; Song and Grandis, 2000).

The STAT family proteins consist of highly conserved structures which comprise six domains ***i)*** N-terminal domain (NTD), which stabilizes STAT dimerization and nuclear import; ***ii***) Coiled-coil domain (CCD), which interacts with regulatory proteins; ***iii***) DNA binding domain (DBD), which recognizes and binds to the promoters of target genes; ***iv***) Linker domain (LD) which links DBD and SH2 domains; ***v***) Src-homology 2 (SH2) domain, which is required for the recognition of tyrosine phosphorylation on receptor subunits; and ***vi)*** Transcription activation domain (TAD), which possesses tyrosine and serine phosphorylation sites critical for maximal transcriptional activation of STAT-regulated genes (**Figure 1.4**) (Becker et al., 1998; Lee et al., 2019; Zhang and Lai, 2014). There are two isoforms of STAT3, α, and β. Both isoforms share similar structures except TAD, which is composed of 34 amino acids in β isoform, while α isoform contains 82 amino acids (Lim and Cao, 2006).

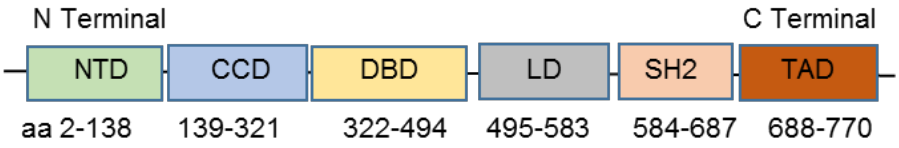

Figure 1.4 An illustration of the structure of STAT3.The STAT3 protein comprises of6 domains, which are important for its various physiological roles. N-terminal domain (*NTD*), Coiled-coil domain (*CCD),* DNA binding domain (*DBD)*, Linker domain (*LD),* Src-homology 2 domain (*SH2)* and Transcription activation domain (*TAD*), are shown.

Phosphorylation of residues, such as Y705 and S727, activates the STAT3 protein, eliciting dimerization and nuclear translocation. This drives the transcription of genes critical for physiological and pathological functions. Classically, STAT3 signaling is triggered by cytokines or growth factors. These receptors then form a complex with glycoprotein 130 (gp130) and Janus Kinases (JAK). STAT3 can be activated by several

non-receptor tyrosine kinases, such as Src or Abl (Firmbach-Kraft et al., 1990; Witthuhn et al., 1994; Yu and Jove, 2004). Once activated, STAT3 drives the cellular expression of *MMP-9*, *c-Myc, Bcl-XL*, and *mcl-1* (Grivennikov et al., 2009; Lee et al., 2009) (**Figure 1.5**).

STAT3 is constitutively active in many tumors, including cells derived from hematolymphoid neoplasms (An et al., 2010). Certain malignant cells possess activated forms of STAT3 upstream regulators due to the translocation of BCR-ABL or somatic mutations in the JAK (Jeong et al., 2008). Mutations in the suppressor of cytokine signaling (SOCS) have also been implicated in STAT3 activation causing defects in pro-apoptotic pathways in cancer (Hou et al., 2017). In addition, the presence of the cytokines and growth factors in the tumor microenvironment activates STAT3 through the JAK/STAT pathway (Hutchins et al., 2013; Tawara et al., 2019).

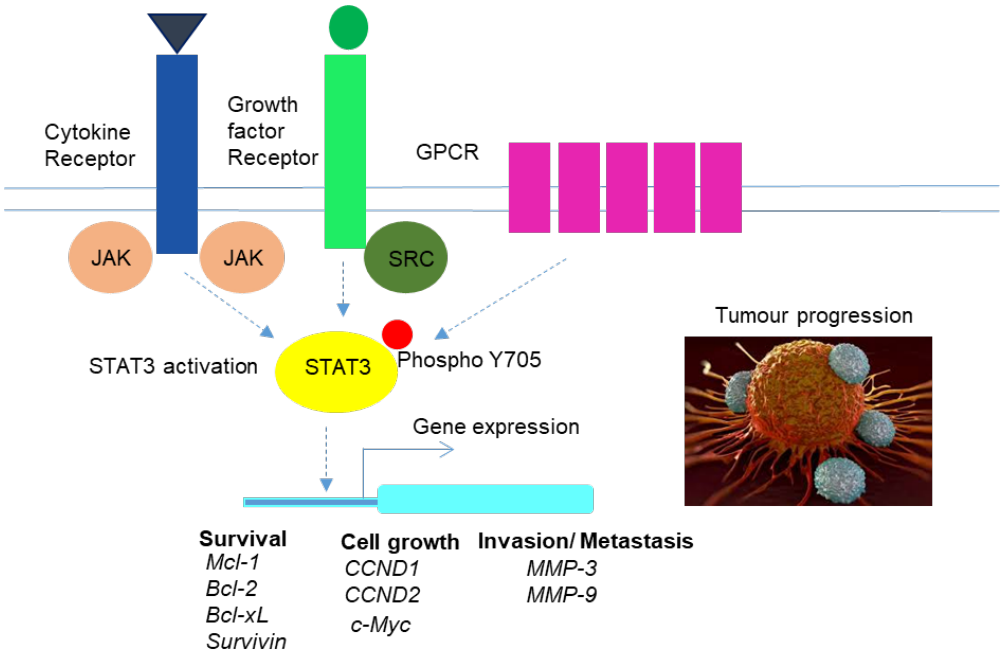

Figure 1.5 A model depicting STAT3 activation and its tumorigenic role**.** Binding of cytokine /growth factors on the corresponding receptor triggers JAK activity, which activates STAT3. Aberrant signaling leads to dysregulation of cell cycle control (*CCND1*, c-Myc), apoptotic (*Mcl-1, BCL-2, BCL-xL,* and *Survivin*) and metastatic genes.

In hematolymphoid malignancies, several mutant variants of STAT3 have been associated with cancer progression. Using online cBioPortal, we identified several mutations in STAT3 in hematolymphoid malignancies (**Figure 1.6**). Activating mutations of STAT3 have been identified in NKTCL, γδT-cell lymphoma (Jiang et al.,

2015; Kucuk et al., 2015), DLBCL (Ohgami et al., 2014), CTCL and in several other NHL patients (Kiel et al., 2014).

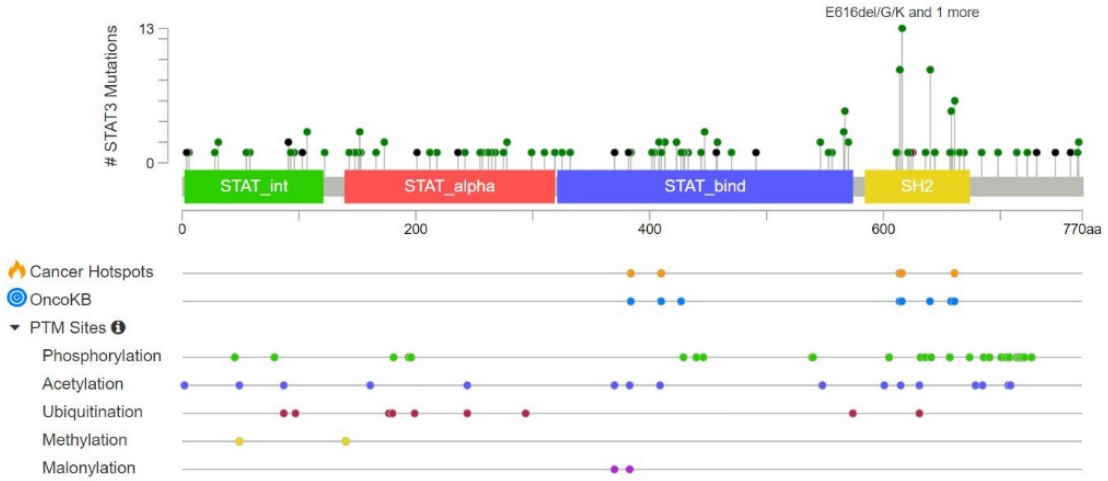

Figure 1.6 Mutational landscape of STAT3 in hematolymphoid malignancies. cBioPortal based mutational analysis indicates frequent mutation of STAT3 in hematolymphoid malignancies and cancer hotpots. Seven and five potential OncoKB sites and hotspots were predicted, respectively. OncoKB is a feature that predicts the oncogenic nature of mutations.

Due to the above-mentioned attributes, STAT3 is an attractive target for pharmacological intervention. While it has been established that STAT3 is a master regulator of tumorigenic pathways and defective apoptosis in cancer, including hematolymphoid malignancies, direct STAT3 inhibitors are yet to be approved for clinical use. This is primarily due to poor pharmacodynamics of peptide inhibitors and non-specific interaction of small inhibitors (Table 1.1). Multiple STAT3-SH2 domain inhibitors, such as Stattic, XPXL, ISS610, STA-21, LL-3, and curcumin have shown anti-cancer activities *in vitro* models, however due lack of potency and selectivity these agents did not reach clinical trials (Edwards et al., 2015; Turkson et al., 2004).

Table 1.1. A list of STAT3 targeted therapeutics and their clinical status. This table is adapted from https://clinicaltrials.gov/ website.

Mode of inhibition of STAT3 function	STAT3 Inhibitors	Status in Clinical trials	Remarks
SH2 domain inhibitors	Stattic	Pre-clinical, in breast, hepatocellular carcinoma	Poor specificity and toxicity profile
	LLL3	Pre-clinical, in glioblastoma	Poor potency
	XPXL	Pre-clinical, in Src-transformed fibroblast	Poor cell permeability & in vivo stability
	OPB-31121	Phase I	Unexpected toxicities
	OPB-51602	Phase I	Unexpected PK properties
	Curcumin	Pre-clinical, in renal cell carcinoma	Lack of specificities and poor PK
	Napabucasin	Phase II	No significant Overall Response Rate
	TT101	Phase I, still recruiting	NA
JAK/ Src inhibitors	SC-43	Phase I, still recruiting	NA
	Dasatinib	Phase II	Toxicities and lack of specificity
	WP1066	Phase I, still recruiting	NA
	AZD1480	Phase I, terminated	Neurological toxicities
STAT3 targeting Oligonucleotides	AZD9150 (Antisense)	Phase II	Promising Overall Response Rate
	STAT3 decoy	Phase 0	Rapid degradation
	STAT3 siRNA	Pre-clinical	Short half-life
	G-quartet (DNA binding)	Pre-clinical	Poor potency

NA, data not available.

OPB-51602 and OPB-31121 have entered early clinical trials, but unpredictable pharmacokinetic profile (PK) and toxicities, including lactic acidosis and peripheral neuropathy, have dampened their prospects (Wong et al., 2015). WP1066, TT101, and napabucasin are currently under phase I trial. Upstream inhibitors such as AZD1480 and

dasatinib have showed toxicity and low efficacy in clinical trials I and II, respectively (Plimack et al., 2013). Other novel strategies include the use of oligonucleotide to target STAT3 using decoy or antisense-based approaches. STAT3 decoy oligonucleotide demonstrated rapid degradation in phase 0 trials (Sen et al., 2012). Thus far, STAT3 targeted oligonucleotide AZD9150 has entered phase II clinical trial displaying remarkable efficacy in lymphoma and NSCLC patients (Hong et al., 2015).

1.5 RNA interference (RNAi) technology to target oncogenes in hematolymphoid malignancies

One strategy to target the aberrantly activated gene is to knock down its expression by RNAi techniques. One of the most commonly applied RNAi techniques is the use of small interfering RNA (siRNA) to post-transcriptionally silence target genes of interest (Hammond et al., 2000). Early efficacy of siRNA molecules in gene silencing in various laboratories led to the exploitation of this promising research tool as a therapeutic agent (Bobbin and Rossi, 2016; Elbashir et al., 2001). But the use of siRNA has been limited due to multiple factors ***i)*** loss of cell viability during electroporation or nucleofection (Mantei et al., 2008) ***ii)*** off-target effects are conventional siRNAs mediated gene depletion (Jackson and Linsley, 2010) ***iii)*** siRNA molecules have shown to trigger unwanted immune responses in vivo (Whitehead et al., 2011) ***iv)*** half-life of siRNA is very short (< 20 minutes) (Zimmermann et al., 2006).

1.5.1 Emergence of Single-stranded DNA based gene-silencing technology

Single-stranded antisense DNA (ssDNA) molecules are a novel class of RNAi agents commonly used as research tools and as therapeutics (Dias and Stein, 2002). This group of RNAi molecules inhibits gene expression via RNase H mediated cleavage of the mRNA in RNA-DNA heteroduplex. RNase H recognizes RNA-DNA heteroduplex and degrades the RNA strand. RNase H1 is a single peptide enzyme, which is responsible for cleavage of target RNA directed by antisense oligonucleotides (Crooke, 2017).

Comparative analysis siRNA and antisense ssDNA molecules revealed that RNase H-dependent cleavage targets the pre-mRNA, whereas siRNAs do not (Juliano et al., 2012; Wang et al., 2016c). However, unmodified ssDNA and siRNA are short-lived owing to susceptibility to nucleases expressed in cells and are often have

insufficient membrane penetration capacity and the low bioavailability. Intrinsic low binding affinity and poor pharmacokinetic (PK) properties of such oligonucleotides dampened the possibility of these molecules to be used as therapeutics (Uhlmann, 2000). Therefore, to improve the stability, delivery, and PK properties of RNAi molecules, several chemical modifications have been suggested (Urban and Noe, 2003). One of the most promising strategies of chemical modifications for applying RNAi technology to the clinic has led to the development of a novel Locked Nucleic acid (LNA) conjugated chimeric ssDNA molecule, called "GapmeR." LNA is a sugar modification in which 4' carbon is bonded to 2'-hydroxy group, forming a 2'4' bicyclic system. The flexibility of furanose structure is compromised and has no conformational isomers (Kurreck et al., 2002). This conformation enhances the hybridization of oligonucleotides to target mRNA and is nuclease resistant.

GapmeR is an ssDNA antisense oligonucleotide conjugated with LNA/cET/2'-O-MOE at the ends. A GapmeR molecule contains a central "gap of 8-10 bases" of antisense DNA which is flanked by modified sugar moiety (**Figure 1.7)** (Castanotto et al., 2015; Fazil et al., 2016). These modifications confer nuclease resistance and aids in unassisted cellular internalization or "gymnosis"(Soifer et al., 2012). Inside the cell, GapmeR forms duplex with mRNA and direct the RNaseH-mediated cleavage, subsequently, causing inhibition of specific gene expression (Liang et al., 2017). Improved target affinity of GapmeR along with sequence specificity can be achieved using upgraded design tools (Dieckmann et al., 2018; Hagedorn et al., 2017).

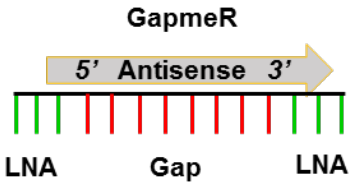

Figure 1.7 An illustration of the structure of a GapmeR molecule. Typically, it contains 3 LNAs as "wings" flanking a central stretch of 8-10 base single-stranded antisense DNA as a "Gap."

1.5.2 RNAi-based therapeutics in clinics

Antisense drugs have amassed immense popularity due to approval and success of antisense oligonucleotides such as fomivirsen and mipoversen, which effectively tackled menace of cytomegalovirus infection and hypercholesterolemia, respectively (Hair et al., 2013). Recently oligonucleotide inotersen was approved by FDA for

neurological disorders (Keam, 2018). Inortersen targets transthyretin, which accumulates to cause peripheral neuropathy and gastrointestinal dysfunction. Hitherto, an antisense drug for cancer, has not been approved.

Currently, several antisense drugs such as cutirsen [2'-O-MOE-PS GapmeR] (Chi et al., 2008), EGFR antisense DNA[PS] (Bauman et al., 2018), trabdersen [2'-O-MOE-PS GapmeR] (Jaschinski et al., 2011), EZN-2938 [LNA-PS GapmeR] (Greenberger et al., 2008) and LErafAON-ETU [DNA-PS liposome] (Dritschilo et al., 2006)are undergoing clinical trials for various cancer forms. The STAT3 targeting antisense AZD9150 [cET-PS GapmeR] is currently under in clinical trial, phase II (Hong et al., 2015).

1.6 Existing gaps in knowledge

An extensive literature survey and regular discussion with collaborators has helped in identifying some of the gaps in knowledge on tumorigenic signaling and its targeting in hematolymphoid malignancies. Very limited studies have reported the involvement of tumorigenic pathways in resistance to HDAC inhibitors in CTCL. This prompted us to investigate the molecular features of HDAC inhibitor resistant CTCL cells.

Recent studies have identified multiple somatic mutations in several genes in a significant proportion of patients with specific subtypes of hematolymphoid malignancies; however, functional involvements of these mutations in disease pathophysiology have not been clearly defined. We have identified that *DDX3X* is frequently mutated in hematolymphoid malignancies, but its exact role remains unknown. Here, we have pursued to explain the potential implication of *DDX3X* mutations in hematolymphoid malignancies. Numerous STAT3 inhibitory modalities are under the pre-clinical phase and clinical trials, yet FDA approval has not been granted. Hence, we sought to develop a novel STAT3 gene silencer with potent anti-cancer activity in hematolymphoid malignancies.

1.7 Hypothesis

The present study was divided into three major parts with the following hypotheses.

H1: The development of drug resistance in hematolymphoid malignancies is a result of acquired defects in pro-apoptotic signaling pathways.

H2: DDX3X plays a crucial role in the aggressiveness and drug resistance in hematolymphoid malignancies.

H3: STAT3 is a master regulator of hematolymphoid malignancies and targeting STAT3 would represent a practical therapeutic approach.

1.8 Aims of the study

Research into the molecular basis of hematolymphoid malignancies has progressed rapidly over the past few years. Key regulatory molecules have been identified, and underlying mechanisms elucidated, providing potential targets for therapeutic intervention. However, molecular changes in drug resistance and the potential involvement of DDX3X in eliciting tumorigenic signaling in hematolymphoid malignancies are not fully understood. Based on our understanding of STAT3's involvement in hematolymphoid malignancies, spectrums of effective molecularly targeted therapeutics have not been explored. Therefore, the three specific aims of the thesis were as follows:

Aim 1: To identify tumorigenic signaling pathways in vorinostat resistant CTCL cells.

In the first part of my study, I asked whether acquired vorinostat resistance in lymphoma cells alters molecular signatures. To address this question in chapter 3 of my thesis, I developed a drug (vorinostat) resistant CTCL cell line ($HuT78_{VR}$) as a cell culture model. I performed RNA-seq, proteomics, bioinformatics, and other molecular analysis.

Aim 2: To investigate the potential involvement of DDX3X in eliciting tumorigenic signaling in hematolymphoid malignancies.

The next question I asked whether DDX3X is involved in hematologic malignancies. To address this question in chapter 4 of my thesis, I correlated DDX3X loss-of-function mutation with the survival of patients with hematolymphoid malignancies. I analyzed the molecular and functional effects of DDX3X loss in CTCL, DLBCL, and NKTCL cells.

Aim 3: To determine STAT3 involvement and develop a novel approach for targeting defective STAT3 signaling pathway in hematolymphoid malignancies.

Finally, I examined STAT3 involvement in the regulation of an immune checkpoint protein PD-L1. I asked whether STAT3 targeted novel antisense molecules can be designed for potential therapeutic applications in hematolymphoid malignancies. In chapter 5 of my thesis, I developed novel gene silencers (GapmeR and epAON molecules) targeting STAT3. I analyzed the efficacy of these gene silencers in inducing apoptosis in cultured lymphoma cells.

Chapter 2

Materials and Methods

2.1 Reagents and antibodies

Details about reagents, antibodies, and assay kits used in this thesis are provided in **Appendix 1**.

2.2 Cells and culture conditions

Peripheral blood lymphocyte (PBL) T-cells were isolated from Leukocyte Reduction System (LRS) cones obtained from healthy volunteers at the Health Science Authority (HSA), Singapore. Stepwise protocol for T-cell isolation has been published as "Isolation of human peripheral T cell lymphocytes", *Methods in Mol Biol,* 2019, that I have authored (Kizhakeyil et al., 2019). Briefly, the blood was diluted with an equal volume of sterilized Phosphate Buffer Saline (PBS). Lymphoprep™ (7 mL) was added to the falcon tube (15 mL), and diluted blood (7 mL) was carefully layered onto Lymphoprep™. The tubes were centrifuged at 1200g for 20 min at room temperature without applying breaks. Peripheral Blood Mononuclear Cells (PBMC), which form a distinct white band near the sample/medium interface, were collected using a Pasteur pipette without disturbing the upper and lower layer (**Figure 2.1**).

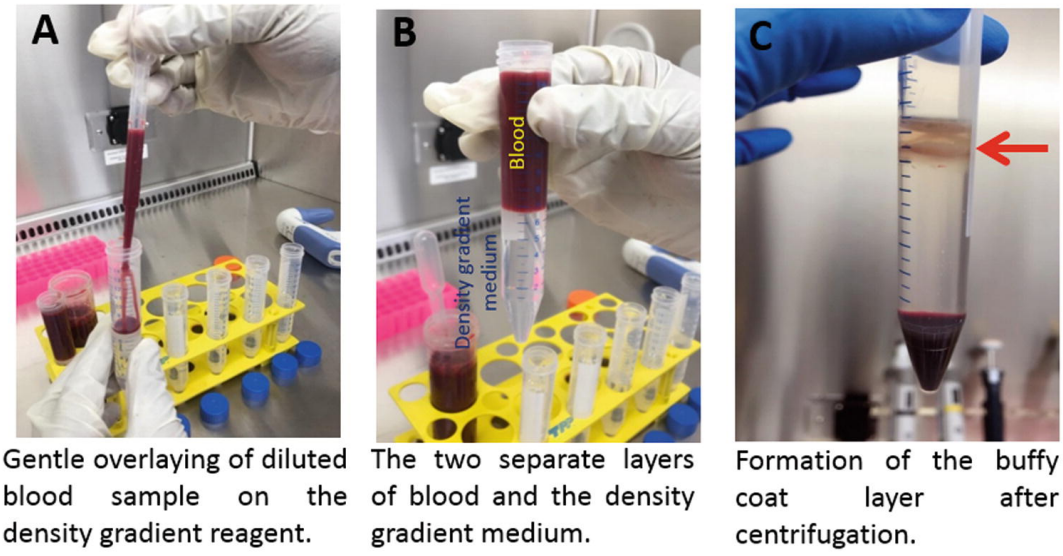

Figure 2.1 Steps of PBMC isolation using density gradient centrifugation. (**A**) A blood sample after dilution in PBS (7 mL) was overlaid on 7 ml of Lymphoprep™. (**B**) Clear demarcation of the blood and the Lymphoprep™. (**C**) Buffy coat interface can be seen as indicated by the red arrow.

PBMCs were washed with PBS at least three times and resuspended in 50 mL of RPMI-1640 medium containing 10% (v/v) heat-inactivated Fetal Bovine Serum (FBS 10%). The cells were transferred and incubated in 150 cm^2 cell culture flask for two h

in an incubator at 37°C in 5%CO_2. PBMCs adhering onto the flasks were discarded, and suspended cells were collected. All experiments were performed as per the guidelines that were approved by the Institutional Review Board (IRB) of Nanyang Technological University Singapore (IRB-2014-09-007, IRB-2016-06-022, and IRB-2018-05-034).

Immortalized cell lines used in this thesis and their culture conditions[#] are summarized in **Table 2.1**.

Table 2.1 A list of cell lines, their origins, and media used for their culture.

S.N.	Cell lines	Sources	Origins	Culture media
1	HuT78	ATCC	Derived from a 53-year-old Caucasian patient with SS	Gibco™ RPMI-1640 with heat-inactivated FBS (10%), Sodium Pyruvate (1 mM) and L-glutamine (2 mM)
2	MyLa	Sigma-Aldrich	Derived from a Caucasian patient with MF	Gibco™ RPMI-1640 with heat-inactivated FBS (10%), Human serum (10%), L-glutamine (2 mM) and 1 ng/ml each of IL-2 and IL-4.
3	MJ	ATCC[*]	Derived from a 50-year-old Caucasian male patient with MF	Gibco™ RPMI-1640 with heat-inactivated FBS (20%) and L-glutamine (2 mM).
4	HH	ATCC	Derived from a 61-year-old Caucasian male patient with SS	Gibco™ RPMI-1640 with heat-inactivated FBS (20%) and L-glutamine (2 mM).
5	Jurkat	ATCC	Derived from a 14-year-old male patient with acute leukemia	Gibco™ RPMI-1640 with heat-inactivated FBS (10%) and L-glutamine (2 mM)
6	K562	ATCC	Derived from a 53-year-old female patient with chronic myelogenous leukemia	Gibco™ RPMI-1640 with heat-inactivated FBS (10%) and L-glutamine (2 mM)
7	NKYS	Obtained from NCCS[*]	Derived from patients with NKTCL	Gibco™ RPMI-1640 with heat-inactivated FBS (10%),

				L-glutamine (2 mM) and 20 ng/ml IL-2
8	SNK1	Obtained from NCCS	Derived from 24-year-old Asian female patient with NKTCL	Gibco™ RPMI-1640 with heat-inactivated FBS (10%), L-glutamine (2mM) and20 ng/ml IL-2
9	SNK6	Obtained from NCCS	Derived from 61-year-old Asian male patient NKTCL	Gibco™ RPMI-1640 with heat-inactivated (10%), L-glutamine (2mM) and 20 ng/ml IL-2
10	Raji	ATCC	Derived from an 11-year-old black patient with Burkitt Lymphoma (BL)	Gibco™ RPMI-1640 with heat-inactivated FBS (10%) and L-glutamine (2mM)
11	Raji shDOXY[$]	Obtained from Dr. Nicholas Grigoropoulos Lab	Derived from an 11-year-old black patient with BL	Gibco™ RPMI-1640 with heat-inactivated FBS (10%), L-glutamine (2 mM) and 1 µg/mL puromycin
12	U2932	Obtained from Dr. Nicholas Grigoropoulos Lab	Derived from a 29-year-old female patient with DLBCL	Gibco™ RPMI-1640 with heat-inactivated FBS (10%) and L-glutamine (2 mM)
13	U2932 shDOXY[$]	Obtained from Dr. Nicholas Grigoropoulos Lab	Derived from a 29-year-old female patient with DLBCL	Gibco™ RPMI-1640 with heat-inactivated FBS (10%), L-glutamine (2 mM) and 1 µg/mL puromycin
14	HBL-1	Obtained from Dr. Nicholas Grigoropoulos Lab	Derived from a 65-year-old male patient with DLBCL	Gibco™ RPMI-1640 with heat-inactivated FBS (10%) and L-glutamine (2mM)
15	HBL-1 shDOXY[$]	Obtained from Dr. Nicholas Grigoropoulos Lab	Derived from a 65-year-old male patient with DLBCL	Gibco™ RPMI-1640 with heat-inactivated FBS (10%) and 1 µg/mL puromycin
16	BJAB	Obtained from Dr. Nicholas Grigoropoulos Lab	Derived from a 5-year-old female patient with BL	Gibco™ RPMI-1640 with heat-inactivated FBS (10%) and L-glutamine (2 mM)

17	BJAB shDOXY[$]	Obtained from Dr. Nicholas Grigoropoulos Lab	Derived from a 5-year-old female patient with BL	Gibco™ RPMI-1640 with heat-inactivated FBS (10%), L-glutamine (2 mM) and 1 µg/mL puromycin
18	BLA4	Obtained from Dr. Nicholas Grigoropoulos Lab	Derived from patients with BL	Gibco™ RPMI-1640 with heat-inactivated FBS (10%) and L-glutamine (2 mM)
19	MuTu	Obtained from Dr. Nicholas Grigoropoulos Lab	Derived from patients with BL	Gibco™ RPMI-1640 with heat-inactivated FBS (10%) and L-glutamine (2 mM)

Note:

All the media were supplemented with antibiotics -Penicillin-Streptomycin (1%).

[#]The cells were always maintained at 37 °C in 5% CO_2.

[*]ATCC- American Type Cell Culture NCCS-National Cancer Centre Singapore

[$]U2932 and BJAB cells expressing tetracycline-inducible DDX3X shRNA constructs were obtained from Dr. Nicholas Grigoropoulos lab [Singapore General Hospital (SGH), Singapore]. DDX3X shRNA expression was induced to knockdown DDX3X in U2392 shDOXY, Raji shDOXY, HBL-1 shDOXY, and BJAB shDOXY cells by treatment with doxycycline (100 ng/mL) and incubating for 48 h.

2.3 RNAi-mediated gene silencing

We applied multiple approaches to knockdown target genes, including *DDX3X* and *STAT3*. These included uses of siRNA, GapmeR, and novel "end-protected Antisense Oligo Nucleotide" (epAON) to deplete expression of the target gene. siRNA molecules are 20-25 bases long double-stranded RNA, which deplete gene expression in RNA Induced Silencing Complex (RISC) dependent manner. GapmeR is a single-stranded DNA molecule that relies on RNaseH activity to silence target genes. We have developed novel epAON molecules that can enter cells in gymnotic fashion and silence target genes. Details of design, synthesis, and protocol for treatment with gene silencers are as follows:

2.3.1 siRNA transfection

siRNA was transfected into cells using nucleofection system (Amaxa 4D-Nucleofector^{TM}system), according to manufacturer's recommendations (Lonza, Muenchensteinerstrasse Basel). Cells (1.0 $\times 10^6$) were resuspended in 20 µL nucleofection buffer (**Table 2.2**) and were transferred into 16 well nucleocuvette. Dharmacon™ Human SMART pool anti-DDX3X siRNA (3 µL) for DDX3X knockdown was added to well-containing cells (**Table 2.2**). ON-TARGET plus Non-targeting Control Pool was used as a mock control. The nucleocuvette was placed on the 4D-Nucleofector core unit and nucleofection programme was performed using pulse codes provided by manufacturers.

Later, 16-well nucleocuvette containing transfected cells were incubated at 37°C in 5%$CO_2$for 2 min. Complete culture medium (80 µL) was added to cells in the cuvette and incubated further for an additional 30 min. Transfected cells were resuspended in 2 mL medium and transferred into 6-well culture plate and incubated at 37°C in 5%CO_2 for 72 h for further analysis.

Table 2.2 A list of nucleofection buffer and pulse code used for the various cell lines.

Cell lines	Type of nucleofection buffers	Solution volume	Supplement volume	Pulse codes
Primary T cell	P3	32.8 µL	7.2 µL	ES111
HuT78, NKYS, MJ, SNK1, SNK6, MyLa	SF	41.1 µL	8.9 µL	DS123
Raji	SF	41.1 µL	8.9 µL	DD124

2.3.2 Design and synthesis of GapmeR and cellular treatments

The details about the design and selection of GapmeR molecules have been published in an article entitled "GapmeR cellular internalization by macropinocytosis induces sequence-specific gene silencing in human primary T-cells" (Fazil et al., 2016). *Detailed "add-and-analyse" protocol of GapmeR-mediated gene silencing in T-cells have been published in the Methods in Molecular Biology (2019), entitled "GapmeR-mediated gene silencing in motile T-cells", which I have co-authored* (Fazil et al., 2019).

GapmeR molecules were designed using "design tool" of Exiqon (Qiagen, Singapore). The primary design parameters include ***i***) optimal target sequence accessibility, ***ii***) antisense off-target evaluation, and ***iii***) optimal oligonucleotide design. The design tool selects target sequences based on local secondary structure prediction, which ensures high potency. Sequence alignments of antisense sequence are screened to avoid off target effects on spliced and unspliced mRNA. GapmeR properties such as length of primary sequence, melting temperature of GapmeR, and self-complementarity positions play decisive role in its antisense activity.

To optimize GapmeR technology in T-cells, we designed GapmeR molecules targeted against CG-NAP, talin, CD11a, PKCζ and stathamin which represented a broad range of molecular mass proteins. Two or more constructs selected against each protein are provided in **Appendix 1, Table A1.2.** GapmeR molecules were synthesized by Exiqon's oligonucleotide synthesis services. Lyophilised GapmeR molecules (5 nMol each) were resuspended in 100 µL RNase free water, aliquoted in microfuge tubes, and stored at -20 °C until further use.

Cells (2×10^5) were seeded in 1 mL RPMI-1640 and transferred into six-well plates. GapmeR molecules were added to the wells containing cells to be treated. Non-specific GapmeR molecules were used as control along with cells without any GapmeR. The concentrations of GapmeR molecules that were used in the experiments were typically in the range of 100 nM – 1000 nM. Optimum concentration of GapmeR for efficient knockdown is based on the gene of interest and cell lines used. Cells were incubated with GapmeR for a period of 72 or 96 h in 37 °C in 5% CO_2 before harvesting for any functional analysis.

2.3.3 Design and synthesis epAON and cellular treatments

In pursuit of novel antisense oligonucleotides, we developed gene silencer "epAON". The epAON was designed by flanking primary antisense sequence as of GapmeR with regions of G quadruplex (GQ) forming nucleotides using WebDSV online tool. The primary sequence is provided in **Appendix 1, Table A1.2**. epAON molecules were synthesised using Integrated DNA Technologies, Singapore.

Lyophilised epAON (25 mg) was dissolved in potassium-containing PBS [2.7 mM KCl] (8 mL) and was aliquoted in PCR tubes (50 µL). The tubes were positioned

on slots of thermocyler (Bio-Rad Laboratories GmbH, Germany) and GQ formation programme was executed as follows: Thermal cycle was set to the following: 95 °C for 5 min; gradual decrease to 55 °C by -0.5 °C/cycle in 80 cycles; 55 °C for 5 min; gradual decrease to 10 °C by -0.5 °C/cycle in 90 cycles.

Cells (2×10^5cells/well in 1 mL RPMI-1640) were into seeded 6-well plates. The gene targeting epAON molecules were added to the wells containing the cells. Non-specific epAON molecules served as control along with untreated cells. The concentrations of epAON molecules used in the experiments were typically in the range of 500 nM -2000 nM. Cells were incubated with epAON for a period of 72 h or 96 h at 37 °C in 5% CO_2 before harvesting for further functional analysis.

2.3.4 shRNA mediated DDX3X knockdown

Three hairpin shRNA constructs, CTL shRNA, DDX3X shRNA#1, and DDX3X shRNA#2 were used to generate shRNA cell lines. The hairpin sequences of the shRNAs are mentioned in **Appendix 1, Table A1.2**. Retroviral packaging plasmids 1μg of pHIT60 (gag-pol, kind gift of Dr. Louis Staudt, National Cancer Institute, USA) and 1μg of pHITEA6*3 (envelope) were used together with 4 μg of a retroviral construct to transfect each 10 cm^2 dish of HEK-293T, after mixing with 1 ml of Opti-MEM media (Invitrogen) and 18 μL of TransIT-293 (Mirus). The viral supernatant was harvested 48h after transfection and filtered through a 0.45 μM filter. For transduction of the lymphoma cell lines, $1\text{-}2 \times 10^6$ target cells were resuspended with viral supernatant and infected by centrifugation (1500 × g, 90 min at 32 °C) with the addition of 10 μg/mL Polybrene (INSIGHT biotechnology) and 25 μM HEPES (ThermoFisher) in 12 or 24 well plates. Viral supernatant was replaced with fresh media immediately after centrifugation. Cells were maintained at 37 °C with 5% CO2 in RPMI supplemented with 10% of tetracycline-free FBS and 1% of Penicillin/ streptomycin for another 48 h and puromycin was added in (1.5 ug/ml) for the selection of transduced cells until the percentage of GFP-expressing cells reached more than 98%. DDX3X shRNA expression was induced to knockdown DDX3X in U2392 shDOXY, Raji shDOXY, HBL-1 shDOXY, and BJAB shDOXY cells by treatment with doxycycline (100 ng/mL) and incubating for 48 h.

2.4 Development and selection of vorinostat resistant HuT78 cells ($HuT78_{VR}$)

HuT78 cells were cultured with stepwise increasing concentrations of vorinostat (50 nM at each step) starting at 10 nM over a period of 4 months. These cells were transferred to 96 well plates and were selected against 2 μM vorinostat. The colony with best cell viability and growth was then passaged in a stepwise fashion, with 100 nM increments until a concentration of 4 μM vorinostat was reached in an additional 2 months. These drug-resistant cells were termed as "$HuT78_{VR}$".

2.5 7AAD staining-based live dead assay

Cells (1.0×10^5) collected after various treatment conditions depending on the type of experiment were centrifuged at 1,500 rpm for 10 min. Cell Pellets were collected, washed with PBS, and resuspended into Falcon™ round-bottom polystyrene tubes. Cell pellets were stained with 100 μL of 7-AAD (500 ng/ml) dye for 5 min at room temperature and analyzed by flow-cytometry. At least 20,000 events per sample were acquired using BD LSR Fortessa X-20 flow cytometer (NJ, USA). Fluorescence emission was collected at 650nm. Cells that stained positive for 7-AAD were gated as dead cells. Data were analyzed and processed using FlowJo® software (OR, USA).

2.6 Rhodamine 123-based drug expulsion assay

HuT78 and $HuT78_{VR}$ cells (1.0×10^5 cells) were resuspended in RPMI-1640 culture medium containing 0.5 μg/mL rhodamine 123 and incubated for 2 h at 37 °C in 5% CO_2. Subsequently, cells were washed with cold PBS (4°C) and analyzed using a BD LSR Fortessa X-20 flow cytometer (NJ, USA). Fluorescence emission was collected at 525 nm. Data were processed using FlowJo® software (OR, USA).

2.7 Cell cycle analysis

Cells (1.0×10^5) collected after various treatment conditions depending on the type of experiment were centrifuged at 1,500 rpm for 10 min. Cell pellets were washed and resuspended in 70% ethanol and incubated overnight at -20 °C. Subsequently, cell pellets were collected, washed with PBS (pH 7.2) and resuspended in 500 μL staining solution [0.1 mg/mL Propidium Iodide (PI) and 0.6% Triton-X in PBS] to which 500 μL RNase A solution (200 U/mL in PBS) was added. Cells were stained for 30 min at 37 °C in 5% CO2 and were subsequently examined using a BD LSR Fortessa X-20 flow

cytometer (NJ, USA) in PE channel. Data was analysed and processed using cell cycle platform in FlowJo® software (OR, USA).

2.8 Dihydro ethidium (DHE) assay for evaluating reactive oxygen species (ROS)

Cells (1.0×10^5) collected after various treatment conditions depending on the type of experiment were centrifuged at 1,500 rpm for 10 min. Cellular pellets were collected, washed with PBS (pH 7.2) and resuspended in 100 µL of DHE (5 µM) and incubated at room temperature for 20 min. PBS (200 µL) was added to cells and cells were analyzed using a BD LSR Fortessa X-20 flow cytometer (NJ, USA).Fluorescence emission was collected at 578 nm. Cells positive for DHE staining were gated as positive for presence of ROS. Live cells were gated based on PI-based staining. Data were analysed and processed using cell cycle platform in FlowJo® software (OR, USA).

2.9 Tetra Methyl Rhodamine, Methyl ester (TMRM) assay for evaluating mitochondrial membrane potential

Cells (1.0×10^5) collected after various treatment conditions depending on the type of experiments were centrifuged at 1,500 rpm for 10 min. Cell pellets were collected, washed with PBS (pH 7.2) and resuspended in 100 µL of TMRM solution (1 µM), and incubated at room temperature for 20 min. PBS (200 µL) was added to cells and cells were analyzed using a BD LSR Fortessa X-20 flow cytometer (NJ, USA). Fluorescence emission was collected at 615 nm. Cell stained positive for the TMRM were gated as mitochondrial membrane intact cells. Data were analyzed and processed using cell cycle platform in FlowJo® software (OR, USA).

2.10 MTS-based cell viability assay

Cell viability was determined by using CellTiter 96® aqueous One solution cell proliferation assay kit as per manufacturer's instructions (Promega, WI, USA). Briefly, Cells (1.0×10^4 cells) in 100 µL medium were seeded in triplicates in a 96-well plate according to treatment condition. MTS solution (20 µL) was added into each well and incubated at 37 °C in 5% CO_2 for 3-4h. Absorbance at 490 nm was measured using a Cytation 3 micro-plate reader (BioTek, VT, US). The $OD_{490\ nm}$ of untreated cells was normalized as 100%.

2.11 Annexin V/PI-staining based flow cytometry analysis

Apoptotic cells were evaluated using Alexa Fluor® 488 Annexin V/Dead Cell Apoptosis Kit according to manufactures instructions (Thermo Fisher Scientific, WA, USA). After, the completion of treatment, cells (1.0×10^5 cells) were centrifuged at 1,500 rpm for 10 min. Pellets were collected, washed with PBS and resuspended 100 µL Annexin binding buffer containing (5 µL FITC-conjugated annexin-V and 1 µL of propidium iodide) and incubated in ice for 20 min. These cells were subsequently analysed using a BD LSR Fortessa X-20 flow cytometer (NJ, USA). Fluorescence emission was collected at 499 nm and 617 nm, respectively. Data were analysed and processed using cell cycle platform in FlowJo® software (OR, USA).

2.12 Determination of RNA concentration

The RNA contents in cell lysates were determined using NanoDrop 2000/2000c instrument (Thermo Fisher scientific, Massachusetts, USA). Briefly, 1 µL elution buffer was loaded on the pedestal and blank reading for RNA quantification programme was executed as auto zero. Subsequently, cell lysate was loaded on the pedestal and optical density was recorded at 280 nm and 260 nm. The concentration was automatically calculated and displayed on the tab of the NanoDrop software.

2.13 Agarose gel electrophoresis

Agarose gel (1%) was prepared by dissolving 0.5 g of Agarose in 50 ml Tris Acetate Ethylene diamine tetra acetic acid (TAE) buffer (**Appendix 2, table A2.5**). The mixture was heated using microwave oven for 1 minute and 1 µL of SYBR safe was added upon cooling of the gel. The molten mixture was slowly poured on the horizontal gel casting tray unit (Bio-Rad, 27 International Business Park, Singapore). Once the gel was polymerized, it was soaked in 1X TAE buffer. Oligonucleotide samples (10 µL) mixed with 6X loading dye (2 µL) were pipetted into the wells of the agarose gel and placed on Mini-Sub Cell GT unit tray (Bio-Rad, 27 International Business Park, Singapore). Electrophoresis was carried out at 150 V / 25 mAmp (Biorad PowerPac) for ~10 min. DNA bands were visualized image using ChemiDoc (Bio-Rad, 27 International Business Park, Singapore)

2.14 Quantitative reverse transcription polymerase chain reaction (qRT-PCR)

Detailed stepwise protocol has been published in the Methods in Molecular Biology (2019) entitled "Quantitative real time PCR for transcriptional changes in T-lymphocytes", for which I am the first author (Kizhakeyil and Verma, 2019). Briefly, cells (3.0×10^5) from different treatment conditions were centrifuged at 8,000 rpm for 10 min. Total RNA was extracted using BioBasic Inc Ez-10 spin column total RNA mini-preps super kit (Ontario, Canada) or RNeasy isolation kit (Qiagen, Hilden, Germany) according to the manufacturer's instructions. The cDNA was synthesised using M-MuLV Reverse Transcriptase and oligo DT primer from New England BioLabs (MA, US) and Promega (Wisconsin, US), respectively. The composition of cDNA master mix is provided in **Appendix 2 Table A2.6**. The qRT-PCR was performed using 2X SYBR master mix using per manufacturer's instructions (Primer Design, Camberley GU15 3AD, U K) and primer sets provided in **Appendix 1 Table A.1.3**. SYBR® Green PCR Master Mix was mixed as mentioned in **Appendix 2 Table A2.7**. Applied Biosystems thermocycler (CA, USA) was used to synthesis cDNA as per instructor's manual. Thermal cycle was set to the following: 95 °C for 10 mins; (95 °C for 15 s; 60 °C for 1 min; 95 °C for 15 s) x 40 cycles ; 95 °C for 15 s; 60 °C for 1 min (gradual increase to 95 °C for 5 mins); 95 °C for 15 s**.**

2.15 Quantification of miRNA

The miRNA quantification was performed using the miRCURY LNA RT PCR kit II (Exiqon, Denmark). Polyadenylation of miRNA and reverse transcription reaction step were carried out in a single step. Total mRNA was extracted using BioBasic Inc Ez-10 spin column total RNA mini-preps super kit (Ontario, Canada) or RNeasy isolation kit (Qiagen, Hilden, Germany) according to the manufacturer's instructions. Template (5ng/ul) RNA was used to cDNA. The composition of reverse transcription master mix is listed in **Appendix 2 Table A2.8**.

Reverse transcription thermo-cycling parameters were as follows: 42 °C for 60 min and 95 °C for 5 min. The reaction mixture consisting of amplified cDNA was stored at 4 °C. The cDNA template was diluted (60X) in RNase free water. Quantitative PCR was performed using the miRCURY LNA SYBR green PCR kit (Exiqon, Denmark) with miR150 and U6 miRNAs as an internal control (**Appendix 2 Table A2.9)**.The reaction setup of miRCURY LNA miRNA PCR was as follows:

Thermal cycle was set to the following: 95 °C for 2 mins; (95 °C for 15 s; 55 °C for 1 min; 95 °C for 15 s) x 40 cycle; 95 °C for 15 s; 60 °C for 1 min (gradual increase to 95 °C for 5 mins); 95 °C for 15 s**.**

2.16 Cell lysis for quantification of protein

Cells (3.0×10^5) collected after various treatment conditions depending on the experiments were centrifuged at 8,500 rpm for 10 min. Cell lysis buffer (CLB)was added to the pellets and incubated on ice for 1 h (**Appendix 2 Table A2.4**). Cellular debris were removed by centrifugation at 13,000 rpm for 15 min at 4°C. Clear supernatant was collected and stored at -80 °C.

2.17 Determination of protein concentration

Amounts of protein in cellular lysates were estimated using Bradford assay kit according to manufacturer's instructions (Bio-Rad Laboratories GmbH, Germany). Briefly, 1 µl of each cell lysate/bovine serum albumin (BSA) standards were mixed with 100 µl of Bio-Rad staining solution (diluted 1:5) and incubated for 5 min at room temperature. Absorbance at 595 nm was measured using a Cytation 3 micro-plate reader (BioTek, VT, US). Standard curve was plotted using BSA standards. Absorbance values at OD_{595nm} of corresponding BSA concentrations were plotted to derive straight line equation. Protein concentration was calculated using BSA standard curve.

2.18 Immuno-precipitation (IP)

IP is a method to identify molecules that interact with specific proteins. Cell lysate (300 mL) was mixed with 5 µL of primary antibody. This mixture was incubated overnight at 4 °C with gentle mixing on a rocker-shaker. Rabbit or Mouse IgG antibody, depending on the species of the bait antibody was used as a control. To each tube, 30 µL of the protein A agarose beads were added. Samples incubated at 4 °C with gentle mixing on a rocker shaker. The immuno-precipitated complexes were collected by centrifugation at 3,000×*g* for 2 min at 4 °C. Supernatant was discarded and the pellets were washed 5 times with 1 ml CLB by centrifugation at 3,000×*g* for 2 min. Each pellet was resuspended in 25-100 µL Laemmli sample buffer (**Appendix 2 Table A2.12**) to a final concentration of 1X sample buffer and boiled at 95 °C for 5 min. These samples were centrifuged for 1 min at 12,000×*g* at room temperature and clear supernatant (IP sample) was collected. These IP samples were stored at -70 °C for further use.

2.19 Sodium Dodecyl Sulphate-Polyacrylamide gel electrophoresis (SDS-PAGE)

Protein levels and their phosphorylation status were evaluated using western immunoblotting. SDS-PAGE is the first step prior to immunoblot assay. Protein (10µg) from cellular extracts was heated with 5X Laemmli sample buffer (**Appendix 2 Table A2.12**) for 5 min. The gel apparatus (ATTO Corporation, Japan) was assembled according to the manufacturer's instructions. The gel was quickly poured in between the two glass plates until the acrylamide solution reached 1 cm below the plastic combs. The gel solidifies in approximately 20 min at room temperature. The components of resolving gel and stacking gel are provided in **Appendix 2, Table A2.10** and **A2.11,** respectively. The stacking gel solution was poured on top of the resolving gel. The plastic combs were inserted into the stacking gel to make protein sample loading wells. The combs were removed from the gel, and any gel lanes that were not straight were straightened using a gel-loading tip. Gels were placed into the electrophoresis box that was filled with 1X SDS-PAGE running buffer (**Appendix 2, Table A2.13**). Equal amounts of protein samples and the protein molecular weight ladder were loaded into the wells. Electrophoresis was carried out at 300 V / 25 mA using Biorad PowerPac per gel for ~ 1.5 h until the dye front had reached just above the gel base, at which stage electrophoresis was discontinued.

2.20 Western Immunoblotting

Resolved proteins on the SDS-PAGE were transferred to polyvinylidene fluoride (PVDF) or Nitrocellulose (NC) membrane using wet transfer technique according to the manufacturer's instructions (Bio-Rad, 27 International Business Park, Singapore). The PVDF membrane (0.45 µm) was activated by soaking it in methanol for 1 min. NC (0.20 µm) membrane does not require pre-activation with methanol. The membranes were then immersed in transfer buffer (**Appendix 2, Table A2.14)** for 10 min at room temperature. A gel sandwich was made by placing 4 sheets of Whatman 3 mm filter paper (pre-soaked in transfer buffer) in cassette along with sponges. The PVDF/NC membrane was then placed on top of the filter papers and kept moist by flooding it with transfer buffer. The gel was then placed on top of the membrane and any air bubbles between the gel and membrane were carefully removed. Another 4 sheets of Whatman 3 mm filter (pre-soaked in transfer buffer) and sponge were placed on top of the gel. The cassette was tightly secured and placed in the Western blotting transfer apparatus

containing transfer buffer and ice packet. Electrophoretic transfer of proteins was performed for ~90 min at 100 mAmp / 300 V per gel using Biorad PowerPac.

2.21 Immuno-detection and development of blots

After blotting of proteins on the membrane, non-protein bound sites on the PVDF membrane were blocked by incubating the membrane in freshly prepared 5% non-fat milk in PBST (Blocking solution, **Appendix 2**) for 1 hour at room temperature with constant gentle agitation. Blots were washed three times with 0.1% Tween in PBS (PBST) and incubated with appropriate primary antibodies (diluted according to the manufacturer's instructions in blocking buffer) overnight at 4°C with constant agitation (**Appendix 1, Table A1.4**). Following incubation with the primary antibody, blots were washed five times with PBST to remove any unbound antibody. Blots were then incubated with the relevant horseradish peroxidase (HRP)- conjugated secondary antibody (diluted according to the manufacturer's instructions in blocking buffer) for 1 h at room temperature with constant agitation. Unbound secondary antibody was removed by washing the membrane 5 times with PBST for 10 minutes.

Western Lightning® Plus enhanced chemi-luminescence reagent (PerkinElmer, MA, USA) or Amersham western blot ECL (GE, Chicago) was used to visualize the immunoreactive bands using light-sensitive film. Membranes were then exposed to Kodak film for the appropriate time-period (range 15 sec to 10 min). Exposed films were developed using an automatic developer machine (Compact2, protech medical system, SMITECH Asia, Singapore). Alternatively, immuno-reactive bands were visualized using ChemiDoc (Bio-Rad, 27 International Business Park, Singapore) and images were captured for densitometric quantification. Densitometric analyses of the western blots were performed by using Image J software (Research Services Branch, National Institute of Mental Health, Bethesda, Maryland, USA). The relative values of the samples were determined by giving an arbitrary value of 100.0 to the respective control samples of each experiment.

2.22 Enzyme-Linked ImmunoSorbent Assay (ELISA)

The levels of secreted cytokines were evaluated by ELISA according to manufacturer's recommendation and details are provided in **Appendix 1, Table A1.5**. Nunc MaxiSorp plates was coated with a capture antibody by adding 50 µL of 1X capture antibody

resuspended in coating buffer and was incubated overnight at 4 °C. Next, the wells were washed 3 times with 300 µL of washing buffer (PBS). The wells were blocked with 50 µL of blocking buffer and were incubated for 1h at room temperature. Next, plates were washed and 50 µL of standards/ cell culture supernatants/ diluted serum were added to the wells and incubated overnight at 4 °C or 2 h at room temperature. The plates were washed 4 times and 50 µL of detection antibody was added and was incubated for 1 h. Later, the plates were again subjected to washing and 50 µL of streptavidin-HRP was added to wells and incubated for 20 min. The plates were washed for 3 times and the remaining buffer was soaked by placing the plates on tissue for 1 min. 50 µL of 3,3',5,5'-Tetramethylbenzidine (TMB) solution was added to each well and were then incubated for 20 min. Stop solution (25 µL) was added to each well, and plates were read at OD_{450} and OD_{570} using a microplate reader. The standard curve was plotted using absorbance values of concentration standards provided by manufacturers (**Appendix 1, Table A1.5**). Based on this equation, concentrations of probed cytokines were determined.

2.23 High Content Analysis (HCA)

A 96-well tissue-culture plate was coated with poly L-lysine (PLL) or goat anti-human IgG Fc. Plates were washed three times with PBS and stored at 4°C containing 100 µL PBS in each well for further use. Cells were transferred to the pre-coated plates and were incubated for 1 h at 37°C in a cell incubator. Cells were fixed by adding 4% paraformaldehyde (PFA), permeabilized in 0.5% Triton-X100 and stained for tubulin, actin, and nucleus. Plates were scanned using an automated microscope (IN Cell Analyzer 2200 HCA platform, GE Healthcare, Buckinghamshire, England). Images were analysed using IN Cell Investigator software (GE Healthcare) that automatically quantified cell number and cell 1/form factor.

2.24 Confocal microscopy

Cells were visualized using confocal imaging. Cells (3.0×10^4) collected after various treatment conditions depending on the experiments were allowed to adhere on the Nunc™ Lab-Tek™ II Chamber Slide™ System (Thermo Fisher Scientific, Singapore). The cells on the slides were fixed by 4% paraformaldehyde (PFA) for 30 min. Cells were washed twice in PBS and were permeabilized with 0.3% Triton X-100. The slides were blocked by the addition of blocking buffer (3 % v/v serum in PBS). A cover slip was placed on top of the slide and incubated for 30 min at room temperature.

Unbound goat serum was removed by carefully washing the slide three times in PBS. The diluted primary antibody solution (1: 100 in blocking buffer) was added to the cells on the slide and was incubated for 2 h at room temperature. The unbound primary antibody was removed by washing with PBS. The appropriate secondary antibodies with fluorescent conjugates (1:200 in blocking buffers) and/or nuclear stain were added to the cells on slide and incubated for 1 h at room temperature in the dark. The slides were finally washed three times in PBS. One drop of DAKO mounting medium (Dako A/S, Denmark) was placed on top the fluorescently stained cells and a coverslip was mounted on the slides. Slides were then immediately analyzed or alternatively stored at 4°C in the dark and analyzed later. Fluorescence microscopy was performed by Zeiss confocal workstation attached to Zeiss LSM 800 laser module (Carl Zeiss, Thornwood, NY). Images were acquired and processed using Zeiss software (Carl Zeiss). At least 5 different microscopic fields were observed for each sample.

2.25 Cell migration and invasion assay

In vitro migration assay was carried out using the Corning 5.0 µm pore Polycarbonate Membrane Insert (Corning, NY, USA) in a 24-well plate, as per the manufacturer's recommendations. Briefly, 1.5×10^5 cells were serum starved for 2h and seeded in 200µL of serum free medium in the upper chamber, which was pre-coated with BD Matrigel™ Basement Membrane (BD science, Singapore) as per instructions in manual. The corresponding lower chamber was filled with 500 µL 10% human serum media. Cells were allowed to migrate for 24 h, and cells migrated to the lower chamber were transferred to a PLL coated 96-well plate, fixed with 4% paraformaldehyde and stained with Hoechst 33342 for quantification using HCA.

2.26 Real-time chemotaxis assay

The chemotaxis assay was performed using A special type of plate an electronic "cell invasion/ and migration plate" (CIM-Plate® 16) (ACEA Biosciences) were used to perform real-time chemotaxis assay. The CIM-Plate® 16 is a 16-well electronically integrated Boyden chamber composed of upper and lower chambers. The base of the upper chamber is a polyethylene terepthalate (PET) microporous membrane that allows cells to migrate towards the chemoattractant in the lower chamber. The bottom side of the PET membrane is coated with gold microelectrode sensors that generate "impedance" signals based on cell adhesion and migration. Impedance signals are

captured in real-time enabling a quantitative kinetic measurement of cell migration from the upper chamber to the lower chamber. This plate consists of 16-well inserts which are coated with gold electrodes that detect electrical impedance.

These plates were assembled by CIM assembly tool that has demarcated indentations for holding lower chambers. Membrane inserts of the wells were coated with diluted IgG-Fc solution (50 µL) was incubated overnight at 4°C. Next day, the wells were washed with PBS and 50µL of rICAM-1 solution was added to the plate which was incubated at 37°C cell culture incubator for 2 h. The upper chamber of the CIM-Plate 16 was detached and 165 µL pre-warmed medium containing chemo-attractant (50 ng/mL SDF1α) fill in each well of the lower chamber. The plates were staged on the cradles and "Run" was pressed in the control unit software take the background reading. The values obtained as the background impedance of cell culture media were used as reference impedance for calculating "Cell Index". Plate from the RT analyzer cradle was taken out and medium was removed from all the wells. The pre-treated activated T-cells or HuT78 cells (1 X 10^6) resuspended in 100 µL medium were added to each of the wells. T-cell LFA-1 activation buffer (5 µL of 1 M $MgCl_2$ and 1.5 µL of 0.5 M EGTA) were added to the wells of the CIM-Plate 16. Intuitive software automatically calculates "Cell index", performs statistical analysis (average and standard deviation) and plots the values in real-time as a function of time.

2.27 RNA-seq analysis

Total RNA was extracted using RNeasy isolation kit (Qiagen, Hilden, Germany). RNA integrity was assessed using 2100 Bioanalyzer (Agilent, California, USA) and paired raw reads were generated using the HiSeq 2500 (Illumina) platform by NGS services facility of NovogeneAIT (NovogeneAIT Genomics Singapore Pte Ltd, Singapore). These raw reads uploaded onto the National Supercomputing Centre (NSCC) Singapore server and aligned using the HISAT2 version 2.1.0 algorithm (Kim et al., 2015). Subsequently, the aligned sequences were sorted using SAM tools 1.3 (Li et al., 2009). Using feature counts, a program under the Bioconductor package "Rsubread", the mapped reads were counted for genomic features such as exons and chromosomal locations (Liao et al., 2013). The summarised output table was fed into another Bioconductor package "DESeq2", which uses a negative binomial distribution model to test for differential expression (Love et al., 2014). Differentially expressed

genes (DEGs) were identified using a cut-off of 2-fold change and a false discovery rate (FDR) of less than 0.05. The gene list generated was also put through Ingenuity Pathway Analysis, IPA (QIAGEN Inc.) to identify top diseases and functions as well as pathways associated with the genes that are significantly expressed.

2.28 Stable isotope labelled amino acid in cell culture-based proteomics analysis (SILAC)

SILAC Proteomic analysis was performed in collaboration with the Bioprocessing Technology Institute Singapore. Briefly, HuT78 and HuT78$_{VR}$ cells were grown in light ($^{12}C_6$ L-Lysine) and heavy ($^{13}C_6$ L-Lysine) labelled media for at least three passages in SILAC protein quantitation kit (LysC) RPMI-1640 according to manufacturer's recommendation (Thermo Fisher Scientific, Massachusetts, USA). Cells were lysed in 5× pellet volume of lysis buffer (5% sodium dodecyl sulfate, 50 mM Tris, pH 7.5), sonicated on ice at max power (UP50H Ultrasonic Processor, Hielscher) for 3× 10 s pulses with 30 s pause in between, and clarified by centrifugation at 16,000×g for 10 min. Protein concentration was measured using Pierce BCA Protein Assay Kit (Thermo Fisher Scientific, Massachusetts, USA). Equal amount of heavy- and light-labelled sample pairs were mixed, and an aliquot of 35 μg from each mixed sample was reduced with 20 mM dithiothreitol (DTT) for 5 min at 95°C before being fractionated on a 10% SDS-PAGE gel (Bio-Rad). A total of 8 bands were excised from each sample lane. Sample gel pieces were washed thrice with wash buffer (50% acetonitrile (ACN), 25 mM NH_4HCO_3) and twice with ACN, and air-dried before incubation with 25 mM DTT in 50 mM NH_4HCO_3 for 1 h at 56°C and with 50 mM iodoacetamide in 50 mM NH_4HCO_3 for 30 min in the dark. Gel pieces were washed with wash buffer and ACN as before, and air-dried prior to digestion with 10 ng/μL trypsin (Promega) in 25 mM NH_4HCO_3 for 16 h at 37 °C. Peptides were extracted by sonicating the gel pieces in an ultrasonic water bath for 5 min, in existing digestion buffer then in extraction buffer (5% formic acid (FA), 50% ACN). Both extracts were pooled, dried in vacuum concentrator (Labconco) and dissolved in loading buffer (1% FA, 2% ACN).

Samples were subsequently analyzed by tandem mass spectrometry (LC-MS/MS) using a nanoACQUITY UPLC System (Waters) coupled to an Orbitrap Elite MS (Thermo Fisher Scientific). Peptides were loaded onto a Symmetry C18 trapping column, 5 μm, 180 μm × 20 mm (Waters) at 8 μL/min for 8 min with 99% Buffer A

(0.1% formic acid) and 1% Buffer B (0.1% formic acid in acetonitrile), and separated on ACQUITY UPLC Peptide BEH C18 column, 1.7 µm, 75 µm × 200 mm (Waters) at 300 nL/min with a gradient of 5-50% B over 100 min and 50-90% B over 10 min. MS data was acquired in data dependent and CID top 10 mode. Full scan MS spectra from m/z 350 to 1,600 were performed followed by sequential MS/MS scans of the 10 most intense peptide ions, with the exclusion of singly charged ions and ions with unassigned charged state. Normalized collision energy for MS/MS was set at 35 V, minimum signal threshold at 1,000 ion counts, isolation width at 2 m/z, activation time at 10 ms, and dynamic exclusion duration at 60 s. Raw MS data files were processed by Proteome Discoverer 2.2 (Thermo Scientific) with percolator node against UniProt human proteome database. Mass tolerance was set at 10 ppm for precursor mass and 0.6 Da for-fragment ion mass, with maximum 2 missed cleavages allowed for full trypsin digest. Carbamidomethylation modification of cysteine was set as static modification; SILAC (^{13}C6) modification of lysine, oxidation of methionine and acetylation of protein N-terminus were set as variable modifications. Unique and razor peptides were used for quantification and samples were normalized by Total peptide amount. Proteins were identified at 1% false discovery rate (FDR) with a minimum of two unique peptides.

2.29 Online repositories, Bioinformatics tools and *in-silico* tools

2.29.1 cBioPortal

The cBioPortal (https://www.cbioportal.org/) for cancer genomics is online repository of cancer genomics data which includes molecular profiling data of cancer tissues and cell lines and genomic features of the corresponding cancer tissues. The portal can be used to extract graphical summaries of gene-level data from multiple platforms, network visualization and analysis, survival analysis, patient-centric queries, and software programmatic access. The cBio Cancer Genomics Portal enables the retrieval of the mutational landscape of genes in specific or pan cancer studies, which can be defined by the user themselves.

2.29.2 International Cancer Genome Consortium (ICGC) portal

The ICGC (https://dcc.icgc.org/) is a comprehensive and holistic data portal on information on genomic lesions in different forms of cancer. This multi-institutional collaborative cancer project employs inter-disciplinary tools and techniques to compile

a wide range of somatic mutations, including single nucleotide mutations, small insertions/deletions, copy number alterations, translocations and other chromosomal structural rearrangements.

2.29.3 Ingenuity Pathway Analysis (IPA)

The IPA software (Ingenuity Systems, www.ingenuity.com) is a bioinformatics tool to perceive datasets such as RNA-seq and proteomic, in relation to previous knowledge on signaling mechanism, functions, and relationships. IPA utilizes the Ingenuity® Knowledge Base, which is an updated repository of biological interactions and functional annotations created from millions of individually modeled relationships between proteins, genes, complexes, cells, tissues, drugs, and diseases.

2.29.4 Protein ANalysis THrough Evolutionary Relationships (PANTHER)

The PANTHER Classification System (http://www.pantherdb.org/) is an online tool to a dataset such as a list of DEGs and predict the functions or influence of these genes on cellular and biological process. Proteins were categorized into families and subfamilies of shared function.

2.30 Safety evaluation of epAON using the mouse model

Twenty-five BALB/c mice were housed at the animal house facility, Singapore Experimental Medicinal Centre, Singapore. Mice were categorized into five experimental groups: ***i)*** PBS ***ii)*** 5 mg/kg NS epAON ***iii)*** 25 mg/kg NS epAON ***iv)*** 5 mg/kg STAT3 epAON ***v)*** 25 mg/kg STAT3 epAON. Mice were administered with intervention through subcutaneous injection (200 µL) with dose regimen of 2 doses\ week for 2 weeks. The mice were monitored and were sacrificed after 15 days. Blood was collected at two time points i) before treatment (from venous sinus) and ii) after sacrifice (cardiac puncture). The organs were collected and frozen in liquid nitrogen. All experiments were performed according to the National Advisory Committee for Laboratory Animal Research guidelines (IACUC #2016/SHS/1252). The number of mice used in experiments were determined by using power analysis. Power analysis helps to evaluate the sample size necessary to detect an effect of give sample size.

1) sample size (n)
2) effect size (µ)

3) significance level (α)= P (Type I error) = probability of finding an effect that is not there

4) power (β) = 1 – P (Type II error) = probability of finding an effect that is there

Given any three, we can determine the fourth.

$N = (Z_{1-\alpha/2} - Z_{\beta})^{2} (\sigma_1^2 + \sigma_2^2)/ (\mu_1^2 - \mu_2^2)$

2.31 Aspartate Aminotransferase Activity (AST) assay

Evaluation of AST levels in serum was performed using AST assay kit as per manufacturer's recommendation (Abcam, Cambridge CB2 0AX, U K). Undiluted serum (5 µL) was adjusted to volume of 50 µL using AST assay buffer provided in the kit and were added to 96 well plates. Positive control provided in the kit was used along with serum samples.

The concentration standards for AST assay were prepared from stock (0.1 M glutamate pyruvate) provided by the manufacturer (Abcam, Cambridge CB2 0AX, U K). 1 mM of glutamate standard was prepared by mixing 10 µL of stock to 990 µL. Assay buffer as own in **Appendix 2, Table A2.16**. Colorimetric Reaction Mix (100 µL) for each assay was formulated in **Appendix 2, Table A2.17**. Reaction Mix (100 µL) was added into each well of standard, samples, and positive controls, which were previously seeded in a 96 well plate. Optical density at 450 nm was measured on a Cytation 3 micro-plate reader (BioTek, VT, US)in a kinetic mode after 10 min, was designated as A_1 and A_{1BG}, and reading after 60 min, was termed as A_2 and A_{2BG}.

The absorbance value of each standard was plotted as a function of the final concentration of glutamate. The trend line equation was derived based on your standard curve data. Activity of AST was calculated as $\Delta A_{450nm} = (A_2 - A_{2BG}) - (A_1 - A_{1BG})$. Amount of glutamate was calculated from Standard of curve of glutamate.

$$AST\ Activity = (B\Delta T x V) * D, \text{ nmol/min/mL} = \text{mU/mL}$$

Where: B = Amount of glutamate from glutamate standard curve. ΔT = reaction time (min). V = original sample volume added into the reaction well (in mL). D = sample dilution factor. Unit Definition: One Unit AST = amount of AST which generates 1.0 µmol of glutamate per min at 37 °C.

2.32 Creatine Kinase (CK) assay

Evaluation of creatine kinase levels in serum collected from mice was performed as using CK assay kit per manufacturer's recommendation (Abcam, Cambridge CB2 0AX, U K). Undiluted serum (2 µL) was adjusted to volume of 50 µL using CK assay buffer provided in the kit and were added to 96 well plate. Positive control provided in the kit was used along with serum samples.

The standards for CK assay was prepared from 1mM NADH standard as shown in **Appendix 2 Table A2.18**. Colorimetric Reaction Mix (100 µL) for each assay was prepared. Master mix was set to ensure consistency and was formulated as provided in **Appendix 2 Table A2.19**. Reaction Mix and background reaction mix was added into each well of standard, samples and positive controls which were previously seeded in a 96 well plate. Optical density at 450 nm was measured on Cytation 3 micro-plate reader (BioTek, VT, US) in a kinetic mode after 10 min, every 2 – 3 min, for at least 60 min at 37 °C protected from light.

The absorbance value of each standard was plotted as a function of the final concentration of NADH. The trend line equation was calculated based on standard curve data.

$$CK\ Activity = (B \Delta T x V) * D,\ nmol/min/mL = mU/mL$$

Where: B = Amount of NADH from NADH standard curve. ΔT = reaction time (min). V = original sample volume added into the reaction well (in mL). D = sample dilution factor. Unit Definition: One Unit CK = amount of CK which generates 1.0 µmol of NADH per min at 37 °C.

2.33 Alanine Transferase (ALT) assay

Evaluation of ALT levels in serum was performed using kit per manufacturer's recommendation (Abcam, Cambridge CB2 0AX, U K). Undiluted serum (2 µL) was adjusted to volume of 20 µL using ALT assay buffer and were added to 96 well plates. Positive control provided in the kit was used along with serum samples.

The standards for ALT assay were prepared from 1 nmol/µL pyruvate standard as shown in **Appendix 2Table A2.20**. Colorimetric Reaction Mix (100 µL) for each assay was formulated as detailed in **Appendix 2Table A2.21**. Master mix was set to ensure consistency. Reaction Mix (100 µL) was added into each well of standard,

samples and positive controls, which were previously seeded in a 96 well plate. Optical density at 570 nm was measured on a Cytation 3 micro-plate reader (BioTek, VT, US) in a kinetic mode after 10 min, every 2 – 3 min, for at least 60 min at 37°C protected from light. The absorbance value of each standard was plotted as a function of the final concentration of pyruvate. The trend line equation derived based on standard curve data.

$$ALTActivity = (B \Delta TxV) * D, \text{ Unit nmol/min/mL} = mU/mL$$

Where: B = Amount of pyruvate from Pyruvate Standard Curve ΔT = reaction time (min). V = original sample volume added into the reaction well (in mL) D = sample dilution factorALT molecular weight: 54.47 g/mol. Unit Definition: One Unit ALT = amount of ALT which generates 1.0 µmol of Pyruvate per min at 37 °C.

2.34 IgG1 assay

IgG1 assay was performed according to manufacturer's instruction (**Appendix 1Table A.1.5**). A 96 well plate was coated with capture antibody by adding 50 µL of 1X capture antibody resuspended in coating buffer and was incubated overnight at 4 °C. Next, the wells were washed 3 times, with 300 µL of washing buffer. The wells were blocked with 50 µL of blocking buffer and were incubated for 1h at room temperature. Next, plates were washed and 50 µL of standards/cell culture supernatants/ diluted serum were added to the wells, followed by the addition of 50 µL of detection antibody, and incubated for 3 h at room temperature. The plates were washed three times, and the remaining buffer was soaked by placing the plates on the tissue for 1 min. TMB solution (50 µL) was added to each well and were then incubated for 20 min. Stop solution (25 µL) was added to each well, and plates were read at OD_{450nm} and OD_{570nm} using a Cytation 3 micro-plate reader (BioTek, VT, US). Using the absorbance values of standards standard curve was plotted. Based on this equation, concentrations of probed cytokines were determined.

2.35 Tissue processing and sectioning

2.35.1 Fixing and processing

The harvested organs were fixed using 4% formaldehyde and 30% sucrose solution. In the tissue processor ASP6025 - Automated Vacuum Tissue Processor, located at level 7 Experimental Medicine Building, NTU, Singapore samples were processed

1. Running through 70% ethanol for 1 h.
2. Running through 95% ethanol (95% ethanol/ 5% methanol) for 1 h.
3. Running through 1st absolute ethanol for 1 h.
4. Running through 2ndabsolute ethanol for 1.5 h.
5. Running through 3rd absolute ethanol for 1.5 h.
6. Running through 4th absolute ethanol for 2h.
7. Running through 1stclearing agent (Xylene or substitute) for 1 h.
8. Running through 2nd clearing agent (Xylene or substitute) for 1 h.
9. Running through1stwax (Paraplast X-tra) at 58°C for 1 h.
10. Running through2nd wax (Paraplast X-tra) at 58°C 1 h.

2.35.2 Embedding tissues in paraffin blocks

The tissue embedding in paraffin was performed using Leica HistoCore Arcadia unit according to manufacturer's instructions (Harbourfront Centre, Singapore). The heat block was switched "on" to melt the paraffin 1 h before adding the tissue cassettes. Processed samples were placed in the cassette and the best mold was chosen based on the size of the tissue. A margin of at least 2 mm of paraffin surrounding all sides of the tissue gives best cutting support. Molten paraffin was poured in mold from paraffin reservoir. Warm forceps were used to transfer tissue into mold, placing cut side down. Paraffin should solidify in 30 min. When the wax was firmly solid and hardened (approx. 30 min) the paraffin block was popped out of the mold. If the wax cracks or the tissues are not aligned well, simply melt them again and start over. Tissue blocks were stored at room temperature.

2.35.3 Paraffin embedded tissue sectioning

Tissues were sectioned using a microtome. Water bath was turned on and was set at temperature was 35-37ºC. Blocks to be sectioned are placed face down on an ice block or heat sink for 10 min. Fresh blade was placed on the microtome; Block was inserted into the microtome chuck, so the wax block faces the blade and was aligned in the vertical plane. The dial was set to cut 10 µM sections. The blade should be placed at angle of 5º. If the block is ribboning well then cut another four sections. Forceps or

fine paintbrushes were used to pick the ribboning sections and were placed on water bath (37°C) and later transferred to glass slide. Slides can be stored overnight at room temperature.

2.35.4 Cryosection

Unfixed tissue samples were frozen in Tissue-Tek® optimum cutting temperature (O.C.T.) (Sakura Finetek USA) in a suitable tissue mold by incubating in -10 °C. OCT is viscous at room temperature and miscible with water but freezes into solid support at −20 °C. Freeze the OCT containing the tissue onto the specialized metal grids that fit onto the Leica CM3050 S Research Cryostat (Harbourfront Centre, Singapore). The tissues were sliced into 5-15 μm sections thick using mechanized blades in a cryostat. If necessary, the temperature of the cutting chamber was adjusted ±5 °C, according to the tissue under study. The sections were transferred to the microscope slide by touching the slide to the sectioned tissue. The slides were fixed and stained for appropriately for confocal microscopy staining protocol.

2.36 Statistical analysis

For comparison of two groups, p-values were calculated by a two-tailed unpaired student's t-test. In all cases $p < 0.05$ was considered to be statistically significant. Statistical analysis was performed with either t-tests (for comparison between two groups) or one-way ANOVA (for comparison among multiple experimental groups) using GraphPad Prism 4.0 software (GraphPad Software, San Diego, CA, USA). *p*-values < 0.05 were considered significant.

Chapter 3

Identification of signaling pathway defects in vorinostat resistant CTCL cells

3.1 Introduction

Despite significant advances in the treatment of hematolymphoid malignancies, drug resistance remains a challenging therapeutic problem and a significant cause of treatment failure. Although molecularly targeted drugs have been successful in the treatment of hematolymphoid malignancies, these drugs exert selective pressure on malignant cells resulting in the outgrowth of drug-resistant clones. It is now well-recognized that the development of drug resistance in cancer is a complex and dynamic process. However, we are still far from understanding the complexity of molecular processes in these malignancies.

Conventional chemotherapy agents, such as histone deacetylase HDAC inhibitors (*e.g.* vorinostat), are widely used to treat hematolymphoid malignancies, including T cell lymphomas; however, poor prognosis in some lymphomas *e.g.* NK/T cell lymphomas may ensue due to frequent occurrence of multi-drug resistance (Housman et al., 2014; Vasan et al., 2019). Multiple lines of clinical evidence have presented vorinostat, an orally bioavailable inhibitor of HDAC, as a popular chemotherapeutic agent for the management of T cell lymphomas due to its known anti-neoplastic properties, high potency (IC_{50} in the nano-molar range) and low toxicity (Marks et al., 2001; Olsen et al., 2007). Vorinostat is a potent inhibitor of enzymatic activity of histone acetylase Class I (HDAC1, HDAC2, HDAC3) and Class II (HDAC6) at nanomolar concentration range (Marks et al., 2001).

However, despite broad biological effects of vorinostat on lymphoma tumors, proven success in clinics and FDA approval for the treatment of cutaneous T-cell lymphoma (CTCL), acquired chemo-resistance remains as a major challenge.

One of the mechanisms by which CTCL cells could become resistant is constitutively increased phosphorylation of STAT family proteins. For example, a panel of CTCL cell lines (HuT78, MyLa, MJ) with persistent high endogenous expression and phosphorylation of STAT1, STAT3, and STAT5 are inherently resistant to vorinostat (Fantin et al., 2008). Increased expression of antioxidant genes has also been associated with vorinostat resistance in the multiple myeloma cell line ARP-1 and leukemic patients (Garcia-Manero et al., 2008; Ungerstedt et al., 2005). Moreover, only a small proportion of patients with refractory CTCL (approx. 30%) respond to vorinostat treatment (Duvic et al., 2007; Olsen et al., 2007). These raise an outstanding question

of why and how patients develop resistance to vorinostat and what other therapeutic choices could be used to manage the disease better.

Although resistance to HDAC inhibitors is a frequently encountered problem in the management of CTCL, molecular mechanisms associated with vorinostat resistance remains poorly understood. We hypothesized that the development of resistance to vorinostat in CTCL is a result of acquired defects in pro-apoptotic signaling pathways.

3.2 Objectives

The goal of this chapter was to understand the molecular mechanism of resistance to vorinostat, which would help to develop better therapeutic strategies to tackle the disease and to identify predictive biomarkers for response to therapy. The main objectives were:

3.2.1 To develop a vorinostat resistant CTCL cell culture model ($HuT78_{VR}$).

3.2.2 To examine genomic and proteomic alterations caused by acquired resistance to vorinostat in $HuT78_{VR}$ cells.

3.2.3 To determine if altered molecular pathways can be targeted to tackle acquired vorinostat resistance in $HuT78_{VR}$ cells.

3.3 Results

3.3.1 Development of a vorinostat resistant CTCL cell culture model

The HuT78 cell line, derived from the blood of a patient with Sezary syndrome, is an established cell culture model of CTCL. Unlike other available hematolymphoid cancer cell lines, HuT78 has no evidence of infection with human T cell lymphotropic virus 1 (HTLV-1). Therefore, we choose to use this cell line as a model to gain insights into the molecular basis of drug resistance in hematolymphoid malignancies. To explore P glycoprotein (P-gp) independent resistance mechanism in acquired HDAC inhibitor resistance, we opined to utilize non p-gp substrate such as vorinostat as a drug model.

To develop resistance to vorinostat, parental HuT78 cells were stepwise exposed to increasing concentrations of vorinostat (dose escalation protocol) ranging from 0.1 μM to 10 μM over a duration of 6 months. A vorinostat-resistant clone of HuT78 maintained in the medium containing 10 μM vorinostat for a prolonged period (>4 weeks) was selected ($HuT78_{VR}$).

Resistance factor is defined as the ratio of IC_{50} of drugs in resistant cells to parental cells. Using the MTS-based cell viability assay, we determined that HuT78$_{VR}$ cells acquired resistance factor (RF) of 18-fold (IC_{50} 36 µM) compared to the parental HuT78 cells (IC_{50}, 2 µM) (**Figure 3.1A**). The IC_{50} dose of vorinostat for parental HuT78 cells (2 µM)) did not induce apoptosis in HuT78$_{VR}$ cells, as determined by Annexin V/PI staining of treated cells and subsequent flow-cytometry analysis (**Figure 3.1B**).

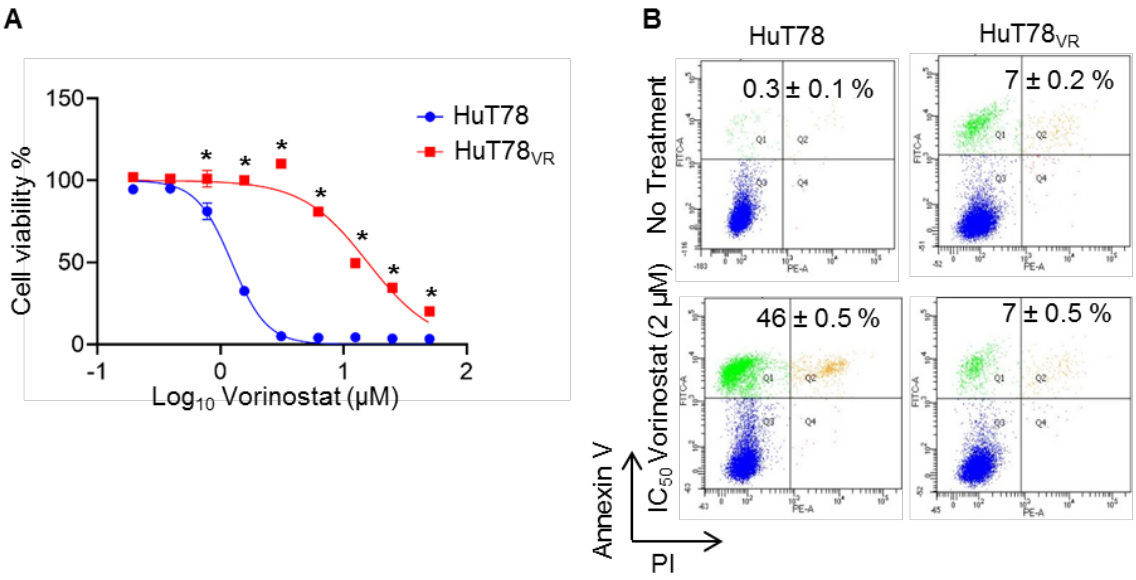

Figure 3.1 Development of vorinostat resistant HuT78$_{VR}$ cell line. **(A)** Parental HuT78 and HuT78$_{VR}$ cells were treated with increasing concentrations of vorinostat (ranging from 1 µM to 100 µM) for 24 h. IC_{50} of vorinostat in both cells was determined by MTS-based cell viability assay and subsequent analysis using the GraphPad Prism software. **(B)** HuT78 and HuT78$_{VR}$cellswere treated with 2 µM vorinostat. After 24 h, apoptosis induction in cells was quantified by cellular staining with Annexin V\PI and subsequent flow-cytometry analysis. (Mean ± S.E.M.; *, p<0.01.

3.3.2 Phenotypic characterization of HuT78$_{VR}$

To understand the growth kinetics of resistant cells, we performed MTS assay on HuT78 and HuT78$_{VR}$ in a time-dependent manner. We found that doubling time for HuT78 and HuT78$_{VR}$ is 61.14 h and 62.55 h, respectively (**Figure 3.2A**). This data suggests that the proliferative rate of HuT78 and HuT78$_{VR}$ is comparable.

Next questioned whether vorinostat resistance causes morphological changes in HuT78$_{VR}$ cells. We captured images of HuT78 and HuT78$_{VR}$ cells using EVOS XL Core Cell Imaging System. HuT78$_{VR}$ cells were polymorphic and comprised of a significant number of cells with a substantially large size in comparison to HuT78 cells (**Figure 3.2B**). Cell-by-cell quantification of cell area using ImageJ software revealed that the average cross-section area of HuT78$_{VR}$ cells were increased by 3-fold in comparison to

parental HuT78 cells (**Figure 3.2C**). We observed that approximately 40% of HuT78$_{VR}$ cells were at least larger than the average size of (212.3 µm^2) of HuT78 cells. Trypan blue-based cell counting showed that these large cells are viable.

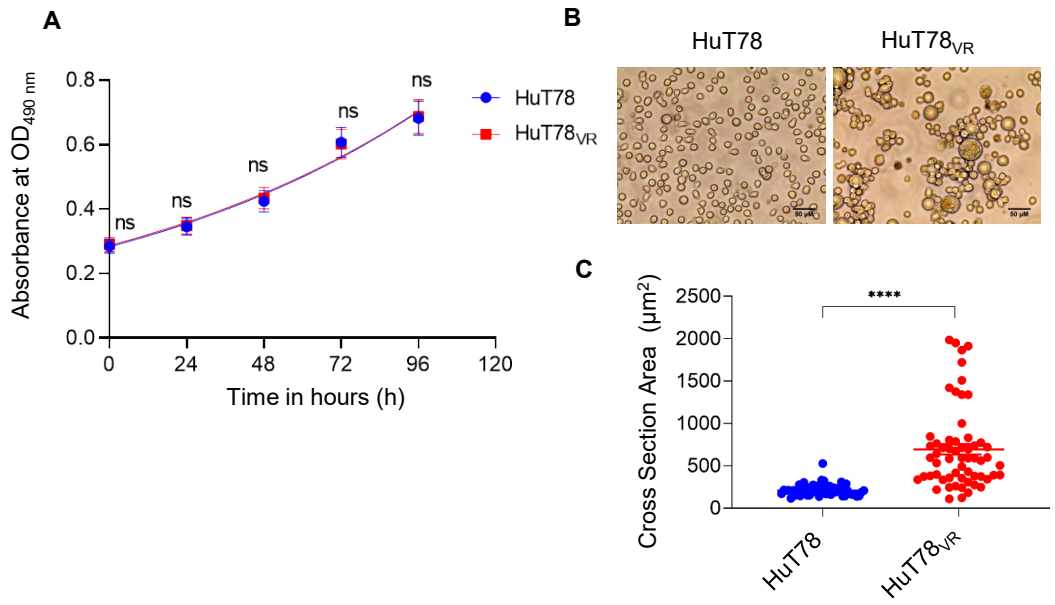

Figure 3.2 Morphological analysis of HuT78$_{VR}$ cell population. **(A)** HuT78 and HuT78$_{VR}$ cells (5.0× 10^4) in 100 µL medium were seeded in triplicates in a 96-well plate. Cells were treated with MTS reagent at different time points, 0, 24, 48, 72 and 96 hours. Absorbance at 490 nm was quantified using spectrophotometer. The growth curve was plotted based on absorbance values using GraphPad prism 8. Data represent three independent experiments. (Mean ± S.E.M; ns, non-significant). **(B)**Bright-field images of parental HuT78 and HuT78$_{VR}$ cells captured by EVOS XL Core Cell Imaging system using 20X objective. Ten different fields were imaged and representative images from three independent experiments are presented. **(C)** Cell-by-cell quantification of cell area (cross-section area, µM^2) was performed using ImageJ software. At least ten microscopic fields were scanned, and representative images are shown Scale bar 50 µm and mean±S.E.M presented. Each dot represents one cell. (****, p<0.0001.)

3.3.3 Vorinostat resistance in HuT78$_{VR}$ cells is independent of drug efflux mechanism

Rhodamine 123 (Rh123) is a fluorescent probe and has been used to measure the efflux activity of P-glycoprotein (P-gp) to determine the multidrug resistance (MDR) phenotype in cancer cells. Using this molecular probe, we evaluated the drug-expelling capacity of HuT78$_{VR}$ by flow-cytometry. We found that the Rh123 dye promptly accumulated in parental HuT78 cells, and almost all cells remained stained, which could mainly be due to the absence\low abundance of P-gp on these cells. In contrast, only 40% of HuT78$_{VR}$ remained positively stained with the Rh123 dye, suggesting the presence of P-gp in HuT78$_{VR}$, which expelled out the dye from these cells (**Figure 3.3A, B**). Several transmembrane transporter proteins, collectively termed as ATP-binding

cassette transporters (ABC-transporters), are known to regulate drug resistance in tumor cells (Choi, 2005). Using qRT-PCR analysis, we detected that ABC transporters ABCB1 and ABCG2 were significantly upregulated in HuT78$_{VR}$ cells, 3- and 5-fold, respectively (**Figure 3.3C**). Notably, expression of the ABCC1 mRNA (Cole, 2014), prominent transporter responsible for drug efflux, was not affected in HuT78$_{VR}$cells (**Figure 3.3C**).

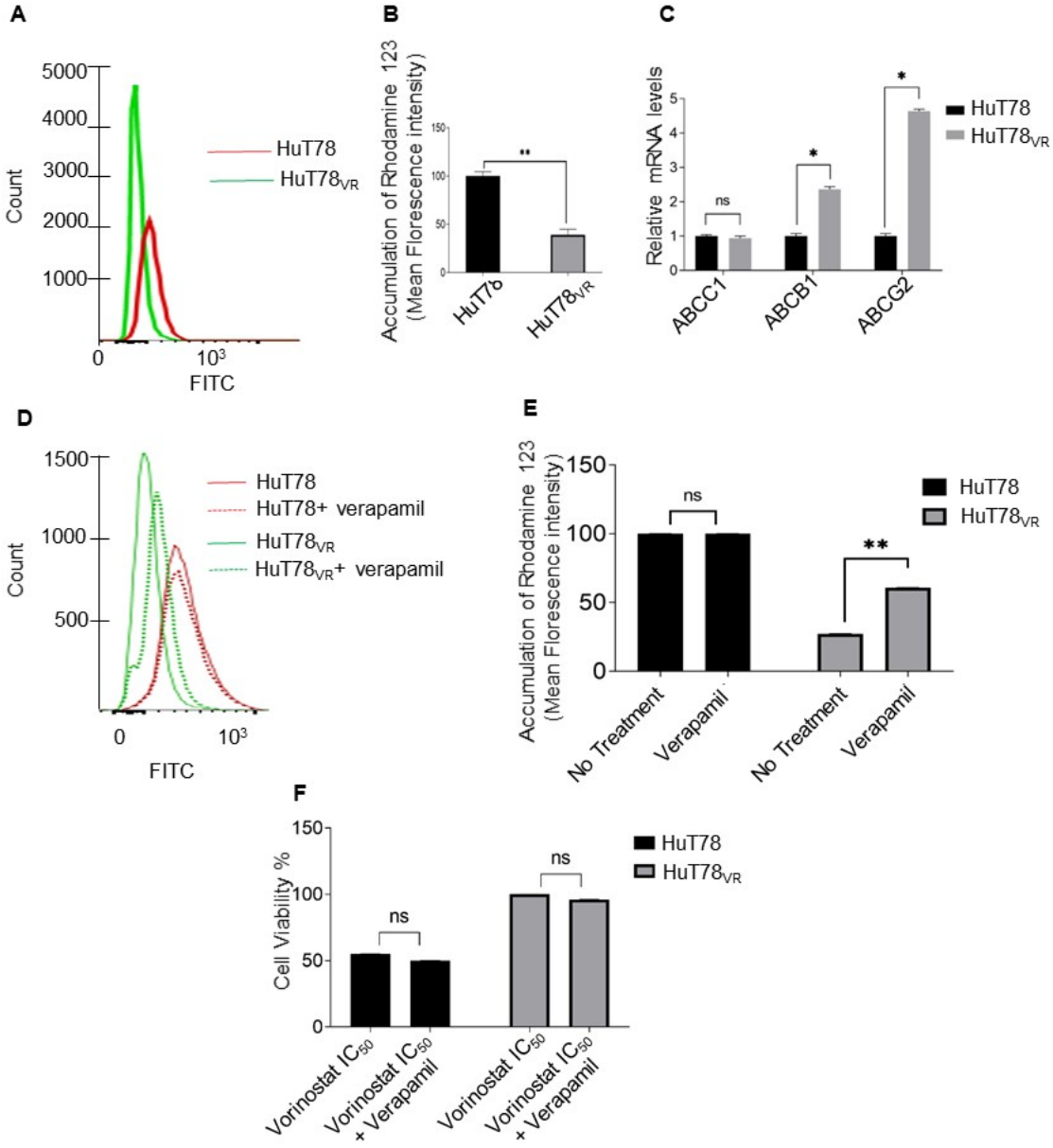

Figure 3.3 Vorinostat resistance is independent of the expression of P-gp pumps in HuT78$_{VR}$ cells. **(A, B)** HuT78 and HuT78$_{VR}$ cells were incubated in Rh123 containing medium for 4h and were analyzed by flow-cytometry. Cells stained with Rh123 are detected in FITC channel. **(C)** Total RNA was extracted from HuT78 and HuT78$_{VR}$ cells, and mRNA levels of ABCC1, ABCB1 and ABCG2 were evaluated by qRT-PCR. The graph is representative data from at least three

independent experiments that were presented (*, p<0.01; ns, non-significant). **(D, E)** HuT78 and HuT78$_{VR}$ cells were pre-treated verapamil (5 μM) for 24 h and later incubated medium containing Rh123 for 4h. Subsequently, cells were analyzed by flow-cytometry. **(E)** Cells treated with or without vorinostat were evaluated for cell viability using MTS assay. (Mean ± S.E.M; *, *p*<0.01; **, *p*<0.001; *ns,* non-significant).

Induction of MDR gene expression is a classical effect of HDAC inhibitors, however not all MDR expressing cells are dependent on P-gp for drug resistance (Peart et al., 2003; Robey et al., 2006; Wang et al., 2016a). To determine whether acquired vorinostat resistance in HuT78$_{VR}$ is dependent on P-gp, we pre-treated HuT78$_{VR}$cells with the P-gp inhibitor verapamil and Rh123 efflux was analysed by flow-cytometry. As expected, the ability of HuT78$_{VR}$ cells to efflux the Rh123 dye was reversed (50% reversal) in the presence of verapamil (**Figure 3.3D, E**). However, the treatment of HuT78$_{VR}$ with vorinostat in the presence of verapamil did not reduce the viability of these cells (**Figure 3.3F**), suggesting that the acquired vorinostat resistance in HuT78$_{VR}$ cells is independent of the drug efflux mechanism.

3.3.4 Transcriptomic analysis of HuT78$_{VR}$

To examine changes in gene expression profiles due to acquired resistance to vorinostat in HuT78$_{VR}$ cells, we performed differential transcriptome analysis by RNA-seq in parental HuT78 (treated with vorinostat) and HuT78$_{VR}$ cells. Out of total 33,000 genes detected, we identified 5,417 genes which were modulated in HuT78$_{VR}$ using DESeq2 [cut-off: False Discovery Rate (FDR) <0.05 and $\log_2$ fold change >1 or <-1]. We prepared a volcano plot to assess and compare gene expression variation between HuT78 and HuT78$_{VR}$ cells (**Figure 3.4A**). Parental HuT78 cells were pre-incubated with vorinostat for 24 h to exclude the direct effects of the drug treatment. Compared to the parental HuT78 cells, a total of 1,962 mRNAs exhibited upregulated expression levels and 3,455 mRNAs exhibited downregulated expression levels in HuT78$_{VR}$ cells, indicating that these mRNAs might have common roles in facilitating vorinostat resistance inHuT78$_{VR}$. The top 50 significantly modulated mRNAs identified from RNA-seq analysis are listed in **Table 3.1**.

Table 3.1 A list of top 50 significantly modulated DEGs in HuT78$_{VR}$cells

Gene symbol	Log_2 fold change	FDR value	Gene symbol	Log_2 fold change	FDR value
IGF2BP1	6.354054	0	GBP2	-3.44722	1.42E-134
FBXO27	4.411328	0	MBNL3	2.909089	2.50E-134
STAT1	-3.0306	1.23E-297	BCL6	-3.30058	2.48E-132
GBP5	-3.48038	1.19E-256	GNL3L	2.270459	2.75E-132
LTB	4.448019	5.57E-241	HDGF	2.156432	2.75E-132
FN1	-5.08991	8.51E-230	MYO1E	-5.58418	4.06E-129
DHRS2	-4.82667	2.07E-206	ANXA1	-2.61947	3.41E-128
SAMD10	4.745468	1.68E-202	LGMN	-2.96167	2.62E-127
CTTN	4.156761	5.58E-189	CCR8	2.878436	1.68E-121
IL27RA	3.141902	1.94E-188	BCL2L1	2.450327	1.29E-120
CHRNA6	3.557336	1.98E-186	CCDC86	2.191273	2.40E-120
UCA1	3.227415	3.69E-186	C14orf132	2.68047	9.52E-117
GPR183	3.464423	3.29E-184	MEPCE	2.634978	1.34E-116
WT1	2.682587	9.45E-175	LPXN	2.453838	4.91E-116
UTP20	3.027612	8.17E-170	MTHFD1L	2.117378	2.18E-114
ABCA7	-3.33141	3.40E-165	RCC2	2.104136	3.68E-111
SLC38A5	3.407878	8.33E-165	ANP32B	2.034292	7.86E-109
RBM3	2.409819	7.90E-164	CTPS1	2.565803	5.91E-108
LANCL2	3.527901	4.02E-159	MYO1B	-4.73237	6.74E-108
PTPN7	3.002749	5.51E-158	RCN1	2.841481	1.13E-102
GTF3C6	3.093105	1.61E-149	CDK2AP1	2.062885	7.05E-102
SLC43A3	2.759248	2.12E-148	FHDC1	-3.46052	1.73E-101
TPMT	-4.57744	1.97E-143	WBSCR16	2.627988	1.83E-101
XCL1	3.976171	2.21E-138	EFCAB4B	2.433225	5.52E-101
ATP6V0A1	-2.38674	2.49E-136	KCTD12	3.26111	9.58E-101

We performed gene ontology (GO) annotation and enrichment analysis of DEGs using the curated PANTHER bioinformatics tool (Mi et al., 2019) to determine which biological processes, cellular components and molecular functions are affected by the DEGs in HuT78$_{VR}$ cells. In the GO pathway enrichment analysis, the most frequently

(top 5) predicted functions of aberrant mRNAs were involved in cellular processes, metabolic processes, biological regulation, localization and multicellular organismal processes (**Figure 3.4B**).

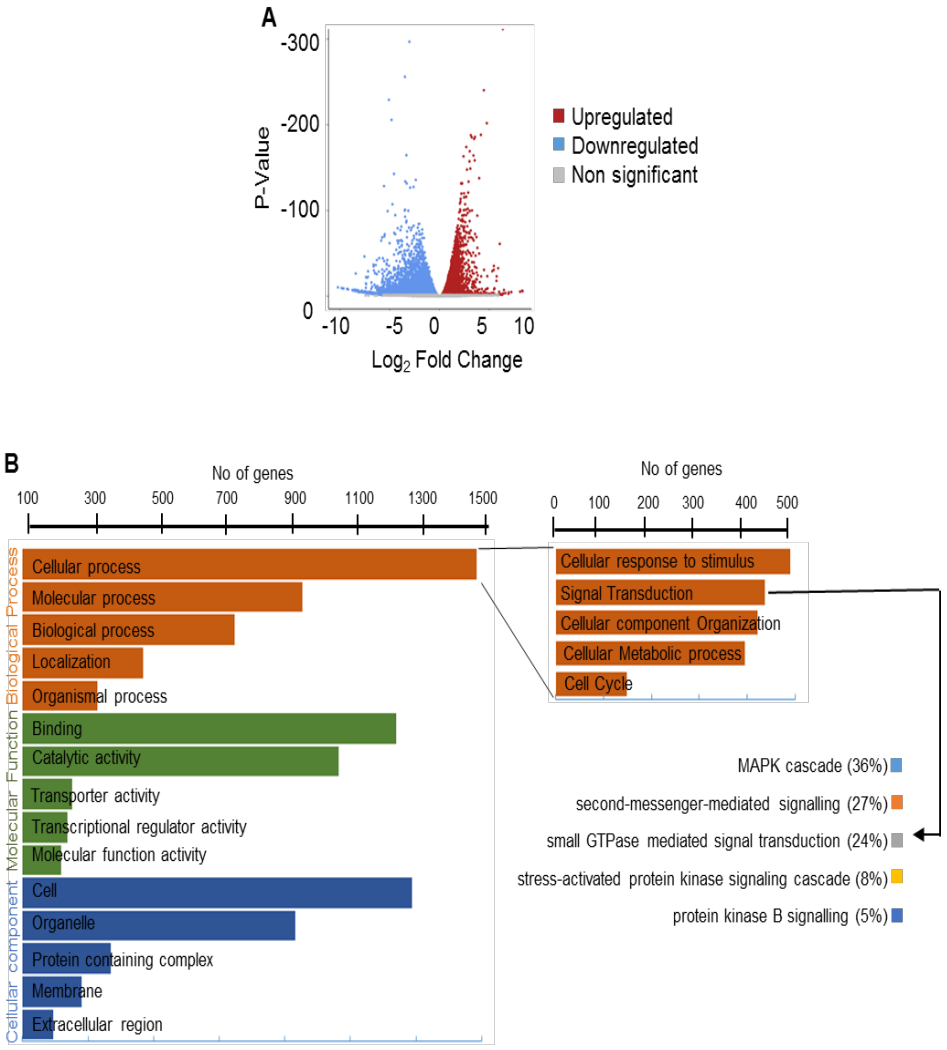

Figure 3.4 RNA-seq and analysis of HuT78$_{VR}$ cells. (**A**) Total RNA was extracted from HuT78$_{VR}$ and mRNA expression of genes was analysed using RNA-seq. Using DEseq, DEGs were identified based on cut off range (False Discovery Rate < 0.05 & log Fold change >1 or <-1) and volcano plot was Galaxy online tool. (B**)** DEGs were uploaded PANTHER gene ontology online tool and Biological process and pathways involved were displayed. Cellular process and signal transduction involved in HuT78$_{VR}$ were further listed from the biological process.

Major cellular processes that were altered due to acquired vorinostat resistance in HuT78$_{VR}$ cells were cellular response to stimulus (34.10%), signal transduction (31.6%), cellular component organization (26.0%), cellular metabolic process (25.4%) and cell communication (10.5%) (**Figure 3.4B**). In particular, several genes involved in MAPK signaling cascade were identified to be involved in vorinostat resistance.

Various intracellular signaling such as MAPK cascade (31%), secondary messenger mediated signaling (30%), small GTPase-mediated signaling (26%), protein kinase B signaling (8%) and stress activated signaling kinase (5%) were modulated in HuT78$_{VR}$ cells (**Figure 3.4B**).

Similarly, the molecular functions modulated in the HuT78$_{VR}$ cells include binding activity, catalytic activity, transporter activity, transcriptional activity, and molecular function activity. Transporter activity relates to molecular function, which is involved in the efflux/influx of macromolecules, small molecules, and ions in cells or between cells. Interestingly, 95 genes (8.9%), which are involved in transporter activity, were significantly modulated in HuT78$_{VR}$ cells (**Figure 3.4B**).

We next performed KEGG pathway analysis using Ingenuity Pathway Analysis (IPA) to determine which pathways are implicated in vorinostat resistance and better define the biological functions of significantly dysregulated mRNAs. We identified DEGs which were variable in parental and resistant cells using DESeq2 [cut-off range: FDR <0.05 and $\log_2$ fold change >1 or <-1] (**Figure 3.5A).** The top network associated with differentially expressed mRNAs are implicated in invasive and migratory properties of tumors (consistency score 11.3) (**Figure 3.5B**). Altered expression levels of a panel of DEGs (*CDKN1A, CCND1, MMP9, IFNG, FASLG* and *VIM*) detected in the IPA regulatory network were confirmed by further evaluating mRNA levels using qRT-PCR (**Figure 3.5C**). Data showed that markers of metastasis MMP9 (8-fold) and VIM (5-fold) were significantly elevated in HuT78$_{VR}$ cells. Interestingly CCND1, one of the genes involved in drug resistance in various forms of cancer, was also significantly elevated by 3-fold (**Figure 3.5C**).

Finally, to confirm the IPA-predicted increase in the invasive behavior of HuT78$_{VR}$ cells, we performed a Matrigel-based trans-well migration assay. HuT78$_{VR}$ cells showed significantly high (6-fold) invasiveness in comparison to the parental HuT78 cells (**Figure 3.5D**), suggesting that HuT78$_{VR}$ acquired a more aggressive phenotype than parental cells.

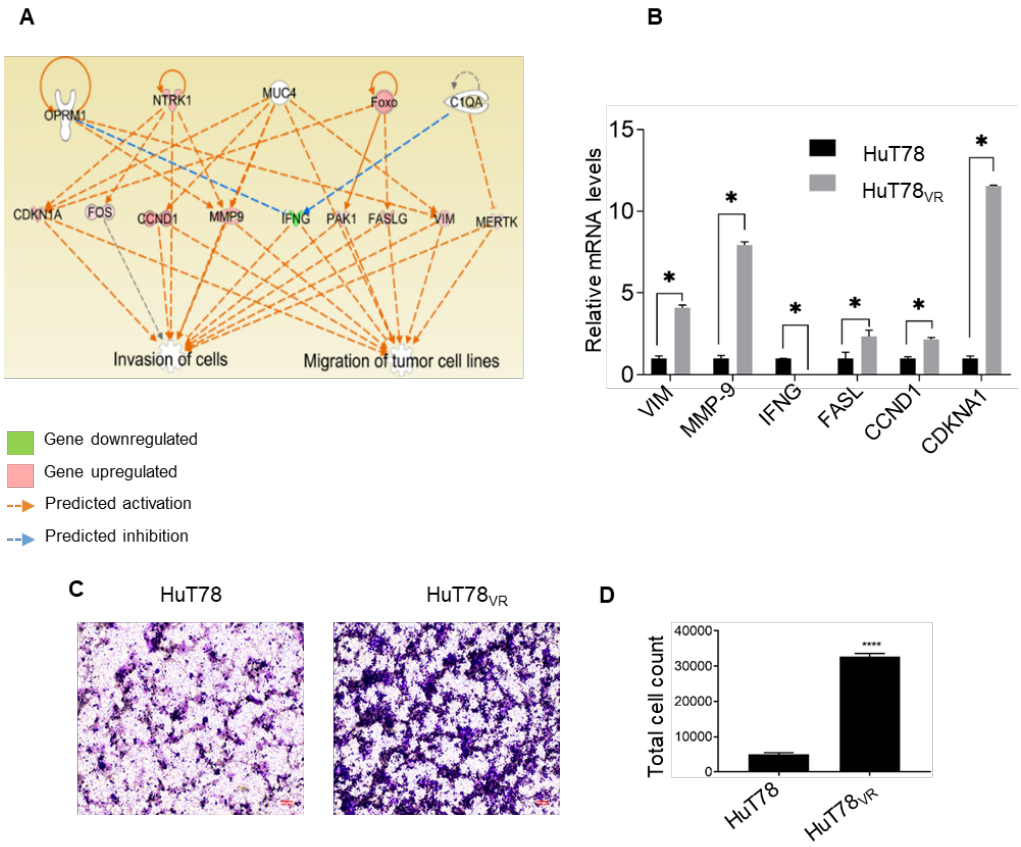

Figure 3.5 Vorinostat resistant cells are highly invasive. **(A)** DEGs were uploaded in IPA server and the core analysis programme was ran, and regulatory effects were predicted. **(B)** Total RNA was extracted and evaluated for mRNA levels of vimentin (*VIM*), Matrix metalloproteinase-9 (*MMP-9*), interferon-gamma (*IFNG*), Fas Ligand TNF(FASL), cyclin D1 (*CCND1*) and cell-dependent kinase inhibitor 1 (*CDKNA1*) was evaluated using qRT-PCR. The graph is representative data from at least three independent experiments was presented. (*, p<0.01; ns, non-significant) **(C)** HuT78 and HuT78$_{VR}$ cells were suspended in serum-free medium and were transferred to the upper chamber of the Boyden chamber coated with matrigel (200 µg/mL) and placed above lower chamber containing human serum (5%) as an attractant. After 16 h, the membrane was washed, fixed and stained with 1% crystal violet. The images were captured with EVOS XL core system at 4X magnification. (**D**) At least 5 microscopic fields were scanned, and representative images are shown Scale bar 10 µm and data was presented for one field (Mean ± S.E.M; ****, *p*<0.0001).

3.3.5 Profiling of Differentially Expressed Proteins (DEPs) in HUT78$_{VR}$

To determine changes in the entire proteome in HuT78$_{VR}$ cells due to acquired resistance to vorinostat, we performed SILAC (stable isotope labeling of amino acids in cell culture) based quantitative proteomic analysis. Both parental HuT78 cells and HuT78$_{VR}$ cells were subjected to SILAC labelling, which were then analyzed by LC/MS mass-spectrometry. Quantitative proteomic analysis between paired samples prepared from both forward and reverse staining yielded a total of 3,389 proteins. Of these proteins, we identified as 371 DEPs in HuT78$_{VR}$ cells of which 200 proteins being downregulated and 171 overexpressed [cut-off: FDR ≤0.01, minimum 2 unique peptides

per protein and Log_2 fold change >1 or <-1] (**Appendix 4, Table A4.1**). Top 50 dysregulated DEPs (25 upregulated and 25 downregulated) based on Log_2 fold change are listed in **Table 3.2**.

Table 3.2 A list of dysregulated 50 DEPs based on fold change.

Gene Symbol	q-value[#]	Log_2 Fold change	Gene Symbol	q-value	Log_2 Fold change
MUC1	0	6.64385619	QSOX2	0	-6.64385619
UNC119B	0	6.64385619	TRMT11	0	-6.64385619
TUT1	0	6.64385619	WAPL	0	-6.64385619
RTN2	0	6.64385619	CENPV	0	-6.64385619
TPPP	0	6.64385619	PCGF5	0	-6.64385619
CA2	0	6.64385619	TRAPPC6B	0	-6.64385619
ISG15	0	6.64385619	SLC35F2	0	-6.64385619
PCCA	0	6.64385619	TMEM192	0	-6.64385619
EPHX1	0	6.64385619	PTPMT1	0	-6.64385619
CKB	0	6.64385619	TOPBP1	0	-6.64385619
ENO3	0	6.64385619	HVCN1	0	-6.64385619
PTMS	0.001	6.64385619	THOC3	0	-6.64385619
MAOA	0	6.64385619	TMEM209	0	-6.64385619
AHR	0	6.64385619	PYM1	0	-6.64385619
NUDT1	0	6.64385619	CDK19	0	-6.64385619
STXBP1	0	6.64385619	UPF3B	0	-6.64385619
RIPK1	0	6.64385619	NHEJ1	0	-6.64385619
NAB2	0	6.64385619	BRD7	0	-6.64385619
FAM111B	0	6.64385619	SIRT5	0	-6.64385619
KCTD12	0	6.64385619	USE1	0	-6.64385619
REEP6	0	6.64385619	ZC3H7B	0	-6.64385619
RPP25	0	6.64385619	ZMYND8	0	-6.64385619
WDR35	0	6.64385619	GIT1	0	-6.64385619
BLVRB	0	6.102868054	UFC1	0	-6.64385619
ITGA1	0	5.785694396	HEBP2	0	-6.64385619

[#]q-value is a p-value that has been adjusted for the False Discovery Rate (FDR) and is used to estimate the FDR, e.g. a q-value threshold of 0.05 yields a FDR of 5% among all features called significant.

We next performed GO annotation and enrichment analysis of DEPs identified in HuT78$_{VR}$ cells with respect to biological functions (**Figure 3.6A**). The majority of DEPs have known functions in cellular processes, metabolic processes, biological regulation, localization, and response to stimuli. DEPs involved in the cellular processes mainly regulate the metabolic process (42.20%), cellular components (28.9%), cellular responses to a stimulus (25.20%), signal transduction (19.30%), and cell cycle (11.10%) (**Figure 3.6A**). Among major signaling pathways altered in HuT78$_{VR}$ cells include small GTPase-mediated signaling (45%), stress-activated signaling kinase (22%), intrinsic apoptotic signaling pathway (11%), second messenger-mediated signaling (11%) and MAPK cascade (11 %) **(Figure 3.6A)**.

Similar to the observations in RNAseq, we noticed that modulation of transporter activity in HuT78$_{VR}$ cells. We found that six genes (ATP6VOA1, VAT1, SFXN3, ATP11C, NDUFA4, and SLC7A1), which are involved in transporter activity were significantly modulated in HUT78$_{VR}$ cells (**Figure 3.6A**).

We used IPA to understand the directionality of cellular processes. IPA analysis predicted that the regulatory effect of cell death in HuT78$_{VR}$was inhibited through the down-regulation of pro-apoptotic proteins (consistency score 3.2) (**Figure 3.6B**). Caspase-3, a known pro-apoptotic protein, was significantly downregulated in the regulatory network, suggesting its involvement in the attenuation of cell death signaling. To verify the observed changes in caspase-3 expression, we performed Western immunoblot assay. We found that the expression levels of caspase-3 and BID were significantly reduced by 2- and 0.5-fold in HuT78$_{VR,}$ respectively (**Figure 3.5C**). It is important to note that in RNAseq analysis, we did not find any significant decreases in mRNA expression of caspase 3 and BID.

Protein levels of survivin and BCL-XL were unperturbed in HuT78$_{VR}$ cells. Overall, these datasets suggest that resistance to vorinostat in HuT78$_{VR}$ cells could be due to acquired defects in apoptotic machinery, which might have augmented the survivability of HuT78$_{VR}$.

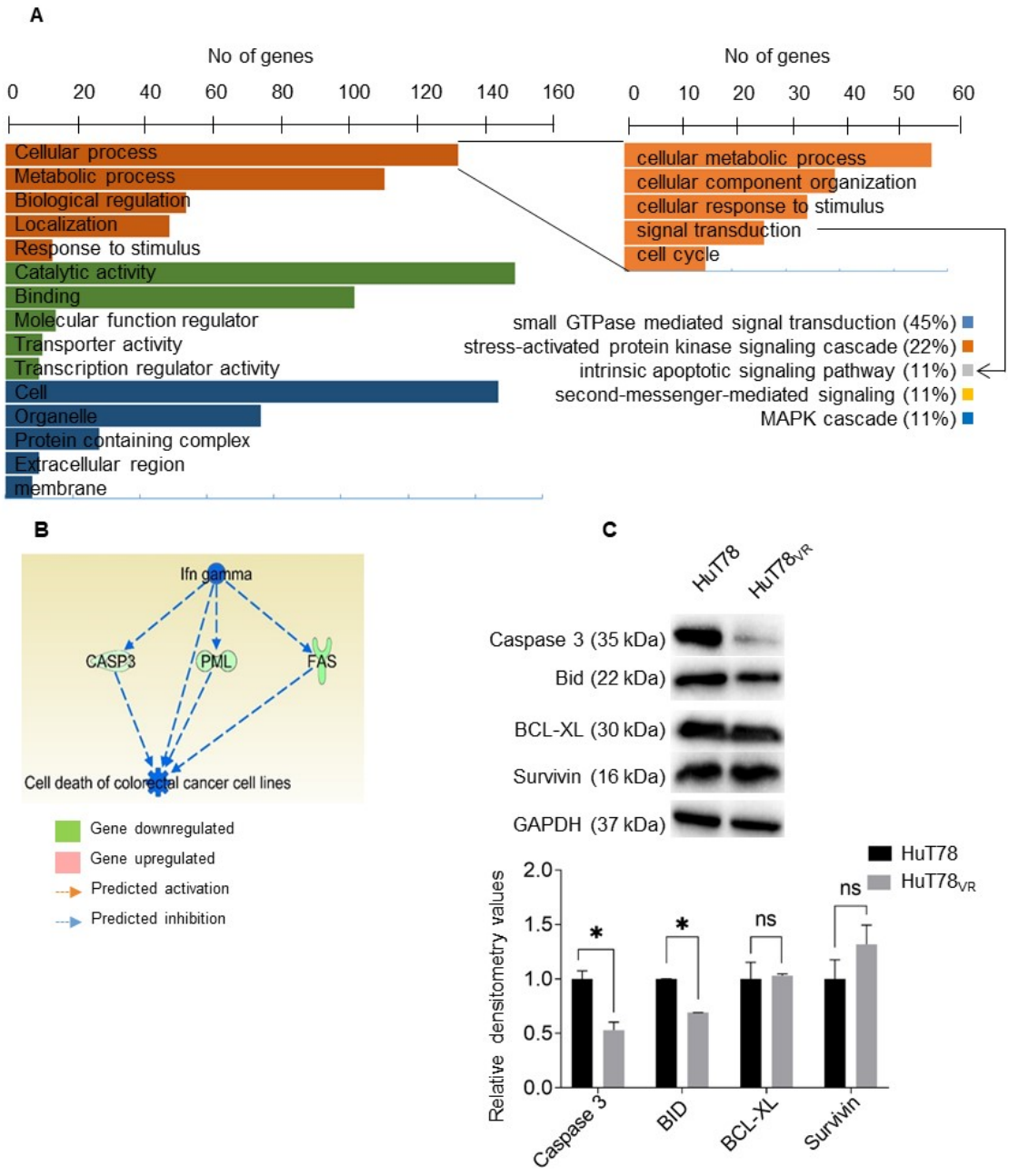

Figure 3.6 SILAC-based quantitative proteomics analysis of HuT78$_{VR}$cells. **(A)** Gene ontology analysis was performed using PANTHER (**C**) List of the cellular process involved in HuT78$_{VR}$. List of signaling transduction involved in HuT78$_{VR}$. (**B)** Regulatory networks with high consistency score were predicted using IPA. **(C)** HuT78 and HuT78$_{VR}$ cells were lysed, equal amount proteins were resolved in different gels and subjected to immunoblot assay. Each blot probed with caspase-3, BID, BCL-XL and Survivin antibodies. These blots were reproved for GAPDH (loading control). Densitometry values were plotted using image J analysis and representative data from at least three independent experiments was presented. (Mean ± S.E.M; *, p<0.01; *ns*, non-significant).

3.3.6 Integrated analysis of DEPs and DEGs

Mutually inclusive altered genes in DEPs and DEGs were identified using GeneVenn tool (**Figure 3.7A**). A correlation graph of gene expression and protein expression of 54 genes, which were common DEGs and DEPs, were plotted using GraphPad Prism. The basal correlation between genes at transcriptomic and proteomic levels showed an *R*-value of 0.56 (**Figure 3.7B**).

Further bioinformatics analysis of canonical pathways, which were modulated in DEGs and DEPs identified inhibition of death signaling. It was noted that the protein kinase A (PKA) signaling, Aryl hydrocarbon (ARH) signaling and ERK (Extracellular-signal-regulated kinase) signaling were active in HuT78$_{VR}$ cells (**Figure 3.7C**). We evaluated the status of various kinases and transcription regulators in the two pools of genes and found that RAF1 (Rapidly Accelerated Fibrosarcoma) and ERK kinase were significantly activated (**Figure 3.7D**). RAF1 is the upstream regulator of ERK signaling, which is involved in signal transmission from receptors to transcription factors. It regulates the expression of pro-proliferative and anti-apoptotic genes such as cyclin D1, Bcl-2. To further understand the intricate interaction of networks of 54 common genes that were altered in both DEPs and DEGs, we selected the most significant biological networks based on the IPA score (**Figure 3.7E**). We found that several molecules, including LGALS1 (Galectin), MUC1 (mucin) and CA2 (carbonic anhydrase) involved in the regulation of active ERK signaling are upregulated in HuT78$_{VR}$ cells (Alam et al., 2013; Canto de Souza et al., 2017; Hirose et al., 2019).

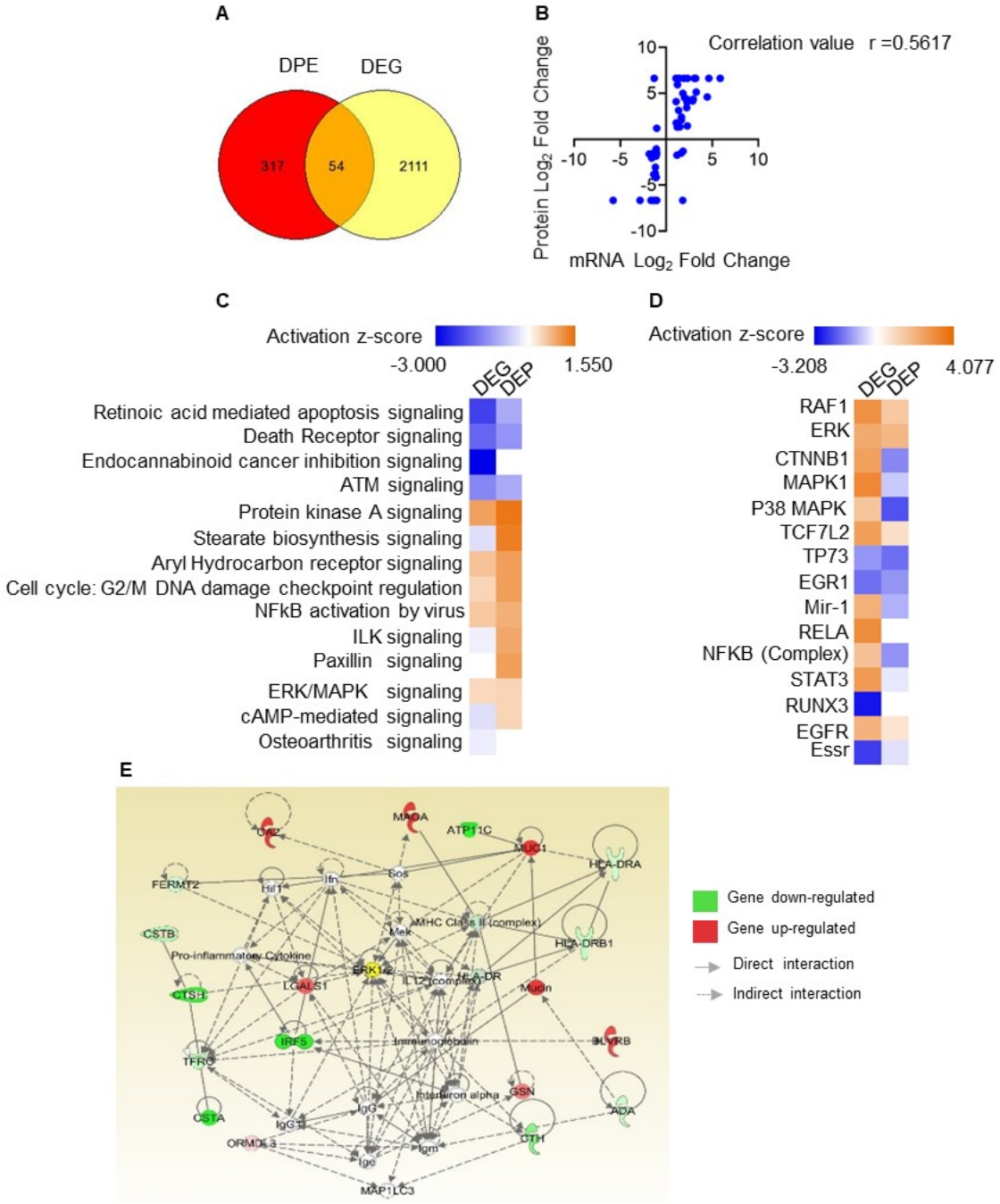

Figure 3.7 Integrated analyses of DEGs and DEPs envisaged defective apoptotic signaling. **(A)** Genes, which are common in DPE and DEG, were segregated using GeneVenn tool. **(B)** Fold change of 54 genes in DPE and DEG were plotted using a correlation graph in GraphPad. **(C, D)** Canonical pathways and upstream regulators of DEGs and DEPs were predicted using comparison analysis tool in IPA. **(E)** Regulatory network enriched in both DPE and DEG as displayed in IPA.

3.3.7 ERK signaling is significantly upregulated in HuT78$_{VR}$

Along with the transmission of the mitogenic signals, protein kinase A (PKA) signaling and Aryl hydrocarbon (ARH) signaling are transmitted through ERK\AKT\mTOR pathways.

Using Western immunoblot analysis, we confirmed that the phosphorylated forms of ERK (Thr202 and Tyr204) were significantly upregulated (>3-fold increase) compared to parental HuT78 cells (**Figure 3.8A**). Moreover, consistent with the RNA-seq data, phosphorylated forms of STAT3 (Tyr705 and Ser727) were significantly downregulated (2-fold reduction) in HuT78$_{VR}$ cells (**Figure 3.8B**).

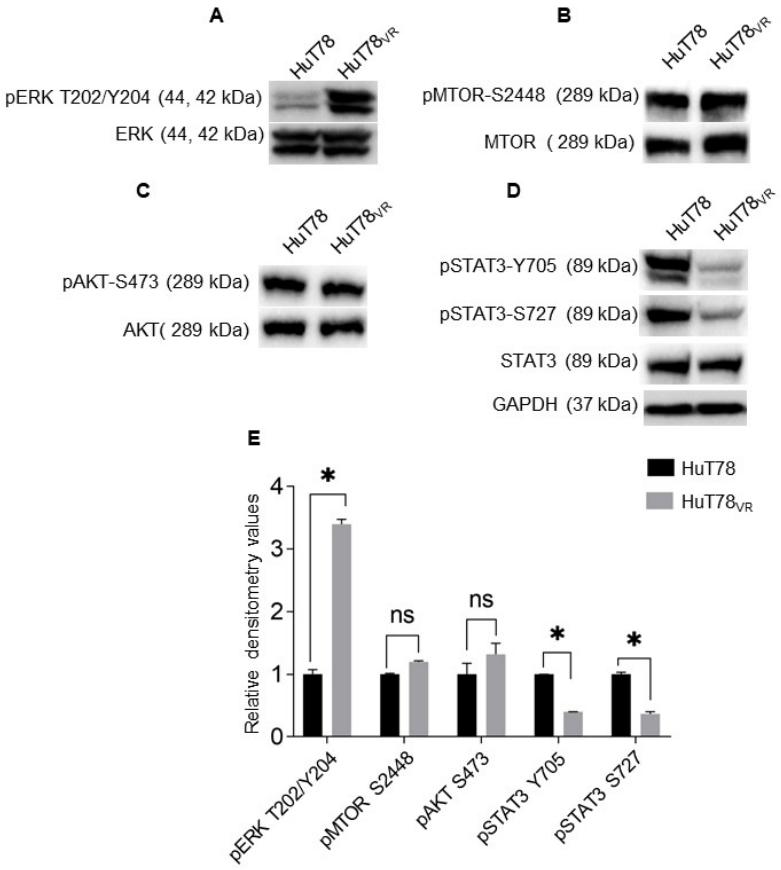

Figure 3.8 Activation of signaling pathways in HuT78$_{VR}$. HuT78 and HuT78$_{VR}$ cells were lysed and normalized for equal amounts of proteins using Bradford assay. Six different paired set of lanes of HuT78 and HuT78$_{VR}$ were resolved on gels (3 pairs in one gel each), transferred on pVDF membrane and were probed for pERK (T202/Y204), ERK (**A**), pMTOR (S2488), pMTOR (**B**), pAKT (S473), AKT (**C**), pSTAT3 (Y705), pSTAT3 (S727) and STAT3 (**D).** Note that phosphorylated and total forms of proteins were probed on different membrane. Only GAPDH was re-probed on same membrane (**E**). Densitometry values were plotted using ImageJ analysis and representative data from at least three independent experiments were presented (Mean ± S.E.M; *, p<0.01).

It is important to mention that we detected significant downregulation of phosphorylated forms of STAT3 in acquired drug resistance model HuT78$_{VR}$ cells. This was in line with observation of Chakraborty and his group, who showed that romidepsin resistant cells have low levels of phosphoSTAT3 (Y705) (Chakraborty et al., 2013). On the contrary, persistent activation of STAT1, STAT3, and STAT5 correlate with intrinsic resistance to vorinostat. Molecular analysis of skin biopsies from non-

responder MF/SS CTCL patients from the phase IIb trial of vorinostat, showed differential activation of STAT1 and STAT3 (Fantin et al., 2008). Similarly, we have observed that the depletion of STAT3 in HuT78 cells increases sensitivity to vorinostat (**Appendix Figure A5.1**). These data reiterate the highly complex role of STAT3 in the mechanism of vorinostat resistance in CTCL depending on whether resistance is intrinsic or acquired. We did not detect any significant changes in phosphorylated forms of AKT and mTOR proteins.

3.3.8 HuT78$_{VR}$ cells are sensitive to ERK inhibitors

To further understand the consequences of ERK-mediated signaling perturbation in HuT78$_{VR}$ cells, we treated HuT78$_{VR}$ with ERK inhibitors (FR180204 or sorafenib). We noticed that HuT78$_{VR}$ cells remained sensitive to FR180204 and sorafenib with Resistance Factor (RF) values 1.2 and 1.9, respectively (**Figure 3.9**). These results are consistent with earlier reports demonstrating that the romidepsin-resistant HuT78 cell line was exquisitely sensitive to MEK inhibitors (Chakraborty et al., 2013). HuT78$_{VR}$ cells showed cross-resistance to doxorubicin (topoisomerase inhibitor; RF=8), one of the components of CHOP therapy, which is effective in managing NHL. HuT78$_{VR}$ cells acquired cross-resistance to other HDAC inhibitors also, such as panobinostat (RF=30), romidepsin (RF=35) and trichostatin (RF=30) (**Fig 3.9**). Surprisingly, we found that resistant cells were sensitive to JAK/STAT inhibitor. It has been previously reported that these inhibitors downregulate ERK signaling (Horiguchi et al., 2010; Stivala et al., 2019). This could be a possible explanation for the sensitivity of HuT78$_{VR}$ cells to JAK/STAT inhibitors.

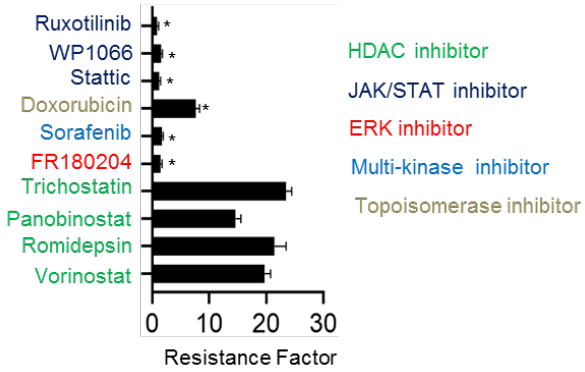

Figure 3.9 Effect of kinase inhibitors on the sensitivity of HUT78$_{VR}$. HuT78$_{VR}$ cells were treated with ruxotilinib, WP1066, static, doxorubicin, sorafenib, FR180204, trichostatin, panobinostat, romidepsin or vorinostat for 48 h and cell viability was evaluated using MTS assay. Representative data from at least three independent experiments were presented (Mean ± S.E.M; *, p<0.01).

3.4 Discussion

Systemic chemotherapy, mainly R-CHOP, remains the standard first-line treatment regimen for most NHL patients. In addition, based on encouraging results in clinical trials and FDA approvals, potent HDAC inhibitors (*e.g.* romidepsin, vorinostat) have emerged as important chemotherapeutic regimens for the management of NHLs and other hematolymphoid malignancies. Unfortunately, malignant cells always become resistant to drugs leading to relapse and therapeutic failure (Robey et al., 2011). Limited knowledge of the mechanism of resistance to vorinostat further poses a huge challenge to its success, mainly as a single agent therapy. Therefore, exploring the molecular mechanism of vorinostat resistance is of great significance. In this study, we developed a highly resistant CTCL cell line HuT78$_{VR}$. We selected the HuT78 cell line because it is one of the well-studied *in vitro* models for response and activity of HDAC inhibitors (Chakraborty et al., 2013; Piekarz et al., 2004). To our knowledge, HuT78$_{VR}$ is the first isogenic vorinostat resistant model of HuT78. We characterized morphological and phenotypic changes in HuT78$_{VR}$ and performed multi-omics analysis to dissect the mechanism of vorinostat resistance in HuT78$_{VR}$ cells. This chapter of my thesis uncovers several DEGs and DEPs involved in the acquired resistance to vorinostat in CTCL cells, elucidates the mechanism of resistance and suggests potential molecular targets with therapeutic implications.

We observed a significant increase in the cell size of HuT78$_{VR}$. An increase in size is one of the features found in drug-resistant tumor cells, probably due to the accumulation of xenobiotic compounds in cellular compartments (Niepel et al., 2017). P-glycoproteins modulates cell volume through its regulatory effect on chlorine selective channel. Previous studies have shown that swelling is a common occurrence in cells with high expression of MDR genes (Sardini et al., 1994; Wang et al., 1998). A previous study did not report changes in cell size in romidepsin-resistant HuT78 cells (Piekarz et al., 2004).

HuT78$_{VR}$ cells showed significantly enhanced invasive and migratory characteristics in comparison to the parental HuT78 cells. Aggressive migratory and invasive capabilities are known in several other drug-resistant cancer cells (Jeon et al., 2016; Takata et al., 2015). Another study demonstrated significant upregulation of the cell adhesion protein LAIR2 in HDAC inhibitor-resistant peripheral blood and skin

localized T cells from CTCL patients and suggested LAIR2 as one of the potential prognostic and predictive markers of HDAC inhibitor resistance in CTCL (Andrews et al., 2019).

In our RNA-seq analysis, DEGs in HuT78$_{VR}$ included the upregulation of the INSR, IGF1R, MMP-9 and VIM, which was consistent with a previous study on romidepsin-resistant HuT78 cells that reported upregulation of INSR, IGF1R, MMP-9 and downregulation of PDGFR, NTRK2, TNFSF10 (Chakraborty et al., 2013). The involvement of these genes in promoting invasiveness reasserts our observation on enhanced migratory properties of HuT78$_{VR}$. RNA-seq analysis suggested that massive revamping of gene expression indicating perturbation of signaling axis regulated by GTP and MAPK signaling. These modulations in transcriptomic levels further support the enhanced invasive characteristics of HuT78$_{VR}$ cells.

Role of transporter channels have been extensively studied in drug resistance of hematolymphoid malignancies such as DLBCL, CTCL, and NKTCL (Yagi et al., 2013; Yamaguchi et al., 1995). Transporter genes such as ABCC1, ABCB1, and ABCG2 have been implicated in resistance drugs in multitudes of cancer, including hematolymphoid malignancies (Robey et al., 2018). Mode of action of these transporters depends on their ability to flush out chemotherapeutic drugs from the cells (Sharom, 2008). RNAseq and SILAC analysis of HuT78$_{VR}$ cells showed that genes involved in transporter activities were modulated in vorinostat resistant cells. Our results suggest that HuT78$_{VR}$ have higher drug expulsion capabilities and upregulated P-gp expression. However, the failure of verapamil in re-sensitizing the HuT78$_{VR}$ cells towards vorinostat indicates that the mechanism of vorinostat resistance does not involve transporter genes. This reiterated the findings of Peart *et al*. group that action of vorinostat is independent of P-gp expression. The increase in the mRNA levels of P-gp proteins can be attributed to the class effect on the de-acetylation inhibitors (Peart et al., 2003). This implicates that role of transporter genes may not be a critical component in vorinostat resistant model of CTCL.

It has been reported that stable knockout of BID and BIM in lymphoma cells make them less responsive to the therapeutic effect of vorinostat in *in-vivo* xenograft models (Lindemann et al., 2007). Previously, Chakraborty *et al*. have shown that BIM expression is significantly downregulated in romidepsin resistant CTCL cells

(Chakraborty et al., 2013). Inconsistent with these observations, our SILAC-based protein quantification of HuT78$_{VR}$ and subsequent IPA analysis advocate the defective cell death signaling machinery in HuT78$_{VR}$ cells as a dominant factor of vorinostat resistance. Downregulation of caspase 3 and BID was evident in our proteomics datasets, which implies attenuation of the apoptosis mechanism in HuT78$_{VR}$ cells.

Correlation of genes modulated in DEGs and DEPs in HuT78$_{VR}$ was basal. However, our data showed that both mRNA and protein levels of certain genes such as galectin, mucin and carbonic anhydrase were unregulated. Galectin has been implicated in sorafenib drug resistance in liver cancer as a prognostic marker (Takata et al., 2015). Previously, mucin and carbonic anhydrase were identified as potential biomarkers in CTCL (Cengiz et al., 2015; Jain et al., 2015; Thode et al., 2015).

Previously, Chakraborty et al. have shown that ERK signaling is upregulated in romidepsin resistant HuT78 cells and is involved in downregulation of BIM in resistant cells (Chakraborty etal, 2015). It has been demonstrated in this study that romidepsin resistant HuT78 cells exhibit exquisite sensitivity towards ERK inhibitors. It is important to mention that HuT78 cells harbor activating NRAS^{Q61K} mutation, which leads to enhanced ERK signaling (Kiessling et al., 2017). The cBioPortal-based search of NRAS in CTCL and multiple myeloma showed that 14% of 258 samples were mutated. These mutations were oncogenic in nature and led to the activation of ERK signaling (Cerami et al., 2012; Gao et al., 2013). The high propensity of ERK activation due to mutational aberration might lead to vorinostat resistance in CTCL and multiple myeloma. In summary, we identified the upregulation of the ERK pathway that may contribute to vorinostat-resistance in HuT78$_{VR}$ cells and may represent an important target for therapeutic development.

Cross-resistance of HuT78$_{VR}$ towards other HDAC inhibitors (*e.g.* romidepsin) was consistent with the observation made by other groups (Chakraborty et al., 2013). Surprisingly, HuT78$_{VR}$ cells were resistant to doxorubicin; also, a vital component of CHOP therapy (Coiffier et al., 2002). Doxorubicin resistance may be attributed to an increase of cyclin D1 in HuT78$_{VR}$. Cyclin D1 is involved in the migration of drug resistance in lymphoma cells (Body et al., 2017; Rosenwald et al., 2003).

We have found that HuT78$_{VR}$ cells express low levels of phosphorylated STAT3. However, the exact role of STAT3 in the acquired drug resistance model remains

unexplored. Investigating the role of STAT3 in acquired drug resistance will help in uncovering the pathogenesis of CTCL.

In conclusion, this chapter provides substantial information about molecular processes involved in vorinostat resistance in hematolymphoid malignancies. These studies are the first to connect molecular changes in both mRNA and protein expression to vorinostat resistance in CTCL patient-derived HuT78 cells. In particular, increased ERK signaling is an important driver for vorinostat resistance, suggesting its utility as prognostic and predictive markers. Our results also suggest that ERK inhibitors could be potential candidates for combinatorial therapeutics in vorinostat-resistant lymphomas. Further studies will be required to define the exact role of ERK in the pathogenesis and progression MF/SS, as well as its potential as a predictive marker and therapeutic target in various subsets of hematolymphoid malignancies.

Chapter 4

DDX3X involvement in hematolymphoid malignancies

4.1 Introduction

Increasing advances in next-generation sequencing (NGS) and cutting-edge molecular techniques have provided compelling evidence that hematolymphoid malignancies are genetically heterogeneous. While several cytogenetic alterations can predict responses to chemotherapies and good prognosis among patients with hematologic malignancies, several genetic alterations, including somatic mutations, have been associated with adverse prognosis and poor survival.

Genetic characterization has helped to define genetic biomarker delineating specific entities of hematologic malignancies, and many of these alterations have been included in the 2016 revision of the World Health Organization (WHO) classification of hematopoietic and lymphoid malignancies (Swerdlow et al., 2016). In 2018, WHO-EORTC classifications for cutaneous lymphoma were updated (Willemze et al., 2019). However, there are still several less-defined genetic alterations that have not been linked to hematologic malignancies. Therefore, those less recognized genetic alterations or mutations are neither evaluated in standard clinical practice nor examined to check therapeutic responses. For example, large numbers of genes have been found to be mutated in Diffused Large B-cell Lymphoma (DLBCL) and Natural Killer T cell Lymphoma (NKTCL); but, the majority of these genes affect only a minority of cases (Choi et al., 2015; Mottok et al., 2019; Schmitz et al., 2018). Given the growing number of somatic alterations being identified in hematologic neoplasms, the examination of a limited number of genes may not be sufficient to understand the complexity of these diseases. It is thus imperative to elucidate the biological significance of less-common mutations.

Recent studies have performed comprehensive genomic analysis of a cohort of patients with DLBCL, the most commonly diagnosed subtype of Non-Hodgkin's Lymphomas (NHL), using whole-exome sequencing (WES) and identified frequent occurrence of mutation in the *DEAD-box helicase 3, X-linked* (*DDX3X*) gene (Arthur et al., 2018; Reddy et al., 2017). DDX3X is an ATP-dependent RNA helicase and plays an integral role in RNA metabolism (Takahashi et al., 2018). In addition, it displays a high level of ATPase activity (Epling et al., 2015; Kim and Myong, 2016; Riva and Maga, 2019)and is involved in multiple cancer-related cellular processes, including transcriptional regulation (Chao et al., 2006), messenger ribonucleoprotein assembly,

pre-mRNA splicing (Merz et al., 2007), mRNA export (Lai et al., 2008), translation (Geissler et al., 2012; Lai et al., 2010; Soto-Rifo and Ohlmann, 2013), cell cycle control (Schroder, 2010), cell adhesion (Chen et al., 2015) and signal transduction (Soulat et al., 2008). About 3-5% of DLBCL cases were found to have mutations in the *DDX3X* (Arthur et al., 2018; Reddy et al., 2017). Moreover, recurrent loss of function somatic mutations in *DDX3X* have been associated with worse prognosis and chemotherapy resistance in NKTCL and Chronic Lymphoid Leukaemia (CLL) patients (Dufva et al., 2018; Jiang et al., 2015).

Loss of DDX3X has previously been associated with the upregulation of tumorigenic signaling of ERK and NF-κB in hematolymphoid malignancies (Jiang et al., 2015). In chapter 3, we identified a crucial involvement of ERK signaling in activating resistance to vorinostat in $HuT78_{VR}$. Moreover, previous reports suggest that both ERK and STAT3 are actively involved in drug resistance in hematolymphoid malignancies (Chakraborty et al., 2013; Fantin et al., 2008).

Therefore, it was hypothesized that DDX3X could have a crucial role in the aggressiveness and drug resistance in DLBCL and NKTCL cells and may also play a role in cutaneous T-cell Lymphoma (CTCL), a heterogeneous spectrum with different aggressiveness.

4.2 Objectives

The goal of this chapter was to understand the potential involvement of DDX3X in hematolymphoid malignancies, with a focus on cells of DLBCL, NKTCL, and CTCL. Specific objectives were:

4.2.1 To examine the mutational status and expression of DDX3X in hematolymphoid malignancies.

4.2.2 To determine the molecular effects of DDX3X loss in cells derived from lymphomas, including CTCL, DLBCL, NKTCL.

4.2.3 To define functional involvements of DDX3X in hematolymphoid malignancies.

4.3 Results

4.3.1 Recurrent *DDX3X* mutations in hematolymphoid malignancies

To perform a general evaluation of *DDX3X* mutations across hematolymphoid malignancies, we searched cBioPortal, an online repository of genomic data of cancer samples (Gao et al., 2013). The available database from 19,584 samples revealed 58 missense and 20 truncating mutations in the *DDX3X* gene associated with a diverse range of hematologic cancers. Specifically, *DDX3X* was mutated in 49 out of 1,343 DLBCL cases (3.6%) (**Appendix 4, Table A4.2**). A previous study using tissue samples from 25 Japanese NKTCL patients identified that 3 cases (12%) had mutations in the *DDX3X* gene by conventional Sanger sequencing (Dobashi et al., 2016); while another study in China showed recurrent loss-of-function mutations in *DDX3X* in 21 out of 105 (20.0%) NKTCL subjects by NGS (Jiang et al., 2015). We could not identify potential *DDX3X* mutations in CTCL cases, as relevant data about the presence of *DDX3X*somatic mutations in CTCL patients was not available in the cBioPortal repository.

Further annotation using the OncoKB tool predicted 15 somatic mutations in the "helicase ATP-binding" and the "helicase C-terminal" domains (**Figure 4.1**), the two main catalytic domains of the *DDX3X* gene. Of these variants, five mutations (I214Tfs*7, Q309*, X342_splice, D354G and T369Nfs*14) were found in the helicase ATP-binding domain and 10 mutations (S410F/T411Pfs*9, T418Sfs*15, S429Kfs*29, X439_splice, S456Ffs*40, S489*, Y525H, R528H, R534H\C and P568Cfs*5) in the helicase C-terminal domain (**Figure 4.1**). Among these 15 mutations, 11 were truncating mutations (*indicated by black dots*) and thus expected to cause loss of function of DDX3X (**Figure 4.1**).

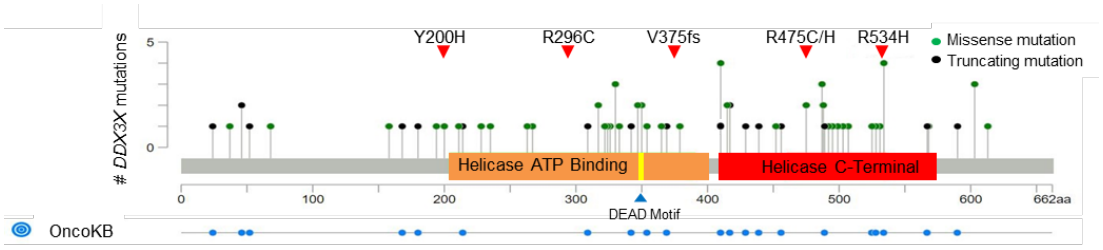

Figure 4.1 Mutational landscape of *DDX3X*. Using cBioPortal and OncoKB, mutations in the *DDX3X* gene in lymphoid malignancies were collated. Red arrows point to damaging *DDX3X* mutations in the "helicase ATP-binding" domain and in the "helicase C-terminal" domain identified by whole-exome sequencing of biopsies from DLBCL patients.

Further analysis using PolyPhen-2, a tool that predicts the impact of an amino-acid substitution (mutation) on the function of a protein (Adzhubei et al., 2010) predicted that D354G, Y525H, R528H, and R534H/C missense mutations would have "probably damaging" consequences on DDX3X functions (**Table 4.1**).

Table 4.1 PolyPhen-2 scores of missense mutations and their predicted consequences in hematolymphoid malignancies.

SN.	Protein Change	HumVar Prediction Score	Consequence
1	D354G	0.652	Possibly damaging
2	Y525H	1	Probably damaging
3	R528H	0.96	Probably damaging
4	R534H/C	0.998/ 0.998	Probably damaging

To validate the presence of somatic mutations in lymphoma patients, a collaboration was established with the clinician Dr. Nicholas Grigoropoulos, Singapore General Hospital (SGH), Singapore. Dr. Grigoropoulos provided genome sequencing datasets (WES) of tumor biopsies from 9 different patients with R/R-DLBCL treated with R-CHOP or similar regimens (8 taken at the time of diagnosis and one at relapse). Methodologies used in the WES analysis of the above nine patient samples and relevant ethics statement are provided in the **Appendix 4**.We identified that*DDX3X* was the most frequently mutated gene in this R/R-DLBCL cohort, with lesions identified in 4 out of 9 cases (44%) (**Table 4.2**). A total of 5 damaging *DDX3X* mutations were identified (PolyPhen-2 score = 1) in the catalytic domains; R296C and V375fs in the “helicase ATP-binding” domain and R475C/H and R534H in the “helicase C-terminal” domain (**Figure 4.1,** *indicated by red arrowheads*). All the identified *DDX3X* mutations were confirmed to be somatic. Of note, R475C/H and R534H mutations have previously been reported in Burkitt’s lymphoma (BL) (Richter et al., 2012). These results suggest that *DDX3X* mutations may be prognostically important in DLBCL and other hematologic neoplasms, NHLs, and are thus candidate driver lesions in these malignancies.

Table 4.2 DDX3X variants identified by WES in 4 out of 9 cases with R/R-DLBCL.

Case ID	Age/ Sex	MYC/BCL2/BCL6 translocation status	TP53 mutation status	DDX3X mutations in DLBCL			
				Nucleotide change	Amino acid change	Domain affected	PolyPhen score
WES1	53/F	M.Y.C. trans +ve, BCL2 trans +ve, BCL6 trans -ve	W.T.	c.1423C>T	R475C	Helicase C-terminal domain	1
				c.598T>C	Y200H	--	1
WES3	59/M	M.Y.C. trans -ve, BCL2 trans +ve, BCL6 trans -ve	W.T.	c.1424G>A	R475H	Helicase C-terminal domain	1
WES4	52/M	M.Y.C. trans +ve, BCL2 trans +ve, BCL6 trans -ve	R273C	c.1118_1119insG	V375fs*8	Helicase ATP binding domain	Frameshift
WES7	55/F	MYC trans -ve, BCL2 trans -ve, BCL6 trans -ve	WT.	c.886C>T	R296C	Helicase ATP binding domain	1
				c.1601G>A	R534H	Helicase C-terminal domain	1

Note: DLBCL patient samples were analyzed by Dr. Grigoropoulos, Singapore General Hospital (SGH), Singapore.

4.3.2 DDX3X mutations are associated with worse clinical outcomes

We performed Kaplan-Meier analysis based on the available data from 223 DLBCL cases in cBioPortal. This analysis revealed that patients with mutant *DDX3X* (n=14) had significantly worse median overall survival (OS) (41.13 months) compared to wild-type (WT) cases (211.07 months, n=209) (**Figure 4.2A**). Further analysis showed that the 5-year OS of patients with *DDX3X* mutations was only 22% compared to 72% for patients with WT*DDX3X.* Furthermore, median disease-free survival (DFS) of DLBCL cases with *DDX3X* mutations was worse than WT cases (although

statistically insignificant due to values obtained from a limited number of patients, n=7) (**Figure 4.2B**). OS and DFS analysis of patients with other NHL subtypes (CTCL and NKTCL) carrying *DDX3X* mutations could not be performed due to a lack of relevant information in the data repositories.

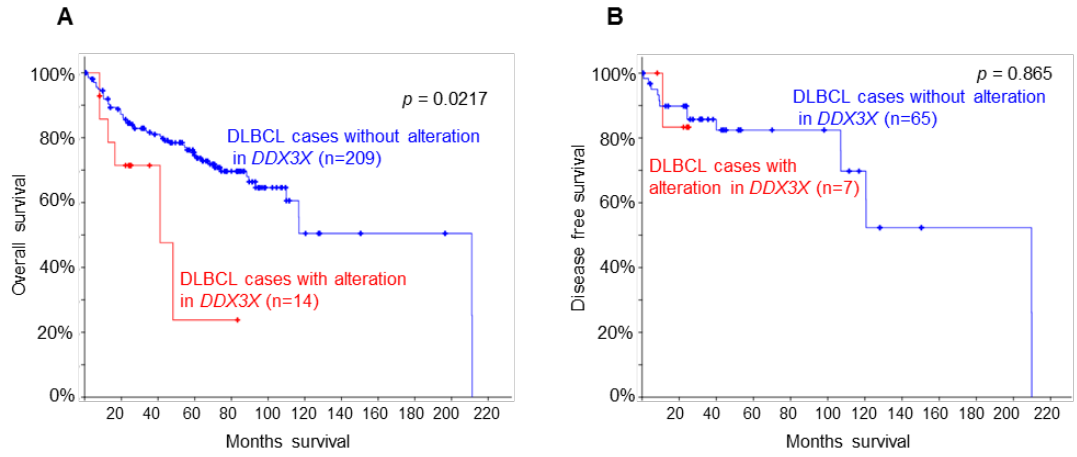

Figure 4.2 Genomic lesions in DDX3X cause poor prognosis in patients with DLBCL. Kaplan-Meier survival analysis of DLBCL patients with mutations in the *DDX3X* gene showing overall survival (**A**) and disease-free survival(**B**) in comparison to that with DLBCL cases having no alteration in the *DDX3X* gene.

4.3.3 DDX3X is abundantly expressed in cultured NHL cells

We analyzed DDX3X protein expression levels in a panel of 9 different cell lines derived from patients with various NHL subtypes – CTCL (HuT78, HH, MJ, MyLa), DLBCL (U2392), NKTCL (NKYS, SNK6), and BL (BJAB, Raji).In addition to the above 9 NHL cell lines, we included an acute T cell leukemia cell line Jurkat and a chronic myeloid leukemia cell line K562 line as controls since the expression of DDX3X protein has previously been shown in these two cell types (Arvaniti et al., 2014; Soto-Rifo and Ohlmann, 2013). Western immunoblot analysis showed variable levels of DDX3X expression in all the cell lines assessed in this study (**Figure 4.3A**). This suggests that changes in DDX3X expression levels may underlie the transformation from functioning lymphocytes. The discrepancy of increase of the DDX3X expression in these NHL cell lines remains unclear, but one may argue the possibility of compensatory responses. Since the expression of DDX3X was abundant in HuT78 cells and this cell line expresses WT DDX3X (Mondejar et al., 2017), we selected this CTCL cell line for most of the experiments involving DDX3X knockdown to obtain functional readouts. Confocal microscopy showed a polarized but punctate staining pattern of

DDX3X protein expression in HuT78 cells, mainly localizing in the cytoplasm (**Figure 4.3B**).

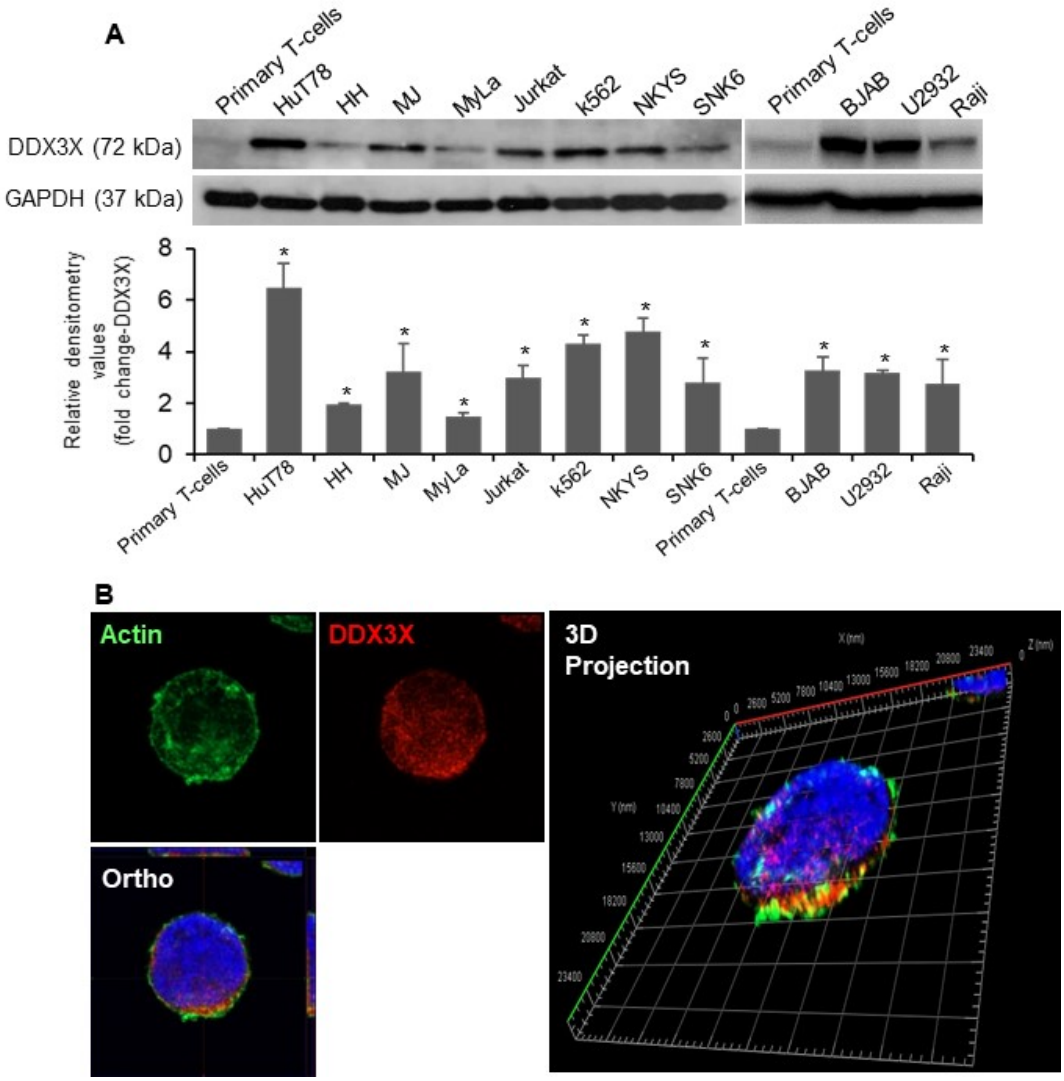

Figure 4.3 DDX3X expression and localization in a panel of cell lines derived from patients with NHL **(A)** Cellular lysates (20 µg each) from HuT78, HH, MJ, MyLa, Jurkat, K562, NKYS, SNK6, BJAB, U2932 and Raji cells were subjected to Western immunoblot analysis for DDX3X expression. Cell lysate from human primary T-cells was used as a control. Blots were re-probed for GAPDH as a loading control. Relative densitometry graphs of DDX3X expression are presented (mean ± SEM, *, $p<0.05$)**(B)** HuT78 cells were immuno-stained for DDX3X (*red*), actin (*green, to visualize cytoplasmic region*) and nuclei (*blue*), and imaged by Zeiss confocal microscope using 63X oil objective. Representative datasets from at least three independent experiments are presented.

4.3.4 DDX3X knockdown in cultured CTCL, NKTCL and DLBCL cells

To mimic the loss of function *DDX3X* lesions in lymphomas, we knocked-down DDX3X in a panel of cell lines derived from patients with CTCL (HuT78, MJ, MyLa), DLBCL (U2392, HBL-1), BL (Raji, BJAB), or NKTCL (NKYS, SNK1, SNK6) using the siRNA-or shRNA-mediated gene silencing technique. We generated stable DLBCL cell lines U2932, BJAB, Raji, and HBL-1 expressing doxycycline-inducible DDX3X shRNA constructs. The qRT-PCR analysis of cells following siRNA-or shRNA-mediated knockdown showed significant depletion of DDX3X mRNA (> 80%, depletion) in all the cells analyzed (**Figure 4.4A, B**).

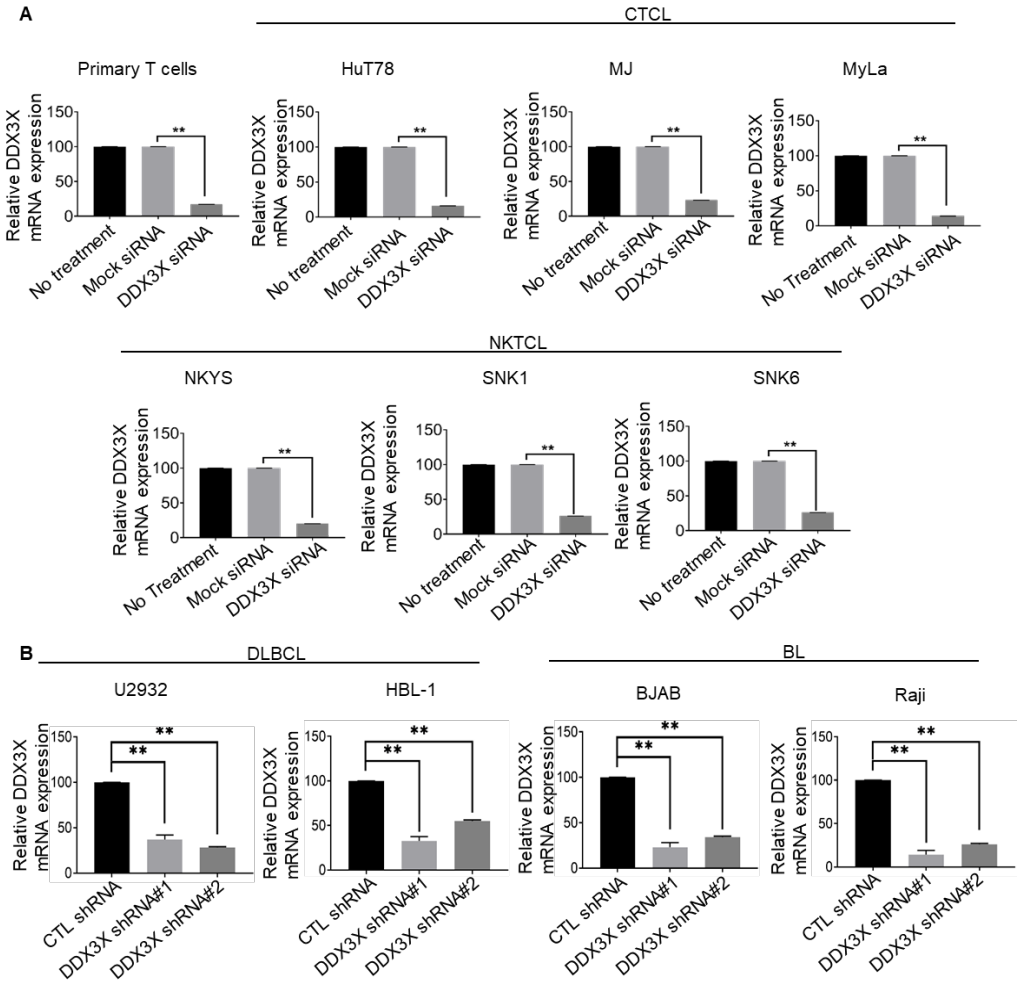

Figure 4.4 qRT-PCR analysis of DDX3X-depleted N.H.L. cells. (**A**) CTCL (HuT78, MJ, MyLa) and NKTCL (NKYS, SNK1, SNK6) cells line were nucleofected with DDX3X siRNA/ Mock siRNA (control) for a period of 72. Total RNA was extracted and evaluated for mRNA expression of DDX3X using qRT-PCR. (**B**) Doxycycline-inducible DDX3X shRNA constructs expressing U2932, BJAB, Raji, and HBL-1 cells were incubated with 100 ng/mL doxycycline for 48 h. Total RNA was extracted and evaluated for mRNA expression of DDX3X using qRT-PCR. Representative datasets from at least three independent experiments are presented (mean ± SEM). *, p<0.05; **, p<0.01.

Further analysis of siRNA-mediated knockdown cells by Western immunoblotting. Results on the depletion of DDX3X protein in primary T cells, HuT78, MJ, and NKYS are provided (**Figure 4.5A**). The expression of DDX3X was depleted in DLBCL (U2932, HBL-1) and BL (BJAB, Raji) cells following incubation with doxycycline for 48h. Western immunoblot analysis of U2932, BJAB, Raji, and HBL-1 cells following doxycycline-induced DDX3X silencing confirmed DDX3X depletion in these cells (**Figure 4.5B**).

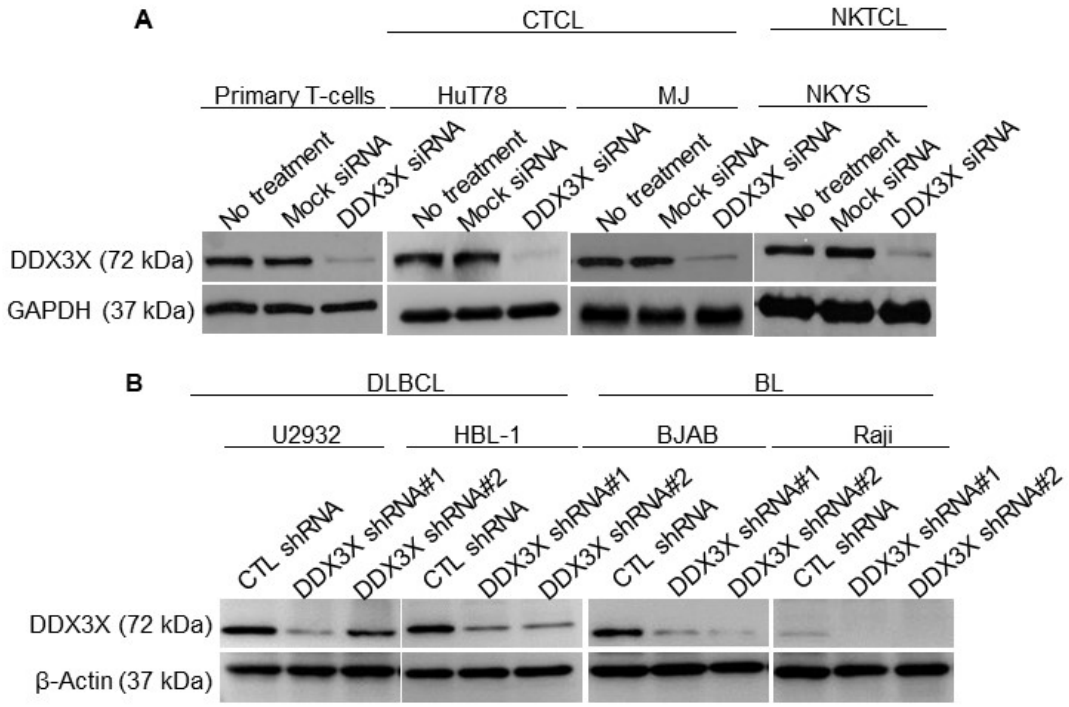

Figure 4.5 Western immunoblot analysis of DDX3X-depleted cells of hematolymphoid malignancies. **(A)** Cell lysates from DDX3X-depleted primary T-cells, HuT78, NKYS, and MJ cells were immunoblotted for the evaluation of DDX3X expression and re-probed for GAPDH as a loading control. **(B)** Doxycycline-inducible DDX3X shRNA constructs expressing U2932, BJAB, Raji, and HBL-1 cells were incubated with 100 ng/mL doxycycline for 48 h. Cell lysates were immunoblotted for the evaluation of DDX3X expression and re-probed with anti-β-actin as a loading control. Representative datasets from at least three independent experiments are presented.

4.3.5 Transcriptomic analysis of DDX3X-depleted lymphoma cells

We performed RNA-seq analysis of DDX3X-depleted HuT78 cells (this Sézary cell line was chosen as a representative model to study hematolymphoid malignancies) in comparison to WT and identified 1,682 differentially expressed genes [DEGs](fold change >2, False Discovery Rate [FDR] <0.05). A volcano plot prepared for the DEG datasets clearly shows that a substantial number of genes were significantly upregulated or downregulated in DDX3X-depleted HuT78 cells in comparison to control (**Figure**

4.6A). Among the 1,682 DEGs, 922 genes were downregulated, and 760 genes were upregulated in DDX3X-depleted cells relative to the control group. The top 50-dysregulated mRNAs from RNA-seq analysis are listed in **Table 4.3.** GO classification of the DEGs revealed 38% genes that regulate cellular processes, such as signal transduction (**Figure 4.6B**). Other genes that were altered in DDX3X-depleted cells are known to control metabolic processes (23%), biological regulation (19%) and molecular localization (13%) (**Figure 4.6B**). IPA analysis of the RNA-seq datasets showed enhanced activation of cytokine signaling pathways in DDX3X-depleted CTCL cells (**Figure 4.6C**), indicative of increased cell proliferation.

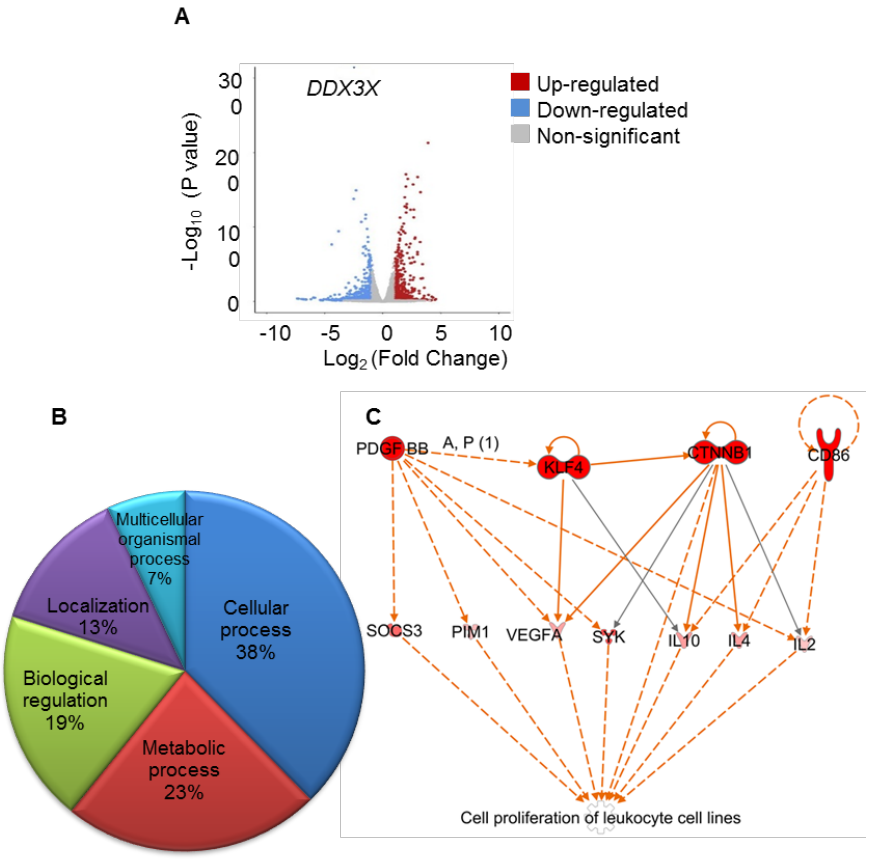

Figure 4.6 RNA-seq analysis of DDX3X-depleted HuT78 cells**.** Total RNA was extracted from WT or DDX3X-depleted HuT78 cells (n=3), and mRNA differential expression of genes was analyzed using RNA-seq. (**A**) A volcano plot showing DEGs in DDX3X-depleted HuT78 cells (fold change Log_2>2, FDR <0.05 , and p<0.05). **(B)** DEGs were analyzed using GO **(C)** DEGs were analyzed using IPA to predict affected protein networks, and a representative network was presented.

Table 4.3 A list of top 50 DEGs in DDX3X-depleted HuT78 cells.

S. N	Gene symbol	Log_2 fold change	FDR value	S. N	Gene symbol	Log_2 fold change	FDR value
1	*DDX3X*	-2.47166	0	26	*CEBPB*	1.654593	5.42E-101
2	*ASS1*	2.934896	0	27	*RRM2*	-1.35213	3.55E-98
3	*INHBE*	3.891941	1.40E-213	28	*PHGDH*	1.572457	2.25E-97
4	*TXNIP*	1.994021	1.93E-171	29	*ESRP1*	1.765227	3.09E-95
5	*SOCS3*	3.00113	9.12E-168	30	*HSPA6*	-3.81415	5.78E-95
6	*RGS16*	2.152629	3.07E-165	31	*VEGFA*	1.753558	9.73E-95
7	*SESN2*	2.608481	8.83E-158	32	*CBX4*	1.371657	2.68E-93
8	*UBALD2*	1.990409	5.32E-155	33	*SPNS3*	1.921787	1.42E-92
9	*MALAT1*	-2.30321	6.61E-150	34	*PLEK*	1.534333	1.08E-90
10	*CHAC1*	3.241475	2.21E-147	35	*HSPA8*	-1.28545	3.19E-87
11	*TSC22D3*	1.886946	1.58E-140	36	*DUSP5*	2.79114	1.31E-86
12	*LMNA*	-2.51151	1.85E-138	37	*RFLNB*	1.458262	3.64E-85
13	*TRIB3*	2.071372	1.24E-131	38	*S100P*	2.755481	5.73E-85
14	*AC092368.3*	1.888136	2.34E-128	39	*MAP1LC3B*	1.468787	3.71E-83
15	*SGK1*	2.000893	3.35E-128	40	*NPTX1*	1.440262	2.32E-82
16	*HOXB9*	2.056824	1.88E-126	41	*PTBP1*	-1.27102	9.80E-81
17	*BBC3*	2.677357	4.91E-124	42	*JDP2*	3.212733	1.60E-80
18	*GPT2*	2.387823	7.95E-124	43	*STC2*	2.3718	3.05E-78
19	*GAB2*	2.00873	4.64E-120	44	*DHRS2*	-4.40207	2.64E-77
20	*HSPA1A*	-1.47062	3.61E-117	45	*TBL1X*	2.021399	3.60E-77
21	*ADM2*	2.670839	1.29E-113	46	*PIM1*	1.346113	4.56E-77
22	*INSIG1*	1.479817	2.54E-113	47	*SLC43A2*	-1.5396	5.66E-75
23	*HSPA1B*	-1.49392	6.18E-112	48	*UTP20*	-1.68077	7.08E-74
24	*NEAT1*	-1.85219	1.61E-107	49	*WIPI1*	2.27102	1.72E-73
25	*CST7*	1.800613	3.23E-105	50	*CEBPG*	1.336653	1.97E-73

4.3.6 Upregulation of IL-10 in DDX3X-depleted cells of hematolymphoid malignancies

Since RNA-seq analysis of DDX3X-depleted HuT78 cells and subsequent IPA showed upregulation of cytokine signaling, we verified the expression levels of cytokines in DDX3X-depleted HuT78 cells in comparison to controls by qRT-PCR. Results showed significant upregulation of IL-2, IL-4, and IL-10 mRNA in DDX3X-depleted HuT78 cells (**Figure 4.7A**). Further analysis by ELISA confirmed a significant increase in the secreted levels of IL-10 in DDX3X-depleted HuT78 cells (**Figure 4.7B**); however, no significant increase in the secreted levels of IL-2 was observed in DDX3X-depleted HuT78 cells (**Figure 4.7C**). We could not detect secreted IL-4 in these cells by ELISA (data not shown), possibly due to very low basal levels of IL-4, which was beyond the detection limit of the kit used. DDX3X-depleted U2932 and BJAB cells showed a more than 2-fold increase in IL-10 mRNA levels (**Figure 4.7D, E**).

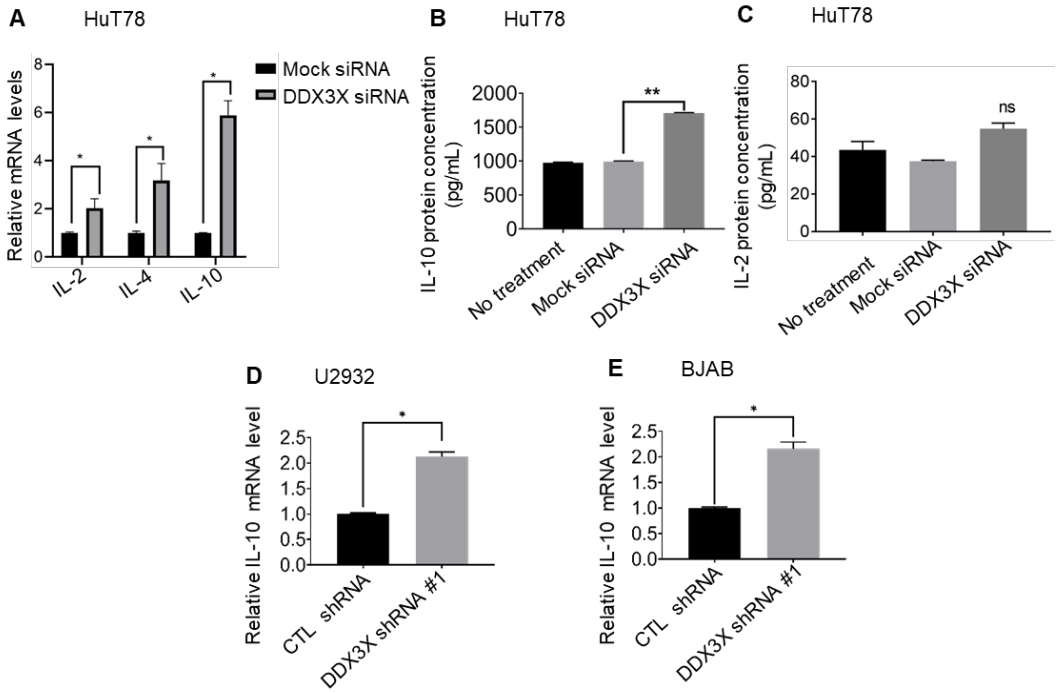

Figure 4.7 DDX3X depletion upregulates cytokine expression in cells of hematolymphoid malignancies. **(A)**HuT78 cells nucleofected with DDX3X siRNA for 72 h were quantified by qRT-PCR. HuT78 cells nucleofected with mock siRNA were used as control. **(B)** Supernatant media from HuT78 cells nucleofected with DDX3X siRNA or Mock siRNA (control) were collected after 72 h, and secreted levels of IL-10 were evaluated using ELISA kit.**(C)** The mRNA levels IL-10 in U2932, and BJAB cells following shRNA-mediated DDX3X knockdown were evaluated using RT-qPCR. Representative data (mean ± SEM) from at least three independent experiments are presented. **, p<0.001; *, p<0.01; *ns*, non-significant.

Further, *in silico* analysis of DEGs using Database for Annotation, Visualization and Integrated Discovery (DAVID) (**Table 4.5**)and Ingenuity Pathway Analysis (IPA) (**Table 4.6**)showed that DDX3X depletion increases cytokine-cytokine receptor interactions and activation of certain transcription regulators such as STAT3 and NFKBIA. These results suggest that *DDX3X* mutations may promote lymphoma growth by impinging upon several important biological processes.

Table 4.5 Top 10 biological pathways altered in DDX3X depleted HuT78 cells based on DAVID analysis.

SN.	Biological Pathways	FDR values
1	Cytokine-cytokine receptor interaction	0.018950459
2	Antigen processing and presentation	0.011091064
3	Hematopoietic cell lineage	0.029780314
4	Allograft rejection	0.024937115
5	Biosynthesis of amino acids	0.041354406
6	Glycine, serine and threonine metabolism	0.115185834
7	Asthma	0.111761789
8	Inflammatory bowel disease (IBD)	0.129008204
9	Jak-STAT signaling pathway	0.153897632
10	Toxoplasmosis	0.200518941

Table 4.6 Top 10 upstream transcriptional regulators altered DDX3X depleted HuT78 cells based on IPA.

SN.	Regulators	p-values	z-scores
1	ATF4	4.42E-10	4.395
2	STAT4	6.69E-09	2.861
3	STAT3	3.79E-07	3.611
4	EGR2	8.45E-06	2.069
5	TP53	1.09E-05	2.774
6	REL.	2.46E-05	2.257
7	CTNNB1	1.33E-04	2.009
8	NFKBIA	4.13E-04	3.041
9	NFIL3	1.26E-03	2.433
10	NUPR1	2.33E-03	3.452

4.3.7 DDX3X depletion does not affect cell cycle progression in cells of hematolymphoid malignancies

We examined the effect of DDX3X depletion on a panel of 4 cell lines (HuT78, Raji, U293, and BJAB). Flow-cytometry analysis of DDX3X-depleted cells showed no significant change in the number of cells at G1, S, and G2 stages of the cell cycle in either of the four NHL cell lines tested in comparison to corresponding controls (**Figure 4.8**). It is important to note that cell cycle distribution varies in each cell line. In HuT78 and Raji cell lines, the G1 population was 65% and 80%, respectively. Whereas in U2932 and BJAB, cell lines in the G1 population were 49.7 % and 44.7%, respectively.

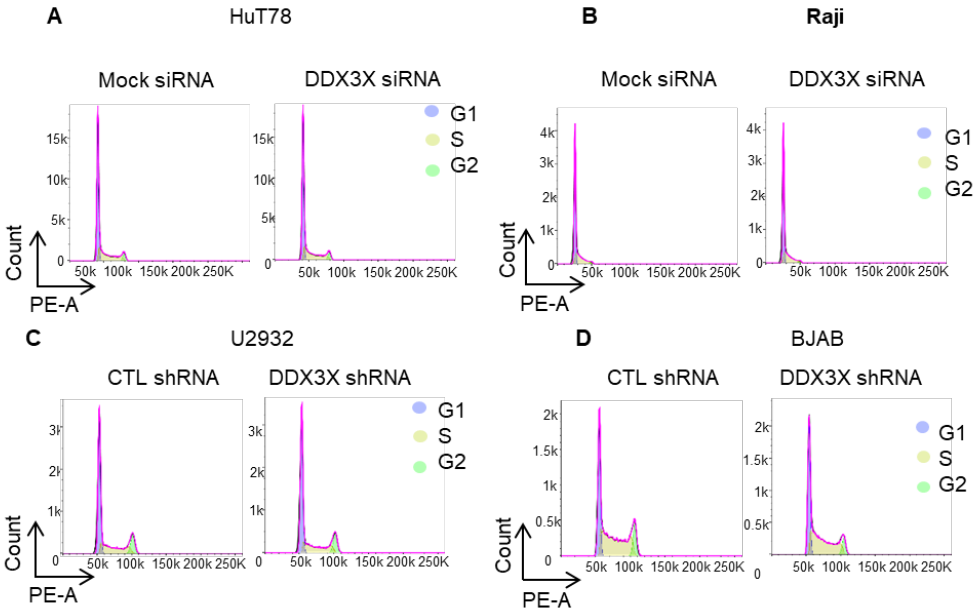

Figure 4.8 DDX3X depletion does not influence the cell cycle of NHL cells. (**A, B**) HuT78 and Raji were nucleofected with DDX3X siRNA/ Mock siRNA (control) and were incubated for 48 hr. These cells were stained with propidium iodide in the presence of RNase and analyzed by flow cytometry. (**C, D**) Doxycycline-inducible DDX3X shRNA construct expressing U2932, BJAB, Raji, and HBL-1 cells were incubated with 100 ng/mL doxycycline for 48 h. These cells were stained with propidium iodide in the presence of RNase and analyzed by flow cytometry.

4.3.8 DDX3X depletion enhances proliferation of cells of hematolymphoid malignancies

Since IPA analysis of DEGs in DDX3X-depleted cells predicted impact on cell proliferation, we examined the effect of DDX3X knockdown in a panel of NHL cell lines by MTS-based cell viability assay. We observed significantly increased proliferation of DDX3X-depletedHuT78, Raji, and SNK1 cells, while the viability of

MJ, SNK6, NKYS, and healthy primary T-cells remained largely unaffected following DDX3X knockdown (**Figure 4.9A**). Similarly, we found that DDX3X depletion causes increased proliferation of Raji and SNK1 cells, while the viability of MJ, SNK6, NKYS, and primary T-cells remained largely unaffected following DDX3Xknockdown (**Figure 4.9A)**. We further observed that DDX3X loss did not cause apoptosis in these NHL cells (**Figure 4.9B**).

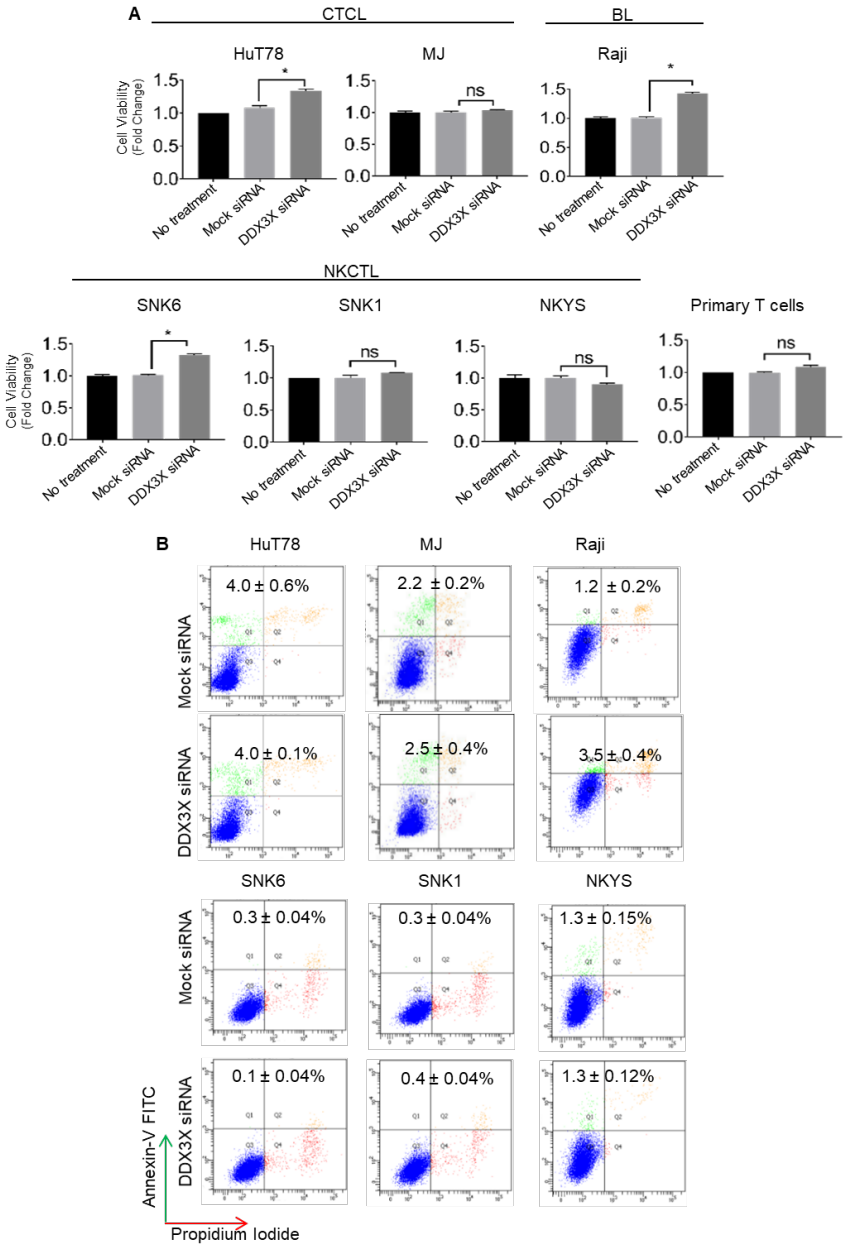

Figure 4.9 DDX3X loss enhances the proliferation of NHL cells. **(A)** Six NHL c**ell lines (**HuT78, Raji, SKN1, SNK6, MJ, and NKYS) and primary T-cells were transfected with DDX3X-targeted siRNA to knockdown DDX3X expression. Non-specific (*Mock*) siRNA was used as a transfection control. The effect of DDX3X knockdown on the viability of cells was quantified by the MTS-based assay. **(B)** The effect of DDX3X knockdown on apoptosis induction in the above

cells was determined by Annexin-V/PI labeling and flow cytometry. Data represent the mean ± SEM of at least three independent experiments. *ns*, not significant; *, $p<0.05$.

4.3.9 DDX3X depletion enhances the chemotactic and migratory potential of cells of hematolymphoid malignancies

Results from Boyden chamber trans-well migration experiments showed significantly increased (>6-fold) migratory potential of DDX3X-depleted HuT78 cells in comparison to control (**Figure 4.10A**). We next performed trans-well migration assay using the xCELLigence RTCA System, which quantifies cell migration in real-time based on impedance measurements. Data showed significantly increased migration of DDX3X-depleted HuT78 cells in comparison to control (**Figure 4.10B**). HuT78 cells exhibit a typical T cell migration pattern in which cells migrate aggressively in the first 2-3 hours of LFA1/ICAM1 stimulation. The invasive potential of DDX3X-depleted HuT78 cells was also significantly enhanced (>3-fold), as analyzed by a matrigel-based assay (**Figure 4.10C**), although we did not observe a significant change in the migratory behavior of U2932 and BJAB cells (**Figure 4.10D, E**). These findings suggest that the effects of DDX3X depletion are cell-type specific.

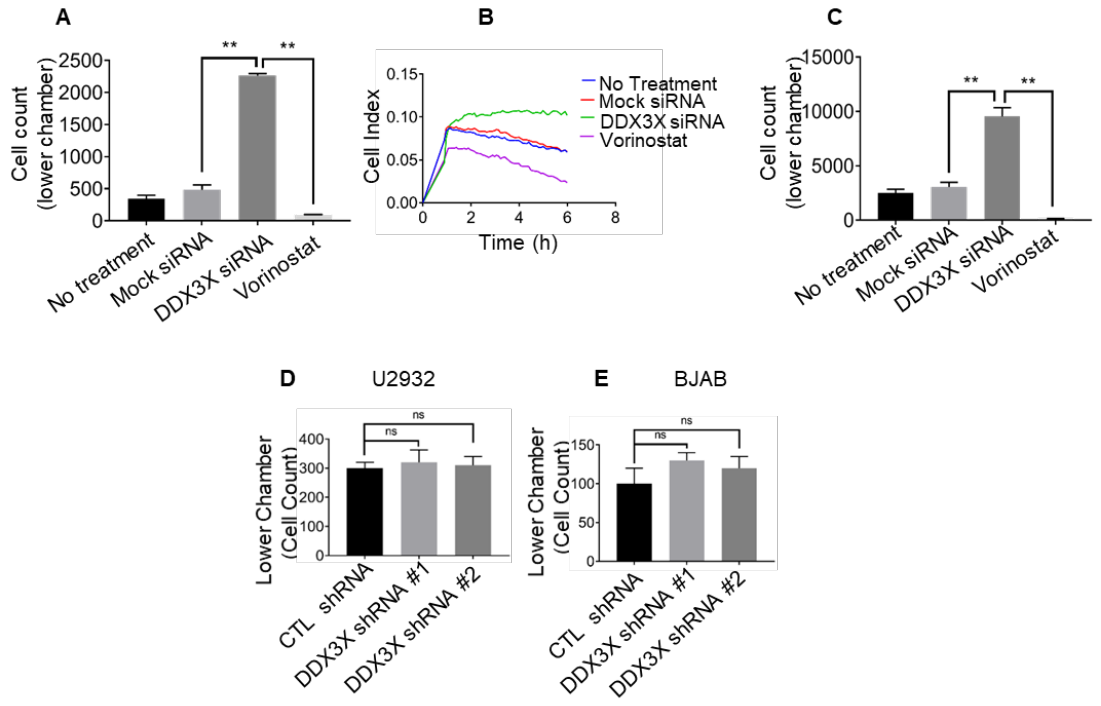

Figure 4.10 Effect of DDX3X loss on migration and invasiveness of NHL cells. **(A, B)** Control or DDX3X-depleted HuT78 cells were serum-starved and allowed to transmigrate towards 10% human serum-enriched medium in the trans-well plates for 24 h and analyzed by HCA **(A)** or real-time impedance-based measurements **(B)**. Cells were treated with vorinostat as a migration inhibitory control. **(C, D, E)** Control or DDX3X-depleted HuT78, U2932, and BJAB

cells were serum-starved and allowed to transmigrate through matrigel towards 10% human serum-enriched medium in the trans-well plates for 24 h and cells in the lower chamber were counted automatically using HCA Data represent the mean ± SEM of 3 independent experiments. *ns*, not significant; **, $p<0.01$; *, $p<0.05$.

4.3.10 DDX3X depletion upregulates vimentin and miR-150 in HuT78 cells

Vimentin is a major cytoskeleton protein component of the intermediate filament, and its overexpression is a critical prerequisite for metastasis in various tumor types (Hu et al., 2004). We detected that the expression of vimentin was significantly upregulated in DDX3X-depleted HuT78 cells (**Figure 4.11A**). Moreover, microRNA-150 (miR-150, a known anti-metastatic molecule in advanced lymphomas) was significantly downregulated in DDX3X-depleted HuT78 cells (**Figure 4.11**). Altogether, the above datasets suggest that DDX3X loss can promote proliferation and invasiveness of lymphoma cells depending upon biological milieu.

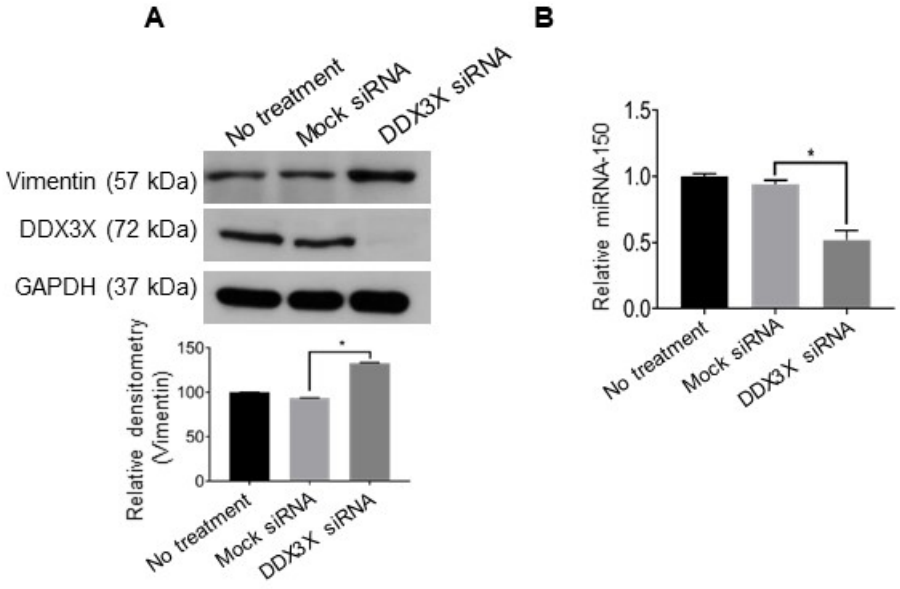

Figure 4.11 DDX3X depletion enhances metastatic markers in HuT78 cells**. (A)** Control or DDX3X-depleted HuT78 cells were analyzed for the expression of vimentin using Western immunoblot. **(G)** Control or DDX3X-depleted HuT78 cells were analyzed for the expression of miRNA-150. Data represent the mean ± SEM of 3 independent experiments. (*ns*, not significant; **, $p<0.01$; *, $p<0.05$).

4.3.11 DDX3X loss in cells of hematolymphoid malignancies enhances STAT3 activation

STAT3 is a well-studied oncogene known to be involved in the progression and severity of several hematological malignancies, including CTCL, DLBCL, and NKTCL(da Silva Almeida et al., 2015; Song et al., 2018; Verma et al., 2010; Woollard

et al., 2016). We observed that DDX3X depletion resulted in significantly enhanced expression of the phosphorylated (Y705) form of STAT3 in NHL cell lines U2932 [3-fold], SNK6 [3-fold], HuT78 [3-fold], MJ [2-fold] and MyLa [4-fold](**Figure 4.12A**). Notably, STAT3 phosphorylation remained unchanged in NKYS cells (**Figure 4.12A**), probably because this cell line expresses mutant STAT3 with high levels of baseline activity. DDX3X expression levels remained unchanged in STAT3-depleted HuT78 cells (**Figure 4.12B**).

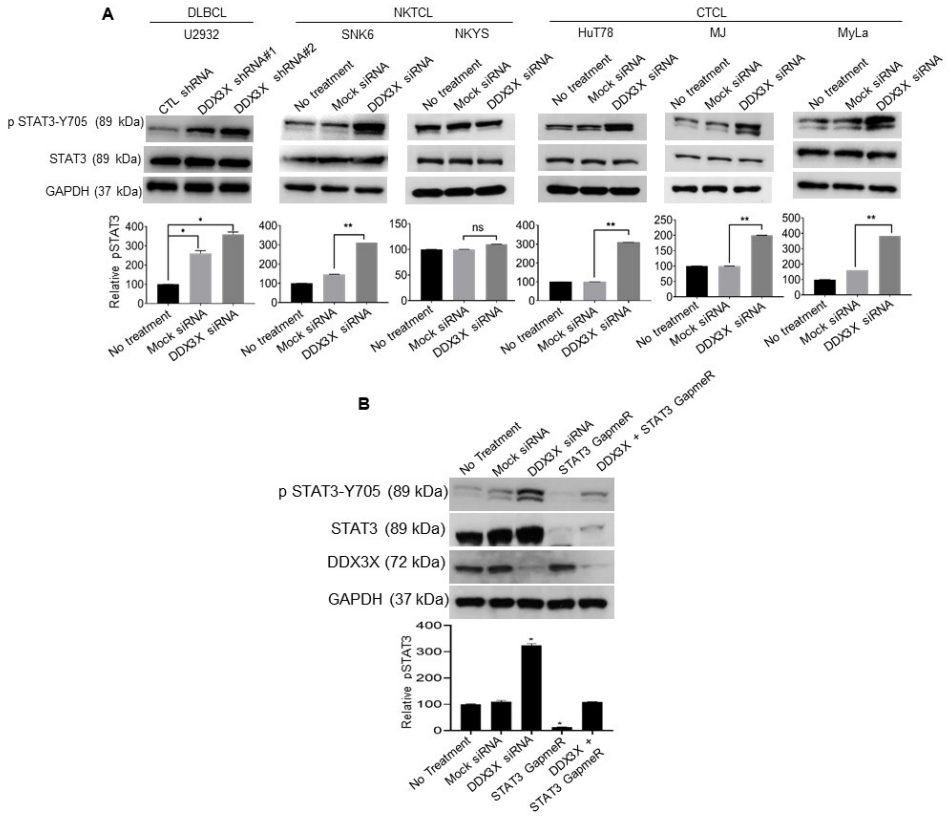

Figure 4.12 Effect of DDX3X loss on STAT3 phosphorylation in NHL cells. (**A**) Control or DDX3X-depleted DLBCL (U2932), NKTCL (SNK, NKYS), and CTCL (HuT78, MJ, MyLa) cells were lysed. Cellular lysates were analyzed to determine the phosphorylation levels of STAT3 by Western immunoblotting. **(B)** HuT78 cells were treated with DDX3X siRNA and STAT3 GapmeR. Cell lysates were collected from the cells and probed with STAT3, DDX3X, pSTAT3(Y705), and GAPDH (loading control) antibodies. Values in densitometry graphs are mean ± SEM from at least three experiments. (*ns*, not significant; **, $p<0.01$; *, $p<0.05$).

Notably, there was no direct interaction between DDX3X and STAT3 as analyzed by the co-immunoprecipitation assay (**Figure 4.13**). These findings suggest that STAT3 hyper-phosphorylation is a downstream effect of DDX3X lesions.

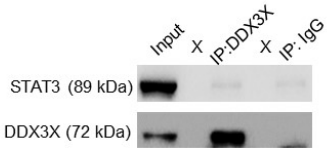

Figure 4.13 DDX3X does not physically interact with STAT3. Cell lysates of HuT78 cells were immuno-precipitated (*IP*) using anti-DDX3X or IgG (control). Subsequently, the immuno-precipitates were resolved on SDS-PAGE and immunoblotted with anti-STAT3. Blots were re-probed with anti-DDX3X as a control. Data represent two independent experiments. **, p <0.001; *, *p*<0.01; ns, non-significant.

4.3.12 DDX3X loss enhances MAPK activation in DLBCL and CTCL cells

The MAPK protein family plays an important role in the development and aggressiveness of hematologic malignancies, and several MAPK-targeted agents are being investigated as therapeutics (Germann et al., 2017). Our RNA-seq analysis of DDX3X-depleted HuT78 cells suggested the activation of the MAPK pathway following DDX3X loss in NHL cells. Using Western immunoblotting, we observed that DDX3X loss in DLBCL (U2932, Raji) and CTCL (HuT78) cell lines caused significantly increased phosphorylation of p42/44 MAPK (**Figure 4.14A, B**). The upregulation of the p42/44 MAPK pathway has previously been reported in DDX3X-depleted NKTCL (Jiang et al., 2015).

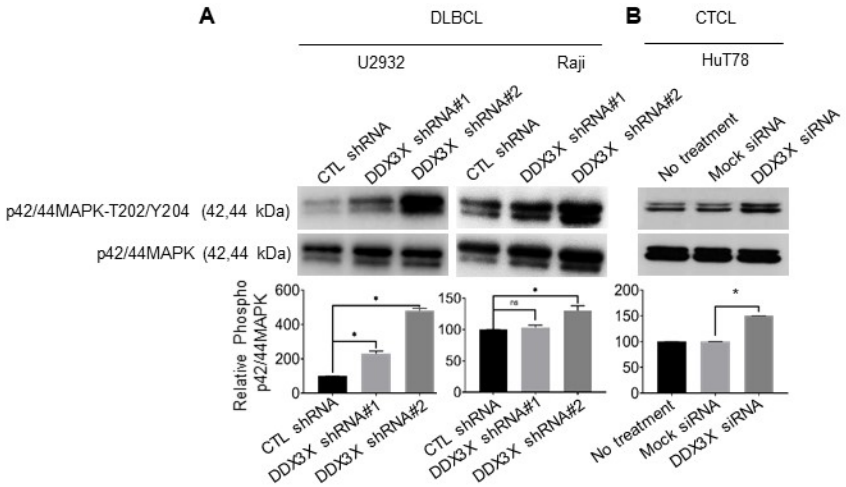

Figure 4.14 Effect of DDX3X loss on phosphorylation of p42/44MAPK in DLBCL and CTCL cells. (**A**)Control or DDX3X-depleted DLBCL (U2932, Raji) and (B) CTCL (HuT78) cells were lysed. Cellular lysates were analyzed to determine the phosphorylation levels of phopsho-p42/44MAPK (T202/Y204) by Western immunoblotting. Values in densitometry graphs are mean ± SEM from at least three independent experiments (*ns*, not significant; *, *p*<0.05).

4.3.13 DDX3X loss upregulates cyclin D1 expression in cells of hematolymphoid malignancies without impacting p53 and p21

Overexpression of cyclin D1 is often seen in hematolymphoid malignancies, including DLBCL (Ok et al., 2014), and has been associated with doxorubicin resistance in gastric cancer (Chang et al., 2006). Here, we observed significantly increased expression of cyclin D1 in DDX3X-depleted U2932 (4-fold) and Raji (4.5-fold) cells as analyzed by qRT-PCR (**Figure 4.15A**). Further analysis using Western immunoblotting confirmed 3-fold elevation in the protein levels of cyclin D1 in DDX3X-depleted U2932and Raji cells (**Figure 4.15B**).

Similarly, we observed that mRNA levels of cyclin D1 are upregulated in DDX3X depleted HuT78 and SNK1 cells. We demonstrated using qRT-PCR that mRNA levels of cyclin D1 upon DDX3X knockdown in HuT78 and SNK1 cells increases by 2.5-fold and 2-fold, respectively (**Figure 4.15C**). Because DDX3X expression levels have been correlated to levels of the well-known tumor suppressors p53 (Sun et al., 2013) and p21 (Chao et al., 2006), we sought to explore these relationships in NHL cells. However, we did not detect any significant change in the expression levels of either p21 or p53 associated with DDX3X loss in HuT78, U2392, BJAB, HBL-1 and Raji cells (**Figure 4.15D, E**).

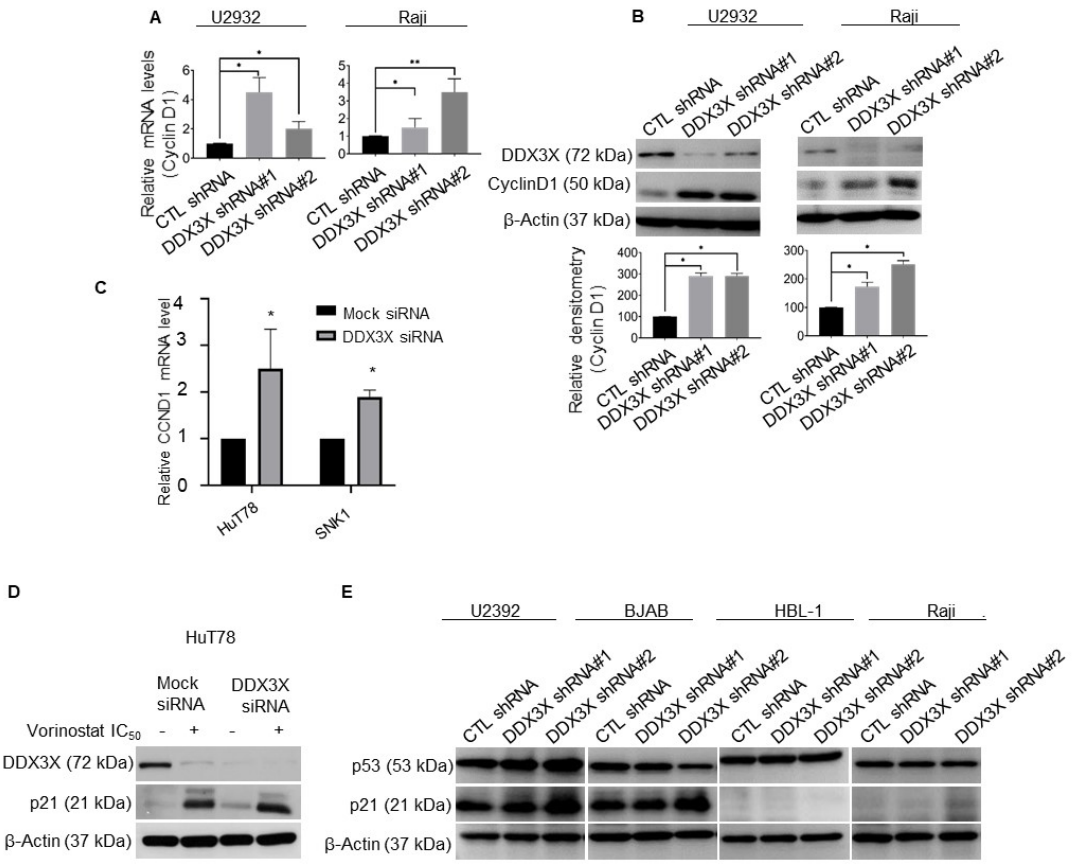

Figure 4.15 DDX3X depletion enhances expression levels of Cyclin D1cells of hematolymphoid malignancies**.** DDX3X shRNA-expressing U2932 and Raji cells were incubated in doxycycline (100 ng/mL) containing medium for 48 h DDX3X depletion and were lysed. (**A**) The relative amount of cyclin D1 mRNA was determined by qRT-PCR. (**B**) Cell lysates were immunoblotted and were probed for cyclin D1, DDX3X, and β-actin. Graphs show mean ± SEM of at least three independent experiments; *p<0.05. *(***C**) HuT78 and SNK1 cells nucleofected with DDX3X siRNA for 72 h were quantified by qRT-PCR. HuT78 cells nucleofected with mock siRNA were used as control. Representative data (mean ± SEM) from at least three independent experiments are presented. **, p<0.001; *, p<0.01; ns, non-significant. **(D)** DDX3X-depleted or control HuT78 cells were treated with vorinostat for 24 h, and cell lysates were probed with anti-p21 and anti-β-actin antibodies. (**E**) DDX3X-depleted or control U2932, BJAB, HBL-1, and Raji cells were lysed, and cell lysates were probed with anti-p53 and anti-p21 antibodies. Blots were re-probed with anti-β-actin as a loading control and presented. Data represent at least three independent experiments.

4.3.14 DDX3X depletion increases drug resistance in cells of hematolymphoid malignancies

Doxorubicin is widely used in the treatment of aggressive B-cell lymphoma (Pfreundschuh et al., 2006). We, therefore, investigated whether the poor prognosis of DLBCL patients with *DDX3X* mutations may be due to increased doxorubicin resistance. DDX3X-depleted DLBCL cell lines (U2932 ad BJAB) were indeed found to have a significantly higher IC_{50} to doxorubicin (**Figure 4.16A**).

To test whether the poor prognosis of NHL patients with *DDX3X* loss-of-function mutations may be due to increased drug resistance, we treated DDX3X-depleted HuT78, SNK1, U2932 and BJAB cells with a panel of commonly used chemotherapeutic agents - HDAC inhibitors [vorinostat, panobinostat, trichostatin, and romidepsin] (Zhang et al., 2019), STAT3 inhibitors [stattic and WP1066] (Schust et al., 2006) and doxorubicin (Pfreundschuh et al., 2006). DDX3X loss caused significant resistance to HDAC inhibitors in HuT78 and SNK1 cells and to doxorubicin in U2932 and BJAB cells (**Figure 4.16B**). Apoptosis-inducing effect of vorinostat was significantly less in DDX3X-depleted HuT78 cells in comparison to WT HuT78 cells (**Figure 4.16B**). We noticed that levels of apoptosis markers such as cleaved caspase-3 and cleaved PARP were significantly downregulated upon depletion of DDX3X (**Figure 4.16C**). Most importantly, DDX3X-depleted N.H.L. cells remained sensitive to pharmacological STAT3 inhibition (**Figure 4.16B**). These results strongly suggest that *DDX3X* mutations cause true chemo-resistance and worse survival, rather than simply being surrogate markers in NHLs.

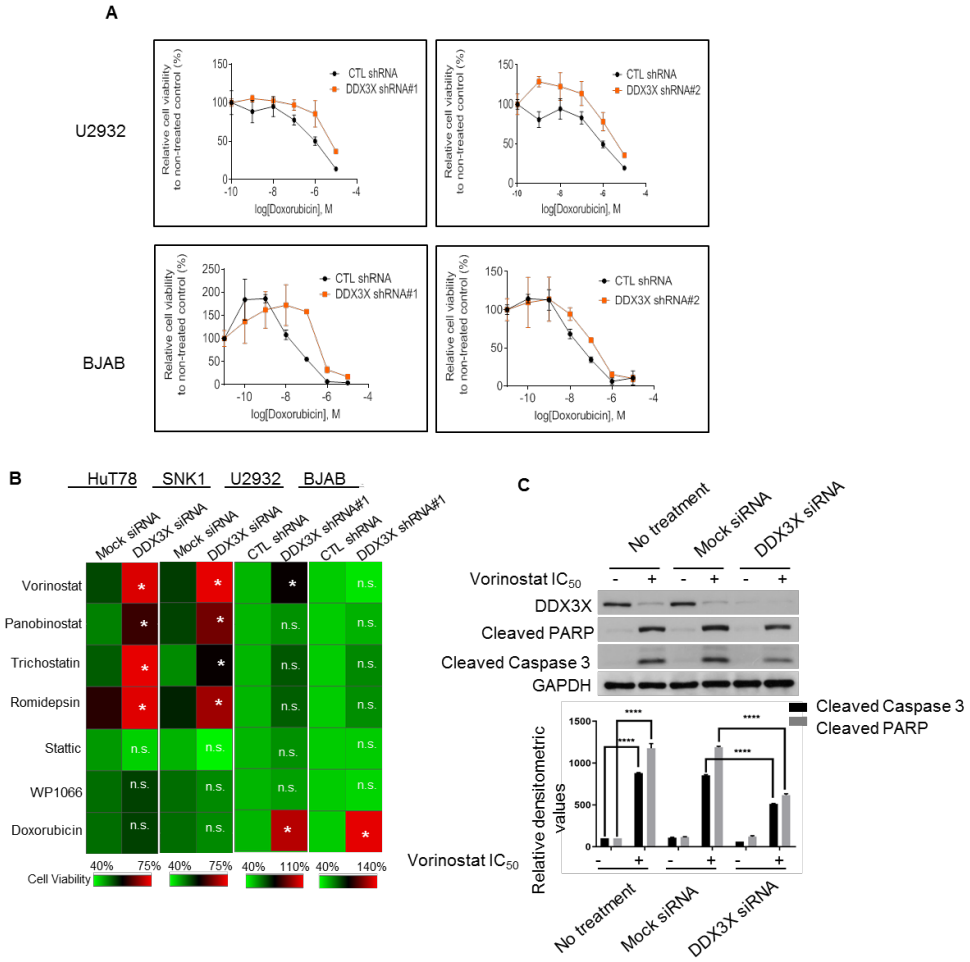

Figure 4.16 DDX3X loss induces resistance to chemotherapeutic agents in hematolymphoid cancer cells *in vitro*. **(A)** Doxycycline-inducible shRNA-mediated DDX3X-depleted U2932 and BJAB cells were seeded into 96-well plates (6000 cells/well). After 24 h, cells were treated with 0.001, 0.01, 0.1, 1, 10 and 100 μM doxorubicin for additional 72 h. Cell viability was evaluated using MTS assay, and the log (doxorubicin) *vs*. normalized response curve derived from 4 independent experiments were plotted using GraphPad Prism.(**B**) DDX3X-depleted HuT78, SKN1, U2932, and BJAB cells were incubated with IC_{50} concentrations (based on WT cells) of vorinostat, panobinostat, trichostatin, romidepsin, stattic, WP1066, or doxorubicin for 48 h. Cell viability was analyzed by the MTS-based assay and the data was converted into color-coded heat-map. Representative data from at least three independent experiments are presented. *, $p<0.05$; **, $p<0.01$; *ns*, non-significant.**(C)** Cellular lysates from control or DDX3X-depleted Hut78 cells following vorinostat treatment were analyzed by Western immunoblotting for the expression of DDX3X, cleaved-PARP and cleaved-caspase 3.Blots were re-probed with anti-GAPDH as a loading control. Relative densitometry graphs (mean±S.E.M) of Western immunoblots obtained from at least two independent experiments were presented. ****, $p<0.001$.

4.4 Discussion

In the current study, we provide several lines of evidence that DDX3X loss in NHL cells exacerbates malignant phenotypes. First, we demonstrate a high prevalence of *DDX3X* mutations in a cohort of patients with R/R-DLBCL and that such mutations

are associated with worse overall survival in DLBCL. Second, DDX3X-depleted cells exhibit enhanced migratory and chemotactic phenotypes. Third, DDX3X loss enhances the phosphorylation of STAT3 and p44/42 MAPK and upregulates the expression of cyclin D1. Finally, DDX3X-depleted CTCL and DLBCL cells are refractory to HDAC inhibitors and doxorubicin, respectively, and yet remain sensitive to STAT3 targeting agents. Collectively, these findings highlight a critical role of DDX3X loss in the progression and chemo-resistance in, some if not all, hematolymphoid malignancies.

Genomic lesions in *DDX3X* have been detected earlier in various forms of hematologic malignancies, including NKTCL (Jiang et al., 2015; Koo et al., 2012), DLBCL (de Miranda et al., 2014; Gunawardana et al., 2014; Mareschal et al., 2016; Morin et al., 2016), hairy cell leukemia (Waterfall et al., 2014), CLL (Quesada et al., 2011), acute lymphoblastic leukemia (ALL) (Zhang et al., 2016) and Burkitt lymphoma (Richter et al., 2012); but, the clinical significance of these lesions was unclear in most cases. Our novel observation of a worse OS in DLBCL patients with mutant *DDX3X* is consistent with the considerably higher prevalence of these lesions in our R/R-DLBCL cohort (44%) compared to that of published unselected cohorts (5-7%) (de Miranda et al., 2014; Reddy et al., 2017). Moreover, our observations are consistent with the adverse prognostic impact of *DDX3X* mutations reported in NKTCL (Jiang et al., 2015) as well as the association with chemo-resistance observed by earlier investigators in CLL (Ojha et al., 2015).

Following on from our clinical findings, we sought to elucidate how *DDX3X* mutations may contribute to the malignant lymphoma phenotype. The *DDX3* gene has two variants, *DDX3X* and *DDX3Y*, which share more than 90% sequence similarity. Mutational analysis using cBioPortal and OncoKB showed critical functional importance of the *DDX3X* variant compared to *DDX3Y*, as the X variant is frequently mutated; whereas, the Y variant is not (mutational data on the *DDX3Y* variant is provided in **Appendix 5, FigureA5.2**). This is consistent with the observation that DDX3X expression is ubiquitous, whereas DDX3Y expression is restricted to the testis (Gueler et al., 2012). In cervical, breast, and hepatocellular carcinoma models, DDX3X has been consistently implicated in cell cycle regulation through alterations in the G1/S cell cycle checkpoint and cell proliferation (Chang et al., 2006). In a study specific to NKTCL pathogenesis, mutated DDX3X resulted in premature entry into the S phase as

the inhibitory control by DDX3X was lost (Jiang et al., 2015). This has been attributed to DDX3X participation in the translational control of cell cycle regulatory factors (Lai et al., 2010).

We have demonstrated an upregulation of a repertoire of cytokines, including IL-2, IL-4, and IL-10 in DDX3X-depleted cells, which may mediate cancer aggressiveness. High expression of IL-10 has been associated with worse prognosis and identified by several studies to play crucial roles in the proliferation and migration in hematological cancers (Wang et al., 2016b; Zhao et al., 2015). Moreover, a high level of IL-4 expressed by follicular helper T-cells (T_{FH}) acts as a tumorigenic factor in follicular lymphoma (Pangault et al., 2010; Rawal et al., 2013).

Micro-RNAs (miRNAs) are a class of small RNA molecules that play crucial regulatory roles in tumor development by binding with the 3′-untranslated region (UTR) of target mRNAs and repressing their translation (Croce, 2009; Esquela-Kerscher and Slack, 2006). For example, low expression of miR-150 has been reported in DLBCL (Mazan-Mamczarz and Gartenhaus, 2013) as well as NKTCL and other T-cell lymphomas (Ballabio et al., 2010; Watanabe et al., 2011). Moreover, loss of DDX3X has had a profound effect on the miRNA profile of leukemic cells, suggesting an important role in miRNA biosynthesis (Zhao et al., 2016). We extend these observations by noting a reduction of miR-150 in DDX3X-depleted lymphoma cells. The expression of miR-150 is downregulated by c-Myc (Chang et al., 2008) and the downregulation of miR-150 can trigger telomerase activation by the upregulation of AKT2, which is a pro-survival serine/threonine kinase known to be overexpressed in B-cell lymphoma. In turn, AKT2 overexpression is associated with increased invasion and metastasis (Arboleda et al., 2003; Xu et al., 2004). Consequently, the downregulation of miR-150 by loss of DDX3X may be another mechanism by which *DDX3X* mutations promote a malignant phenotype in lymphoma.

Chemo-resistance is a critical problem in the treatment of lymphoma, and several studies have shown an association between DDX3X loss of function and adverse prognosis of NKTCL and CLL (Riva and Maga, 2019; Takahashi et al., 2018). In our study, DDX3X loss was sufficient to induce resistance to multiple chemotherapeutics, including the commonly used topoisomerase II inhibitor doxorubicin as well as several epigenetic modifying agents. Moreover, DDX3X loss had a profound influence on the

transcript pool, and induced pro-tumorigenic pathways in lymphoma cells, reaffirming its role as a tumor suppressor gene in this cancer type. Based on our data, DDX3X loss results in the up-regulation of the STAT3 and MAPK pathways, which are known to inhibit apoptosis and decrease response to cytotoxic agents (Liang et al., 2019; Salas et al., 2014). These pathways are thus likely to be key mediators of the tumorigenic effects of *DDX3X* mutations in lymphoma.

Increased Wnt signaling has been associated with *DDX3X* mutations in medulloblastoma (Jones et al., 2012; Pugh et al., 2012; Robinson et al., 2012). However, we did not observe increased Wnt signaling upon DDX3X depletion in other assays (**Appendix 5, FigureA5.3**), suggesting that *DDX3X* mutations can promote lymphoma development through increased activation of the STAT3/MAPK pathway rather than through increased Wnt signaling. Importantly, frameshift and nonsense mutations were not reported in the medulloblastoma studies but were frequently observed in DLBCL, suggesting different mechanisms of action of *DDX3X* lesions between the two cancer types. Wnt inhibitors would, therefore, probably not be a reasonable therapeutic choice for lymphoma patients with these mutations. However, we showed that DDX3X-depleted lymphoma cells retain their sensitivity to STAT3 inhibition. STAT3 inhibitors are currently in early phase clinical trials in breast cancer (Qin et al., 2019b) and would, therefore, be a rational novel drug class to trial in lymphoma patients with *DDX3X* mutations.

In conclusion, the results presented in this chapter of the thesis indicate that loss of function mutations in *DDX3X* are important molecular determinants of disease aggressiveness and treatment response in certain hematolymphoid malignancies. Moreover, the downstream effects of these lesions are likely complex and not limited to a single process or pathway. Further studies are needed in order to gain a complete understanding of the consequences of DDX3X loss in hematolymphoid malignancies. These data will help improve the risk stratification of lymphoma patients and may identify new therapeutic options for a subgroup with poor prognosis.

Chapter 5

Targeting defective STAT3 signaling in hematolymphoid malignancies

5.1 Introduction

Signal transducer and activator of transcription 3 (STAT3) is a member of the STAT family transcription factors known to mediate a plethora of cellular responses to a variety of cytokines and growth factors (Yu and Jove, 2004). Aberrant STAT3 activities underpin the majority of human cancers, including hematolymphoid malignancies, and the prevalence of excessive STAT3 activities has been associated with poor patient prognosis (Song et al., 2018; Zhu et al., 2019).

Emerging evidence from previous and ongoing research has expanded our understanding of STAT3 and STAT3-mediated pathways in cancer(Johnston and Grandis, 2011; Wake and Watson, 2015). Several clinical trials using STAT3-targeted therapeutics are currently ongoing with encouraging outcomes(Wong et al., 2017; Yang et al., 2019). The original findings reported in Chapters 3 and 4 of this thesis and our previous publication "*Oncogenic activation of the STAT3 pathway drives PD-L1 expression in natural killer/T-cell lymphoma, Blood, 2018*", clearly establish a key role of STAT3 in chemoresistance, aggressive phenotypes, and invasive potential of hematolymphoid malignancies.

The use of antisense oligonucleotide molecules is one of the strategies to inhibit the activity of STAT3. However, the triumph of antisense oligonucleotide-mediated gene silencing in lymphoma cells has been impeded due to the suboptimal delivery of oligonucleotides into cells (Yin et al., 2006). Huge loss of cell viability associated with electroporation and nucleofection based delivery methods often dampens the yield of the experiments (Mantei et al., 2008). The use of other delivery vehicles like viral, cationic lipids, and peptides can cause significant cytotoxicity by nonspecific induction of signaling pathways in these cancer cells derived from the hematopoietic lineage (Peer et al., 2007).

Given the existing constraints regarding modulation of genes by silencing in 'hard to transfect' lymphoma cells, it is requisite to explore an alternate approach in these cells. The locked nucleic acid (LNA)-conjugated chimeric single-strand antisense oligonucleotide, called "GapmeR", is an emerging new class of molecules, which can knock down a target gene of interest with precise specificity through the post-transcriptional gene silencing.

5.2. Objectives

Considering that there is an unmet medical need for innovative therapeutic strategies, the development of novel STAT3-targeted inhibitors is urgently needed. Therefore, the goal of this chapter was to develop a novel approach to target defective STAT3 signaling in hematolymphoid malignant cells. The three specific objectives were:

5.2.1 To verify STAT3 involvement in hematolymphoid malignancies.

5.2.2 To design a novel gene silencer for inhibiting STAT3 and validate its cellular uptake and targeting efficiency.

5.2.3 To analyze the efficacy of STAT3 gene silencers in inducing apoptosis in cultured lymphoma cells.

5.3 Results

5.3.1 STAT3 is constitutively activated in cells of lymphoid neoplasms

In Chapter 4, we have demonstrated that DDX3X loss in hematolymphoid cells upregulates STAT3 activation. Here, we examined the expression and activation of STAT3 in a panel of 6 different cell lines derived from patients with various subtypes of hematolymphoid neoplasms – HuT78, MJ and MyLa derived from patients with cutaneous T-cell lymphoma (CTCL) and NKYS, SNK1 and SNK6 derived from patients with NK-T-cell lymphoma (NKTCL). Both the phosphorylation (Y705) and expression of STAT3 in these cells were compared with human primary T cells derived from healthy volunteers (used here as a control).

Cells of hematolymphoid neoplasms express variable levels of STAT3 and its phosphorylated form (Y705) **(Figure 5.1 A, B)**. It was evident from the graph that CTCL cell lines such as HUT78, MJ, and MyLa, displayed higher levels of phosphorylation of STAT3 compared to primary T cells. It has been previously reported that HuT78, MJ, and MyLa cells harbor JAK mutations, which causes persistent activation of STAT3 (Mondejar et al., 2017). Similarly, NKTCL cell lines (NKYS and SNK6) showed elevated levels of phosphorylation of STAT3, whereas SNK1 cells displayed low levels of STAT3 as well as pSTAT3 (Y705). NKYS and SNK6 possess a mutant variant of STAT3, which are constitutively active whereas SNK1 has wildtype STAT3 (Kucuk et al., 2015).

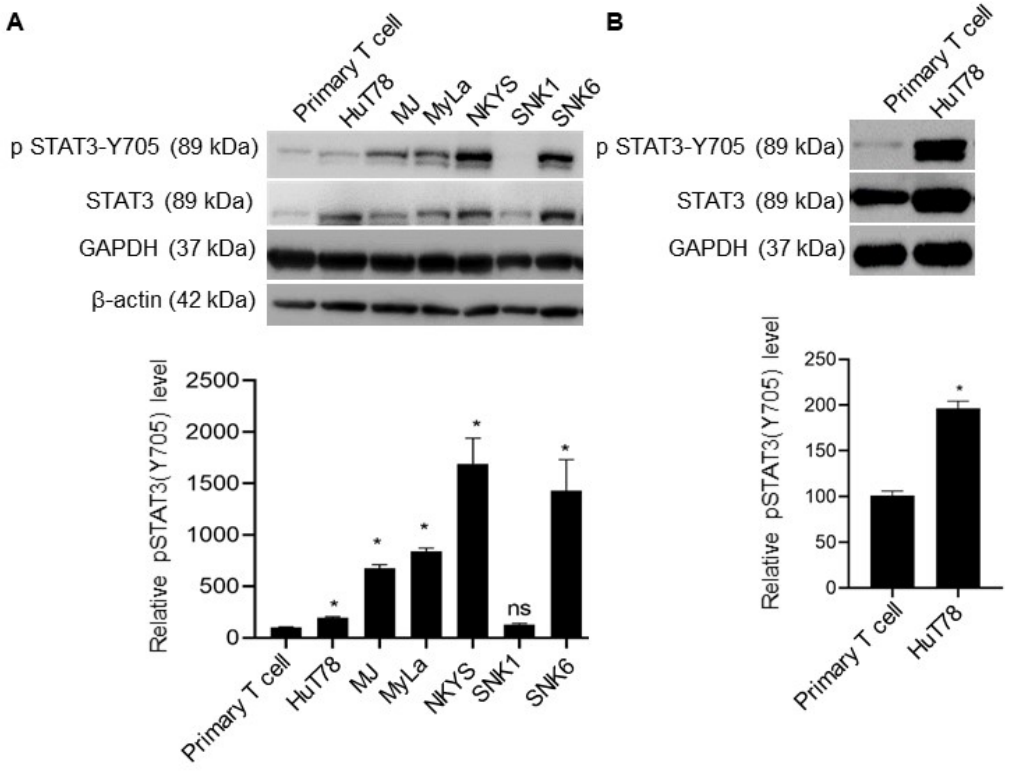

Figure 5.1 Variable levels of phosphorylated STAT3 (Y705) in hematolymphoid malignant cell lines. Cellular lysates from various lymphoid neoplasm, including CTCL (HuT78, MJ and MyLa) and NKTCL (NKYS, SNK1, and SNK6), were immunoblotted and probed with anti STAT3, anti pSTAT3 (Y705) and GAPDH (loading control) antibodies. Cell lysate from human primary T-cells was used as a control. Representative densitometry graphs from three independent experiments were presented (Mean ± SEM; ns, non-significant; *, p<0.05).

5.3.2 Somatic alterations in STAT3 are prevalent in hematolymphoid malignancies

Deep-targeted capture sequencing and analysis of DNA samples obtained from 171 cases with various lymphoma subtypes [101 tumor tissues and 8 cell lines from NKTCL, 8 tumor tissues and 1 cell line from CTCL, 27 tumor tissues from Anaplastic Large Cell Lymphoma (ALC L) and 26 tumor tissues from Peripheral T Cell Lymphoma (PTCL)] by the collaborators at the National Cancer Centre Singapore (NCCS) identified genomic lesions in the *STAT3* gene. Detailed analysis and results have been published in the *Blood,* 2018. Data clearly demonstrated that genomic lesions in the *STAT3* gene are prevalent across all subtypes (78% in NKTCL, 67% in ALCL, 54% in PTCL, and 33% in CTCL). Using *in silico* analysis, we identified several mutations in STAT3, including four novel mutations (p.D427H, p.E616G, p.E616K, and p.E696K), which would have a deleterious effect on the progression on hematolymphoid malignancies (**Appendix 4, Table A4.3; Figure5.2**).

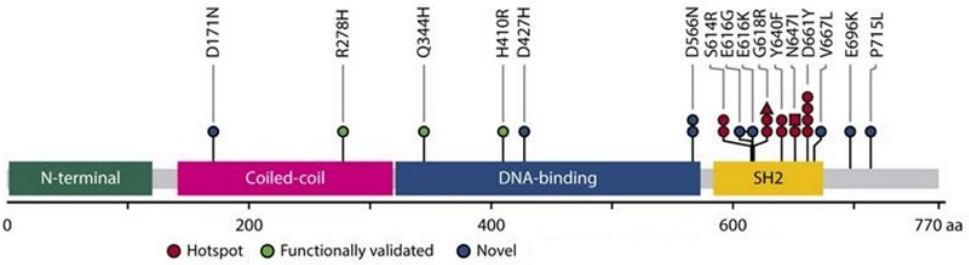

Figure 5.2 STAT3 is frequently mutated in hematolymphoid malignancies. Locations of the novel, functionally validated, and hotspot mutations in STAT3 gene in lymphoid neoplasms.

5.3.3 Aberrant STAT3 activation drives PD-L1 expression in hematolymphoid malignancies

The programmed death-ligand 1 (PD-L1) is a transmembrane protein overexpressed on the surface of malignant cells and plays a major role in tumor evasion from the host immune system (Tseng et al., 2001; Zitvogel and Kroemer, 2012). Several clinical trials and FDA approvals of PD-L1 blocking drugs have established PD-L1 as an important target in cancer, including hematolymphoid malignancies (Kwong et al., 2017; Lai et al., 2017).

The collaborative work with the NCCS research group was extended to determine the functional implications of the identified four mutations and Ba/F3 cells expressing mutant variants of the STAT3 (p.D427H, p.E616G, p.E616K, and p.E696K) were generated. Western immunoblot data clearly showed that the expression of STAT3 mutant variants causes auto-phosphorylation of STAT3 (Y705), even in the absence of stimulation *via* IL-3 (**Figure 5.3A**). Most importantly, NKTCL cell lines with inherent STAT3 mutations (SNT8, SNK6, NKYS) resulting in STAT3 hyper-activation showed upregulation of PD-L1 expression, as analyzed by Western immunoblotting (**Figure 5.3B**) as well as qRT-PCR (**Figure 5.3C**). Furthermore, expression of STAT3-p.E616K and STAT3-p.E616G mutated forms in NKS1 cells significantly increased PD-L1 protein (**Figure 5.3D**) and PD-L1 mRNA levels (**Figure 5.3E**).

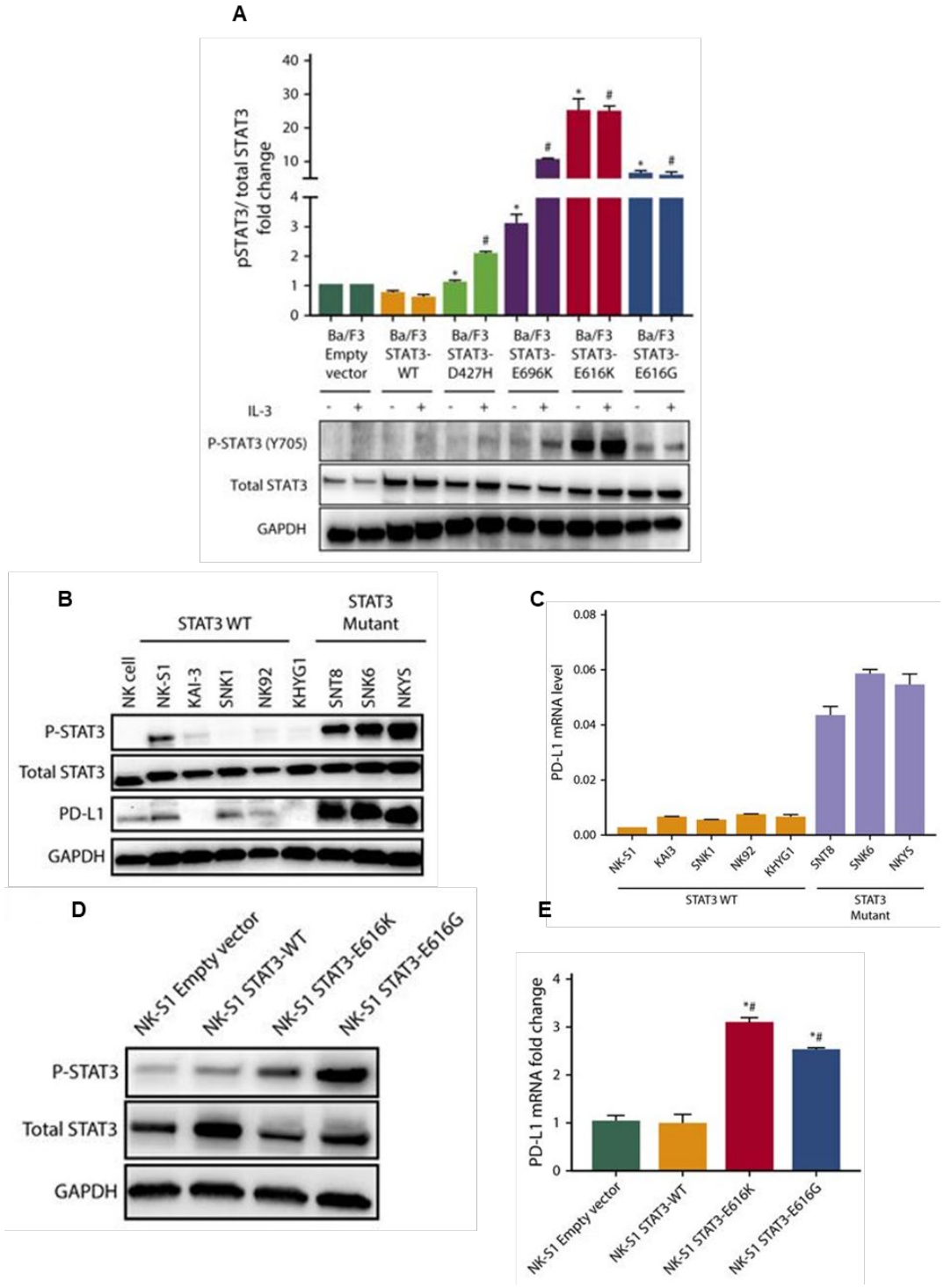

Figure 5.3 STAT3 activation is positively correlated with PD-L1 expression. (**A**) Novel STAT3 mutations cause constitutive STAT3 activity and correlate with PD-L1 expression. (A) Cell lysates were collected from IL-3 treated Ba/F3 cells expressing empty vector, and STAT3 mutants and probed with anti STAT3 and pSTAT3 (705) antibody using immunoblot assay. [*, $p < .05$ compared with STAT3 (-IL3); #, $p < .05$ compared with STAT3 (+IL-3)]. (**B**) Cell lysates from NKTCL cell lines (NKS1, KAI3, SNK1, NK92, KHYG1, SNT8, SNK6, and NKYS) were collected and immunoblotted with anti STAT3 and pSTAT3 (705) antibody, total STAT3, and PD-L1. (**C**) Total mRNA was extracted from NKTCL cell lines, and qRT-PCR was performed with CHMPA2 as control. (**D**) Cell lysates were collected from NK-S1 cells expressing STAT3WT, p.E616K, and p.E616G vectors and immunoblotted for anti pSTAT3 and total STAT3

antibody. (**E**) PD-L1 mRNA in these cells was evaluated qRT-PCR. Relative densitometry and mRNA fold change graphs from three independent experiments were presented (mean ± SEM, **, $p<0.01$).

However, to establish a direct relationship between STAT3 and PD-L1, it is necessary to knockdown STAT3 in lymphoma cells and evaluates its effect on PD-L1 expression. One of the challenging endeavours was to deplete the expression of STAT3 efficiently in 'hard to transfect' lymphoma cells and to examine the effect of STAT3 knockdown on PD-L1 expression. Therefore, we optimized "GapmeR"-mediated gene-silencing technique and evaluated the impact of STAT3 knockdown on PD-L1 appearance. We further developed a novel epAON gene silencer (end-protected antisense oligonucleotide) and assessed its efficacy for potential therapeutic applications.

5.3.4 GapmeR molecules self-internalize into HuT78 cells

We have published the findings presented here as part of the results in the *Nature Scientific Reports,* 2018 entitled "GapmeR cellular internalization by macropinocytosis induces sequence-specific gene silencing in human primary T-cells". In this paper, we have established GapmeR as a self-permeating molecule, which can silence efficiently genes of interest in both human primary T lymphocytes as well as lymphoma cells with high specificity, *i.e.*, no off-target effect.

To examine the cellular uptake of GapmeR in the CTCL cell line HuT78, we added increasing concentrations of FAM-labelled non-targeting GapmeR (10 nM, 50 nM, 100 nM, 250 nM or 500 nM) in the cell culture medium. After 24 h of incubation, GapmeR cellular uptake was analyzed by flow cytometry. Data clearly showed dose-dependent cellular internalization of GapmeR through direct uptake "gymnosis". Almost all the cells (99±0.4%) were transfected with 500 nM FAM-GapmeR in 24 h (**Figure 5.4A**). Similar results on cellular uptake of FAM-GapmeR were obtained when GapmeR molecules were delivered to cells by standard nucleofection protocol (**Figure 5.4B**). We further compared the transfection efficiency of GapmeR (500 nM) using gymnosis and nucleofection protocols at multiple time points (6 h, 24 h, 48 h or 72 h). Comparable amounts of GapmeR cellular uptake was evident upon transfection either through gymnosis or through nucleofection (**Figure 5.4C**). To assess the potential cytotoxicity of GapmeR molecules, we incubated HuT78 cells or human primary T cells isolated from healthy donors in GapmeR containing media for 24 h. There was no

appreciable loss in cell viability due to the incubation of primary T cells with even with a higher concentration of GampeR (1 µM non-targeting GapmeR treated by gymnosis). However, nucleofection procedure caused significant loss in cell viability (**Figure 5.4 D**).

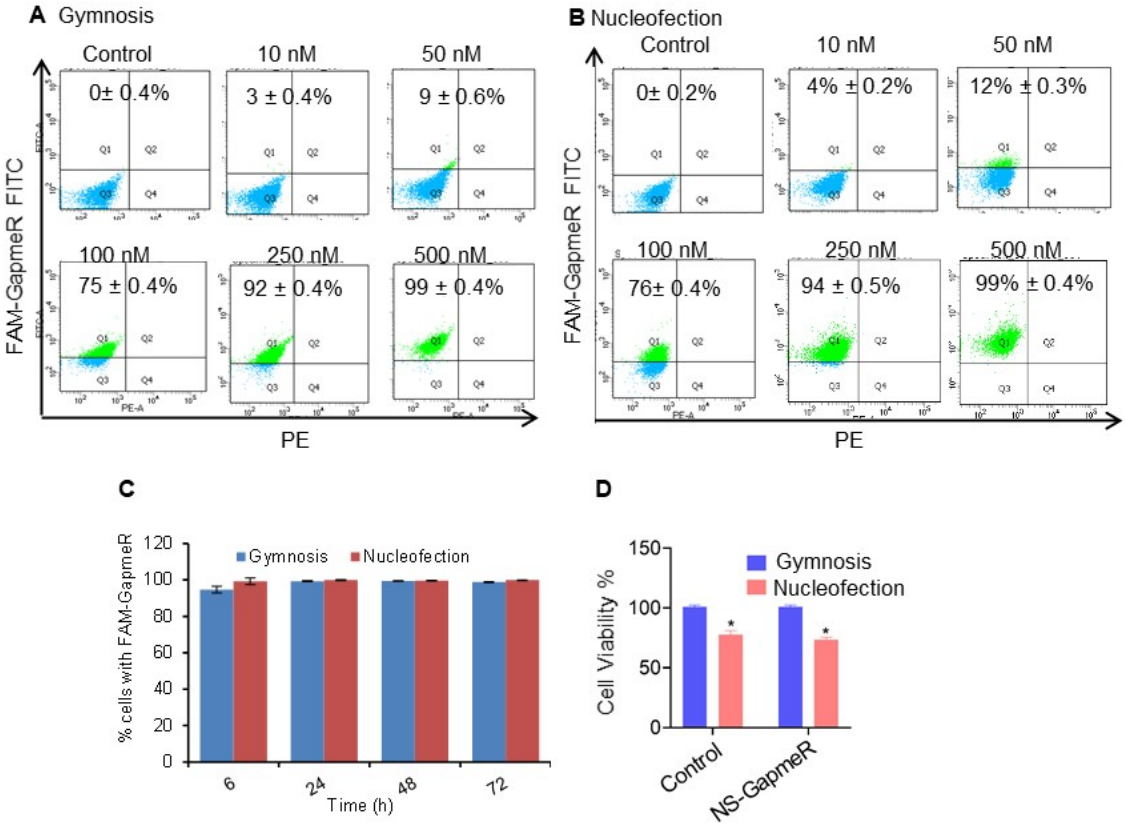

Figure 5.4 Cellular internalization of GapmeR in HuT78 T-cells delivered through gymnosis or nucleofection. (A) HuT78 cells were incubated with 10 nM, 50 nM, 100 nM, 250 nM or 500 nM FAM-GapmeR to allow gymnosis or transfected through nucleofection (B). After 48 h, GapmeR uptake in cells was examined based on the detection of fluorescence intensity at FITC channel by flow-cytometry. (C) HuT78 cells were transfected with 500 nM FAM-GapmeR by gymnosis or nucleofection for 6 h, 24 h, 48 h or 72 h and cells analyzed by flow cytometry for the uptake of GapmeR. (D) HuT78 cells were incubated or nucleofected with NS-GapmeR, and cell viability was evaluated after 48 hours using MTS assay. Representative cell viability graphs from three independent experiments were presented (Mean ± SEM; ns, non-significant; *, p<0.05).

To examine further for cellular internalization of GapmeR, we performed confocal microscopy of FAM-GapmeR-treated HuT78 cells. Confocal microscopic images of HuT78 cells incubated with 500 nM FAM-GapmeR for 48 h showed GapmeR localization in the cytoplasm as well as in the nucleus (**Figure 5.5A**). High Content Analysis (HCA) of HuT78 cells showed a time-dependent increase in the internalization of GapmeR in both cytoplasms as well as the nucleus (**Figure 5.5B**). Similar results on the cellular uptake of FAM-GapmeR were obtained with other

cell-types, including human primary T lymphocytes (published *Nature Scientific Reports,* 2018), primary human dermal fibroblasts, lung epithelial carcinoma cell line A549 and hepatocellular carcinoma cell line HepG2, as visualized by confocal microscopy (**Figure 5.5C**).

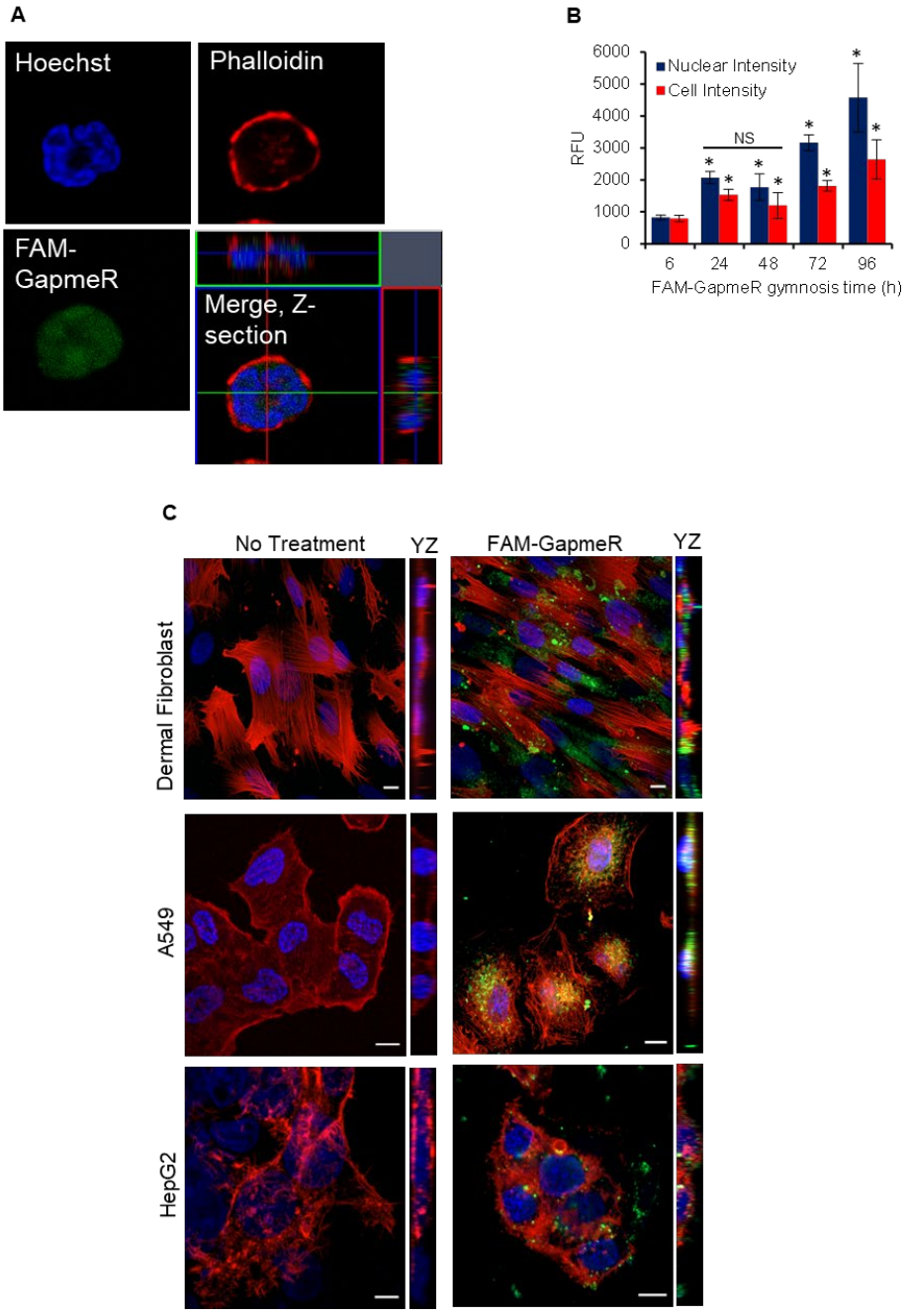

Figure 5.5 Transfection of GapmeR in HuT78 and adherent cancer cells. **(A)** HuT78 cells were treated with nonspecific FAM-GapmeR (500 nM) for 48 h and were fixed and counterstained with phalloidin-rhodamine and Hoechst. Cellular localization of GapmeR was analyzed by confocal microscopy using 63X oil objective. At least 20 microscopic fields were scanned, and representative images were shown. (**B**) Cellular localization of FAM-GapmeR (500nm) delivered through gymnosis for the various time period (6 h, 24 h, 48 h, 72 h, and 96 h) was quantified by High Content Analysis and presented. (**C**) Adherent cell lines (hDF, A549, and HepG2) were

incubated with FAM-GapmeR (500nM) for 48 hr and stained with counterstained with phalloidin-rhodamine and Hoechst. Cellular localization of GapmeR was analysed by confocal microscopy using 40X oil objective. At least 20 microscopic fields were scanned, and representative images were shown. Scale bar 10 µm. Z-sections (YZ) were shown beside each image. The relative fluorescence unit of nuclear intensity and cell intensity of FAM-GapmeR from three independent experiments were presented (mean ± SEM, **, p<0.01).

5.3.5 GapmeR molecules are non-immunogenic

To assess the potential immunogenicity of GapmeR molecules, we incubated human primary T cells isolated from healthy donors in medium containing non-targeting GapmeR molecules (100 nM, 250 nM or 500 nM) for 24 h. We demonstrated using ELISA that secreted levels of IL-2 were not were affected (**Figure 5.6 A**). We noticed that secreted levels of IL-4, IL-5 and IFN-γ were not detected, even though PHA activated cells displayed significant expression of these cytokines (**Figure 5.6C, D, and E**).

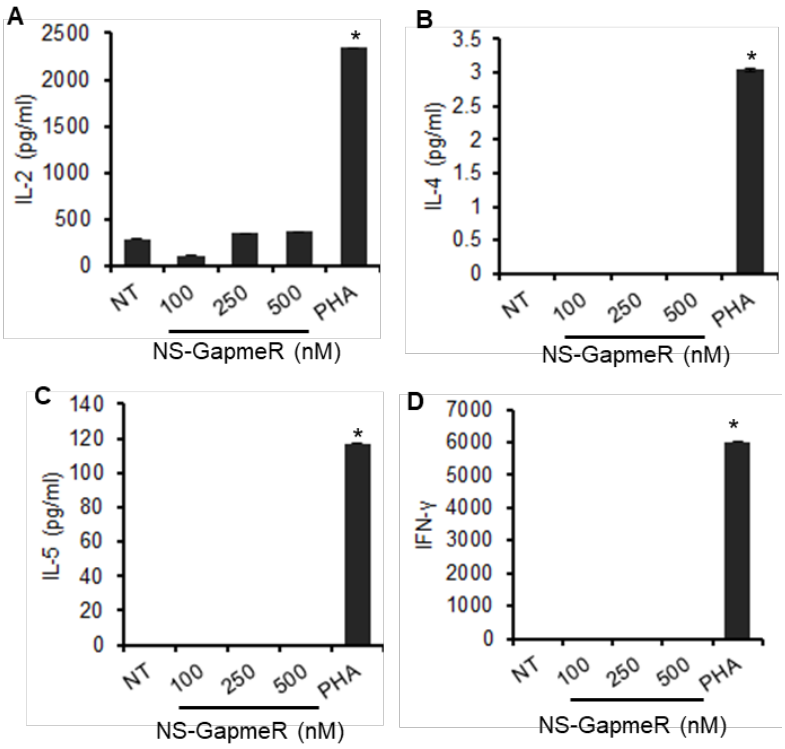

Figure 5.6 GapmeR treatment does not induce an immunogenic response. Human primary T-cells were incubated with various concentration of NS-GapmeR (100 nm, 250 nM or 500 nM) for 24 h. Untreated cells and cells incubated with phytohemagglutinin (*PHA*) as negative and positive controls, respectively. Supernatant was collected, and secreted levels of cytokines IL-2 (**A**), IL-4 (**B**), IL-5 (**C**), and IFN-γ (**D**) were analyzed by ELISA. Data were representative of experiments performed on T-cells purified from at least three different donors. (Mean ± SEM; *, $p < 0.05$).

5.3.6 GapmeR internalization into lymphoma cells is through macropinocytosis

Cellular internalization of small molecules, such as GapmeR, may depend on multiple cell entry processes. These include pinocytosis, phagocytosis, clathrin-mediated endocytosis, or the caveolae-mediated uptake process (Lim and Gleeson, 2011). We have previously shown that GapmeR enters human primary T cells through macropinocytosis. These findings have been published in *Nature Scientific Reports*, 2016. In this study, we used a panel of inhibitors consisting of inhibitors of pinocytosis, phagocytosis, caveolae-mediated uptake, and clathrin-mediated endocytosis to treat primary T cells which were subsequently seeded in FAM-GapmeR containing medium for 6 hr. The cells were examined for the presence of GapmeR using flow cytometry analysis. We noticed that amiloride treatment inhibits the uptake of GapmeR. To confirm whether GapmeR enters into HuT78 cells through a similar mechanism, we immuno-stained FAM-GapmeR-treated HuT78 cells for SNX5 protein (a marker of macropinosome body) and imaged using super-resolution microscopy (Lim et al., 2008). Co-localization of FAM-GapmeR with SNX5-positive macropinosome bodies was clearly detectable in the cytoplasm of GapmeR-treated HuT78 cells (**Figure 5.7 A**). These results confirm that GapmeR cellular internalization in HuT78 occurs mainly through macropinocytosis.

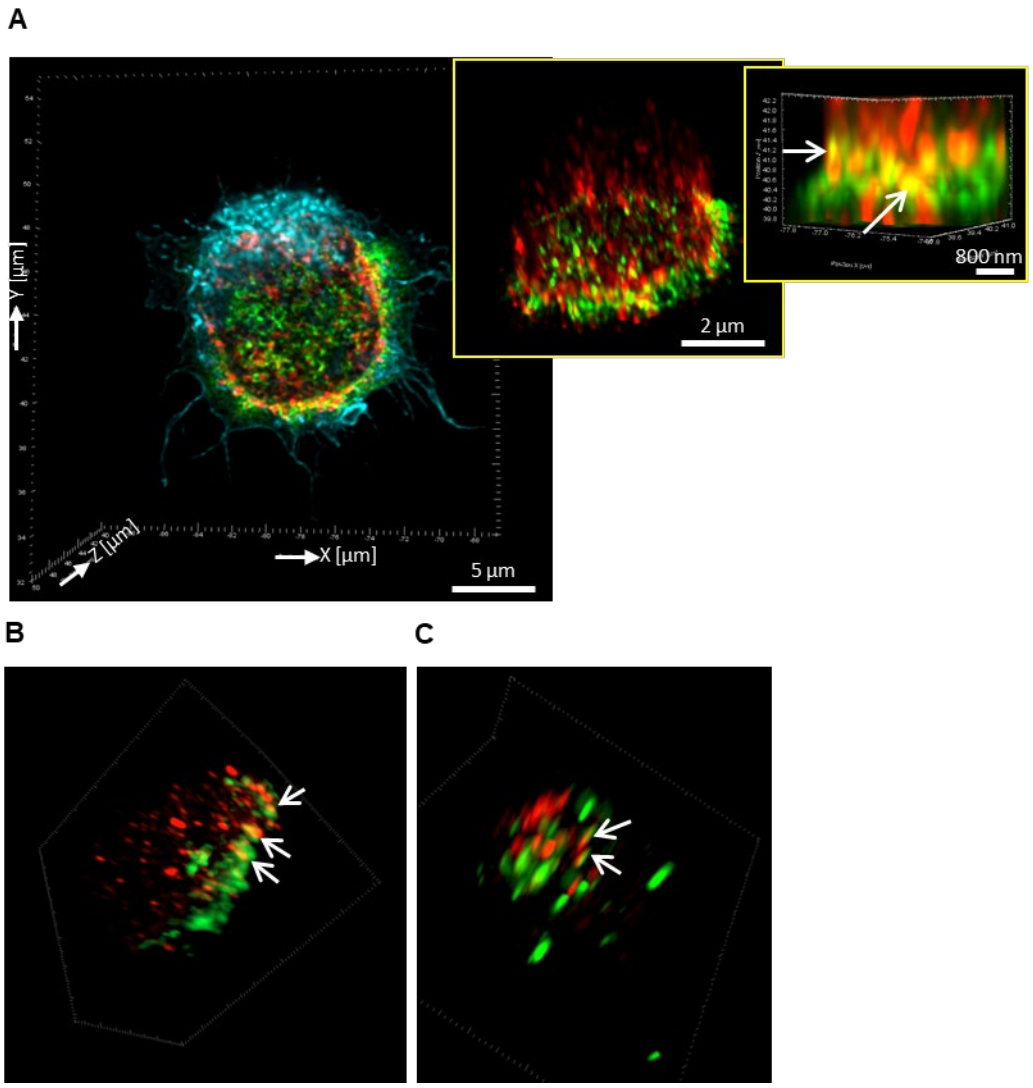

Figure 5.7 GapmeR co-localization with macropinocytosis markerSNX5 in HuT78 cells. **(A, B, C)** HuT78 T-cells treated with FAM-GapmeR (500 nm) for 6 h and stained with the anti-SNX5 antibody. Subsequently, cells were counterstained with secondary antibody (Alexa Fluor® 568, red) and Phalloidin Alexa Fluor® 647 and imaged by super-resolution microscopy. Zoomed-in images clearly indicated the co-localization of GapmeR and SNX5. The corresponding scales are indicated in the images.

5.3.7 Design of GapmeR molecules targeting STAT3

Using genomic sequence information and Exiqon's "Design-Tool," three different GapmeR molecules targeting STAT3 were designed for initial screening. The oligonucleotide sequences of the GapmeR molecules are provided in **Table 5.1**. A non-targeting oligonucleotide sequence was selected and used as nonspecific (NS) GapmeR control (**Table 5.1**).

Table 5.1 A list of GapmeR molecules against STAT3.

GapmeR Molecules	Sequences[α]
NS-GapmeR	AACACGTCTATACGC
STAT3-GapmeR1	GATCGTCGAAGCATTA
STAT3-GapmeR2	GTGTCACACAGATAAA
STAT3-GapmeR3	AGCACCTTCACCATTA

[α]Bases denoted in green are Locked Nucleic Acids.

5.3.8. GapmeR-mediated STAT3 knockdown in cells of hematolymphoid neoplasms

For initial optimization to determine the STAT3 gene silencing efficacy of GapmeR molecules, HuT78 cells were used as a representative cell culture model. Cells were incubated with the three STAT3 targeting GapmeR molecules for varying time periods (24 h, 48 h, 72 h, or 96 h), and STAT3 knockdown was analyzed by Western immunoblotting (**Figure 5.8 A, B & C**). We identified STAT3-GapmeR2 (referred to as STAT3-GapmeR in the following sections) as the most effective design among the three designs tested (**Figure 5.8 B**).

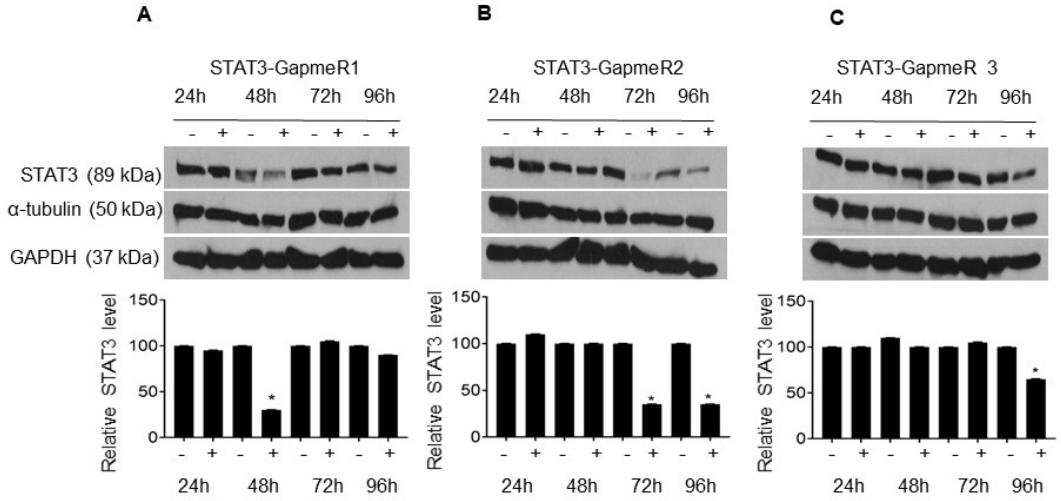

Figure 5.8 Screening of STAT3-GapmeRs.HuT78 cells were treated with 500nm of STAT3 - GapmeR1 (**A**), STAT3-GapmeR2 (**B**), and STAT3-GapmeR3 (**C**) for the duration of 24h, 48h, 72h, and 96 h. The cell lysates were immunoblotted with anti- STAT3, α-tubulin, and GAPDH antibodies. The relative densitometry graph represents data from at least two independent experiments (mean ± SEM, *, p<0.05).

We further validated the gene-silencing efficacy of STAT3-GapmeR in 6 different cell lines: three from CTCL (HuT78, MJ, and HH) and three from NKTCL (NKYS, SNK6, and SNK1). We observed variable but significant levels of STAT3 knockdown in all the cell types tested, ranging from 65-90% knockdown (**Figure 5.9**). The observed variability of the efficiency of knockdown could be due to cell type-specific differences in cellular uptake and turnover of target protein expression.

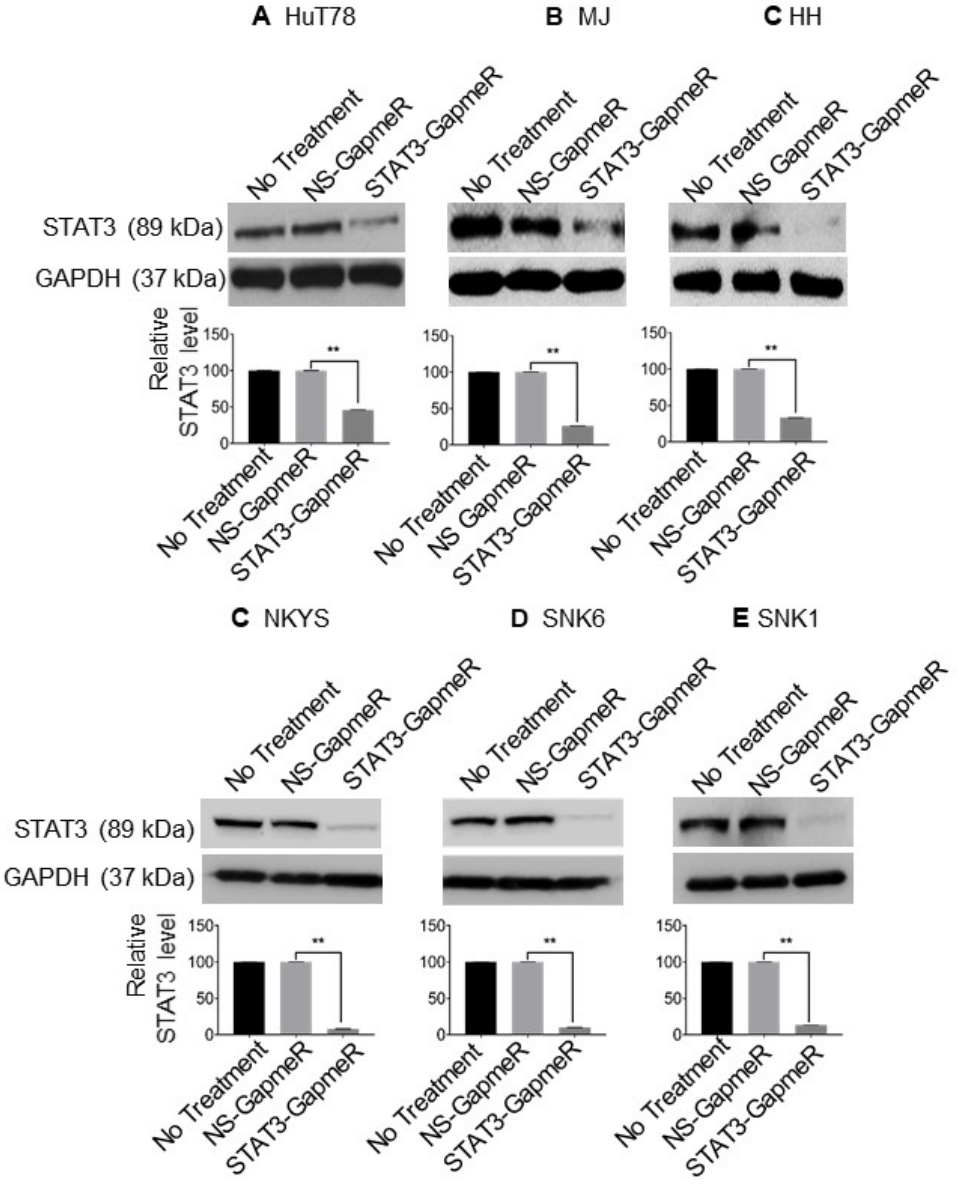

Figure 5.9 GapmeR silences STAT3 expression in cells derived from CTCL and NKTCL. CTCL cell lines [HuT78 (**A**), MJ (**B**) and HH (**C**)] and NKTCL cell lines [NKYS (**C**), SNK6 (**D**) and SNK1 (**F**)] were treated with STAT3 GapmeR (500 nM) and NS GapmeR (500 nM). Cell lysates SNK1 (**E**) were collected after 72 hr, and protein levels of STAT3 were determined using immunoblot assay. The relative densitometry graph represents data from at least three independent experiments (mean ± SEM, *, p<0.05).

5.3.9 STAT3 regulates PD-L1 expression in NKTCL

To validate the correlation between STAT3 and PD-L1 expression as observed in NKTCL cells (**Figure 5.3**), we knocked-down STAT3 in NKYS and SNK6 cell lines using STAT3-GapmeR. We observed that STAT3 depletion in both cell lines significantly decreased the expression of PD-L1 protein (**Figure 5.10A**) as well as mRNA levels (**Figure 5.10B**). In contrast, overexpression of STAT3 in these cells significantly increased PD-L1 expression (detailed experiments and data presented and published in the *Blood*, 2018). These findings suggest that STAT3 regulates PD-L1 through transcriptional control.

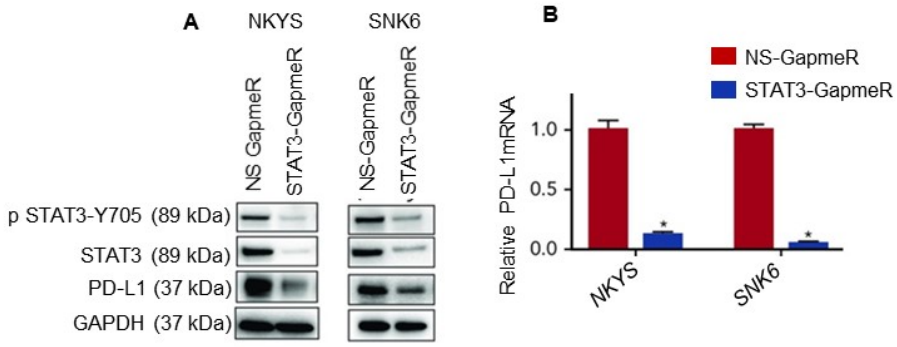

Figure 5.10 STAT3 knockdown in NKTCL cells diminishes expression of PD-L1 (A) NKTCL cell line (NKYS and SNK6) were treated with STAT3 GapmeR (1000 nm) for 72 hr. Cell lysates were collected and immunoblotted with anti pSTAT3 (Y705), total STAT3, PD-L1, and GAPDH (loading control). **(B)** Total RNA was extracted from STAT3 GapmeR treated NKYS, and SNK6 cells RT-qPCR was performed on the extracted mRNA from and to detect *PD-L1* mRNA. Relative graphs of mRNA expression are presented (mean ± SEM; *, $p<0.05$).

5.3.10 Design of end protected Antisense OligoNucleotide (epAON) targeting STAT3

Guanine-rich D.N.A. sequences can fold into four-stranded, non-canonical secondary structures called "G-quadruplex" (GQ) and are found in a various genomic location such as telomere, promoters and untranslated regions (Huppert and Balasubramanian, 2005). Following a specific protocol of a series of controlled heating and cooling, G-rich sequences form GQ. structure in the presence of salts (Bates et al., 1999; Bishop et al., 1996). We conceived the development of a novel gene silencer by replacing the LNA sequences of GapmeR with primary sequences that form the GQ. structure and protect the antisense oligonucleotide from nuclease-mediated destruction (**Figure 5.11A**). This antisense molecule was termed as "epAON". The sequences of nonspecific and STAT3-targeting epAON (STAT3-epAON) are provided in **Table 5.2**.

Table 5.2 A list of epAON molecules.

SN.	Targets	Sequences
epAON (5'→3')		
1.	NS-epAON	TTGGGTGGGTGGGTGGGTAACACGTCTATACGCTTGGGTGGGTGGGTGGGT
2.	STAT3 epAON	TTGGGTGGGTGGGTGGGTGTGTCACACAGATAAATTGGGTGGGTGGGTGGGT

[α]Bases denoted in green are end protecting nucleic acid sequence, which forms the"GQ. structure".

We confirmed the formation of GQ. structure in epAON molecules by circular dichroism (CD) spectroscopy, which displays characteristic CD spectra peaks at 240 nm and 260 nm. (**Figure 5.11B-D**). No peak was observed in oligonucleotide without the end-protecting sequence (**Figure 5.11E**). These results confirmed that ends of epAON molecules form GQ. structure.

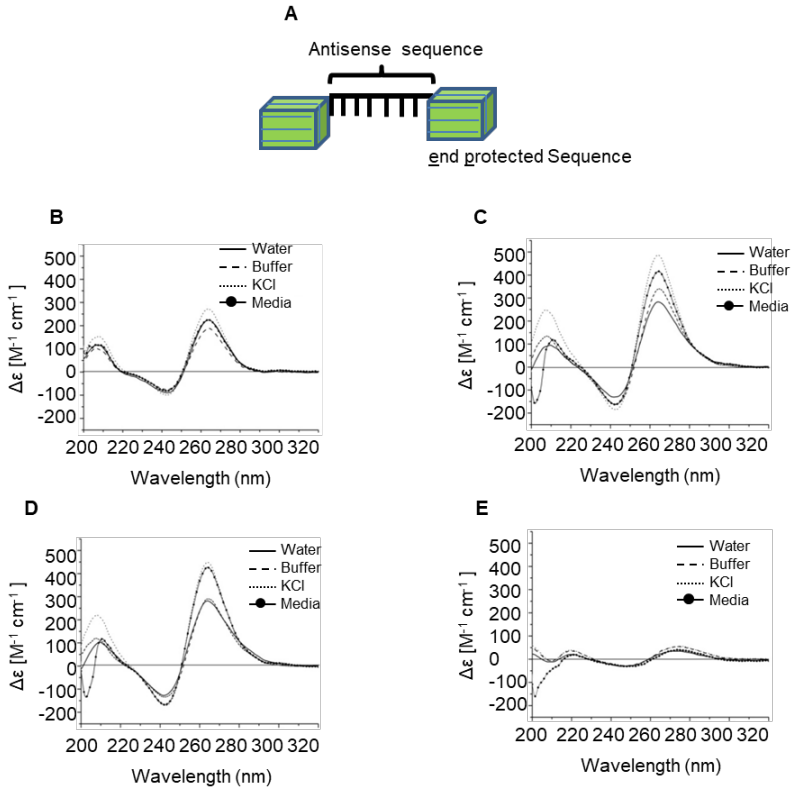

Figure 5.11 Designing of STAT3-epAON. (**A**) Nucleic acid Sequence of STAT3 GapmeR 2 and Control GapmeR was flanked by end protecting sequence "G quartets". CD spectra of G quartet nucleotide (**B**), epAON STAT3 (**C**), and non- specific epAON (**D**) using different conditions such as media, water, and salt buffer. (**E**) CD spectra of DNA sequence without end protecting sequence.

5.3.11 epAON molecules are nuclease resistant

Next, to determine the stability of epAON, we incubated epAON molecules in buffer and serum-containing media for different time points such as 12, 24, and 72 hr. We resolved these mixtures using gel electrophoresis and observed oligonucleotide bands on gel (Figure 5.12 A). This data suggested that epAON molecules are stable in serum for at least 72 h. We noticed that epAON molecules had reduced electrophoretic mobility, possibly due to binding with the serum protein.

To determine nuclease resistant properties of epAON, we subjected epAON to DNase treatment and resolved on agarose gel (1.5%). We found that epAON molecules remain stable upon DNase treatment. However, the control 27mer oligo was digested (Figure 5.12 B). We showed that epAON molecules are stable in serum and are nuclease resistant.

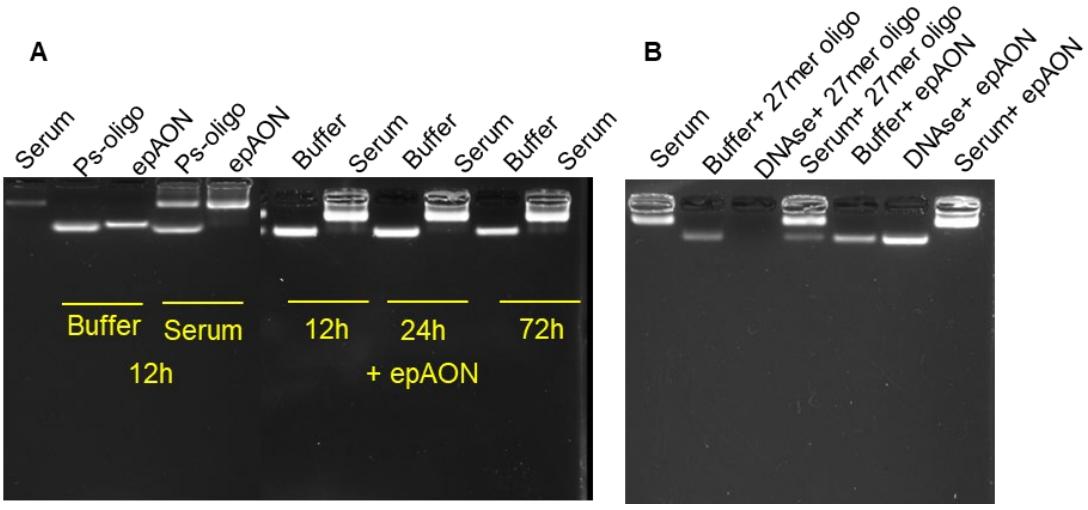

Figure 5.12 Effect of nucleases on epAON. (**A**) PS oligo and epAON were incubated for various time points 12 h, 24 h, and 72 h in serum and KCL buffer. The oligonucleotides were mixed with gel loading dye, resolved by gel electrophoresis, and visualized by SYBR safe staining (**B**) epAON were treated with DNase for 2h and resolved by gel electrophoresis and visualized by SYBR safe staining.

5.2.12 epAON molecules self-internalize in HuT78 cells through macropinocytosis

To determine cellular uptake of epAON, we incubated nonspecific FAM-epAON (250 nm, 500 nm or 1 μM) with HuT78 cells for various time points (6 h, 24 h, 48 h or 72 h). Distribution of FAM-epAON in cytoplasm and nucleus was analyzed using High Content Analysis (HCA) of HuT78 cells treated with FAM-epAON. We

observed a dose-dependent increase of nuclear as well as cytoplasmic intensities of FAM-epAON (**Figure 5.13**).

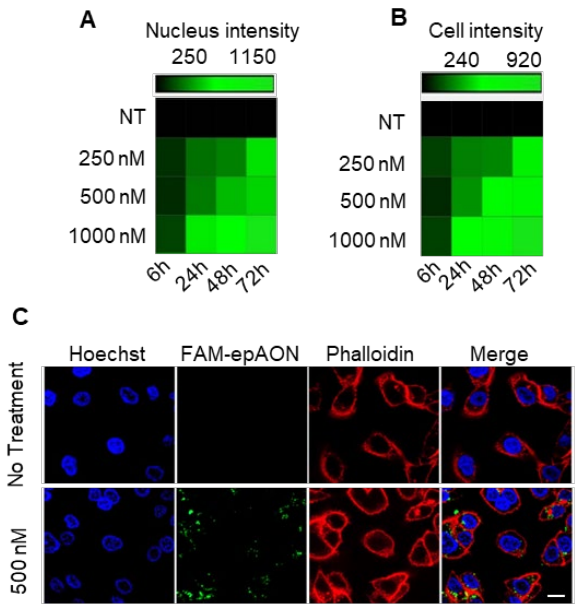

Figure 5.13 Cellular internalization of epAON by HuT78. (**A**, **B**) HuT78 cells treated with FAM epAON (250 nm. 500 nm and 1000 nm) were delivered through gymnosis for various period (6 h, 24 h, 48 h, 72 h and 96 h). Nuclear and cellular localization of FAM epAON was quantified by High Content Analysis (*cell intensity* and *nuclear intensity*) and presented. (**C**) HuT78 cells treated for 24 h with FAM epAON were fixed and counter stained with Phalloidin-Rhodamine and Hoechst. GapmeR cellular localization was analysed by confocal microscopy using 40X oil objective. At least 20 microscopic fields were scanned, and representative images are shown Scale bar 10 µm. Z-sections (YZ) are shown besides each image.

We pre-treated HuT78 cells with a panel of endocytosis inhibitors [pinocytosis inhibitor amiloride (1 mM - 4 mM), phagocytosis inhibitor cytochalasin D (1 µM, 5 µM or 25 µM), caveolae-mediated uptake inhibitor filipin (1 µg/mL, 5 µg/mL or 25 µg/mL) and clathrin-mediated endocytosis inhibitor chlorpromazine (1 µM, 5 µM or 25 µM)] for 30 min before incubating cells with FAM-epAON. After 24 h, the cellular uptake of epAON was evaluated using flow-cytometry analysis (**Figure 5.14 A**). There was no appreciable inhibition of epAON uptake upon pre-treatment with filipin, chlorpromazine, or cytochalasin D (**Figure 5.14 B, C, and D**). We observed a dose-dependent inhibition of epAON uptake in amiloride-treated cells with 81.4% inhibition at 4 mM amiloride (**Figure 5.14 E**). This suggested that epAON enters HuT78 cells through macropinocytosis.

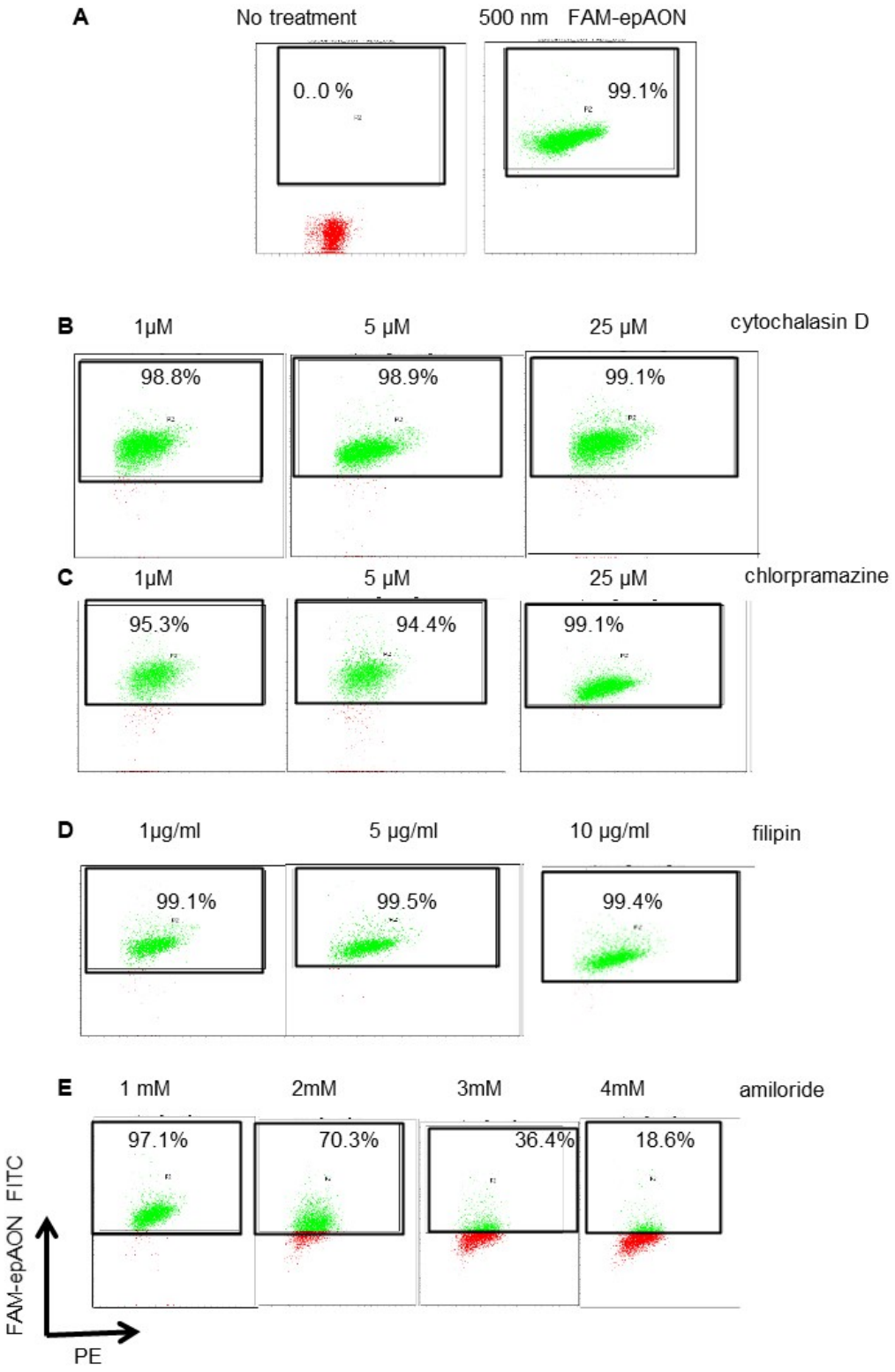

Figure 5.14 Effect of endocytosis inhibitors on epAON cellular internalization in HuT78 cells. (**A**) HuT78 cells were untreated or 500 nM FAM-labeled epAON. HuT78 cells pre-treated with (**B**) cytochalasin D [1, 5 and 25 μM], (**C**) chlorpromazine [1, 5 and 25 μM], (D) filipin [1, 5 and 25 μg/mL] and amiloride [1-4 mM] for 30 min. Pre-treated cells were incubated in FAM epAON (500nM) and were analyzed using flow cytometry.

Amiloride inhibits the activity of Na(+)/(H+) antiporters, which decreases cytosolic pH (Grinstein et al., 1989). Acidification of cytosol causes deactivation of rac1 and cd42 signaling pathways, which are involved in macropinosome formation (Koivusalo et al., 2010). These studies suggest that cellular pH is a crucial determinant of oligonucleotide uptake by cells.

It is important to note that the concentrations of inhibitors for the pre-treatment of HuT78 cells were selected based on our previously optimized protocols, published in *Nature Scientific Reports,* 2016.

5.3.13 epAON-mediated knockdown of STAT3 in cells of hematolymphoid malignancies

We evaluated the efficiency of STAT3-epAON-mediated STAT3 gene silencing in hematolymphoid cells. We demonstrate using qRT-PCR and Western immunoblotting, that treatment of HuT78 cells with STAT3-epAON significantly depletes the expression of STAT3 mRNA (>70% knockdown) (**Figure 5.15A**) and the STAT3 protein (>65% knockdown) (**Figure 5.15B**). Similarly, STAT3-epAON efficiently silenced STAT3 in MyLa and NKS1 cells with knockdown efficiency of 60% and 80%, respectively (**Figure 5.15C, D**). Both STAT3-GapmeR and STAT3-epAON molecules were equally effective in the depletion of STAT3 (**Figure 5.15D**).

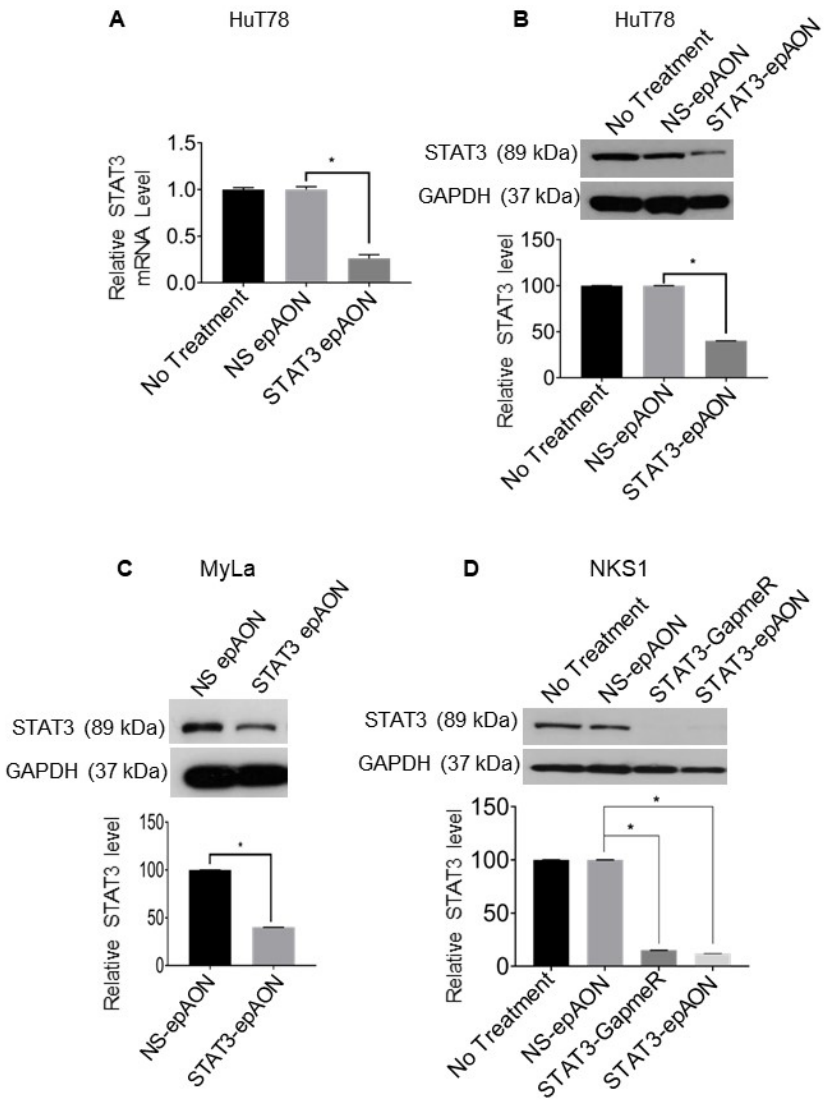

Figure 5.15 STAT3-epAON- mediated depletion of STAT3 expression in CTCL and NKTCL cells. (**A**) HuT78 cells were treated with STAT3 epAON for 72 hrs. Cells were harvested, lysed, and mRNA levels of STAT3 were evaluated using qRT-PCR. Relative graphs of STAT3 mRNA from three independent experiments were presented (mean ± SEM, *, p<0.01). Cell lysates from HuT78 (**A**), MyLa (**B**), and NKS1 (**C**) cells treated with STAT3-epAON were extracted and were immunoblotted with anti-STAT3 and anti-GAPDH (loading control) antibodies. STAT3-GapmeR was used as a positive control in the NKS1 cell line model. **(**Relative densitometry graphs of STAT3 expression are presented (mean ± SEM, *, p<0.01).

5.3.14 STAT3-epAON-mediated depletion of STAT3 induces apoptosis in cells of hematolymphoid malignancies

Persistent activation of STAT3 in lymphoma cells is involved in evasion from apoptosis. We examined whether STAT3-epAON-mediated depletion of STAT3 decreases the viability of cells of hematolymphoid malignancies. We demonstrated using MTS assay that treatment of HuT78, MyLa, and NKS1 cells with STAT3-epAON decreases cell viability by 50%, 60%, and 50%, respectively (**Figure 5.16A**). We

confirmed the induction of apoptosis in these cell lines using AnnexinV/PI staining and flow cytometry analysis. We found that STAT3-epAON induces significant levels of apoptosis in HuT78 (35 ± 2.1%), MyLa (55 ± 2.0%), and NKS1 cells (68.4 ± 3.2%) (**Figure 5.16 B**).

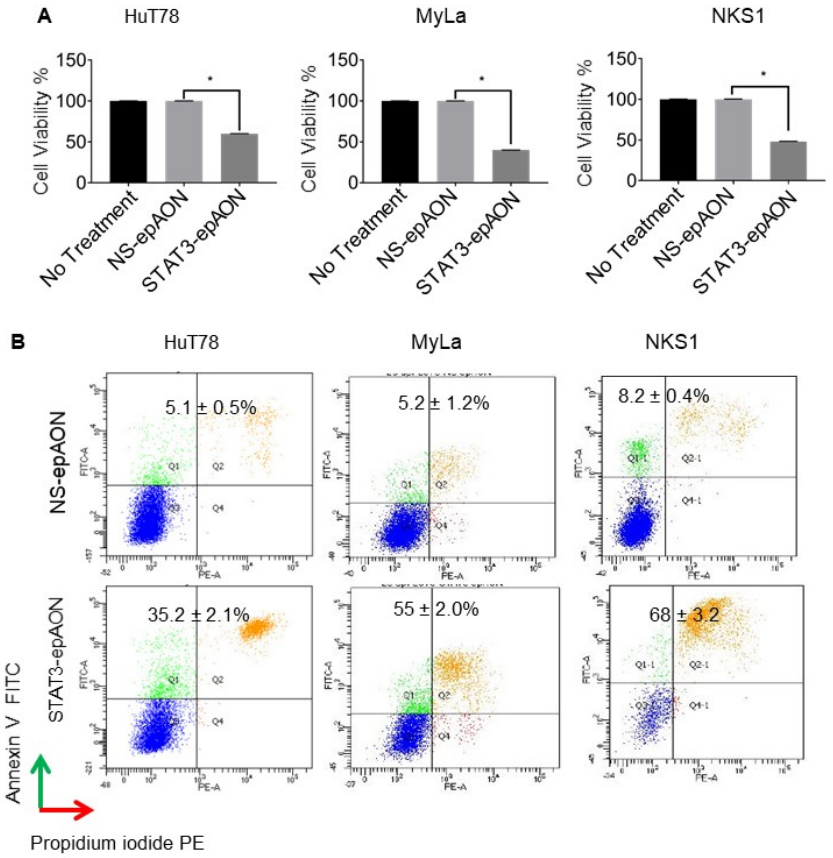

Figure 5.16 STAT3-epAON induces apoptosis in CTCL and NKTCL cell lines. (**A, B**) HuT78, MyLa, and NKS1 cells were treated with STAT3-epAON, and cell viability was evaluated after 5 days of incubation using MTS based assay. (B) Above mentioned cells were evaluated for apoptosis using Annexin V/PI staining-based flow cytometry. Annexin V and PI Stained cells are quantified based on fluorescence intensity detected in Annexin V-FITC channel and propidium iodide-PE channel of flow cytometry, respectively. Representative graphs of cell viability from 3 independent experiments were presented (mean ± SEM, **, p<0.01).

Finally, we demonstrated that STAT3-epAON-mediated depletion of STAT3 causes a significant decrease in the phosphorylated form of STAT3 (Y705) and survivin, a key anti-apoptotic protein in hematolymphoid malignancies (**Appendix 5, Figure A5.4**).

5.4 Discussion

In this chapter, we have demonstrated that alterations in the STAT3 signaling are highly prevalent in hematolymphoid malignancies suggesting that targeting the

STAT3 would be of therapeutic benefit to such patients. Oncogenic activation of STAT3 has been associated with poor prognosis and drug refractoriness in patients with hematolymphoid malignancies (Dufva et al., 2018; Kucuk et al., 2015). We also provided evidence for GapmeR mediated gene silencing of STAT3 in cell lines derived from CTCL and NKTCL. This chapter also reported a novel STAT3 antisense molecule with remarkable knockdown efficiency in lymphoma cell culture models.

Thus far, we are the first group to report PD-L1 expression correlates with STAT3 activation in NKTCL cells. We silenced STAT3 expression in NKTCL cells and examined the implication on PD-L1 regulation. Several groups have shown that PD-L1 expression and STAT3 activation are positively correlated in lung cancer as well as head and neck cancer (Bu et al., 2017; Fujita et al., 2015). This suggests a potential synergistic effect when combining STAT3 inhibitors and anti-PD1/PD-L1 antibodies in the treatment of NKTCL. Targeting STAT3 has the potential to not only directly inhibit tumor growth but also overcome tumor-induced immunosuppression to enhance anti-tumor efficacy.

In line with our observation, various studies have shown targeting STAT as an effective therapeutic approach in managing hematolymphoid malignancies. However, successes of STAT3 inhibitors/silencers are bleak due to a lack of specificity and efficacy. Hence no drugs have been approved, which directly targets STAT3. Here, we showed that GapmeR/epAON-mediated-silencing approach might be an effective alternative to specifically target STAT3. In this chapter, we specifically designed chimeric GapmeR molecules that can internalize and target STAT3. We also developed a novel epAON molecule, which can deplete the expression of STAT3 and induce apoptosis in CTCL and NKTCL cell lines.

Delivery of gene silencers remains one of the major hurdles in the success of antisense-based therapeutics. Oligonucleotides are impermeable to cells due to the charge composition and require liposomal or nanoparticle formulation for delivery into cells (Akhtar et al., 1991; Juliano et al., 2008). We have shown that GapmeR molecules can self-internalize into cells through macropinocytosis. Our study is first to show that GapmeR internalizes in “hard to transfect” cells (**Figure 5.17**).

Limited studies have been conducted on GapmeR based silencing of oncogenes in cell-derived from lymphoma cells. cEt STAT3-GapmeR showcased exquisite

silencing effect on STAT3 expression in SUP-M2 and KARPAS299 cells (Hong et al., 2015). In this chapter, we used LNA-based GapmeR to silence STAT3 in cell lines derived from CTCL and NKTCL.

In pursuit of novel STAT3 gene silencers, we developed epAON molecules, which are composed of antisense sequence and protective GQ forming nucleotides. AS1411, a G-quadruplex structure-based aptamer, is currently under investigation for the supra-molecular delivery system of drugs (Carvalho et al., 2019). We conceived a design of the STAT3 antisense molecule, which is, based on G quartet structure, which is cell-permeable as well as nuclease resistant (Bates et al., 1999; Dapic et al., 2003).

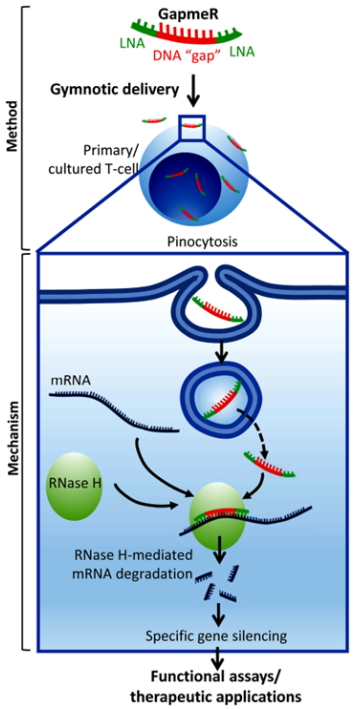

Figure 5.17 An illustration of Gymnotic uptake of GapmeR in T cells. GapmeR enters cells through macropinocytosis and causes to specific gene silencing through RNaseH-mediated cleavage.

We have shown that epAON enters HuT78 cells through macropinocytosis. Different mechanisms of internalization of GQ structures have been proposed, which include endocytosis, macropinocytosis (Reyes-Reyes et al., 2010; Soundararajan et al., 2009).

We have demonstrated in this study that STAT3-epAON molecules were stable in serum-containing medium and were not degraded upon DNase treatment. GQ forming nucleotides are nuclease resistant and are stable in serum-containing medium (Choi et al., 2010).

STAT3-epAON effectively silences STAT3 expression in cell lines derived from CTCL and NKTCL. Finally, we demonstrated that STAT3-epAON mediated STAT3 depletion causes apoptosis in HuT78, MJ, and NKS1 cells. NS-epAON does not influence the gene expression profile of HuT78 and does not induce cell death, indicating the absence of nonspecific effects on cells. High efficacy of STAT3-epAON to deplete STAT3 and induce apoptosis in hematolymphoid malignant cells encouraged us to translate this novel technology into potential therapeutics.

Subsequently, we have evaluated the safety profile of NS-epAON and STAT3-epAON in mouse models. We have demonstrated epAON molecules were tolerated in mice. We noticed that the treatment of mice with epAON did not affect the weight of the mice. Similarly, we demonstrated that serum levels of alanine transferase, aspartate transferase, creatine kinase, and IgG1 level were not perturbed upon treatment of mice with epAON (**Appendix 5, Figure A5.5**). We also showed that epAON is remarkably localized to the liver and kidney (**Appendix 5, Figure A5.6**). These observations suggest that epAON are safe and do not cause toxic effects on mice. We anticipate that epAON alone or in combination with a delivery system such as thermo-gelling polymer will display anti-tumor activity in preclinical models. STAT3-epAON is a potential antisense therapeutic agent to treat malignancies with oncogenic activation of STAT3.

In conclusion, we have shown the prevalence of frequent STAT3 mutation in hematolymphoid malignancies and its influence on the expression of immune checkpoint molecules such as PD-L1. This chapter provided essential insights in antisense mediated gene targeting in "hard to transfect" lymphoma cells. We have established "add and analyze" protocol of antisense technology in suspension cell lines, which has been published in the *Methods in Mol Biol,* 2019. We also reported a novel STAT3 antisense molecule "STAT3-epAON," which is cell-permeable and effectively depleted STAT3 expression inducing apoptosis in hematolymphoid malignant cells. This study presented a potential candidate for novel anticancer drug development targeting STAT3.

Chapter 6

General Discussion

6.1 Contribution of this thesis to the understanding of hematolymphoid malignancies

Since the first published description of hematolymphoid malignancy in 1832 by Thomas Hodgkin, significant progress has been made to understand this group of diseases (Lichtman, 2008). There have been progressive and seminal advances, over the past decade, in the understanding of the molecular basis of hematologic neoplasms. It has now been widely recognized that hematolymphoid malignancies are much more complex than initially thought. The inherent complexity of these malignancies presents a formidable intellectual challenge. The Non-Hodgkin lymphoma represents major groups of hematolymphoid malignancies

Due to the multifaceted nature of a diverse range of phenotypes and multiple hematopoietic cell types involved in hematologic cancer, this thesis employed a multidisciplinary approach and concepts to advance the knowledge in this area of hematolymphoid malignancies. It provided additional information on tumorigenic pathways, primarily mediated *via* DDX3X or STAT3 alteration in the drug resistance mechanism of hematolymphoid malignancies and developed a novel strategy to target these oncogenic pathways. In the first segment of the thesis, we sought to understand the molecular features of HDAC inhibitor-resistant CTCL cells. In the subsequent segment, we investigated the potential impact of DDX3X mutation on eliciting oncogenic signaling and drug resistance in hematolymphoid malignancies. Finally, I developed a novel gene silencer to target STAT3 and induced apoptosis in malignant cells.

6.1.1 Importance of STAT3 and ERK pathways in lymphoma vorinostat resistance

How can we be more successful in managing patients who are refractory to certain chemotherapeutics? While a number of genes, proteins, and signaling pathways that we identified to be altered in vorinostat-resistant HuT78$_{VR}$ cells in chapter 3 of this thesis, they may serve as a credible rationale for selecting pharmacological targets. At the same time, chapter 3 provides some basic starting points to study the drug-resistance mechanisms in hematologic malignancies.

We have revealed in chapter 3, that vorinostat resistant cells have enhanced invasive characteristics using transcriptomic analysis. A recent report has shown that

genes, which are involved in migration, are upregulated in drug-resistant CTCL patients(Andrews et al., 2019). These metastatic markers may emerge as potential predictors of HDACi-resistance in CTCL. In Chapter 3, we provided evidence for attenuated apoptotic machinery in vorinostat resistant cells, which is a general characteristic of drug-resistant cells. Proteomic analysis of HuT78$_{VR}$ identified ERK signaling as a decisive oncogenic signaling pathway, which activated in acquired drug-resistant cells. This chapter provided substantial evidence that ERK signaling plays a crucial role in the acquired drug resistance model.

Interestingly, we observed that STAT3 is significantly downregulated in acquired drug resistance model HuT78$_{VR}$ cells, which was similar to the observation of Chakraborty and his group. Our data support the previous finding on the variable levels of phosphorylated STAT3 in drug-resistant cells, and that STAT3 has a complex role in pathogenesis and drug resistance in CTCL. Vorinostat resistant CTCL cells were cross-resistant to other HDAC inhibitors and doxorubicin, suggesting that patients, who fail to respond to CHOP, may also be resistant to vorinostat. HuT78$_{VR}$ is sensitive to ERK inhibitors, suggesting the use of ERK inhibitors as drug modality to circumvent HDAC inhibitor resistance in CTCL. The current work provides proof of the concept that the use of ERK inhibitors may be a possible approach in overcoming vorinostat resistant CTCL. This will need to be explored in animal studies and/or clinical trials. This model can be a potential platform for clinicians and researchers to interrogate multidrug resistance and to investigate on vorinostat resistance. The development of the acquired drug-resistant model is a painstaking process, which requires immense time (more >6 months) and is labor-intensive. Our vorinostat resistant model can serve as a system to screen panels of drugs, which can augment in devising novel regimens in clinical cases with drug refractoriness. In addition, it would aid researchers to investigate the underlying mechanism of resistance mimicking a scenario where patients are refractory to chemotherapy due to acquired resistance.

6.1.2 DDX3X loss as a crucial driver for disease aggressiveness in hematolymphoid malignancies

DDX3X is frequently mutated in hematolymphoid malignancies, such as DLBCL and NKTCL (Jiang et al., 2015; Reddy et al., 2017). Nevertheless, limited numbers of studies have shown the causality of *DDX3X* alteration in these lymphoid neoplasms.

Chapter 4 provided evidence on the association of DDX3X alteration and poor prognosis in DLBCL patients. Transcriptomic signatures of DDX3X ablated NHL cells, and its gene enrichment analysis predicted oncogenic features such as enhanced proliferation and invasiveness of cells. Oncogenic activation of STAT3/ERK upon DDX3X depletion in cell lines derived from lymphoid neoplasm is one of the highlights of the study. STAT3 is commonly implicated with poor prognosis and chemoresistance in DLBCL, CTCL, and NKTCL (Huang et al., 2013; Kiel et al., 2014; Kucuk et al., 2015). In our knowledge, this is the first report that establishes the tumor-suppressive role of DDX3X in DLBCL and CTCL. The drug sensitivity profile of DDX3X depleted cells showed resistance to vorinostat, doxorubicin and other HDACi but sensitive JAK/STAT inhibitors. DDX3X depletion enhanced mRNA and protein levels of cyclin D1, which is associated with doxorubicin resistance (Ji et al., 2018).

Our studies have two main implications in determining the clinical outcome of chemotherapy treatment. Firstly, the status of DDX3X mutation could explain the low response of chemotherapy and augment decision-making determining targeted therapeutic strategies. Application of these concepts of prediction markers and stratification reduces the chemotherapeutic side effects and financial costs. Next, targeting JAK/STAT pathway is a viable option for treating patients with altered DDX3X.

While only speculation at this stage, these possibilities could account for clinically unexplained anomalies caused by DDX3X loss-of-function relevant to hematolymphoid malignancies and associated processes, such as invasiveness and metastasis. Moreover, these observations can be extrapolated to other cancer forms where DDX3X acts as a tumor suppressor gene. Although the various molecular mechanisms involved in DDX3X-mediated pathways in hematolymphoid malignancies still require clarification, we propose DDX3X as a novel driver in disease development and aggressiveness.

6.1.3 STAT3-epAON as a novel drug targeting STAT3 in hematolymphoid malignancies

In the previous two segments of the thesis, we have demonstrated the oncogenic signaling pathways involved in drug resistance of hematolymphoid cells. We have shown that targeting ERK and STAT3 signaling circumvents drug resistance in CTCL

and DLBCL cells, respectively. In the final segment, we have designed a novel gene silencer targeting the oncogenic signaling pathway with anti-cancer activities in hematolymphoid malignancies.

The clinical efficacy of STAT3 targeted therapeutics is well established, and many STAT3 inhibitors are currently under clinical trials for decades. However, none of the STAT3 inhibitors were successful in FDA approval (Wake and Watson, 2015). This prompted us to design and develop a new generation of agents targeting STAT3. Data presented in Chapter 5 clearly indicates that a novel STAT3 targeting compound STAT3-epAON can inhibit the growth of cells derived from hematolymphoid malignancies and inducing apoptosis in these cell types. We characterized the biological effects of epAON and GapmeR antisense molecules in terms of their cellular uptake in human T lymphoma cell line HuT78 as well as primary T cells. We established that STAT3-epAON is safe *in vivo* and *in vivo* (**Appendix 5, Figure A5.5**).

Also, of interest was the finding that STAT3 regulates the expression of PD-L1. Using STAT3-targeted GapmeR, we delineated the relation between STAT3 and PD-L1 expression in NKTCL (Song et al., 2018). We demonstrated that inhibition of STAT3 causes a decrease in mRNA and protein levels of PD-L1. These datasets suggest that STAT3 inhibitors may serve as a potential candidate for combination therapeutics, and targeting STAT3/PD-L1 axis would improve the efficacy of immunotherapy in NKTL, and possibly PTCL. Through further studies, we remain optimistic that the novel STAT3-epAON will prolong patient survival in the years ahead. Optimization of explicit clinical strategy and approaches by clinicians and researchers will improve clinical outcomes and minimize possible side effects or complications.

6.2 Limitations of the study

This thesis illuminated our understanding of role oncogenic signaling involved in drug resistance of hematolymphoid malignancies and strived to devise strategies to target oncogenes in these lymphoid neoplasms. However, it is critical to mention the limitation of the study, which play a crucial role in shaping the prospects of the thesis.

Limited availability of CTCL patient samples restricted the use of the clinical drug resistance model. Hence, the investigation on vorinostat resistance was performed in the cell culture model. In our study, we have identified and validated certain

phenotypic features of HuT78$_{VR}$ cells such as enhanced migration and increased cell size. However, the consequences of these enhanced features have not been covered in this thesis. We had demonstrated the upregulation of ERK in HuT78$_{VR}$ cells; however, we were unable to perform validation in non-responders to vorinostat treatment due to limited access for clinical samples.

Vorinostat-resistant CTCL model loses its insensitivity to vorinostat upon culturing in the absence of drug pressure (**Appendix 5, Figure A5.6**). This suggested that acquired resistance in this model was a temporal epigenetic regulation rather than permanent genetic alteration (Xavier et al., 2016). Reversibility of HuT78$_{VR}$ sensitivity to vorinostat further increases the existing complexity in drug resistance. These observations have led to the postulation that epigenetic regulation may play a crucial role in HDAC resistance in CTCL.

Chapter 4 explains the connotation of DDX3X mutation in chemoresistance on NHL. One of the limitations of this study was that the drug sensitivity of DDX3X-depleted cells was tested in a panel of a limited number of drugs. Another limitation of our survival analysis is the retrospective nature of the cBioPortal cohort and our consequent inability to perform multivariable analysis to confirm if *DDX3X* mutations are independent predictors of poor survival. Our demonstration of increased resistance to doxorubicin and retained sensitivity to STAT3 inhibition in DDX3X depleted cells argues for an independent influence of DDX3X on cancer drug response.

Identification of a novel, simple, and reproducible biomarkers has proved very challenging in DLBCL, and we, therefore, propose that the prognostic significance of *DDX3X* mutations be validated in a large prospective cohort. The relative rarity of *DDX3X* mutations in DLBCL prevents us from validating our *in vitro* findings on clinical samples, so the precise role of these lesions in lymphoma patients remains in question. Demonstration of reversion of key features such as drug resistance and activation of oncogenic signaling pathways through re-expression DDX3X protein in shRNA cell lines DDX3X/ siRNA depleted cells could have confirmed that these effects were specific to DDX3X depletion.

Nevertheless, the current study provides important clues in many aspects of the role of DDX3X in lymphoma and strongly suggests that these uncommon lesions ought to be evaluated thoroughly, particularly regarding their prognostic significance.

We have developed antisense molecule STAT3 epAON, which shows exquisite knockdown efficiency in *vitro* models. Nonetheless, it is imperative to evaluate knockdown efficiency and anti-cancer activity of epAON in the xenograft mice model. To proceed in this direction, we had completed the safety evaluation of epAON molecules in mice model.

6.3 Future directions

Much of the current general understanding of the molecular mechanisms involved in the initiation and development of hematolymphoid malignancies has been based on the studies performed on a limited type of cells and variants. Defective tumorigenic pathways associated with clinically diverse forms of hematolymphoid malignancies are still far from being elucidated and constitute a major challenge for future studies.

The projects reported herein have generated substantial data and formed a foundation upon which subsequent studies can be pursued. We believe that several differential genes and proteins identified in HuT78$_{VR}$ reported in Chapter 3 represent a basic form of the altered signaling network, which might be exploited for their functional involvement and to understand molecular mechanisms in drug resistance. Our investigation on acquired vorinostat resistance in HuT78$_{VR}$ cells has postulated the role of epigenetic regulation in drug resistance. However, we have not yet correlated the role of epigenetic regulation with multidrug resistance. It would be interesting to perform the CHIP-seq analysis of HuT78$_{VR}$ cells, which will reveal the role clonal evolution and *trans*-regulatory apparatus and cis-regulatory elements, such as transcription factors (TFs), promoters and super-enhancers (SEs) in acquired resistance to HDAC inhibitors in hematologic malignancies.

The HuT78$_{VR}$ cell line, in Chapter 3, serves as a model for screening compounds that may be effective for targeting drug-resistant lymphomas. While we presented data on screening of few compounds for their efficacy in killing HuT78$_{VR}$ cells, it would be interesting to screen a larger panel of novel and traditional antineoplastic agents to get a comprehensive view of chemoresistance in the current therapeutic landscape. Such analyses may also help to identify more classes of drugs that can be used to treat patients with *DDX3X* loss of function mutations.

We have demonstrated activation of ERK as a key event in acquired vorinostat resistance in CTCL cells. It is imperative to correlate clinical drug resistance and ERK activation in CTCL. It is important to determine ERK expression in various CTCL cell lines and correlate with sensitivity to vorinostat. Another approach could use the lentiviral mediated expression of an active mutant of ERK in CTCL cell lines and evaluate drug sensitivity in the modified cells. Finally, examining levels of metastatic markers and ERK activation in non-responder to HDAC treatment will provide evidence on the involvement of the above-mentioned features in drug resistance.

Little is known about cell-type specific signaling pathways that are controlled by the *DDX3X*. We are only beginning to understand that the proper functioning of DDX3X is crucial in hematologic cancer using experiments in the *in vitro* setting and a limited number of patient samples. It would be important to know how *DDX3X* is regulated in hematopoietic cells and how *DDX3X* controls many factors unique to these cell types. Association of DDX3X and EBV virus in lymphoid neoplasms has interested many research groups; however, no significant conclusion has been achieved. Therefore, a holistic view of the mechanisms pertaining to DDX3X's involvement in hematologic malignancies will be imperative to open new avenues for promising therapeutics. To understand the clinical significance of *DDX3X* mutation in hematolymphoid malignancies, it would be important to analyze larger cohort of patients. Although limited numbers of studies have uncovered the genomic landscape of lymphoid neoplasm and have reported the occurrence of *DDX3X* mutations, none of the studies has investigated the functional implications of the *DDX3X* gene. This void in the understanding of genomic lesions in the local cohort would provide us an opportunity to scrutinize and extrapolate our findings and observations of the thesis.

We have ventured into exploring the therapeutic potential of STAT3-epAON. Based on our observations on the safety profile of epAON in the mouse model, we have designed a dose regimen schedule for testing the efficacy of STAT3-epAON in the mouse model. It would be interesting to test epAON alone/ or in combination with a delivery system such as thermo-gelling polymer and evaluate anti-tumor activity in mouse models. STAT3 epAON is a potential antisense therapeutic agent to treat malignancies with oncogenic activation of STAT3.

6.4 Conclusion

This thesis highlights on various molecular cues involved in drug resistance of hematolymphoid malignancies and provides a strategic solution to target the genes involved.

Our study contributes to the insights to oncogenic signaling pathways involved in the acquired drug-resistant model of CTCL. We have shown that acquired drug resistance involves changes in the invasiveness behavior of cells suggesting the aggressive representation of CTCL on skin. Along with it, we have proven that the upregulation of ERK signaling as a decisive factor in refractory CTCL and targeting this pathway would circumvent vorinostat resistance. This study provides an explanation for the use of ERK inhibitors to treat CTCL patients, refractory to HDAC inhibitor-based therapy.

This thesis establishes a firm basis for the implication of genomic alteration in DDX3X through whole-exome sequencing and biological repository. This thesis reports occurrence of DDX3X mutation in DLBCL cohorts and further validates its implication in cell culture models. Our study shows that loss of DDX3X is a key event to instigate cancer progression in NHL and drug resistance and previously less-known phenomena of STAT3 activation in DDX3X depleted cells. Our study shows that *CCND1* is one of the key determinants of drug resistance in DDX3X altered NHL. These observations will augment the risk stratification of lymphoma patients with DDX3X alteration and may identify alternative therapeutic treatment for this subgroup with poor prognosis.

This thesis furnishes substantial evidence on the role of oncogenic activation of STAT3 in the regulatory expression of the immune checkpoint, PD-L1 in NKTCL, and provides support to the clinical reports on the use of PD-L1 inhibitors in the clinical treatment of NKTCL. STAT3 has been eluding therapy due to a lack of potent inhibitors. Our study contributes to the development of a promising antisense molecule "epAON" that can target STAT3 and elicit anti-cancer activities in cells with oncogenic activation of STAT3.

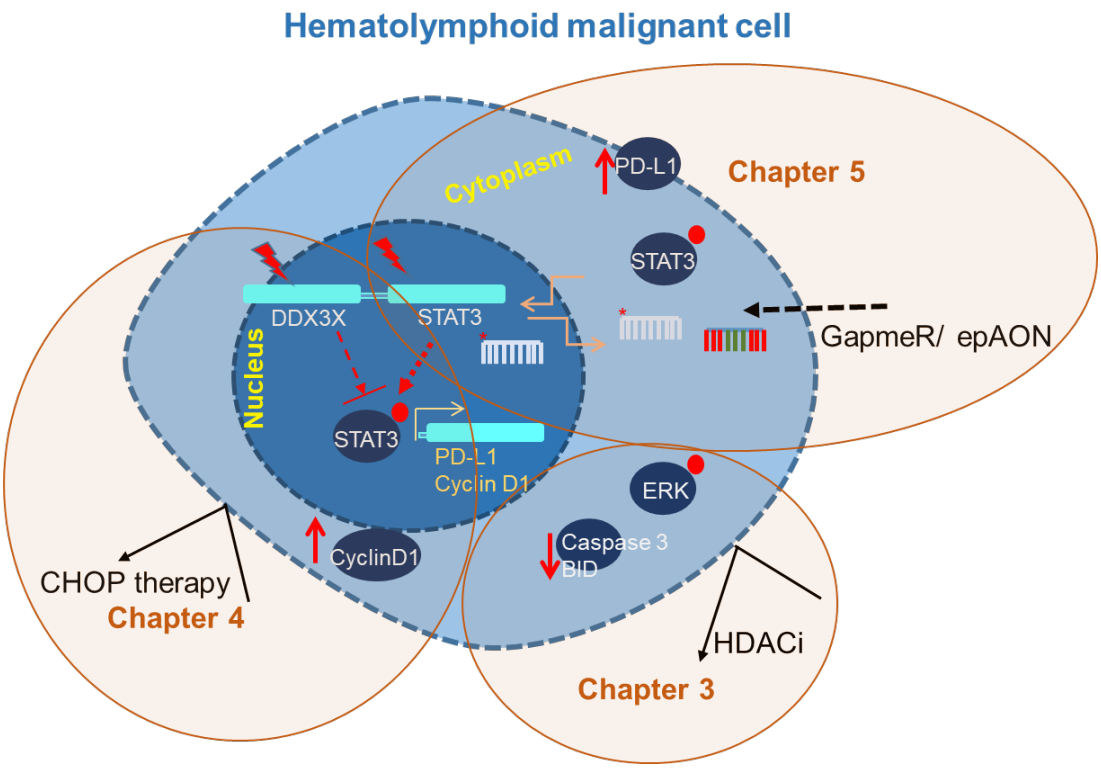

Figure 6.1 An illustration summarizing findings presented in the thesis. In chapter 3, we identified the upregulation of phosphorylation of p42/44 MAPK in acquired drug resistance along with attenuation of death machinery through the downregulation of Caspase3 and BID. In chapter 4, the influence of DDX3X mutation in lymphoid neoplasms was investigated. We showed that DDX3X altered patients have a poor survival rate, probably due to poor response to chemotherapy. DDX3X depletion causes phosphorylation of STAT3 and expression cyclin D1, which are key determinants of drug resistance. In chapter 5, we first established that oncogenic STAT3 mutations cause PD-L1 expression, and this regulatory axis was validated using GapmeR technology. Finally, we developed a novel gene silencer to target STAT3.

6.5 Intellectual property

The work described in this thesis is a part of fundamental research primarily aimed at understanding the biology of hematolymphoid cancer cells. Therefore, the results presented in this thesis may not have significant immediate potential as an object of intellectual property. However, to explore such possibility (if any), in addition to the publicly accessible literature databases (including PubMed and Web of Science), an extensive multi-parameter and multi-boolean comprehensive Patent search were carried out using the worldwide patent search WIPO (World Intellectual Property Organisation) and the European Patent Office search engine ESP@CENET. Currently, we are exploring the possibilities of patenting epAON.

6.6 Translational benefits of this work

Despite the fact that we could not perform *in vivo* testing of STAT3-epAON, the results presented here have narrowed the gap between fundamental research and clinical benefits to the patients in several ways. For example, this thesis contributes to a better understanding of molecular mechanisms underlying drug resistance in lymphoma cells as well as attempting an approach to screen other drugs that could be potentially useful in CTCL vorinostat resistance. The vorinostat resistant HuT78$_{VR}$ cell culture model developed in this study could be used for screening and discovering lead compounds that could be effective in drug-resistant cases. In an era of increased demand for new *in vitro* cell culture model systems, HuT78$_{VR}$ will provide pharmaceutical and life science researchers a robust, stable, and advanced platform for drug screening. HuT78$_{VR}$ cells should accelerate pharmaceutical research and drug discovery processes by easily identifying candidate drugs affecting resistant variants. The optimization of GapmeR-mediated gene silencing processes to knockdown genes of interest reported in Chapter 5 of this thesis provides fast and reliable solutions to gene silencing applications. Overall, discoveries made in this thesis has the potential to be translated to clinical benefit, particularly understanding complex disease phenotypes associated with hematolymphoid malignancies.

6.7 Importance of this thesis in the societal context

Hematolymphoid malignancies, including Hodgkin's and non-Hodgkin's lymphomas (NHL), afflict a huge population across the world, leading to death and financial liabilities. These diseases cause a huge burden in social and economic terms and can affect children, young adults, and the elderly, and their incidence increases with age. In 2018, lymphomas and leukemia combined accounted for approximately 5% of all cancers across the world. Quality of life of patients with hematologic cancer is usually impaired, and the 5-year survival rates of these diseases vary depending on the type and stages of tumors. In the US, the survival rate of NHL and leukemia are 74 % and 65 %, respectively.

Among the Asian countries, Singapore has the highest age-standardized incidence rate of NHL (10.1). In Singapore, lymphoid neoplasm accounts for 6.8% and 4.4% of total cancer in males and females, respectively. The incidences of lymphoid neoplasm have nearly doubled over the past five decades. More importantly, the strong

predilection of certain forms of lymphoid neoplasm such as NKTCL in the East Asian population is evident in Singapore.

Despite intensive research, a very limited number of drug modalities have been innovated for treatment or cure of hematolymphoid malignancies. The use of R-CHOP and HDAC inhibitors remains the bedrock of treatment of the majority of hematolymphoid malignancy cases. The success of molecularly targeted therapeutics in clinical trials, including STAT3 targeted agents, has been variable and largely disappointing. Nevertheless, STAT3 remains one of the most important targets for therapeutic intervention and provides a common avenue for the development of novel drugs. Therefore, a holistic overview of the signal transduction and biochemical mechanisms that blood cancer cells use to survive, proliferate, and metastasize may lead to better treatment options for this complex group of diseases.

In this thesis, we report a crucial role of DDX3X in disease aggressiveness, which would attract the interests of clinicians and scientists for further research. The demonstration that a novel STAT3 targeting epAON is capable of inhibiting lymphoma cell growth and inducing apoptosis explains its beneficial effects. Thus, STAT3-epAON may be used therapeutically to down-regulate STAT3 expression in hematolymphoid cancer cells. Findings presented in this thesis have led to the concept that the effective inhibition of STAT3 might propose an ingenious rationale-based clinical strategy for this complex group of hematolymphoid diseases.

References

Adzhubei, I.A., S. Schmidt, L. Peshkin, V.E. Ramensky, A. Gerasimova, P. Bork, A.S. Kondrashov, and S.R. Sunyaev. 2010. A method and server for predicting damaging missense mutations. *Nat Methods*. 7:248-249.

Aggarwal, S., H. Topaloglu, and S. Kumar. 2015. Systematic Review Of Burden Of Cutaneous T-Cell Lymphoma. *Value in Health*. 18:A438.

Akhtar, S., S. Basu, E. Wickstrom, and R.L. Juliano. 1991. Interactions of antisense DNA oligonucleotide analogs with phospholipid membranes (liposomes). *Nucleic acids research*. 19:5551-5559.

Al-Hakeem, D.A., S. Fedele, R. Carlos, and S. Porter. 2007. Extranodal NK/T-cell lymphoma, nasal type. *Oral Oncol*. 43:4-14.

Alam, M., R. Ahmad, H. Rajabi, A. Kharbanda, and D. Kufe. 2013. MUC1-C oncoprotein activates ERK-->C/EBPbeta signaling and induction of aldehyde dehydrogenase 1A1 in breast cancer cells. *J Biol Chem*. 288:30892-30903.

An, X., A.K. Tiwari, Y. Sun, P.R. Ding, C.R. Ashby, Jr., and Z.S. Chen. 2010. BCR-ABL tyrosine kinase inhibitors in the treatment of Philadelphia chromosome positive chronic myeloid leukemia: a review. *Leuk Res*. 34:1255-1268.

Andrews, J.M., J.A. Schmidt, K.R. Carson, A.C. Musiek, N. Mehta-Shah, and J.E. Payton. 2019. Novel cell adhesion/migration pathways are predictive markers of HDAC inhibitor resistance in cutaneous T cell lymphoma. *EBioMedicine*. 46:170-183.

Arboleda, M.J., J.F. Lyons, F.F. Kabbinavar, M.R. Bray, B.E. Snow, R. Ayala, M. Danino, B.Y. Karlan, and D.J. Slamon. 2003. Overexpression of AKT2/protein kinase Bbeta leads to up-regulation of beta1 integrins, increased invasion, and metastasis of human breast and ovarian cancer cells. *Cancer Res*. 63:196-206.

Arthur, S.E., A. Jiang, B.M. Grande, M. Alcaide, R. Cojocaru, C.K. Rushton, A. Mottok, L.K. Hilton, P.K. Lat, E.Y. Zhao, L. Culibrk, D. Ennishi, S. Jessa, L. Chong, N. Thomas, P. Pararajalingam, B. Meissner, M. Boyle, J. Davidson, K.R. Bushell, D. Lai, P. Farinha, G.W. Slack, G.B. Morin, S. Shah, D. Sen, S.J.M. Jones, A.J. Mungall, R.D. Gascoyne, T.E. Audas, P. Unrau, M.A. Marra, J.M. Connors, C. Steidl, D.W. Scott, and R.D. Morin. 2018. Genome-wide discovery of somatic regulatory variants in diffuse large B-cell lymphoma. *Nat Commun*. 9:4001.

Arvaniti, K., A. Papadioti, M. Kinigopoulou, V. Theodorou, K. Skobridis, and G. Tsiotis. 2014. Proteome Changes Induced by Imatinib and Novel Imatinib Derivatives in K562 Human Chronic Myeloid Leukemia Cells. *Proteomes*. 2:363-381.

Au, W.Y., A.C. Chan, and Y.L. Kwong. 1998. Scrotal skin ulcer in a patient with a previous tonsillectomy because of natural killer cell lymphoma. *Am J Dermatopathol*. 20:582-585.

Ballabio, E., T. Mitchell, M.S. van Kester, S. Taylor, H.M. Dunlop, J. Chi, I. Tosi, M.H. Vermeer, D. Tramonti, N.J. Saunders, J. Boultwood, J.S. Wainscoat, F. Pezzella, S.J. Whittaker, C.P. Tensen, C.S. Hatton, and C.H. Lawrie. 2010. MicroRNA expression in Sezary syndrome: identification, function, and diagnostic potential. *Blood*. 116:1105-1113.

Bates, P.J., J.B. Kahlon, S.D. Thomas, J.O. Trent, and D.M. Miller. 1999. Antiproliferative activity of G-rich oligonucleotides correlates with protein binding. *J Biol Chem*. 274:26369-26377.

Bauman, J.E., U. Duvvuri, S. Thomas, W.E. Gooding, D.A. Clump, B. Karlovits, A. Wehbe, F.R. Miller, S. Kim, M. Sen, D.E. Heron, J.R. Grandis, and A. Argiris. 2018. Phase 1 study of EGFR-antisense DNA, cetuximab, and radiotherapy in head and neck cancer with preclinical correlatives. *Cancer*. 124:3881-3889.

Becker, S., B. Groner, and C.W. Muller. 1998. Three-dimensional structure of the Stat3beta homodimer bound to DNA. *Nature*. 394:145-151.

Bi, X.W., H. Wang, W.W. Zhang, J.H. Wang, W.J. Liu, Z.J. Xia, H.Q. Huang, W.Q. Jiang, Y.J. Zhang, and L. Wang. 2016. PD-L1 is upregulated by EBV-driven

LMP1 through NF-kappaB pathway and correlates with poor prognosis in natural killer/T-cell lymphoma. *J Hematol Oncol*. 9:109.

Bishop, J.S., J.K. Guy-Caffey, J.O. Ojwang, S.R. Smith, M.E. Hogan, P.A. Cossum, R.F. Rando, and N. Chaudhary. 1996. Intramolecular G-quartet motifs confer nuclease resistance to a potent anti-HIV oligonucleotide. *J Biol Chem*. 271:5698-5703.

Bobbin, M.L., and J.J. Rossi. 2016. RNA Interference (RNAi)-Based Therapeutics: Delivering on the Promise? *Annu Rev Pharmacol Toxicol*. 56:103-122.

Body, S., A. Esteve-Arenys, H. Miloudi, C. Recasens-Zorzo, G. Tchakarska, A. Moros, S. Bustany, A. Vidal-Crespo, V. Rodriguez, R. Lavigne, E. Com, I. Casanova, R. Mangues, O. Weigert, A. Sanjuan-Pla, P. Menéndez, B. Marcq, J.-M. Picquenot, P. Pérez-Galán, F. Jardin, G. Roué, and B. Sola. 2017. Cytoplasmic cyclin D1 controls the migration and invasiveness of mantle lymphoma cells. *Scientific Reports*. 7:13946.

Bol, G.M., V. Raman, P. van der Groep, J.F. Vermeulen, A.H. Patel, E. van der Wall, and P.J. van Diest. 2013. Expression of the RNA helicase DDX3 and the hypoxia response in breast cancer. *PLoS One*. 8:e63548.

Bray, F., J. Ferlay, I. Soerjomataram, R.L. Siegel, L.A. Torre, and A. Jemal. 2018. Global cancer statistics 2018: GLOBOCAN estimates of incidence and mortality worldwide for 36 cancers in 185 countries. *CA Cancer J Clin*. 68:394-424.

Bromberg, J.F., M.H. Wrzeszczynska, G. Devgan, Y. Zhao, R.G. Pestell, C. Albanese, and J.E. Darnell, Jr. 1999. Stat3 as an oncogene. *Cell*. 98:295-303.

Bu, L.L., G.T. Yu, L. Wu, L. Mao, W.W. Deng, J.F. Liu, A.B. Kulkarni, W.F. Zhang, L. Zhang, and Z.J. Sun. 2017. STAT3 Induces Immunosuppression by Upregulating PD-1/PD-L1 in HNSCC. *J Dent Res*. 96:1027-1034.

Burg, G., W. Kempf, A. Cozzio, J. Feit, R. Willemze, S.J. E, R. Dummer, E. Berti, L. Cerroni, S. Chimenti, J.L. Diaz-Perez, F. Grange, N.L. Harris, D.V. Kazakov, H. Kerl, M. Kurrer, R. Knobler, C.J. Meijer, N. Pimpinelli, E. Ralfkiaer, R. Russell-Jones, C. Sander, M. Santucci, W. Sterry, S.H. Swerdlow, M.H. Vermeer, J. Wechsler, and S. Whittaker. 2005. WHO/EORTC classification of cutaneous lymphomas 2005: histological and molecular aspects. *J Cutan Pathol*. 32:647-674.

Cai, Q., J. Cai, Y. Fang, and K.H. Young. 2019. Epstein-Barr Virus-Positive Natural Killer/T-Cell Lymphoma. *Front Oncol*. 9:386.

Campbell, J.J., R.A. Clark, R. Watanabe, and T.S. Kupper. 2010. Sezary syndrome and mycosis fungoides arise from distinct T-cell subsets: a biologic rationale for their distinct clinical behaviors. *Blood*. 116:767-771.

Canto de Souza, L., G. Provensi, D. Vullo, F. Carta, A. Scozzafava, A. Costa, S.D. Schmidt, M.B. Passani, C.T. Supuran, and P. Blandina. 2017. Carbonic anhydrase activation enhances object recognition memory in mice through phosphorylation of the extracellular signal-regulated kinase in the cortex and the hippocampus. *Neuropharmacology*. 118:148-156.

Carvalho, J., A. Paiva, M.P. Cabral Campello, A. Paulo, J.-L. Mergny, G.F. Salgado, J.A. Queiroz, and C. Cruz. 2019. Aptamer-based Targeted Delivery of a G-quadruplex Ligand in Cervical Cancer Cells. *Scientific reports*. 9:7945.

Castanotto, D., M. Lin, C. Kowolik, L. Wang, X.Q. Ren, H.S. Soifer, T. Koch, B.R. Hansen, H. Oerum, B. Armstrong, Z. Wang, P. Bauer, J. Rossi, and C.A. Stein. 2015. A cytoplasmic pathway for gapmer antisense oligonucleotide-mediated gene silencing in mammalian cells. *Nucleic Acids Res*. 43:9350-9361.

Catlett-Falcone, R., T.H. Landowski, M.M. Oshiro, J. Turkson, A. Levitzki, R. Savino, G. Ciliberto, L. Moscinski, J.L. Fernandez-Luna, G. Nunez, W.S. Dalton, and R. Jove. 1999. Constitutive activation of Stat3 signaling confers resistance to apoptosis in human U266 myeloma cells. *Immunity*. 10:105-115.

Cengiz, F.P., S. Beyaztas, B. Gokce, O. Arslan, and O.O. Guler. 2015. Catalase, carbonic anhydrase and xanthine oxidase activities in patients with mycosis fungoides. *J Enzyme Inhib Med Chem*. 30:212-215.

Cerami, E., J. Gao, U. Dogrusoz, B.E. Gross, S.O. Sumer, B.A. Aksoy, A. Jacobsen, C.J. Byrne, M.L. Heuer, E. Larsson, Y. Antipin, B. Reva, A.P. Goldberg, C. Sander, and N. Schultz. 2012. The cBio cancer genomics portal: an open platform for exploring multidimensional cancer genomics data. *Cancer Discov*. 2:401-404.

Chakraborty, A.R., R.W. Robey, V.L. Luchenko, Z. Zhan, R.L. Piekarz, J.P. Gillet, A.V. Kossenkov, J. Wilkerson, L.C. Showe, M.M. Gottesman, N.L. Collie, and S.E. Bates. 2013. MAPK pathway activation leads to Bim loss and histone deacetylase inhibitor resistance: rationale to combine romidepsin with an MEK inhibitor. *Blood*. 121:4115-4125.

Chang, P.C., C.W. Chi, G.Y. Chau, F.Y. Li, Y.H. Tsai, J.C. Wu, and Y.H. Wu Lee. 2006. DDX3, a DEAD box RNA helicase, is deregulated in hepatitis virus-associated hepatocellular carcinoma and is involved in cell growth control. *Oncogene*. 25:1991-2003.

Chang, T.C., D. Yu, Y.S. Lee, E.A. Wentzel, D.E. Arking, K.M. West, C.V. Dang, A. Thomas-Tikhonenko, and J.T. Mendell. 2008. Widespread microRNA repression by Myc contributes to tumorigenesis. *Nat Genet*. 40:43-50.

Chao, C.H., C.M. Chen, P.L. Cheng, J.W. Shih, A.P. Tsou, and Y.H. Lee. 2006. DDX3, a DEAD box RNA helicase with tumor growth-suppressive property and transcriptional regulation activity of the p21waf1/cip1 promoter, is a candidate tumor suppressor. *Cancer Res*. 66:6579-6588.

Chen, B., H. Li, X. Zeng, P. Yang, X. Liu, X. Zhao, and S. Liang. 2012. Roles of microRNA on cancer cell metabolism. *J Transl Med*. 10:228.

Chen, H.H., H.I. Yu, W.C. Cho, and W.Y. Tarn. 2015. DDX3 modulates cell adhesion and motility and cancer cell metastasis via Rac1-mediated signaling pathway. *Oncogene*. 34:2790-2800.

Cheung, M.M., J.K. Chan, and K.F. Wong. 2003. Natural killer cell neoplasms: a distinctive group of highly aggressive lymphomas/leukemias. *Semin Hematol*. 40:221-232.

Chi, K.N., A. Zoubeidi, and M.E. Gleave. 2008. Custirsen (OGX-011): a second-generation antisense inhibitor of clusterin for the treatment of cancer. *Expert Opin Investig Drugs*. 17:1955-1962.

Chim, C.S., W.Y. Au, T.W. Shek, J. Ho, C. Choy, S.K. Ma, H.M. Tung, R. Liang, and Y.L. Kwong. 2001. Primary CD56 positive lymphomas of the gastrointestinal tract. *Cancer*. 91:525-533.

Choi, C.H. 2005. ABC transporters as multidrug resistance mechanisms and the development of chemosensitizers for their reversal. *Cancer Cell Int*. 5:30.

Choi, E.W., L.V. Nayak, and P.J. Bates. 2010. Cancer-selective antiproliferative activity is a general property of some G-rich oligodeoxynucleotides. *Nucleic Acids Res*. 38:1623-1635.

Choi, J., G. Goh, T. Walradt, B.S. Hong, C.G. Bunick, K. Chen, R.D. Bjornson, Y. Maman, T. Wang, J. Tordoff, K. Carlson, J.D. Overton, K.J. Liu, J.M. Lewis, L. Devine, L. Barbarotta, F.M. Foss, A. Subtil, E.C. Vonderheid, R.L. Edelson, D.G. Schatz, T.J. Boggon, M. Girardi, and R.P. Lifton. 2015. Genomic landscape of cutaneous T cell lymphoma. *Nat Genet*. 47:1011-1019.

Clark, R.A., R. Watanabe, J.E. Teague, C. Schlapbach, M.C. Tawa, N. Adams, A.A. Dorosario, K.S. Chaney, C.S. Cutler, N.R. Leboeuf, J.B. Carter, D.C. Fisher, and T.S. Kupper. 2012. Skin effector memory T cells do not recirculate and provide immune protection in alemtuzumab-treated CTCL patients. *Sci Transl Med*. 4:117ra117.

Coiffier, B. 2004. Effective immunochemotherapy for aggressive non-Hodgkin's lymphoma. *Semin Oncol*. 31:7-11.

Coiffier, B., E. Lepage, J. Briere, R. Herbrecht, H. Tilly, R. Bouabdallah, P. Morel, E. Van Den Neste, G. Salles, P. Gaulard, F. Reyes, P. Lederlin, and C. Gisselbrecht. 2002. CHOP chemotherapy plus rituximab compared with CHOP alone in elderly patients with diffuse large-B-cell lymphoma. *N Engl J Med*. 346:235-242.

Coiffier, B., C. Thieblemont, E. Van Den Neste, G. Lepeu, I. Plantier, S. Castaigne, S. Lefort, G. Marit, M. Macro, C. Sebban, K. Belhadj, D. Bordessoule, C. Ferme, and H. Tilly. 2010. Long-term outcome of patients in the LNH-98.5 trial, the first randomized study comparing rituximab-CHOP to standard CHOP chemotherapy in DLBCL patients: a study by the Groupe d'Etudes des Lymphomes de l'Adulte. *Blood*. 116:2040-2045.

Cole, S.P. 2014. Multidrug resistance protein 1 (MRP1, ABCC1), a "multitasking" ATP-binding cassette (ABC) transporter. *J Biol Chem*. 289:30880-30888.

Croce, C.M. 2009. Causes and consequences of microRNA dysregulation in cancer. *Nat Rev Genet*. 10:704-714.

Crooke, S.T. 2017. Molecular Mechanisms of Antisense Oligonucleotides. *Nucleic Acid Ther*. 27:70-77.

da Silva Almeida, A.C., F. Abate, H. Khiabanian, E. Martinez-Escala, J. Guitart, C.P. Tensen, M.H. Vermeer, R. Rabadan, A. Ferrando, and T. Palomero. 2015. The mutational landscape of cutaneous T cell lymphoma and Sezary syndrome. *Nat Genet*. 47:1465-1470.

Dalal, M.R., S.A. Mitchell, C. McCloskey, E.A. Zagadailov, and A. Gautam. 2017. EPIDEMIOLOGICAL AND HUMANISTIC BURDEN OF CUTANEOUS T-CELL LYMPHOMAS: RESULTS OF a SYSTEMATIC REVIEW. *Hematological Oncology*. 35:389-390.

Dang, T.P. 2012. Notch, apoptosis and cancer. *Adv Exp Med Biol*. 727:199-209.

Dapic, V., V. Abdomerovic, R. Marrington, J. Peberdy, A. Rodger, J.O. Trent, and P.J. Bates. 2003. Biophysical and biological properties of quadruplex oligodeoxyribonucleotides. *Nucleic Acids Res*. 31:2097-2107.

Darnell, J.E., Jr., I.M. Kerr, and G.R. Stark. 1994. Jak-STAT pathways and transcriptional activation in response to IFNs and other extracellular signaling proteins. *Science*. 264:1415-1421.

de Miranda, N.F., K. Georgiou, L. Chen, C. Wu, Z. Gao, A. Zaravinos, S. Lisboa, G. Enblad, M.R. Teixeira, Y. Zeng, R. Peng, and Q. Pan-Hammarstrom. 2014. Exome sequencing reveals novel mutation targets in diffuse large B-cell lymphomas derived from Chinese patients. *Blood*. 124:2544-2553.

Deeks, E.D. 2017. Ibrutinib: A Review in Chronic Lymphocytic Leukaemia. *Drugs*. 77:225-236.

Dias, N., and C.A. Stein. 2002. Antisense oligonucleotides: basic concepts and mechanisms. *Mol Cancer Ther*. 1:347-355.

Dieckmann, A., P.H. Hagedorn, Y. Burki, C. Brugmann, M. Berrera, M. Ebeling, T. Singer, and F. Schuler. 2018. A Sensitive In Vitro Approach to Assess the Hybridization-Dependent Toxic Potential of High Affinity Gapmer Oligonucleotides. *Mol Ther Nucleic Acids*. 10:45-54.

Dobashi, A., N. Tsuyama, R. Asaka, Y. Togashi, K. Ueda, S. Sakata, S. Baba, K. Sakamoto, K. Hatake, and K. Takeuchi. 2016. Frequent BCOR aberrations in extranodal NK/T-Cell lymphoma, nasal type. *Genes Chromosomes Cancer*. 55:460-471.

Dritschilo, A., C.H. Huang, C.M. Rudin, J. Marshall, B. Collins, J.L. Dul, C. Zhang, D. Kumar, P.C. Gokhale, A. Ahmad, I. Ahmad, J.W. Sherman, and U.N. Kasid. 2006. Phase I study of liposome-encapsulated c-raf antisense

oligodeoxyribonucleotide infusion in combination with radiation therapy in patients with advanced malignancies. *Clin Cancer Res*. 12:1251-1259.

Dufva, O., M. Kankainen, T. Kelkka, N. Sekiguchi, S.A. Awad, S. Eldfors, B. Yadav, H. Kuusanmaki, D. Malani, E.I. Andersson, P. Pietarinen, L. Saikko, P.E. Kovanen, T. Ojala, D.A. Lee, T.P. Loughran, Jr., H. Nakazawa, J. Suzumiya, R. Suzuki, Y.H. Ko, W.S. Kim, S.S. Chuang, T. Aittokallio, W.C. Chan, K. Ohshima, F. Ishida, and S. Mustjoki. 2018. Aggressive natural killer-cell leukemia mutational landscape and drug profiling highlight JAK-STAT signaling as therapeutic target. *Nat Commun*. 9:1567.

Duvic, M., R. Talpur, X. Ni, C. Zhang, P. Hazarika, C. Kelly, J.H. Chiao, J.F. Reilly, J.L. Ricker, V.M. Richon, and S.R. Frankel. 2007. Phase 2 trial of oral vorinostat (suberoylanilide hydroxamic acid, SAHA) for refractory cutaneous T-cell lymphoma (CTCL). *Blood*. 109:31-39.

Eckschlager, T., J. Plch, M. Stiborova, and J. Hrabeta. 2017. Histone Deacetylase Inhibitors as Anticancer Drugs. *Int J Mol Sci*. 18.

Edwards, L.J., M. Mizui, and V. Kyttaris. 2015. Signal transducer and activator of transcription (STAT) 3 inhibition delays the onset of lupus nephritis in MRL/lpr mice. *Clin Immunol*. 158:221-230.

Egashira, M., N. Kawamata, K. Sugimoto, T. Kaneko, and K. Oshimi. 1999. P-glycoprotein expression on normal and abnormally expanded natural killer cells and inhibition of P-glycoprotein function by cyclosporin A and its analogue, PSC833. *Blood*. 93:599-606.

Elbashir, S.M., W. Lendeckel, and T. Tuschl. 2001. RNA interference is mediated by 21- and 22-nucleotide RNAs. *Genes Dev*. 15:188-200.

Epling, L.B., C.R. Grace, B.R. Lowe, J.F. Partridge, and E.J. Enemark. 2015. Cancer-associated mutants of RNA helicase DDX3X are defective in RNA-stimulated ATP hydrolysis. *J Mol Biol*. 427:1779-1796.

Esquela-Kerscher, A., and F.J. Slack. 2006. Oncomirs - microRNAs with a role in cancer. *Nat Rev Cancer*. 6:259-269.

Fantin, V.R., A. Loboda, C.P. Paweletz, R.C. Hendrickson, J.W. Pierce, J.A. Roth, L. Li, F. Gooden, S. Korenchuk, X.S. Hou, E.A. Harrington, S. Randolph, J.F. Reilly, C.M. Ware, M.E. Kadin, S.R. Frankel, and V.M. Richon. 2008. Constitutive activation of signal transducers and activators of transcription predicts vorinostat resistance in cutaneous T-cell lymphoma. *Cancer Res*. 68:3785-3794.

Fazil, M., S.T. Ong, M.L.S. Chalasani, A. Kizhakeyil, and N.K. Verma. 2019. GapmeR-Mediated Gene Silencing in Motile T-Cells. *Methods Mol Biol*. 1930:67-73.

Fazil, M.H., S.T. Ong, M.L. Chalasani, J.H. Low, A. Kizhakeyil, A. Mamidi, C.F. Lim, G.D. Wright, R. Lakshminarayanan, D. Kelleher, and N.K. Verma. 2016. GapmeR cellular internalization by macropinocytosis induces sequence-specific gene silencing in human primary T-cells. *Sci Rep*. 6:37721.

Firmbach-Kraft, I., M. Byers, T. Shows, R. Dalla-Favera, and J.J. Krolewski. 1990. tyk2, prototype of a novel class of non-receptor tyrosine kinase genes. *Oncogene*. 5:1329-1336.

Fisher, R.I., E.R. Gaynor, S. Dahlberg, M.M. Oken, T.M. Grogan, E.M. Mize, J.H. Glick, C.A. Coltman, Jr., and T.P. Miller. 1993. Comparison of a standard regimen (CHOP) with three intensive chemotherapy regimens for advanced non-Hodgkin's lymphoma. *N Engl J Med*. 328:1002-1006.

Fornecker, L.M., L. Muller, F. Bertrand, N. Paul, A. Pichot, R. Herbrecht, M.P. Chenard, L. Mauvieux, L. Vallat, S. Bahram, S. Cianferani, R. Carapito, and C. Carapito. 2019. Multi-omics dataset to decipher the complexity of drug resistance in diffuse large B-cell lymphoma. *Sci Rep*. 9:895.

Friedberg, J.W. 2011. Relapsed/refractory diffuse large B-cell lymphoma. *Hematology Am Soc Hematol Educ Program*. 2011:498-505.

Fujita, Y., S. Yagishita, K. Hagiwara, Y. Yoshioka, N. Kosaka, F. Takeshita, T. Fujiwara, K. Tsuta, H. Nokihara, T. Tamura, H. Asamura, M. Kawaishi, K. Kuwano, and T. Ochiya. 2015. The clinical relevance of the miR-197/CKS1B/STAT3-mediated PD-L1 network in chemoresistant non-small-cell lung cancer. *Mol Ther*. 23:717-727.

Furumai, R., A. Matsuyama, N. Kobashi, K.H. Lee, M. Nishiyama, H. Nakajima, A. Tanaka, Y. Komatsu, N. Nishino, M. Yoshida, and S. Horinouchi. 2002. FK228 (depsipeptide) as a natural prodrug that inhibits class I histone deacetylases. *Cancer Res*. 62:4916-4921.

Gao, J., B.A. Aksoy, U. Dogrusoz, G. Dresdner, B. Gross, S.O. Sumer, Y. Sun, A. Jacobsen, R. Sinha, E. Larsson, E. Cerami, C. Sander, and N. Schultz. 2013. Integrative analysis of complex cancer genomics and clinical profiles using the cBioPortal. *Sci Signal*. 6:pl1.

Garcia-Manero, G., H. Yang, C. Bueso-Ramos, A. Ferrajoli, J. Cortes, W.G. Wierda, S. Faderl, C. Koller, G. Morris, G. Rosner, A. Loboda, V.R. Fantin, S.S. Randolph, J.S. Hardwick, J.F. Reilly, C. Chen, J.L. Ricker, J.P. Secrist, V.M. Richon, S.R. Frankel, and H.M. Kantarjian. 2008. Phase 1 study of the histone deacetylase inhibitor vorinostat (suberoylanilide hydroxamic acid [SAHA]) in patients with advanced leukemias and myelodysplastic syndromes. *Blood*. 111:1060-1066.

Geissler, R., R.P. Golbik, and S.E. Behrens. 2012. The DEAD-box helicase DDX3 supports the assembly of functional 80S ribosomes. *Nucleic Acids Res*. 40:4998-5011.

Germann, U.A., B.F. Furey, W. Markland, R.R. Hoover, A.M. Aronov, J.J. Roix, M. Hale, D.M. Boucher, D.A. Sorrell, G. Martinez-Botella, M. Fitzgibbon, P. Shapiro, M.J. Wick, R. Samadani, K. Meshaw, A. Groover, G. DeCrescenzo, M. Namchuk, C.M. Emery, S. Saha, and D.J. Welsch. 2017. Targeting the MAPK Signaling Pathway in Cancer: Promising Preclinical Activity with the Novel Selective ERK1/2 Inhibitor BVD-523 (Ulixertinib). *Mol Cancer Ther*. 16:2351-2363.

Greenberger, L.M., I.D. Horak, D. Filpula, P. Sapra, M. Westergaard, H.F. Frydenlund, C. Albaek, H. Schroder, and H. Orum. 2008. A RNA antagonist of hypoxia-inducible factor-1alpha, EZN-2968, inhibits tumor cell growth. *Mol Cancer Ther*. 7:3598-3608.

Grinstein, S., D. Rotin, and M.J. Mason. 1989. Na+/H+ exchange and growth factor-induced cytosolic pH changes. Role in cellular proliferation. *Biochim Biophys Acta*. 988:73-97.

Grivennikov, S., E. Karin, J. Terzic, D. Mucida, G.Y. Yu, S. Vallabhapurapu, J. Scheller, S. Rose-John, H. Cheroutre, L. Eckmann, and M. Karin. 2009. IL-6 and Stat3 are required for survival of intestinal epithelial cells and development of colitis-associated cancer. *Cancer Cell*. 15:103-113.

Gueler, B., S.B. Sonne, J. Zimmer, B. Hilscher, W. Hilscher, N. Graem, E. Rajpert-De Meyts, and P.H. Vogt. 2012. AZFa protein DDX3Y is differentially expressed in human male germ cells during development and in testicular tumours: new evidence for phenotypic plasticity of germ cells. *Hum Reprod*. 27:1547-1555.

Gunawardana, J., F.C. Chan, A. Telenius, B. Woolcock, R. Kridel, K.L. Tan, S. Ben-Neriah, A. Mottok, R.S. Lim, M. Boyle, S. Rogic, L.M. Rimsza, C. Guiter, K. Leroy, P. Gaulard, C. Haioun, M.A. Marra, K.J. Savage, J.M. Connors, S.P. Shah, R.D. Gascoyne, and C. Steidl. 2014. Recurrent somatic mutations of PTPN1 in primary mediastinal B cell lymphoma and Hodgkin lymphoma. *Nat Genet*. 46:329-335.

Hagedorn, P.H., B.R. Hansen, T. Koch, and M. Lindow. 2017. Managing the sequence-specificity of antisense oligonucleotides in drug discovery. *Nucleic Acids Res*. 45:2262-2282.

Hair, P., F. Cameron, and K. McKeage. 2013. Mipomersen sodium: first global approval. *Drugs*. 73:487-493.

Hammond, S.M., E. Bernstein, D. Beach, and G.J. Hannon. 2000. An RNA-directed nuclease mediates post-transcriptional gene silencing in Drosophila cells. *Nature*. 404:293-296.

Hanahan, D., and R.A. Weinberg. 2011. Hallmarks of cancer: the next generation. *Cell*. 144:646-674.

Hans, C.P., D.D. Weisenburger, T.C. Greiner, R.D. Gascoyne, J. Delabie, G. Ott, H.K. Muller-Hermelink, E. Campo, R.M. Braziel, E.S. Jaffe, Z. Pan, P. Farinha, L.M. Smith, B. Falini, A.H. Banham, A. Rosenwald, L.M. Staudt, J.M. Connors, J.O. Armitage, and W.C. Chan. 2004. Confirmation of the molecular classification of diffuse large B-cell lymphoma by immunohistochemistry using a tissue microarray. *Blood*. 103:275-282.

He, Y., D. Zhang, Y. Yang, X. Wang, X. Zhao, P. Zhang, H. Zhu, N. Xu, and S. Liang. 2018. A double-edged function of DDX3, as an oncogene or tumor suppressor, in cancer progression (Review). *Oncol Rep*. 39:883-892.

Hirose, I., A. Kanda, K. Noda, and S. Ishida. 2019. Glucocorticoid receptor inhibits Muller glial galectin-1 expression via DUSP1-dependent and -independent deactivation of AP-1 signalling. *J Cell Mol Med*. 23:6785-6796.

Hogbom, M., R. Collins, S. van den Berg, R.M. Jenvert, T. Karlberg, T. Kotenyova, A. Flores, G.B. Karlsson Hedestam, and L.H. Schiavone. 2007. Crystal structure of conserved domains 1 and 2 of the human DEAD-box helicase DDX3X in complex with the mononucleotide AMP. *J Mol Biol*. 372:150-159.

Hong, D., R. Kurzrock, Y. Kim, R. Woessner, A. Younes, J. Nemunaitis, N. Fowler, T. Zhou, J. Schmidt, M. Jo, S.J. Lee, M. Yamashita, S.G. Hughes, L. Fayad, S. Piha-Paul, M.V. Nadella, M. Mohseni, D. Lawson, C. Reimer, D.C. Blakey, X. Xiao, J. Hsu, A. Revenko, B.P. Monia, and A.R. MacLeod. 2015. AZD9150, a next-generation antisense oligonucleotide inhibitor of STAT3 with early evidence of clinical activity in lymphoma and lung cancer. *Sci Transl Med*. 7:314ra185.

Horiguchi, A., T. Asano, K. Kuroda, A. Sato, J. Asakuma, K. Ito, M. Hayakawa, M. Sumitomo, and T. Asano. 2010. STAT3 inhibitor WP1066 as a novel therapeutic agent for renal cell carcinoma. *British Journal of Cancer*. 102:1592-1599.

Hou, H.A., J.W. Lu, T.Y. Lin, C.H. Tsai, W.C. Chou, C.C. Lin, Y.Y. Kuo, C.Y. Liu, M.H. Tseng, Y.C. Chiang, Y.L. Peng, J.L. Tang, Z. Gong, L.I. Lin, and H.F. Tien. 2017. Clinico-biological significance of suppressor of cytokine signaling 1 expression in acute myeloid leukemia. *Blood Cancer J*. 7:e588.

Housman, G., S. Byler, S. Heerboth, K. Lapinska, M. Longacre, N. Snyder, and S. Sarkar. 2014. Drug resistance in cancer: an overview. *Cancers (Basel)*. 6:1769-1792.

Howlader, N., A.B. Mariotto, C. Besson, G. Suneja, K. Robien, N. Younes, and E.A. Engels. 2017. Cancer-specific mortality, cure fraction, and noncancer causes of death among diffuse large B-cell lymphoma patients in the immunochemotherapy era. *Cancer*. 123:3326-3334.

Hu, L., S.H. Lau, C.H. Tzang, J.M. Wen, W. Wang, D. Xie, M. Huang, Y. Wang, M.C. Wu, J.F. Huang, W.F. Zeng, J.S. Sham, M. Yang, and X.Y. Guan. 2004. Association of Vimentin overexpression and hepatocellular carcinoma metastasis. *Oncogene*. 23:298-302.

Huang, X., B. Meng, J. Iqbal, B.B. Ding, A.M. Perry, W. Cao, L.M. Smith, C. Bi, C. Jiang, T.C. Greiner, D.D. Weisenburger, L. Rimsza, A. Rosenwald, G. Ott, J. Delabie, E. Campo, R.M. Braziel, R.D. Gascoyne, J.R. Cook, R.R. Tubbs, E.S. Jaffe, J.O. Armitage, J.M. Vose, L.M. Staudt, T.W. McKeithan, W.C. Chan, B.H. Ye, and K. Fu. 2013. Activation of the STAT3 signaling pathway is associated with poor survival in diffuse large B-cell lymphoma treated with R-CHOP. *J Clin Oncol*. 31:4520-4528.

Huppert, J.L., and S. Balasubramanian. 2005. Prevalence of quadruplexes in the human genome. *Nucleic acids research*. 33:2908-2916.
Hutchins, A.P., D. Diez, and D. Miranda-Saavedra. 2013. The IL-10/STAT3-mediated anti-inflammatory response: recent developments and future challenges. *Brief Funct Genomics*. 12:489-498.
Jackson, A.L., and P.S. Linsley. 2010. Recognizing and avoiding siRNA off-target effects for target identification and therapeutic application. *Nat Rev Drug Discov*. 9:57-67.
Jaffe, E.S. 2009. The 2008 WHO classification of lymphomas: implications for clinical practice and translational research. *Hematology Am Soc Hematol Educ Program*:523-531.
Jain, S., D. Stroopinsky, L. Yin, J. Rosenblatt, M. Alam, P. Bhargava, R.A. Clark, T.S. Kupper, K. Palmer, M.D. Coll, H. Rajabi, A. Pyzer, M. Bar-Natan, K. Luptakova, J. Arnason, R. Joyce, D. Kufe, and D. Avigan. 2015. Mucin 1 is a potential therapeutic target in cutaneous T-cell lymphoma. *Blood*. 126:354-362.
Jaschinski, F., T. Rothhammer, P. Jachimczak, C. Seitz, A. Schneider, and K.H. Schlingensiepen. 2011. The antisense oligonucleotide trabedersen (AP 12009) for the targeted inhibition of TGF-beta2. *Curr Pharm Biotechnol*. 12:2203-2213.
Jawed, S.I., P.L. Myskowski, S. Horwitz, A. Moskowitz, and C. Querfeld. 2014. Primary cutaneous T-cell lymphoma (mycosis fungoides and Sezary syndrome): part II. Prognosis, management, and future directions. *J Am Acad Dermatol*. 70:223 e221-217; quiz 240-222.
Jeon, J.H., D.K. Kim, Y. Shin, H.Y. Kim, B. Song, E.Y. Lee, J.K. Kim, H.J. You, H. Cheong, D.H. Shin, S.T. Kim, J.H. Cheong, S.Y. Kim, and H. Jang. 2016. Migration and invasion of drug-resistant lung adenocarcinoma cells are dependent on mitochondrial activity. *Exp Mol Med*. 48:e277.
Jeong, E.G., M.S. Kim, H.K. Nam, C.K. Min, S. Lee, Y.J. Chung, N.J. Yoo, and S.H. Lee. 2008. Somatic mutations of JAK1 and JAK3 in acute leukemias and solid cancers. *Clin Cancer Res*. 14:3716-3721.
Ji, Z.P., L. Qiang, and J.L. Zhang. 2018. Transcription activated p73-modulated cyclin D1 expression leads to doxorubicin resistance in gastric cancer. *Exp Ther Med*. 15:1831-1838.
Jiang, L., Z.H. Gu, Z.X. Yan, X. Zhao, Y.Y. Xie, Z.G. Zhang, C.M. Pan, Y. Hu, C.P. Cai, Y. Dong, J.Y. Huang, L. Wang, Y. Shen, G. Meng, J.F. Zhou, J.D. Hu, J.F. Wang, Y.H. Liu, L.H. Yang, F. Zhang, J.M. Wang, Z. Wang, Z.G. Peng, F.Y. Chen, Z.M. Sun, H. Ding, J.M. Shi, J. Hou, J.S. Yan, J.Y. Shi, L. Xu, Y. Li, J. Lu, Z. Zheng, W. Xue, W.L. Zhao, Z. Chen, and S.J. Chen. 2015. Exome sequencing identifies somatic mutations of DDX3X in natural killer/T-cell lymphoma. *Nat Genet*. 47:1061-1066.
Johnston, P.A., and J.R. Grandis. 2011. STAT3 signaling: anticancer strategies and challenges. *Mol Interv*. 11:18-26.
Johnstone, R.W. 2002. Histone-deacetylase inhibitors: novel drugs for the treatment of cancer. *Nat Rev Drug Discov*. 1:287-299.
Jones, D.T., N. Jager, M. Kool, T. Zichner, B. Hutter, M. Sultan, Y.J. Cho, T.J. Pugh, V. Hovestadt, A.M. Stutz, T. Rausch, H.J. Warnatz, M. Ryzhova, S. Bender, D. Sturm, S. Pleier, H. Cin, E. Pfaff, L. Sieber, A. Wittmann, M. Remke, H. Witt, S. Hutter, T. Tzaridis, J. Weischenfeldt, B. Raeder, M. Avci, V. Amstislavskiy, M. Zapatka, U.D. Weber, Q. Wang, B. Lasitschka, C.C. Bartholomae, M. Schmidt, C. von Kalle, V. Ast, C. Lawerenz, J. Eils, R. Kabbe, V. Benes, P. van Sluis, J. Koster, R. Volckmann, D. Shih, M.J. Betts, R.B. Russell, S. Coco, G.P. Tonini, U. Schuller, V. Hans, N. Graf, Y.J. Kim, C. Monoranu, W. Roggendorf, A. Unterberg, C. Herold-Mende, T. Milde, A.E. Kulozik, A. von Deimling, O. Witt, E. Maass, J. Rossler, M. Ebinger, M.U. Schuhmann, M.C. Fruhwald, M. Hasselblatt, N. Jabado, S. Rutkowski, A.O. von Bueren, D. Williamson, S.C.

Clifford, M.G. McCabe, V.P. Collins, S. Wolf, S. Wiemann, H. Lehrach, B. Brors, W. Scheurlen, J. Felsberg, G. Reifenberger, P.A. Northcott, M.D. Taylor, M. Meyerson, S.L. Pomeroy, M.L. Yaspo, J.O. Korbel, A. Korshunov, R. Eils, S.M. Pfister, and P. Lichter. 2012. Dissecting the genomic complexity underlying medulloblastoma. *Nature*. 488:100-105.

Juliano, R., M.R. Alam, V. Dixit, and H. Kang. 2008. Mechanisms and strategies for effective delivery of antisense and siRNA oligonucleotides. *Nucleic Acids Res*. 36:4158-4171.

Juliano, R.L., X. Ming, and O. Nakagawa. 2012. Cellular uptake and intracellular trafficking of antisense and siRNA oligonucleotides. *Bioconjug Chem*. 23:147-157.

Keam, S.J. 2018. Inotersen: First Global Approval. *Drugs*. 78:1371-1376.

Kiel, M.J., T. Velusamy, D. Rolland, A.A. Sahasrabuddhe, F. Chung, N.G. Bailey, A. Schrader, B. Li, J.Z. Li, A.B. Ozel, B.L. Betz, R.N. Miranda, L.J. Medeiros, L. Zhao, M. Herling, M.S. Lim, and K.S. Elenitoba-Johnson. 2014. Integrated genomic sequencing reveals mutational landscape of T-cell prolymphocytic leukemia. *Blood*. 124:1460-1472.

Kiessling, M.K., J.P. Nicolay, T. Schlor, C.D. Klemke, D. Suss, P.H. Krammer, and K. Gulow. 2017. NRAS mutations in cutaneous T cell lymphoma (CTCL) sensitize tumors towards treatment with the multikinase inhibitor Sorafenib. *Oncotarget*. 8:45687-45697.

Kim, D., B. Langmead, and S.L. Salzberg. 2015. HISAT: a fast spliced aligner with low memory requirements. *Nat Methods*. 12:357-360.

Kim, Y., and S. Myong. 2016. RNA Remodeling Activity of DEAD Box Proteins Tuned by Protein Concentration, RNA Length, and ATP. *Mol Cell*. 63:865-876.

Kizhakeyil, A., S.T. Ong, M. Fazil, M.L.S. Chalasani, P. Prasannan, and N.K. Verma. 2019. Isolation of Human Peripheral Blood T-Lymphocytes. *Methods Mol Biol*. 1930:11-17.

Kizhakeyil, A., and N.K. Verma. 2019. Quantitative Real-Time PCR for Evaluating Transcriptional Changes in T-Lymphocytes. *Methods Mol Biol*. 1930:59-66.

Koivusalo, M., C. Welch, H. Hayashi, C.C. Scott, M. Kim, T. Alexander, N. Touret, K.M. Hahn, and S. Grinstein. 2010. Amiloride inhibits macropinocytosis by lowering submembranous pH and preventing Rac1 and Cdc42 signaling. *J Cell Biol*. 188:547-563.

Koo, G.C., S.Y. Tan, T. Tang, S.L. Poon, G.E. Allen, L. Tan, S.C. Chong, W.S. Ong, K. Tay, M. Tao, R. Quek, S. Loong, K.W. Yeoh, S.P. Yap, K.A. Lee, L.C. Lim, D. Tan, C. Goh, I. Cutcutache, W. Yu, C.C. Ng, V. Rajasegaran, H.L. Heng, A. Gan, C.K. Ong, S. Rozen, P. Tan, B.T. Teh, and S.T. Lim. 2012. Janus kinase 3-activating mutations identified in natural killer/T-cell lymphoma. *Cancer Discov*. 2:591-597.

Kubuschok, B., G. Held, and M. Pfreundschuh. 2015. Management of diffuse large B-cell lymphoma (DLBCL). *Cancer Treat Res*. 165:271-288.

Kucuk, C., B. Jiang, X. Hu, W. Zhang, J.K. Chan, W. Xiao, N. Lack, C. Alkan, J.C. Williams, K.N. Avery, P. Kavak, A. Scuto, E. Sen, P. Gaulard, L. Staudt, J. Iqbal, W. Zhang, A. Cornish, Q. Gong, Q. Yang, H. Sun, F. d'Amore, S. Leppa, W. Liu, K. Fu, L. de Leval, T. McKeithan, and W.C. Chan. 2015. Activating mutations of STAT5B and STAT3 in lymphomas derived from gammadelta-T or NK cells. *Nat Commun*. 6:6025.

Kurreck, J., E. Wyszko, C. Gillen, and V.A. Erdmann. 2002. Design of antisense oligonucleotides stabilized by locked nucleic acids. *Nucleic Acids Res*. 30:1911-1918.

Kwok, G., T.C. Yau, J.W. Chiu, E. Tse, and Y.L. Kwong. 2016. Pembrolizumab (Keytruda). *Hum Vaccin Immunother*. 12:2777-2789.

Kwong, Y.L., T.S.Y. Chan, D. Tan, S.J. Kim, L.M. Poon, B. Mow, P.L. Khong, F. Loong, R. Au-Yeung, J. Iqbal, C. Phipps, and E. Tse. 2017. PD1 blockade with pembrolizumab is highly effective in relapsed or refractory NK/T-cell lymphoma failing l-asparaginase. *Blood*. 129:2437-2442.

Kwong, Y.L., and P.L. Khong. 2011. Central palatal perforation in nasal natural killer cell lymphoma. *Br J Haematol*. 152:2.

Lai, J., P. Xu, X. Jiang, S. Zhou, and A. Liu. 2017. Successful treatment with anti-programmed-death-1 antibody in a relapsed natural killer/T-cell lymphoma patient with multi-line resistance: a case report. *BMC Cancer*. 17:507.

Lai, M.C., W.C. Chang, S.Y. Shieh, and W.Y. Tarn. 2010. DDX3 regulates cell growth through translational control of cyclin E1. *Mol Cell Biol*. 30:5444-5453.

Lai, M.C., Y.H. Lee, and W.Y. Tarn. 2008. The DEAD-box RNA helicase DDX3 associates with export messenger ribonucleoproteins as well as tip-associated protein and participates in translational control. *Mol Biol Cell*. 19:3847-3858.

Landau, D.A., E. Tausch, A.N. Taylor-Weiner, C. Stewart, J.G. Reiter, J. Bahlo, S. Kluth, I. Bozic, M. Lawrence, S. Bottcher, S.L. Carter, K. Cibulskis, D. Mertens, C.L. Sougnez, M. Rosenberg, J.M. Hess, J. Edelmann, S. Kless, M. Kneba, M. Ritgen, A. Fink, K. Fischer, S. Gabriel, E.S. Lander, M.A. Nowak, H. Dohner, M. Hallek, D. Neuberg, G. Getz, S. Stilgenbauer, and C.J. Wu. 2015. Mutations driving CLL and their evolution in progression and relapse. *Nature*. 526:525-530.

Lee, H., A. Herrmann, J.H. Deng, M. Kujawski, G. Niu, Z. Li, S. Forman, R. Jove, D.M. Pardoll, and H. Yu. 2009. Persistently activated Stat3 maintains constitutive NF-kappaB activity in tumors. *Cancer Cell*. 15:283-293.

Lee, H., A.J. Jeong, and S.K. Ye. 2019. Highlighted STAT3 as a potential drug target for cancer therapy. *BMB Rep*. 52:415-423.

Leuchte, K., M. Schlaak, R. Stadler, S. Theurich, and M. von Bergwelt-Baildon. 2017. Innovative Treatment Concepts for Cutaneous T-Cell Lymphoma Based on Microenvironment Modulation. *Oncology Research and Treatment*. 40:262-269.

Li, H., B. Handsaker, A. Wysoker, T. Fennell, J. Ruan, N. Homer, G. Marth, G. Abecasis, R. Durbin, and S. Genome Project Data Processing. 2009. The Sequence Alignment/Map format and SAMtools. *Bioinformatics*. 25:2078-2079.

Li, H.K., R.T. Mai, H.D. Huang, C.H. Chou, Y.A. Chang, Y.W. Chang, L.R. You, C.M. Chen, and Y.H. Lee. 2016. DDX3 Represses Stemness by Epigenetically Modulating Tumor-suppressive miRNAs in Hepatocellular Carcinoma. *Sci Rep*. 6:28637.

Liang, F., C. Ren, J. Wang, S. Wang, L. Yang, X. Han, Y. Chen, G. Tong, and G. Yang. 2019. The crosstalk between STAT3 and p53/RAS signaling controls cancer cell metastasis and cisplatin resistance via the Slug/MAPK/PI3K/AKT-mediated regulation of EMT and autophagy. *Oncogenesis*. 8:59.

Liang, X.H., H. Sun, J.G. Nichols, and S.T. Crooke. 2017. RNase H1-Dependent Antisense Oligonucleotides Are Robustly Active in Directing RNA Cleavage in Both the Cytoplasm and the Nucleus. *Mol Ther*. 25:2075-2092.

Liao, Y., G.K. Smyth, and W. Shi. 2013. The Subread aligner: fast, accurate and scalable read mapping by seed-and-vote. *Nucleic Acids Res*. 41:e108.

Lichtman, M.A. 2008. Battling the hematological malignancies: the 200 years' war. *Oncologist*. 13:126-138.

Lim, C.P., and X. Cao. 2006. Structure, function, and regulation of STAT proteins. *Mol Biosyst*. 2:536-550.

Lim, J.P., and P.A. Gleeson. 2011. Macropinocytosis: an endocytic pathway for internalising large gulps. *Immunol Cell Biol*. 89:836-843.

Lim, J.P., J.T. Wang, M.C. Kerr, R.D. Teasdale, and P.A. Gleeson. 2008. A role for SNX5 in the regulation of macropinocytosis. *BMC Cell Biol*. 9:58.

Lindemann, R.K., A. Newbold, K.F. Whitecross, L.A. Cluse, A.J. Frew, L. Ellis, S. Williams, A.P. Wiegmans, A.E. Dear, C.L. Scott, M. Pellegrini, A. Wei, V.M. Richon, P.A. Marks, S.W. Lowe, M.J. Smyth, and R.W. Johnstone. 2007. Analysis of the apoptotic and therapeutic activities of histone deacetylase inhibitors by using a mouse model of B cell lymphoma. *Proc Natl Acad Sci U S A*. 104:8071-8076.

Liu, Y., J. Huang, W. Li, Y. Chen, X. Liu, and J. Wang. 2018. Meta-analysis of STAT3 and phospho-STAT3 expression and survival of patients with breast cancer. *Oncotarget*. 9:13060-13067.

Love, M.I., W. Huber, and S. Anders. 2014. Moderated estimation of fold change and dispersion for RNA-seq data with DESeq2. *Genome Biol*. 15:550.

Makita, S., and K. Tobinai. 2017. Mogamulizumab for the treatment of T-cell lymphoma. *Expert Opin Biol Ther*. 17:1145-1153.

Mann, B.S., J.R. Johnson, M.H. Cohen, R. Justice, and R. Pazdur. 2007. FDA approval summary: vorinostat for treatment of advanced primary cutaneous T-cell lymphoma. *Oncologist*. 12:1247-1252.

Mansoori, B., A. Mohammadi, S. Davudian, S. Shirjang, and B. Baradaran. 2017. The Different Mechanisms of Cancer Drug Resistance: A Brief Review. *Adv Pharm Bull*. 7:339-348.

Mantei, A., S. Rutz, M. Janke, D. Kirchhoff, U. Jung, V. Patzel, U. Vogel, T. Rudel, I. Andreou, M. Weber, and A. Scheffold. 2008. siRNA stabilization prolongs gene knockdown in primary T lymphocytes. *Eur J Immunol*. 38:2616-2625.

Mareschal, S., S. Dubois, P.J. Viailly, P. Bertrand, E. Bohers, C. Maingonnat, J.P. Jais, B. Tesson, P. Ruminy, P. Peyrouze, C. Copie-Bergman, T. Fest, T. Jo Molina, C. Haioun, G. Salles, H. Tilly, T. Lecroq, K. Leroy, and F. Jardin. 2016. Whole exome sequencing of relapsed/refractory patients expands the repertoire of somatic mutations in diffuse large B-cell lymphoma. *Genes Chromosomes Cancer*. 55:251-267.

Marie, J.P. 2001. Drug resistance in hematologic malignancies. *Curr Opin Oncol*. 13:463-469.

Markham, A. 2017. Copanlisib: First Global Approval. *Drugs*. 77:2057-2062.

Marks, P., R.A. Rifkind, V.M. Richon, R. Breslow, T. Miller, and W.K. Kelly. 2001. Histone deacetylases and cancer: causes and therapies. *Nat Rev Cancer*. 1:194-202.

Mazan-Mamczarz, K., and R.B. Gartenhaus. 2013. Role of microRNA deregulation in the pathogenesis of diffuse large B-cell lymphoma (DLBCL). *Leuk Res*. 37:1420-1428.

Mebratu, Y., and Y. Tesfaigzi. 2009. How ERK1/2 activation controls cell proliferation and cell death: Is subcellular localization the answer? *Cell Cycle*. 8:1168-1175.

Merz, C., H. Urlaub, C.L. Will, and R. Luhrmann. 2007. Protein composition of human mRNPs spliced in vitro and differential requirements for mRNP protein recruitment. *RNA*. 13:116-128.

Mi, H., A. Muruganujan, D. Ebert, X. Huang, and P.D. Thomas. 2019. PANTHER version 14: more genomes, a new PANTHER GO-slim and improvements in enrichment analysis tools. *Nucleic Acids Res*. 47:D419-D426.

Mondejar, R., C. Perez, A. Onaindia, N. Martinez, J. Gonzalez-Rincon, H. Pisonero, J.P. Vaque, L. Cereceda, M. Santibanez, M. Sanchez-Beato, and M.A. Piris. 2017. Molecular basis of targeted therapy in T/NK-cell lymphoma/leukemia: A comprehensive genomic and immunohistochemical analysis of a panel of 33 cell lines. *PLoS One*. 12:e0177524.

Mondello, P., S. Cuzzocrea, M. Navarra, and M. Mian. 2016. 90 Y-ibritumomab tiuxetan: a nearly forgotten opportunityr. *Oncotarget*. 7:7597-7609.

Moreton, P., and P. Hillmen. 2003. Alemtuzumab therapy in B-cell lymphoproliferative disorders. *Semin Oncol*. 30:493-501.

Morin, R.D., S. Assouline, M. Alcaide, A. Mohajeri, R.L. Johnston, L. Chong, J. Grewal, S. Yu, D. Fornika, K. Bushell, T.H. Nielsen, T. Petrogiannis-Haliotis, M. Crump, A. Tosikyan, B.M. Grande, D. MacDonald, C. Rousseau, M. Bayat, P. Sesques, R. Froment, M. Albuquerque, Y. Monczak, K.K. Oros, C. Greenwood, Y. Riazalhosseini, M. Arseneault, E. Camlioglu, A. Constantin, Q. Pan-Hammarstrom, R. Peng, K.K. Mann, and N.A. Johnson. 2016. Genetic Landscapes of Relapsed and Refractory Diffuse Large B-Cell Lymphomas. *Clin Cancer Res*. 22:2290-2300.

Mottok, A., S.S. Hung, E.A. Chavez, B. Woolcock, A. Telenius, L.C. Chong, B. Meissner, H. Nakamura, C. Rushton, E. Vigano, C. Sarkozy, R.D. Gascoyne, J.M. Connors, S. Ben-Neriah, A. Mungall, M.A. Marra, R. Siebert, D.W. Scott, K.J. Savage, and C. Steidl. 2019. Integrative genomic analysis identifies key pathogenic mechanisms in primary mediastinal large B-cell lymphoma. *Blood*. 134:802-813.

Niepel, M., M. Hafner, M. Chung, and P.K. Sorger. 2017. Measuring Cancer Drug Sensitivity and Resistance in Cultured Cells. *Curr Protoc Chem Biol*. 9:55-74.

Noone, A.M., K.A. Cronin, S.F. Altekruse, N. Howlader, D.R. Lewis, V.I. Petkov, and L. Penberthy. 2017. Cancer Incidence and Survival Trends by Subtype Using Data from the Surveillance Epidemiology and End Results Program, 1992-2013. *Cancer Epidemiol Biomarkers Prev*. 26:632-641.

Nowakowski, G.S., and M.S. Czuczman. 2015. ABC, GCB, and Double-Hit Diffuse Large B-Cell Lymphoma: Does Subtype Make a Difference in Therapy Selection? *Am Soc Clin Oncol Educ Book*:e449-457.

Ohgami, R.S., L. Ma, A. Monabati, J.L. Zehnder, and D.A. Arber. 2014. STAT3 mutations are present in aggressive B-cell lymphomas including a subset of diffuse large B-cell lymphomas with CD30 expression. *Haematologica*. 99:e105-107.

Ojha, J., C.R. Secreto, K.G. Rabe, D.L. Van Dyke, K.M. Kortum, S.L. Slager, T.D. Shanafelt, R. Fonseca, N.E. Kay, and E. Braggio. 2015. Identification of recurrent truncated DDX3X mutations in chronic lymphocytic leukaemia. *Br J Haematol*. 169:445-448.

Ok, C.Y., Z.Y. Xu-Monette, A. Tzankov, D.P. O'Malley, S. Montes-Moreno, C. Visco, M.B. Moller, K. Dybkaer, A. Orazi, Y. Zu, G. Bhagat, K.L. Richards, E.D. Hsi, J. Han van Krieken, M. Ponzoni, J.P. Farnen, M.A. Piris, J.N. Winter, L.J. Medeiros, and K.H. Young. 2014. Prevalence and clinical implications of cyclin D1 expression in diffuse large B-cell lymphoma (DLBCL) treated with immunochemotherapy: a report from the International DLBCL Rituximab-CHOP Consortium Program. *Cancer*. 120:1818-1829.

Olsen, E.A., Y.H. Kim, T.M. Kuzel, T.R. Pacheco, F.M. Foss, S. Parker, S.R. Frankel, C. Chen, J.L. Ricker, J.M. Arduino, and M. Duvic. 2007. Phase IIb multicenter trial of vorinostat in patients with persistent, progressive, or treatment refractory cutaneous T-cell lymphoma. *J Clin Oncol*. 25:3109-3115.

Pangault, C., P. Ame-Thomas, P. Ruminy, D. Rossille, G. Caron, M. Baia, J. De Vos, M. Roussel, C. Monvoisin, T. Lamy, H. Tilly, P. Gaulard, K. Tarte, and T. Fest. 2010. Follicular lymphoma cell niche: identification of a preeminent IL-4-dependent T(FH)-B cell axis. *Leukemia*. 24:2080-2089.

Peart, M.J., K.M. Tainton, A.A. Ruefli, A.E. Dear, K.A. Sedelies, L.A. O'Reilly, N.J. Waterhouse, J.A. Trapani, and R.W. Johnstone. 2003. Novel mechanisms of apoptosis induced by histone deacetylase inhibitors. *Cancer Res*. 63:4460-4471.

Peer, D., P. Zhu, C.V. Carman, J. Lieberman, and M. Shimaoka. 2007. Selective gene silencing in activated leukocytes by targeting siRNAs to the integrin lymphocyte function-associated antigen-1. *Proceedings of the National Academy of Sciences of the United States of America*. 104:4095-4100.

Pfreundschuh, M., L. Trumper, A. Osterborg, R. Pettengell, M. Trneny, K. Imrie, D. Ma, D. Gill, J. Walewski, P.L. Zinzani, R. Stahel, S. Kvaloy, O. Shpilberg, U. Jaeger, M. Hansen, T. Lehtinen, A. Lopez-Guillermo, C. Corrado, A. Scheliga, N. Milpied, M. Mendila, M. Rashford, E. Kuhnt, M. Loeffler, and G. MabThera International Trial. 2006. CHOP-like chemotherapy plus rituximab versus CHOP-like chemotherapy alone in young patients with good-prognosis diffuse large-B-cell lymphoma: a randomised controlled trial by the MabThera International Trial (MInT) Group. *Lancet Oncol*. 7:379-391.

Piekarz, R.L., R. Frye, H.M. Prince, M.H. Kirschbaum, J. Zain, S.L. Allen, E.S. Jaffe, A. Ling, M. Turner, C.J. Peer, W.D. Figg, S.M. Steinberg, S. Smith, D. Joske, I. Lewis, L. Hutchins, M. Craig, A.T. Fojo, J.J. Wright, and S.E. Bates. 2011. Phase 2 trial of romidepsin in patients with peripheral T-cell lymphoma. *Blood*. 117:5827-5834.

Piekarz, R.L., R. Frye, M. Turner, J.J. Wright, S.L. Allen, M.H. Kirschbaum, J. Zain, H.M. Prince, J.P. Leonard, L.J. Geskin, C. Reeder, D. Joske, W.D. Figg, E.R. Gardner, S.M. Steinberg, E.S. Jaffe, M. Stetler-Stevenson, S. Lade, A.T. Fojo, and S.E. Bates. 2009. Phase II multi-institutional trial of the histone deacetylase inhibitor romidepsin as monotherapy for patients with cutaneous T-cell lymphoma. *J Clin Oncol*. 27:5410-5417.

Piekarz, R.L., R.W. Robey, Z. Zhan, G. Kayastha, A. Sayah, A.H. Abdeldaim, S. Torrico, and S.E. Bates. 2004. T-cell lymphoma as a model for the use of histone deacetylase inhibitors in cancer therapy: impact of depsipeptide on molecular markers, therapeutic targets, and mechanisms of resistance. *Blood*. 103:4636-4643.

Plimack, E.R., P.M. Lorusso, P. McCoon, W. Tang, A.D. Krebs, G. Curt, and S.G. Eckhardt. 2013. AZD1480: a phase I study of a novel JAK2 inhibitor in solid tumors. *Oncologist*. 18:819-820.

Pugh, T.J., S.D. Weeraratne, T.C. Archer, D.A. Pomeranz Krummel, D. Auclair, J. Bochicchio, M.O. Carneiro, S.L. Carter, K. Cibulskis, R.L. Erlich, H. Greulich, M.S. Lawrence, N.J. Lennon, A. McKenna, J. Meldrim, A.H. Ramos, M.G. Ross, C. Russ, E. Shefler, A. Sivachenko, B. Sogoloff, P. Stojanov, P. Tamayo, J.P. Mesirov, V. Amani, N. Teider, S. Sengupta, J.P. Francois, P.A. Northcott, M.D. Taylor, F. Yu, G.R. Crabtree, A.G. Kautzman, S.B. Gabriel, G. Getz, N. Jager, D.T. Jones, P. Lichter, S.M. Pfister, T.M. Roberts, M. Meyerson, S.L. Pomeroy, and Y.J. Cho. 2012. Medulloblastoma exome sequencing uncovers subtype-specific somatic mutations. *Nature*. 488:106-110.

Qin, B.B., D.F. Tang, M.L. Ni, W. Gao, and M.Z. Zhang. 2019a. The aberrant activation of Wnt pathway caused by beta-catenin mutation and its prognostic significance in NK/T-cell lymphoma. *Neoplasma*. 66:20-27.

Qin, J.J., L. Yan, J. Zhang, and W.D. Zhang. 2019b. STAT3 as a potential therapeutic target in triple negative breast cancer: a systematic review. *J Exp Clin Cancer Res*. 38:195.

Quesada, V., L. Conde, N. Villamor, G.R. Ordonez, P. Jares, L. Bassaganyas, A.J. Ramsay, S. Bea, M. Pinyol, A. Martinez-Trillos, M. Lopez-Guerra, D. Colomer, A. Navarro, T. Baumann, M. Aymerich, M. Rozman, J. Delgado, E. Gine, J.M. Hernandez, M. Gonzalez-Diaz, D.A. Puente, G. Velasco, J.M. Freije, J.M. Tubio, R. Royo, J.L. Gelpi, M. Orozco, D.G. Pisano, J. Zamora, M. Vazquez, A. Valencia, H. Himmelbauer, M. Bayes, S. Heath, M. Gut, I. Gut, X. Estivill, A. Lopez-Guillermo, X.S. Puente, E. Campo, and C. Lopez-Otin. 2011. Exome sequencing identifies recurrent mutations of the splicing factor SF3B1 gene in chronic lymphocytic leukemia. *Nat Genet*. 44:47-52.

Ramanathan, S., F. Jin, S. Sharma, and B.P. Kearney. 2016. Clinical Pharmacokinetic and Pharmacodynamic Profile of Idelalisib. *Clin Pharmacokinet*. 55:33-45.

Rawal, S., F. Chu, M. Zhang, H.J. Park, D. Nattamai, S. Kannan, R. Sharma, D. Delgado, T. Chou, H.Y. Lin, V. Baladandayuthapani, A. Luong, F. Vega, N. Fowler, C. Dong, R.E. Davis, and S.S. Neelapu. 2013. Cross talk between follicular Th cells and tumor cells in human follicular lymphoma promotes immune evasion in the tumor microenvironment. *J Immunol*. 190:6681-6693.

Reddy, A., J. Zhang, N.S. Davis, A.B. Moffitt, C.L. Love, A. Waldrop, S. Leppa, A. Pasanen, L. Meriranta, M.L. Karjalainen-Lindsberg, P. Norgaard, M. Pedersen, A.O. Gang, E. Hogdall, T.B. Heavican, W. Lone, J. Iqbal, Q. Qin, G. Li, S.Y. Kim, J. Healy, K.L. Richards, Y. Fedoriw, L. Bernal-Mizrachi, J.L. Koff, A.D. Staton, C.R. Flowers, O. Paltiel, N. Goldschmidt, M. Calaminici, A. Clear, J. Gribben, E. Nguyen, M.B. Czader, S.L. Ondrejka, A. Collie, E.D. Hsi, E. Tse, R.K.H. Au-Yeung, Y.L. Kwong, G. Srivastava, W.W.L. Choi, A.M. Evens, M. Pilichowska, M. Sengar, N. Reddy, S. Li, A. Chadburn, L.I. Gordon, E.S. Jaffe, S. Levy, R. Rempel, T. Tzeng, L.E. Happ, T. Dave, D. Rajagopalan, J. Datta, D.B. Dunson, and S.S. Dave. 2017. Genetic and Functional Drivers of Diffuse Large B Cell Lymphoma. *Cell*. 171:481-494 e415.

Reyes-Reyes, E.M., Y. Teng, and P.J. Bates. 2010. A new paradigm for aptamer therapeutic AS1411 action: uptake by macropinocytosis and its stimulation by a nucleolin-dependent mechanism. *Cancer Res*. 70:8617-8629.

Rezvani, A.R., and D.G. Maloney. 2011. Rituximab resistance. *Best Pract Res Clin Haematol*. 24:203-216.

Richter, J., M. Schlesner, S. Hoffmann, M. Kreuz, E. Leich, B. Burkhardt, M. Rosolowski, O. Ammerpohl, R. Wagener, S.H. Bernhart, D. Lenze, M. Szczepanowski, M. Paulsen, S. Lipinski, R.B. Russell, S. Adam-Klages, G. Apic, A. Claviez, D. Hasenclever, V. Hovestadt, N. Hornig, J.O. Korbel, D. Kube, D. Langenberger, C. Lawerenz, J. Lisfeld, K. Meyer, S. Picelli, J. Pischimarov, B. Radlwimmer, T. Rausch, M. Rohde, M. Schilhabel, R. Scholtysik, R. Spang, H. Trautmann, T. Zenz, A. Borkhardt, H.G. Drexler, P. Moller, R.A. MacLeod, C. Pott, S. Schreiber, L. Trumper, M. Loeffler, P.F. Stadler, P. Lichter, R. Eils, R. Kuppers, M. Hummel, W. Klapper, P. Rosenstiel, A. Rosenwald, B. Brors, R. Siebert, and I.M.-S. Project. 2012. Recurrent mutation of the ID3 gene in Burkitt lymphoma identified by integrated genome, exome and transcriptome sequencing. *Nat Genet*. 44:1316-1320.

Riva, V., and G. Maga. 2019. From the magic bullet to the magic target: exploiting the diverse roles of DDX3X in viral infections and tumorigenesis. *Future Medicinal Chemistry*. 11:1357-1381.

Robey, R.W., A.R. Chakraborty, A. Basseville, V. Luchenko, J. Bahr, Z. Zhan, and S.E. Bates. 2011. Histone deacetylase inhibitors: emerging mechanisms of resistance. *Mol Pharm*. 8:2021-2031.

Robey, R.W., K.M. Pluchino, M.D. Hall, A.T. Fojo, S.E. Bates, and M.M. Gottesman. 2018. Revisiting the role of ABC transporters in multidrug-resistant cancer. *Nature Reviews Cancer*. 18:452-464.

Robey, R.W., Z. Zhan, R.L. Piekarz, G.L. Kayastha, T. Fojo, and S.E. Bates. 2006. Increased MDR1 expression in normal and malignant peripheral blood mononuclear cells obtained from patients receiving depsipeptide (FR901228, FK228, NSC630176). *Clin Cancer Res*. 12:1547-1555.

Robinson, G., M. Parker, T.A. Kranenburg, C. Lu, X. Chen, L. Ding, T.N. Phoenix, E. Hedlund, L. Wei, X. Zhu, N. Chalhoub, S.J. Baker, R. Huether, R. Kriwacki, N. Curley, R. Thiruvenkatam, J. Wang, G. Wu, M. Rusch, X. Hong, J. Becksfort, P. Gupta, J. Ma, J. Easton, B. Vadodaria, A. Onar-Thomas, T. Lin, S. Li, S. Pounds, S. Paugh, D. Zhao, D. Kawauchi, M.F. Roussel, D. Finkelstein, D.W. Ellison, C.C. Lau, E. Bouffet, T. Hassall, S. Gururangan, R. Cohn, R.S. Fulton, L.L. Fulton, D.J. Dooling, K. Ochoa, A. Gajjar, E.R. Mardis, R.K. Wilson, J.R.

Downing, J. Zhang, and R.J. Gilbertson. 2012. Novel mutations target distinct subgroups of medulloblastoma. *Nature*. 488:43-48.

Rosenwald, A., G. Wright, A. Wiestner, W.C. Chan, J.M. Connors, E. Campo, R.D. Gascoyne, T.M. Grogan, H.K. Muller-Hermelink, E.B. Smeland, M. Chiorazzi, J.M. Giltnane, E.M. Hurt, H. Zhao, L. Averett, S. Henrickson, L. Yang, J. Powell, W.H. Wilson, E.S. Jaffe, R. Simon, R.D. Klausner, E. Montserrat, F. Bosch, T.C. Greiner, D.D. Weisenburger, W.G. Sanger, B.J. Dave, J.C. Lynch, J. Vose, J.O. Armitage, R.I. Fisher, T.P. Miller, M. LeBlanc, G. Ott, S. Kvaloy, H. Holte, J. Delabie, and L.M. Staudt. 2003. The proliferation gene expression signature is a quantitative integrator of oncogenic events that predicts survival in mantle cell lymphoma. *Cancer Cell*. 3:185-197.

Salas, S., C. Jiguet-Jiglaire, L. Campion, C. Bartoli, F. Frassineti, J.L. Deville, A. Maues De Paula, F. Forest, P. Jezequel, J.C. Gentet, and C. Bouvier. 2014. Correlation between ERK1 and STAT3 expression and chemoresistance in patients with conventional osteosarcoma. *BMC Cancer*. 14:606.

Sardini, A., G.M. Mintenig, M.A. Valverde, F.V. Sepulveda, D.R. Gill, S.C. Hyde, C.F. Higgins, and P.A. McNaughton. 1994. Drug efflux mediated by the human multidrug resistance P-glycoprotein is inhibited by cell swelling. *J Cell Sci*. 107 (Pt 12):3281-3290.

Schmitz, R., G.W. Wright, D.W. Huang, C.A. Johnson, J.D. Phelan, J.Q. Wang, S. Roulland, M. Kasbekar, R.M. Young, A.L. Shaffer, D.J. Hodson, W. Xiao, X. Yu, Y. Yang, H. Zhao, W. Xu, X. Liu, B. Zhou, W. Du, W.C. Chan, E.S. Jaffe, R.D. Gascoyne, J.M. Connors, E. Campo, A. Lopez-Guillermo, A. Rosenwald, G. Ott, J. Delabie, L.M. Rimsza, K. Tay Kuang Wei, A.D. Zelenetz, J.P. Leonard, N.L. Bartlett, B. Tran, J. Shetty, Y. Zhao, D.R. Soppet, S. Pittaluga, W.H. Wilson, and L.M. Staudt. 2018. Genetics and Pathogenesis of Diffuse Large B-Cell Lymphoma. *N Engl J Med*. 378:1396-1407.

Schmitz, R., R.M. Young, M. Ceribelli, S. Jhavar, W. Xiao, M. Zhang, G. Wright, A.L. Shaffer, D.J. Hodson, E. Buras, X. Liu, J. Powell, Y. Yang, W. Xu, H. Zhao, H. Kohlhammer, A. Rosenwald, P. Kluin, H.K. Muller-Hermelink, G. Ott, R.D. Gascoyne, J.M. Connors, L.M. Rimsza, E. Campo, E.S. Jaffe, J. Delabie, E.B. Smeland, M.D. Ogwang, S.J. Reynolds, R.I. Fisher, R.M. Braziel, R.R. Tubbs, J.R. Cook, D.D. Weisenburger, W.C. Chan, S. Pittaluga, W. Wilson, T.A. Waldmann, M. Rowe, S.M. Mbulaiteye, A.B. Rickinson, and L.M. Staudt. 2012. Burkitt lymphoma pathogenesis and therapeutic targets from structural and functional genomics. *Nature*. 490:116-120.

Schroder, M. 2010. Human DEAD-box protein 3 has multiple functions in gene regulation and cell cycle control and is a prime target for viral manipulation. *Biochem Pharmacol*. 79:297-306.

Schust, J., B. Sperl, A. Hollis, T.U. Mayer, and T. Berg. 2006. Stattic: a small-molecule inhibitor of STAT3 activation and dimerization. *Chem Biol*. 13:1235-1242.

Sehn, L.H. 2010. A decade of R-CHOP. *Blood*. 116:2000-2001.

Sen, M., S.M. Thomas, S. Kim, J.I. Yeh, R.L. Ferris, J.T. Johnson, U. Duvvuri, J. Lee, N. Sahu, S. Joyce, M.L. Freilino, H. Shi, C. Li, D. Ly, S. Rapireddy, J.P. Etter, P.K. Li, L. Wang, S. Chiosea, R.R. Seethala, W.E. Gooding, X. Chen, N. Kaminski, K. Pandit, D.E. Johnson, and J.R. Grandis. 2012. First-in-human trial of a STAT3 decoy oligonucleotide in head and neck tumors: implications for cancer therapy. *Cancer Discov*. 2:694-705.

Sharom, F.J. 2008. ABC multidrug transporters: structure, function and role in chemoresistance. *Pharmacogenomics*. 9:105-127.

Siegel, R.L., K.D. Miller, and A. Jemal. 2019. Cancer statistics, 2019. *CA Cancer J Clin*. 69:7-34.

Snijders Blok, L., E. Madsen, J. Juusola, C. Gilissen, D. Baralle, M.R. Reijnders, H. Venselaar, C. Helsmoortel, M.T. Cho, A. Hoischen, L.E. Vissers, T.S. Koemans,

W. Wissink-Lindhout, E.E. Eichler, C. Romano, H. Van Esch, C. Stumpel, M. Vreeburg, E. Smeets, K. Oberndorff, B.W. van Bon, M. Shaw, J. Gecz, E. Haan, M. Bienek, C. Jensen, B.L. Loeys, A. Van Dijck, A.M. Innes, H. Racher, S. Vermeer, N. Di Donato, A. Rump, K. Tatton-Brown, M.J. Parker, A. Henderson, S.A. Lynch, A. Fryer, A. Ross, P. Vasudevan, U. Kini, R. Newbury-Ecob, K. Chandler, A. Male, D.D.D. Study, S. Dijkstra, J. Schieving, J. Giltay, K.L. van Gassen, J. Schuurs-Hoeijmakers, P.L. Tan, I. Pediaditakis, S.A. Haas, K. Retterer, P. Reed, K.G. Monaghan, E. Haverfield, M. Natowicz, A. Myers, M.C. Kruer, Q. Stein, K.A. Strauss, K.W. Brigatti, K. Keating, B.K. Burton, K.H. Kim, J. Charrow, J. Norman, A. Foster-Barber, A.D. Kline, A. Kimball, E. Zackai, M. Harr, J. Fox, J. McLaughlin, K. Lindstrom, K.M. Haude, K. van Roozendaal, H. Brunner, W.K. Chung, R.F. Kooy, R. Pfundt, V. Kalscheuer, S.G. Mehta, N. Katsanis, and T. Kleefstra. 2015. Mutations in DDX3X Are a Common Cause of Unexplained Intellectual Disability with Gender-Specific Effects on Wnt Signaling. *Am J Hum Genet*. 97:343-352.

Soifer, H.S., T. Koch, J. Lai, B. Hansen, A. Hoeg, H. Oerum, and C.A. Stein. 2012. Silencing of gene expression by gymnotic delivery of antisense oligonucleotides. *Methods Mol Biol*. 815:333-346.

Song, J.I., and J.R. Grandis. 2000. STAT signaling in head and neck cancer. *Oncogene*. 19:2489-2495.

Song, T.L., M.L. Nairismagi, Y. Laurensia, J.Q. Lim, J. Tan, Z.M. Li, W.L. Pang, A. Kizhakeyil, G.C. Wijaya, D.C. Huang, S. Nagarajan, B.K. Chia, D. Cheah, Y.H. Liu, F. Zhang, H.L. Rao, T. Tang, E.K. Wong, J.X. Bei, J. Iqbal, N.F. Grigoropoulos, S.B. Ng, W.J. Chng, B.T. Teh, S.Y. Tan, N.K. Verma, H. Fan, S.T. Lim, and C.K. Ong. 2018. Oncogenic activation of the STAT3 pathway drives PD-L1 expression in natural killer/T-cell lymphoma. *Blood*. 132:1146-1158.

Soto-Rifo, R., and T. Ohlmann. 2013. The role of the DEAD-box RNA helicase DDX3 in mRNA metabolism. *Wiley Interdiscip Rev RNA*. 4:369-385.

Soulat, D., T. Burckstummer, S. Westermayer, A. Goncalves, A. Bauch, A. Stefanovic, O. Hantschel, K.L. Bennett, T. Decker, and G. Superti-Furga. 2008. The DEAD-box helicase DDX3X is a critical component of the TANK-binding kinase 1-dependent innate immune response. *EMBO J*. 27:2135-2146.

Soundararajan, S., L. Wang, V. Sridharan, W. Chen, N. Courtenay-Luck, D. Jones, E.K. Spicer, and D.J. Fernandes. 2009. Plasma membrane nucleolin is a receptor for the anticancer aptamer AS1411 in MV4-11 leukemia cells. *Mol Pharmacol*. 76:984-991.

Stivala, S., T. Codilupi, S. Brkic, A. Baerenwaldt, N. Ghosh, H. Hao-Shen, S. Dirnhofer, M.S. Dettmer, C. Simillion, B.A. Kaufmann, S. Chiu, M. Keller, M. Kleppe, M. Hilpert, A.S. Buser, J.R. Passweg, T. Radimerski, R.C. Skoda, R.L. Levine, and S.C. Meyer. 2019. Targeting compensatory MEK/ERK activation increases JAK inhibitor efficacy in myeloproliferative neoplasms. *J Clin Invest*. 130:1596-1611.

Su, C.Y., T.C. Lin, Y.F. Lin, M.H. Chen, C.H. Lee, H.Y. Wang, Y.C. Lee, Y.P. Liu, C.L. Chen, and M. Hsiao. 2015. DDX3 as a strongest prognosis marker and its downregulation promotes metastasis in colorectal cancer. *Oncotarget*. 6:18602-18612.

Sun, M., L. Song, Y. Li, T. Zhou, and R.S. Jope. 2008. Identification of an antiapoptotic protein complex at death receptors. *Cell Death Differ*. 15:1887-1900.

Sun, M., T. Zhou, E. Jonasch, and R.S. Jope. 2013. DDX3 regulates DNA damage-induced apoptosis and p53 stabilization. *Biochim Biophys Acta*. 1833:1489-1497.

Suzuki, R., J. Suzumiya, M. Yamaguchi, S. Nakamura, J. Kameoka, H. Kojima, M. Abe, T. Kinoshita, T. Yoshino, K. Iwatsuki, Y. Kagami, T. Tsuzuki, M. Kurokawa, K. Ito, K. Kawa, K. Oshimi, and N.K.-c.T.S. Group. 2010. Prognostic factors for

mature natural killer (NK) cell neoplasms: aggressive NK cell leukemia and extranodal NK cell lymphoma, nasal type. *Ann Oncol*. 21:1032-1040.

Swerdlow, S.H., E. Campo, S.A. Pileri, N.L. Harris, H. Stein, R. Siebert, R. Advani, M. Ghielmini, G.A. Salles, A.D. Zelenetz, and E.S. Jaffe. 2016. The 2016 revision of the World Health Organization classification of lymphoid neoplasms. *Blood*. 127:2375-2390.

Takahashi, K., B. Hu, F. Wang, Y. Yan, E. Kim, C. Vitale, K.P. Patel, P. Strati, C. Gumbs, L. Little, S. Tippen, X. Song, J. Zhang, N. Jain, P. Thompson, G. Garcia-Manero, H. Kantarjian, Z. Estrov, K.A. Do, M. Keating, J.A. Burger, W.G. Wierda, P.A. Futreal, and A. Ferrajoli. 2018. Clinical implications of cancer gene mutations in patients with chronic lymphocytic leukemia treated with lenalidomide. *Blood*. 131:1820-1832.

Takata, K., M.E. Hong, P. Sitthinamsuwan, F. Loong, S.Y. Tan, J.Y. Liau, P.P. Hsieh, S.B. Ng, S.F. Yang, T. Pongpruttipan, S. Sukpanichnant, Y.L. Kwong, Y. Hyeh Ko, Y.T. Cho, W.J. Chng, T. Matsushita, T. Yoshino, and S.S. Chuang. 2015. Primary cutaneous NK/T-cell lymphoma, nasal type and CD56-positive peripheral T-cell lymphoma: a cellular lineage and clinicopathologic study of 60 patients from Asia. *Am J Surg Pathol*. 39:1-12.

Tawara, K., H. Scott, J. Emathinger, A. Ide, R. Fox, D. Greiner, D. LaJoie, D. Hedeen, M. Nandakumar, A.J. Oler, R. Holzer, and C. Jorcyk. 2019. Co-Expression of VEGF and IL-6 Family Cytokines is Associated with Decreased Survival in HER2 Negative Breast Cancer Patients: Subtype-Specific IL-6 Family Cytokine-Mediated VEGF Secretion. *Transl Oncol*. 12:245-255.

Thode, C., A. Woetmann, H.H. Wandall, M.C. Carlsson, K. Qvortrup, C.S. Kauczok, M. Wobser, A. Printzlau, N. Odum, and S. Dabelsteen. 2015. Malignant T cells secrete galectins and induce epidermal hyperproliferation and disorganized stratification in a skin model of cutaneous T-cell lymphoma. *J Invest Dermatol*. 135:238-246.

Tse, E., and Y.L. Kwong. 2016. Diagnosis and management of extranodal NK/T cell lymphoma nasal type. *Expert Rev Hematol*. 9:861-871.

Tse, E., and Y.L. Kwong. 2017. The diagnosis and management of NK/T-cell lymphomas. *J Hematol Oncol*. 10:85.

Tseng, S.Y., M. Otsuji, K. Gorski, X. Huang, J.E. Slansky, S.I. Pai, A. Shalabi, T. Shin, D.M. Pardoll, and H. Tsuchiya. 2001. B7-DC, a new dendritic cell molecule with potent costimulatory properties for T cells. *J Exp Med*. 193:839-846.

Tsujimoto, Y. 1998. Role of Bcl-2 family proteins in apoptosis: apoptosomes or mitochondria? *Genes Cells*. 3:697-707.

Turkson, J., J.S. Kim, S. Zhang, J. Yuan, M. Huang, M. Glenn, E. Haura, S. Sebti, A.D. Hamilton, and R. Jove. 2004. Novel peptidomimetic inhibitors of signal transducer and activator of transcription 3 dimerization and biological activity. *Mol Cancer Ther*. 3:261-269.

Uhlmann, E. 2000. Recent advances in the medicinal chemistry of antisense oligonucleotides. *Curr Opin Drug Discov Devel*. 3:203-213.

Ungerstedt, J.S., Y. Sowa, W.S. Xu, Y. Shao, M. Dokmanovic, G. Perez, L. Ngo, A. Holmgren, X. Jiang, and P.A. Marks. 2005. Role of thioredoxin in the response of normal and transformed cells to histone deacetylase inhibitors. *Proc Natl Acad Sci U S A*. 102:673-678.

Urban, E., and C.R. Noe. 2003. Structural modifications of antisense oligonucleotides. *Farmaco*. 58:243-258.

Vasan, N., J. Baselga, and D.M. Hyman. 2019. A view on drug resistance in cancer. *Nature*. 575:299-309.

Vega, M.I., M. Martinez-Paniagua, A.R. Jazirehi, S. Huerta-Yepez, K. Umezawa, O. Martinez-Maza, and B. Bonavida. 2008. The NF-kappaB inhibitors (bortezomib

and DHMEQ) sensitise rituximab-resistant AIDS-B-non-Hodgkin lymphoma to apoptosis by various chemotherapeutic drugs. *Leuk Lymphoma*. 49:1982-1994.
Verma, N.K., A.M. Davies, A. Long, D. Kelleher, and Y. Volkov. 2010. STAT3 knockdown by siRNA induces apoptosis in human cutaneous T-cell lymphoma line Hut78 via downregulation of Bcl-xL. *Cell Mol Biol Lett*. 15:342-355.
Vonasek, J., P.W. Edslev, F. d'Amore, and H. Hasle. 2019. Brentuximab vedotin monotherapy is an effective treatment in a frail pediatric patient with Down syndrome and classical Hodgkin lymphoma. *Pediatr Blood Cancer*:e28082.
Wake, M.S., and C.J. Watson. 2015. STAT3 the oncogene - still eluding therapy? *FEBS J*. 282:2600-2611.
Wang, H., C. Huang, L. Zhao, H. Zhang, J.M. Yang, P. Luo, B.X. Zhan, Q. Pan, J. Li, and B.L. Wang. 2016a. Histone deacetylase inhibitors regulate P-gp expression in colorectal cancer via transcriptional activation and mRNA stabilization. *Oncotarget*. 7:49848-49858.
Wang, H., L. Wang, P.D. Chi, W.D. Wang, X.Q. Chen, Q.R. Geng, Z.J. Xia, and Y. Lu. 2016b. High level of interleukin-10 in serum predicts poor prognosis in multiple myeloma. *Br J Cancer*. 114:463-468.
Wang, L., X.W. Bi, Y.J. Zhu, Y.Z. He, Q.Y. Lai, Z.J. Xia, and Q.Q. Cai. 2018. IL-2Ralpha up-regulation is mediated by latent membrane protein 1 and promotes lymphomagenesis and chemotherapy resistance in natural killer/T-cell lymphoma. *Cancer Commun (Lond)*. 38:62.
Wang, L., L. Chen, V. Walker, and T.J. Jacob. 1998. Antisense to MDR1 mRNA reduces P-glycoprotein expression, swelling-activated C1- current and volume regulation in bovine ciliary epithelial cells. *J Physiol*. 511 (Pt 1):33-44.
Wang, L., D.Z. Liao, J. Zhang, Z.J. Xia, X.W. Peng, and Y. Lu. 2013. Clinical significance of serum soluble interleukin-2 receptor-alpha in extranodal natural killer/T-cell lymphoma (ENKTL): a predictive biomarker for treatment efficacy and valuable prognostic factor. *Med Oncol*. 30:723.
Wang, S., H. Sun, M. Tanowitz, X.H. Liang, and S.T. Crooke. 2016c. Annexin A2 facilitates endocytic trafficking of antisense oligonucleotides. *Nucleic Acids Res*. 44:7314-7330.
Wang, S.P., W.L. Wang, Y.L. Chang, C.T. Wu, Y.C. Chao, S.H. Kao, A. Yuan, C.W. Lin, S.C. Yang, W.K. Chan, K.C. Li, T.M. Hong, and P.C. Yang. 2009. p53 controls cancer cell invasion by inducing the MDM2-mediated degradation of Slug. *Nat Cell Biol*. 11:694-704.
Watanabe, A., H. Tagawa, J. Yamashita, K. Teshima, M. Nara, K. Iwamoto, M. Kume, Y. Kameoka, N. Takahashi, T. Nakagawa, N. Shimizu, and K. Sawada. 2011. The role of microRNA-150 as a tumor suppressor in malignant lymphoma. *Leukemia*. 25:1324-1334.
Waterfall, J.J., E. Arons, R.L. Walker, M. Pineda, L. Roth, J.K. Killian, O.D. Abaan, S.R. Davis, R.J. Kreitman, and P.S. Meltzer. 2014. High prevalence of MAP2K1 mutations in variant and IGHV4-34-expressing hairy-cell leukemias. *Nat Genet*. 46:8-10.
Whitehead, K.A., J.E. Dahlman, R.S. Langer, and D.G. Anderson. 2011. Silencing or stimulation? siRNA delivery and the immune system. *Annu Rev Chem Biomol Eng*. 2:77-96.
Wilcox, R.A. 2016. Cutaneous T-cell lymphoma: 2016 update on diagnosis, risk-stratification, and management. *Am J Hematol*. 91:151-165.
Willemze, R., L. Cerroni, W. Kempf, E. Berti, F. Facchetti, S.H. Swerdlow, and E.S. Jaffe. 2019. The 2018 update of the WHO-EORTC classification for primary cutaneous lymphomas. *Blood*. 133:1703-1714.
Willemze, R., E.S. Jaffe, G. Burg, L. Cerroni, E. Berti, S.H. Swerdlow, E. Ralfkiaer, S. Chimenti, J.L. Diaz-Perez, L.M. Duncan, F. Grange, N.L. Harris, W. Kempf, H. Kerl, M. Kurrer, R. Knobler, N. Pimpinelli, C. Sander, M. Santucci, W. Sterry,

M.H. Vermeer, J. Wechsler, S. Whittaker, and C.J. Meijer. 2005. WHO-EORTC classification for cutaneous lymphomas. *Blood*. 105:3768-3785.

Wilson, W.H. 2006. Drug resistance in diffuse large B-cell lymphoma. *Semin Hematol*. 43:230-239.

Witthuhn, B.A., O. Silvennoinen, O. Miura, K.S. Lai, C. Cwik, E.T. Liu, and J.N. Ihle. 1994. Involvement of the Jak-3 Janus kinase in signalling by interleukins 2 and 4 in lymphoid and myeloid cells. *Nature*. 370:153-157.

Wong, A.L., R.A. Soo, D.S. Tan, S.C. Lee, J.S. Lim, P.C. Marban, L.R. Kong, Y.J. Lee, L.Z. Wang, W.L. Thuya, R. Soong, M.Q. Yee, T.M. Chin, M.T. Cordero, B.R. Asuncion, B. Pang, S. Pervaiz, J.L. Hirpara, A. Sinha, W.W. Xu, M. Yuasa, T. Tsunoda, M. Motoyama, T. Yamauchi, and B.C. Goh. 2015. Phase I and biomarker study of OPB-51602, a novel signal transducer and activator of transcription (STAT) 3 inhibitor, in patients with refractory solid malignancies. *Ann Oncol*. 26:998-1005.

Wong, A.L.A., J.L. Hirpara, S. Pervaiz, J.-Q. Eu, G. Sethi, and B.-C. Goh. 2017. Do STAT3 inhibitors have potential in the future for cancer therapy? *Expert Opinion on Investigational Drugs*. 26:883-887.

Woollard, W.J., V. Pullabhatla, A. Lorenc, V.M. Patel, R.M. Butler, A. Bayega, N. Begum, F. Bakr, K. Dedhia, J. Fisher, S. Aguilar-Duran, C. Flanagan, A.A. Ghasemi, R.M. Hoffmann, N. Castillo-Mosquera, E.A. Nuttall, A. Paul, C.A. Roberts, E.G. Solomonidis, R. Tarrant, A. Yoxall, C.Z. Beyers, S. Ferreira, I. Tosi, M.A. Simpson, E. de Rinaldis, T.J. Mitchell, and S.J. Whittaker. 2016. Candidate driver genes involved in genome maintenance and DNA repair in Sezary syndrome. *Blood*. 127:3387-3397.

Xavier, C.P., M. Pesic, and M.H. Vasconcelos. 2016. Understanding Cancer Drug Resistance by Developing and Studying Resistant Cell Line Models. *Curr Cancer Drug Targets*. 16:226-237.

Xu, P., X. Liu, J. Ouyang, and B. Chen. 2017. TP53 mutation predicts the poor prognosis of non-Hodgkin lymphomas: Evidence from a meta-analysis. *PLoS One*. 12:e0174809.

Xu, X., M. Sakon, H. Nagano, N. Hiraoka, H. Yamamoto, N. Hayashi, K. Dono, S. Nakamori, K. Umeshita, Y. Ito, N. Matsuura, and M. Monden. 2004. Akt2 expression correlates with prognosis of human hepatocellular carcinoma. *Oncol Rep*. 11:25-32.

Yagi, K., K. Yamamoto, S. Umeda, S. Abe, S. Suzuki, I. Onishi, S. Kirimura, M. Fukayama, A. Arai, M. Kitagawa, and M. Kurata. 2013. Expression of multidrug resistance 1 gene in B-cell lymphomas: association with follicular dendritic cells. *Histopathology*. 62:414-420.

Yamaguchi, M., K. Kita, H. Miwa, K. Nishii, K. Oka, T. Ohno, S. Shirakawa, and M. Fukumoto. 1995. Frequent expression of P-glycoprotein/MDR1 by nasal T-cell lymphoma cells. *Cancer*. 76:2351-2356.

Yang, L., S. Lin, L. Xu, J. Lin, C. Zhao, and X. Huang. 2019. Novel activators and small-molecule inhibitors of STAT3 in cancer. *Cytokine Growth Factor Rev*. 49:10-22.

Yin, J., Z. Ma, N. Selliah, D.K. Shivers, R.Q. Cron, and T.H. Finkel. 2006. Effective gene suppression using small interfering RNA in hard-to-transfect human T cells. *Journal of immunological methods*. 312:1-11.

Yong, W., W. Zheng, J. Zhu, Y. Zhang, X. Wang, Y. Xie, N. Lin, B. Xu, A. Lu, and J. Li. 2009. L-asparaginase in the treatment of refractory and relapsed extranodal NK/T-cell lymphoma, nasal type. *Ann Hematol*. 88:647-652.

Yu, H., and R. Jove. 2004. The STATs of cancer--new molecular targets come of age. *Nat Rev Cancer*. 4:97-105.

Zhang, H.F., and R. Lai. 2014. STAT3 in Cancer-Friend or Foe? *Cancers (Basel)*. 6:1408-1440.

Zhang, J., K. McCastlain, H. Yoshihara, B. Xu, Y. Chang, M.L. Churchman, G. Wu, Y. Li, L. Wei, I. Iacobucci, Y. Liu, C. Qu, J. Wen, M. Edmonson, D. Payne-Turner, K.B. Kaufmann, S.I. Takayanagi, E. Wienholds, E. Waanders, P. Ntziachristos, S. Bakogianni, J. Wang, I. Aifantis, K.G. Roberts, J. Ma, G. Song, J. Easton, H.L. Mulder, X. Chen, S. Newman, X. Ma, M. Rusch, P. Gupta, K. Boggs, B. Vadodaria, J. Dalton, Y. Liu, M.L. Valentine, L. Ding, C. Lu, R.S. Fulton, L. Fulton, Y. Tabib, K. Ochoa, M. Devidas, D. Pei, C. Cheng, J. Yang, W.E. Evans, M.V. Relling, C.H. Pui, S. Jeha, R.C. Harvey, I.L. Chen, C.L. Willman, G. Marcucci, C.D. Bloomfield, J. Kohlschmidt, K. Mrozek, E. Paietta, M.S. Tallman, W. Stock, M.C. Foster, J. Racevskis, J.M. Rowe, S. Luger, S.M. Kornblau, S.A. Shurtleff, S.C. Raimondi, E.R. Mardis, R.K. Wilson, J.E. Dick, S.P. Hunger, M.L. Loh, J.R. Downing, C.G. Mullighan, and P. St. Jude Children's Research Hospital-Washington University Pediatric Cancer Genome. 2016. Deregulation of DUX4 and ERG in acute lymphoblastic leukemia. *Nat Genet*. 48:1481-1489.

Zhang, Q., S. Wang, J. Chen, and Z. Yu. 2019. Histone Deacetylases (HDACs) Guided Novel Therapies for T-cell lymphomas. *Int J Med Sci*. 16:424-442.

Zhao, L., Y. Mao, Y. Zhao, and Y. He. 2016. DDX3X promotes the biogenesis of a subset of miRNAs and the potential roles they played in cancer development. *Sci Rep*. 6:32739.

Zhao, S., D. Wu, P. Wu, Z. Wang, and J. Huang. 2015. Serum IL-10 Predicts Worse Outcome in Cancer Patients: A Meta-Analysis. *PLoS One*. 10:e0139598.

Zhou, P., A.E. Blain, A.M. Newman, M. Zaka, G. Chagaluka, F.R. Adlar, U.T. Offor, C. Broadbent, L. Chaytor, A. Whitehead, A. Hall, H. O'Connor, S. Van Noorden, I. Lampert, S. Bailey, E. Molyneux, C.M. Bacon, S. Bomken, and V. Rand. 2019. Sporadic and endemic Burkitt lymphoma have frequent FOXO1 mutations but distinct hotspots in the AKT recognition motif. *Blood Adv*. 3:2118-2127.

Zhu, F., K.B. Wang, and L. Rui. 2019. STAT3 Activation and Oncogenesis in Lymphoma. *Cancers (Basel)*. 12.

Zimmermann, T.S., A.C. Lee, A. Akinc, B. Bramlage, D. Bumcrot, M.N. Fedoruk, J. Harborth, J.A. Heyes, L.B. Jeffs, M. John, A.D. Judge, K. Lam, K. McClintock, L.V. Nechev, L.R. Palmer, T. Racie, I. Rohl, S. Seiffert, S. Shanmugam, V. Sood, J. Soutschek, I. Toudjarska, A.J. Wheat, E. Yaworski, W. Zedalis, V. Koteliansky, M. Manoharan, H.P. Vornlocher, and I. MacLachlan. 2006. RNAi-mediated gene silencing in non-human primates. *Nature*. 441:111-114.

Zitvogel, L., and G. Kroemer. 2012. Targeting PD-1/PD-L1 interactions for cancer immunotherapy. *Oncoimmunology*. 1:1223-1225.

APPENDICES

Appendix 1

Table A1.1 A list of reagents used in the thesis.

S.N.	Reagents	Sources
1.	Acetone	Merck
2.	Acetonitrile	Sigma-Aldrich, Merck
3.	Acrylamide-bisacrylamide solution, (30%)	Nacalai Tesque
4.	Agarose	Vivantis
5.	Alanine transferase (ALT) assay kit	Abcam
6.	Amaxa 4D nucleofection kits P4 and S3	Lonza
7.	Amiloride	Sigma-Aldrich, Merck
8.	7-Aminoactinomycin D (7-AAD)	Thermo Fisher Scientific
9.	Ammonium bicarbonate	Sigma-Aldrich, Merck
10.	Ammonium persulphate (APS)	Bio-Rad
11.	Alexa Fluor® 488 Annexin V/Dead Cell Apoptosis Kit	ThermoFisher Scientific
12.	Anti-fade mounting medium	Dako, Agilent
13.	Aprotinin	Merck
14.	Aspartate aminotransferase (AST) assay kit	Abcam
15.	BD Matrigel™ basement membrane matrix	BD Bioscience
16.	Bio-Rad protein assay kit	Bio-Rad
17.	Bovine serum albumin (BSA)	Sigma-Aldrich, Merck
18.	Bromophenol blue	Sigma-Aldrich, Merck
19.	CellTiter 96® AQ_{ueous} One Solution cell proliferation assay kit	Promega
20.	Chlorpromazine	Sigma-Aldrich, Merck
21.	Creatine kinase (CK) assay kit	Abcam
22.	Crystal violet	Sigma-Aldrich, Merck
23.	Cytochalasin D	Sigma-Aldrich, Merck

24.	Deoxy nucleotide solution (10 mM)	New England Biolabs
25.	Dihydroethiduim	Sigma-Aldrich, Merck
26.	Dimethyl sulphoxide (DMSO)	Sigma-Aldrich, Merck
27.	Dithiothreitol (DTT)	Sigma-Aldrich, Merck
28.	Doxycycline	Sigma-Aldrich, Merck
29.	Dulbecco's Modified Eagle Medium (DMEM)	Gibco
30.	ECL plus reagent	Amersham GE
31.	Ethanol	Merck
32.	Ethylene diamine tetra acetic acid (EDTA)	Sigma-Aldrich, Merck
33.	Ethylene glycol tetra acetic acid (EGTA)	Sigma-Aldrich, Merck
34.	Fetal bovine serum (FBS)	Gibco
35.	Filipin	Sigma-Aldrich, Merck
36.	Formaldehyde	Sigma-Aldrich, Merck
37.	Formic acid	Sigma-Aldrich, Merck
38.	Gel loading dye 6X	Thermo Fisher Scientific
39.	Glacial acetic acid	Sigma-Aldrich, Merck
40.	Glucose solution (45%)	Sigma-Aldrich, Merck
41.	Glycerol	Sigma-Aldrich, Merck
42.	β-Glycerophosphate	Sigma-Aldrich, Merck
43.	Glycine	Sigma-Aldrich, Merck
44.	HEPES buffer	Sigma-Aldrich, Merck
45.	Hoechst 33342	Sigma-Aldrich, Merck
46.	Human recombinant ICAM-1(rICAM-1)	Sino Biological
47.	Human recombinant Interleukin-2 (IL-2)	Peprotech
48.	Human recombinant Interleukin-4 (IL-4)	Peprotech
49.	Hydrochloric acid (HCL)	Sigma-Aldrich, Merck
50.	Kodak® light sensitive film, carestream	Sigma-Aldrich, Merck

51.	Leupeptin	Sigma-Aldrich, Merck
52.	L-glutamine	Gibco
53.	LNA primers miR150 & U6	Qiagen
54.	Lymphoprep®	Stemcell Technologies
55.	Magnesium chloride ($MgCl_2$)	Sigma-Aldrich, Merck
56.	β-Mercaptoethanol	Sigma-Aldrich, Merck
57.	Methanol	Merck
58.	miRCURY LNA RT Kit	Qiagen
59.	miRCURY LNA SYBR® Green PCR Kits	Qiagen
60.	M-Mulv reverse transcriptase (200 U/µL)	New England Biolabs
61.	*N*,*N*,*N*′,*N*′-Tetramethylethylenediamine (TEMED)	Sigma-Aldrich, Merck
62.	Oligo(dT) primer	Promega
63.	Paraformaldehyde (PFA)	Sigma-Aldrich, Merck
64.	Paraplast X-tra	Sigma-Aldrich, Merck
65.	Penicillin-streptomycin solution (Antibiotics)	Gibco
66.	Phenylmethylsulfonylfluoride (PMSF)	Sigma-Aldrich, Merck
67.	Phosphate buffer 10X	Vivantis
68.	Phytohemagglutinin (PHA)	Thermo Fisher Scientific
69.	Pierce BCA protein assay kit	Thermo Fisher Scientific
70.	Polyvinylidene Flouride PVDF membrane	Bio-Rad
71.	Poly-L lysine	Sigma-Aldrich, Merck
72.	Protein marker spectra broad range	Thermo Fisher Scientific
73.	Puromycin	Sigma-Aldrich, Merck
74.	Rhodamine 123	Sigma-Aldrich, Merck
75.	Rhodamine Phalloidin	Thermo Fisher Scientific
76.	RiboLock RNase inhibitor (40 U/µL)	Thermo Fisher Scientific
77.	RNase free water	

78.	RNase from bovine pancrease	Sigma-Aldrich, Merck
79.	Roswell park memorial institute (RPMI1640)	Gibco
80.	SILAC Protein Quantitation Kit (LysC), RPMI 1640	Thermo Fisher Scientific
81.	siRNAs SMART pool Control Non Specific Dharmacon / Mock siRNA	Thermo Fisher Scientific
82.	siRNAs SMART pool DDX3X Dharmacon	Thermo Fisher Scientific
83.	Sodium bicarbonate	Merck
84.	Sodium chloride (NaCl)	Merck
85.	Soduim Dodecyl Sulphate	Biorad
86.	Sodium fluoride (NaF)	Sigma-Aldrich, Merck
87.	Sodium orthovanadate ($Na_3VO_4 \cdot 2H_2O$)	Gibco
88.	Sodium pyrophosphate ($Na_4P_2O_7$)	Gibco
89.	SYBR green qPCR cocktail (2X)	Primer Design
90.	Tetra methyl ethylene diamine TEMED	Biorad
91.	Tetra methyl rhodamine, methyl ester	Gibco
92.	Tris base	Promega
93.	Triton X-100	Biorad
94.	Tween20	Sigma-Aldrich, Merck
95.	Xylene	Sigma-Aldrich, Merck

Table A1.2 A list of RNAi molecules and their sequences used in the thesis.

S.N.	Targets	Sequence		
GapmeR (5'→3')				
1.	NS	AACACGTCTATACGC		
2.	CG-NAP	ACTAGCCTGTAATTG	GGATGCAATGCTCTTA	
3.	Talin	TTGGCAGTAGGATTGG	CAGAGTGTCAAAGTCA	
4.	CD11a	GATGGTAGTGGCTGAA	ACGTCAATCATTAAAC	
5.	PKCθ	TAGGATGAAACTGGAA	AAGCAGCAGTAGAGTT	
6.	Stathmin	AGGTAATCAATGCAGA	AGGTAATCATTGCAGA	
7.	STAT3	GATCGTCGAAGCATTA	GTGTCACACAGATAAA	AGCACCTTCACCATTA
epAON (5'→3')				
1.	NS	TTGGGTGGGTGGGTGGGTAACACGTCTATACGCTTGGGTGGGTGGGTGGGT		
2.	STAT3 epAON	TTGGGTGGGTGGGTGGGTGTGTCACACAGATAAACGCTTGGGTGGGTGGGTGGGT		
shRNA (5'→3')				
1.	CTL shRNA	CTCTCAACCCTTTAAATCTGATTCAAGAGATCAGATTTAAAGGGTTGAGAG		
2.	DDX3X shRNA#1	GGATCTCGTAGTGATTCAAGATTCAAGAGATCTTGAATCACTACGAGATCC		
3.	DDX3X shRNA#2	GGTAGAATAGTCGAACAAGATTTCAAGAGAATCTTGTTCGACTATTCTACC		

NS, non-specific; CTL, control

Table A1.3 A list of qRT-PCR primers used in the thesis.

S.N.	Gene	**Forward primers** (5'→3')	**Reverse primers** (5'→3')
1.	*ABCB1*	TGATCCGAAATAAGCCCAGG	ACTTCGTTCTCAGGCACATC
2.	*ABCC1*	TGATCCGAAATAAGCCCAGG	ACTTCGTTCTCAGGCACAT

3.	*ABCG2*	AGAACAAGATGGAAGGATCAGTG	CAGGGTCATTCAAGAGTTAGGTC
4.	*ACTB*	AGAGCTACGAGCTGCCTGAC	AGCACTGTGTTGGCGTACAG
5.	*CD11a*	ACCTGGTACATGTGCTTGAC	GACAACTCAGCCACTACCATC
6.	*CG-NAP*	CATCCGACTGACTGAGCTTTTCTTTTG	TTTCCTTTCTATCCCCAACCAC
7.	*c-Myc*	ATTAGGCCGCTCTTACCTTTAC	GTAATCCCAGCACTTTGGGA
8.	*DDX3X*	ATGTGGCAGTGGAAAATGCG	ATATAGCGCCCTTTGCTGGC
10.	*FASLG*	CATAGGTGTCTTCCCATTCCAG	AAAGGAGCTGAGGAAAGTGG
11.	*GAPDH*	TGTAGTTGAGGTCAATGAAGGG	ACATCGCTCAGACACCATG
12.	*IFNG1*	AGTTCCATTATCCGCTACATCTG	GCATCGTTTTGGGTTCTCTTG
13.	*IL-10*	ACCTGCCTAACATGCTTCG	TGTCTGGGTCTTGGTTCTCA
14.	*IL-2*	GCATTTACTGCTGGATTT	GATGTTTCAGTTCTGTGGC
15.	*IL-4*	GAACGTAGGAGGCACTCAATAA	GATAGGGTCTTGTTCTGTCACC
16.	*IL-6*	TTCGGTCCAGTTGCCTCTC	TGGCATTTGTGGTTGGGT CA
17.	*IL-8*	AAGAGAGCTCTGTCTGGACC	GATATTCTCTTGGCCCTT GG
18.	*MMP-9*	CACTGAGGAATGATCTAAGCCC	CGAACTTTGACAGCGACAAG
19.	*Notch-1*	GTGTTCCTGAGTCCCTGTTTAG	CTAAACTGCACTCACAGGCA
20.	*PD-1*	CGGAGAGCTTCGTGCTAAA	CTGTGTTCTCTGTGGACTATGG
21.	*PD-L1*	CCTGCAGGGCATTCCAGAAA	TAGGTCCTTGGGAACCGTGA
22.	*PKCθ*	TACTTTGGCGATTCCTCTGG	CCTACCTTCTGCAATCACTG
23.	*STAT3*	TTCTGGGCACAAACACAAAA	TCAGTCACAATCAGGGAAGC
24.	*STMN*	TTCAAGACCTCAGATTCATGG	AGCCCTCGGTCAAAAGAATC
25.	*VIM*	GGAAAGTTTGGAAGAGGCAG	CGTGAATACCAAGACCTGCTC

Table A1.4 A list of antibodies.

S.N.	Antibodies	Source
1.	Anti-rabbit IgG, HRP-linked #7074	Cell Signalling Technology
2.	Anti-α-Tubulin−FITC antibody, Mouse monoclonal	Sigma-Aldrich, Merck

3.	Goat anti-Mouse IgG (H+L), Superclonal™ Recombinant Secondary Antibody, Alexa Fluor 647	Thermo Fisher Scientific
4.	Goat anti-Rabbit IgG (H+L), Superclonal™ Recombinant Secondary Antibody, Alexa Fluor 647	Thermo Fisher Scientific
5.	Goat polyclonal anti-mouse IgG# P044701	Dako, Agilent
6.	Goat anti-human IgG Fc	Thermo Fisher Scientific
7.	Anti-human Fc-specific IgG	Sigma-Aldrich, Merck
8.	Mouse monoclonal anti-BID #8762	Cell Signalling Technology
9.	Mouse monoclonal anti-CD11a #clone MEM83	Monosan
10.	Mouse monoclonal anti-CG-NAP/AKAP Clone 7/AKAP450	BD Bioscience
11.	Mouse monoclonal anti-GAPDH #C87727	Millipore
12.	Mouse monoclonal anti-PKCθ #SC-1680	Santa Cruz
13.	Normal Rabbit IgG #2729	Cell Signalling Technology
14.	Rabbit monoclonal anti- β-actin #8457	Cell Signalling Technology
15.	Rabbit monoclonal anti-BCL-2 #15071	Cell Signalling Technology
16.	Rabbit monoclonal anti-BIM #2933	Cell Signalling Technology
17.	Rabbit monoclonal anti-caspase-3 #9662	Cell Signalling Technology
18.	Rabbit monoclonal anti-cleaved PARP #5625	Cell Signalling Technology
19.	Rabbit monoclonal anti-DDX3X	Nicholas Grigoropoulous Lab
20.	Rabbit monoclonal anti-DDX3X #A300-474A	Bethyl Laboratories
21.	Rabbit monoclonal anti-EZH2 #5246	Cell Signalling Technology
22.	Rabbit monoclonal anti-GAPDH #5174	Cell Signalling Technology
23.	Rabbit monoclonal anti-MAPK #9102	Cell Signalling Technology
24.	Rabbit monoclonal anti-phospho-MAPK (T202/Y204) #4370	Cell Signalling Technology
25.	Rabbit monoclonal anti-MDR #13342	Cell Signalling Technology
26.	Rabbit monoclonal anti-mTOR #2983	Cell Signalling Technology
27.	Rabbit monoclonal anti-phospho-mTOR (S2448)	Cell Signalling Technology

	#5536	
28.	Rabbit monoclonal anti-STAT3 #12640	Cell Signalling Technology
29.	Rabbit monoclonal anti-phospho-STAT3 (Tyr705) #9145	Cell Signalling Technology
30.	Rabbit monoclonal anti-phospho-STAT3 (Ser727) #9134	Cell Signalling Technology
31.	Rabbit monoclonal anti-talin #4021	Cell Signalling Technology
32.	Rabbit monoclonal anti-phospho-talin (S425) #13589	Cell Signalling Technology
33.	Rabbit monoclonal anti-stathmin #13655	Cell Signalling Technology
34.	Rabbit monoclonal anti-survivin #2808	Cell Signalling Technology
35.	Rabbit monoclonal cleaved anti-caspase-3 #9664	Cell Signalling Technology
36.	Rabbit polyclonal anti-mouse HRP #P0260	Dako, Agilent

Table A1.5 A list of ELISA kits used in the thesis.

S.N.	Target	Manufacturer
1	IFNγ	Human IFNγ Uncoated ELISA kit Invitrogen # ESS0002
2	IgG1	Mouse IgG1 ELISA Kit (ab133045)
2	IL-2	Human IL-2 Uncoated ELISA kit Invitrogen (88-7025)
3	IL-4	Human IL-10 Elisa Ready –Set-Go eBioscience (88-7044)
4	IL-6	Human IL-6 Elisa Ready –Set-Go eBioscience (88-8863)
5	IL-10	Human IL-4 Elisa Ready –Set-Go eBioscience (88-7106)

Addresses of the manufacturers listed above:

Abcam, Discovery Drive Cambridge Biomedical Campus, Cambridge CB2 0AX, UK

Agilent, Santa Clara, California, USA

Bethyl Laboratories, 25043 FM 1097, Montgomery, TX 77356, USA

BD Bioscience, 30 Tuas Ave 2, Singapore

Bio-Rad, 27 International Business Park, Singapore

Cell signalling Technology, Danvers, Massachusetts, USA

Monosan, frontstraat 2c, 5405 pb uden, Netherlands

Peprotech, Rocky Hill, NJ, USA

Promega, 2800 Woods Hollow Road, Madison, WI, USA

Santa Cruz, 10410 Finnell St, Dallas, Texas, USA

Sigma-Alrich, Merck, Darmstadt, Germany

Sino biological, 1400 Liberty Ridge Drive, Suite 101, Wayne, USA

STEMCELL Technologies, Vancouver, Canada

ThermoFisher Scientific, Waltham, Massachusetts, USA

Qiagen, 8 Commonwealth Ln, Singapore

Table A1.6 A list of equipment used in this thesis.

S.N.	Equipment	Manufacturers	Locations
1	Confocal Microscope	Zeiss	Experimental Medicine Building, Level 7, NTU
2	LSR Fortessa	BD Bioscience	Experimental Medicine Building, Level 7, NTU
2	High Content Screening Microscope - IN Cell 2200	GE healthcare	Experimental Medicine Building, Level 7, NTU
3	Microplate Cytation Reader	Biotek	Experimental Medicine Building, Level 4, NTU
4	ASP6025 - Automated Vacuum Tissue Processor	Leica	Experimental Medicine Building, Level 7, NTU
5	Leica EG1150 Modular Tissue Embedding Center	Leica	Experimental Medicine Building, Level 7, NTU
	Leica RM2255 Fully Automated Rotary Microtome	Leica	Experimental Medicine Building, Level 7, NTU
7	X-Ray Developer	SMITECH Asia	Experimental Medicine Building, Level 7, NTU
8	ChemiDoc	BioRad	Experimental Medicine Building, Level 4, NTU
9	StepOnePlus™ Real Time System	Thermofisher Scientific	Experimental Medicine Building, Level 4, NTU
10	Veriti Thermal Cycler	Thermofisher Scientific	Experimental Medicine Building, Level 4, NTU

Appendix 2

Table A2.1 Complete cell culture medium - RPMI

S.N.	Components	Volume
1.	RPMI1640	500 mL
2.	Heat inactivated fetal bovine serum (FBS)	50 mL
3.	Sodium pyruvate solution (100 mM)	5 mL
4.	Penicillin-Streptomycin solution	5 mL

Table A2.2 Complete cell culture medium – DMEM

S.N.	Components	Volume
1.	DMEM	500 mL
2.	Heat inactivated fetal bovine serum (FBS)	50 mL
3.	Penicillin-Streptomycin solution	5 mL

Table A2.3 Cell cryopreservation medium

S.N.	Components	Volume
1.	RPMI1640 / DMEM	4 mL
2.	Heat inactivated fetal bovine serum (FBS)	5 mL
3.	Dimethylsulfoxide (DMSO)	1 mL

Table A2.4 Cell lysis buffer for protein extraction.

S.N.	Components	Concentration
1.	HEPES (pH 7.4)	50 mM
2.	Sodium chloride	150 mM
3.	Magnesium chloride	1.5 mM
4.	Ethylene glycol-bis(β-aminoethyl ether)-N,N,N′,N′-tetraacetic acid	1 mM
5.	Sodium pyrophosphate	10 mM
6.	Sodium fluoride	50 mM
7.	β-glycerophosphate	50 mM
8.	Sodium othovanadate	1 mM
9.	Triton X-100	1% (v/v)
10.	Phenylmethylsulphonyl	2 mM
11.	Leupeptin	10 μg/mL
12.	Aprotinin	10 μg/mL

N.B. Protease and phosphatase inhibitors are added fresh before cell lysis.

Table A2.5 50X Tris base EDTA buffer for gel electrophoresis.

S.N.	Components	Amount
1.	Tris Base	242 gm
2.	Ethylene diamine tetra acetic acid (EDTA)	18.61 gm
3.	Glacial Acetic acid	57.1 ml

Add the Tris base and EDTA to approximately to 700 ml distilled H2O and stir until the Tris base and EDTA are dissolved. Add the acetic acid and adjust the volume to 1 L. The final concentration of TAE solution is 40 mM Tris, 20 mM Acetate and 1mM EDTA and typically has a pH around 8.6 (do not adjust).

Table A2.6 Composition of cDNA master mix.

S.N.	Components	Volume
1.	RNase-free water	2 µL
2.	10 X Reaction buffer	2 µL
3.	Deoxy nucleotide solution (10 mM)	2 µL
4.	RNase inhibitor (40 U/µL)	0.5 µL
5.	M-Mulv reverse transcriptase (200 U/µL)	1 µL
	Total	7.5 µL

Table A2.7 Composition of SYBR qRT-PCR master mix.

S.N.	Components	Volume
1.	Gene specific primer (10 µM)	0.2 µL
2.	2X SYBR green qPCR cocktail	10 µL
3.	RNase-free water	7.4 µL
4.	ROX (high)	0.4 µL
	Total	18 µL

Table A2.8 Composition of miRCURY reverse transcription.

S.N.	Components	Volume
1.	5X miRCURY RT reaction buffer	2 µL
2.	RNase-free water	4.5 µL
3.	10X miRCURY RT Mix	1 µL
4.	Synthetic RNA spike	0.5 µL
5.	Template	2µL
Total		10 µL

Table A2.9 Composition of miRCURY LNA miRNA PCR assay

S.N.	Components	Volume
1.	5X miRCURY SYBR green mastermix	5 µL
2.	RNase-free water	1 µL
3.	ROX reference dye	0.5 µL
4.	PCR primer mix	1 µL
5.	cDNA template	3 µL
Total		10 µL

Table A2.10 Resolving gel solution for SDS-PAGE

S.N.	Component of gel	7%	8%	10 %	12 %
1.	Distilled water	10.03 mL	9.37 mL	3.4 mL	2.7 mL
2.	1.5 M Tris-HCl; pH 8.8	4 mL	4 mL	4 mL	4 mL
3.	10 % w/v SDS	80 µL	80 µL	80 µL	80 µL
4.	10 % w/v APS	80 µL	80 µL	80 µL	80 µL
5.	TEMED	8 µL	8 µL	8 µL	8 µL
6.	Acrylamide-bisacrylamide solution, (30%)	4.67 mL	5.33 mL	2.7 mL	3.4 mL
7.	**Total**	8 mL	8 mL	8 mL	8 mL

Table A2.11 Stacking gel solution for SDS-PAGE

S.N.	Component of gel	4%	5%	6%
1.	Distilled water	3.6 mL	3.4 mL	3.2 mL
2.	1.5 M Tris-HCl; pH 8.8	0.630mL	0.630 mL	0.630mL
3.	10 % w/v SDS	50 µL	50 µL	50 µL

4.	10 % w/v APS	50 µL	50 µL	50 µL
5.	TEMED	5 µL	5 µL	5 µL
6.	Acrylamide-bisacrylamide solution, (30%)	0.67 mL	0.85 mL	1 mL
7.	**Total**	5 mL	5 mL	5 mL

Table A2.12 Laemmli sample buffer (5X SDS-PAGE loading buffer)

S.N.	Components	Concentration
1.	Tris-HCl (pH 6.8)	0.312 M
2.	Sodium Dodecyl Sulphate	10 % w/v
3.	ß-Mercaptoethanol	25 % v/v
4.	Bromophenol blue	0.05 % w/v

Table A2.13 SDS-PAGE running buffer (10X)

S.N.	Components	Weight
1.	Tris base	30 g
2.	Glycine	142 g
3.	Sodium Dodecyl Sulphate	10 g

Dissolve in deionised water to a final volume of 1 L. Dilute 1:10 in deionised water before use.

Table A2.14 Western blot semi-dry transfer buffer

S.N.	Components	Amount
1.	Tris base	5.8 g
2.	Glycine	29 g

Dissolve in deionised water to 800 mL and then add 200 mL methanol was added to a final volume of 1L.

Table A2.15 Components of Western blot stripping buffer

S.N.	Components	Concentration
1.	Sodium Dodecyl Sulphate	2% (w/v)
2.	Tris-HCl (pH 6.8)	50 mM
3.	ß-Mercaptoethanol	100 mM

Table A2.16 Preparation of glutamate standards

S.N	Glutamate Standard (µL)	Assay Buffer (µL)	Final volume standard in well (µL)	Glutamate concentration (nmol/well)
1.	0	50	50	0
2.	2	40	50	2
3.	4	46	50	4
4.	6	44	50	6
5.	8	42	50	8
6.	10	40	50	10 nmol/well

Table A2.17 Components of AST reaction mix

S.N.	Component	Colorimetric reaction mix (µL)
1.	AST assay Buffer	80
2.	Developer	8
3.	AST Enzyme Mix	2
4.	AST substrate	10

Table A2.18 Preparation of NADH standards.

S.N	NADH standard (µL)	Assay buffer (µL)	Final volume standard in well (µL)	NADH concentration (nmol/well)
1.	0	150	50	0
2.	6	144	50	2
3.	12	138	50	4
4.	18	132	50	6
5.	24	126	50	8
6.	30	120	50	10

Table A2.19 Components of CK reaction mix.

S.N.	Component	Reaction mix (µL)	Background reaction mix (µL)
1.	CK assay Buffer	34	36
2.	CK Enzyme mix	2	0
3.	CK Developer	2	2
4.	ATP	2	2
5.	CK substrate	10	10

Table A2.20 Preparation of pyruvate standards

S.N	Pyruvate standard (µL)	Assay buffer (µL)	Final volume standard in well (µL)	Pyruvate concentration in well
1.	0	60	20	0
2.	6	54	20	2
3.	12	48	20	4
4.	18	42	20	6
6.	24	36	20	8
7.	30	30	20	10

Table A2.21 Components of AST reaction mix.

S.N.	Component	Colorimetric reaction mix (µL)
1.	AST assay Buffer	80
2.	Developer	8
3.	AST Enzyme Mix	2
4.	AST substrate	10

Appendix 3

List of Publications, Presentations and Awards

A. Publications

1. **Kizhakeyil A**, Fazil MHUT, Ong ST, Chalasani ML, Low JH, Kottaisamy A, Praseetha P, Verma NK (2019), Isolation of human peripheral T cell lymphocytes, ***Methods Mol Biol*** 1930:11-18. *(Copy enclosed)*
2. Fazil MHUT, Ong ST, Chalasani MLS, Low JH, **Kizhakeyil A**, Mamidi A, Carey FHL, Lakshminarayanan R, Kelleher D, Verma NK (2016), GapmeR cellular internalization by macropinocytosis induces sequence-specific gene silencing in human primary T-cells, ***Sci Rep*** 6:37721. *(Copy enclosed).*
3. Fazil MHUT, Ong ST, Chalasani MLS, **Kizhakeyil A**, Verma NK (2019), GapmeR-mediated gene silencing in motile T-cells. ***Methods Mol Biol*** 1930:67-73. *(Copy enclosed).*
4. **Kizhakeyil A**, Verma NK (2019), Quantitative real time PCR for transcriptional changes in T-lymphocytes. ***Methods Mol Biol*** 1930:59-68. *(Copy enclosed).*
5. Song TL, Nairismägi ML, Laurensia Y, Lim JQ, Tan J, Li ZM, Pang WL, **Kizhakeyil A**, Wijaya GC, Huang DC, Nagarajan S, Chia BK, Cheah D, Liu YH, Zhang F, Rao HL, Tang T, Wong EK, Bei JX, Iqbal J, Grigoropoulos NF, Ng SB, Chng WJ, Teh BT, Tan SY, Verma NK, Fan H, Lim ST, Ong CK (2018), Oncogenic activation of the STAT3 pathway drives PD-L1 expression in natural killer/T-cell lymphoma, ***Blood*** 132 (11):1146-1158. *(Copy enclosed).*
6. Verma NK, Sadeer A, **Kizhakeyil A**, Pang JH, Chiu QYA, Tay S W, Kumar P, Pullarkat SA (2018), Screening of ferrocenyl–phosphines identifies a gold-coordinated derivative as a novel anticancer agent for hematological malignancies, ***RSC Adv*** 8:28960-28968.
7. Ong ST, Chalasani MLS , Fazil MHUT, Prasannan P, **Kizhakeyil A**, Wright GD, Kelleher D, Verma NK (2018), Centrosome- and Golgi-localized protein kinase N-associated protein serves as a docking platform for protein kinase a signaling and microtubule nucleation in migrating T-cells, ***Front Immunol*** 9:397.

8. Liow SS, Dou Q, Kai D, Sugiarto S, Chris YYY , Ryan TKK, Chen X, Wu YL, Ong ST , **Kizhakeyil A**, Verma NK, Tang BZ, Loh XJ (2017), Long-term fluorescent real-time *in vivo* monitoring of drug release by AIE thermogelling polymer, ***Small*** 13:1603404.

9. Verma NK, Fazil MHUT, Ong ST, Chalasani ML, Low JH, Kottaiswamy A, Praseetha P, **Kizhakeyil A,** Kumar S, Panda AK, Freeley M, Smith SM, Boehm BO, Kelleher D (2016), LFA-1/ICAM-1 ligation in human T cells promotes Th1 polarization through a GSK3β signalling dependent Notch pathway, ***J Immunol*** 197(1):108-118.

10. Sandeep K K, **Kizhakeyil A**, Raghavendra R, Verma NK, Lakshminarayanan R, T.S. Sampath K, Mukesh D, Seeram R (2019), Drug loaded electrospun polymer/ceramic composite nanofibrous coatings on titanium for implant related infections, ***Ceram Int.*** 2019: 097.

11. Sandeep K K, Merum S, Raghavendra R, **Kizhakeyil A**, Verma NK, Lakshminarayanan R, T.S. Sampath K, Mukesh D, Seeram R (2019), Modulation of biological properties by grain refinement and surface modification on titanium surfaces for implant-related infections, ***J Mater Sci*** (2019) 54: 13265.

12. Verma NK, Palapetta SM, Ong ST, Fazil MHUT, Chalasani MLS, Prasannan P, **Kizhakeyil A**, Kelleher D (2019), A laboratory model to study T-cell motility. ***Methods Mol Biol*** 1930:19-23.

13. **Kizhakeyil A,** Fazil MHUT, Verma NK (2019), Targeted gene silencing in malignant hematolymphoid cells using GapmeR. ***Methods Mol Biol*** (*in press*).

Manuscript in preparation

14. **Kizhakeyil A**, Poh Z, Ng AS, Prasannan P, Tan SH, Kelleher D, Verma NK (2019), Integrated analysis of transcriptomic and proteomic signatures identifies raf-ERK signaling axis as target in vorinostat resistant CTCL.

15. **Kizhakeyil A**, Zaini NBM, Poh Z, Loh X, AS Ng, Low ZS, Prasannan P, Gong Chun, Tan MGK, Nagarajan C, Huang D, Ong CK, Ong ST, Lim ST, Chng WJ, Follows G, Hodson D, Du MQ, Goh YT, Tan SH, Grigoropoulos N F,Verma NK (2019), DDX3X loss is associated with aggressive phenotypes in non-Hodgkin's lymphomas.

B. Presentations

1. **Kizhakeyil A**, Fazil MHUT, Tan SH, Verma NK (2019) STAT3 as a second line therapeutic target in vorinostat resistant CTCL. *Singapore Health and Biomedical Congress*, October 10-12, 2019 (poster presentation).
2. **Kizhakeyil A**, Loh X, Chi ZH, Fazil MHUT, Ong ST, Rajamani L, Grigoropoulos NF, Kelleher D, Tan SH, Verma NK (2017) DDX3X is a key regulator of metastasis in hematolymphoid malignancies. *Singapore Health and Biomedical Congress*, October 12-14, 2017 (poster presentation).
3. Fazil MHUT, Chirumamilla CS, **Kizhakeyil A,** Low JH, Martin D, Ostade XV, Verma NK (2016) Withaferin A inhibits LFA-1-mediated migration of human T-cells by modulating kinome signatures. *Singapore Health and Biomedical Congress*, September 24-26, 2016 (poster presentation).
4. Chalasani MLS, **Kizhakeyil A**, Yeo I, Kumar P, Verma NK, Lakshminarayanan R (2016) Hyper-charged peptides targeting non-Hodgkin's lymphoma and leukemia. *Peptide and Protein Society of Singapore Symposium* Dec 8-9, 2016 (poster presentation).

C. Award

1. Won the **Best Presentation Award** at LKCMedicine Retreat, 2017 (oral presentation).

Appendix 4

Additional Materials and Methods

A4.1 Whole Exome Sequencing (WES) and analysis

Nine patients included in the study had *de novo* R/R-DLBCL. Patients were being treated with curative intent using R-CHOP or a similar regimen and had one of the following: *i*) primary progressive disease, *ii*) partial response to chemotherapy followed by disease progression within two years of diagnosis, or *iii*) disease relapse within 2 years following a complete response. They were identified using the Addenbrooke's Hospital lymphoma database and their fulfilment of inclusion criteria was confirmed by reviewing case records. Patient selection was based solely on tissue availability and verbal telephonic consents were sought from either the patients or their surviving relatives and documented in the hospital notes before retrieving archived materials. The study was approved by the ethics review board of Cambridge University Hospitals NHS Foundation Trust (05/Q1604/10) and conducted in accordance with the Declaration of Helsinki.

Tissue sections (10 μm) prepared from formalin-fixed paraffin-embedded tissue blocks on glass slides were dewaxed using a standard xyelene/ethanol series. Tissue samples were crudely dissected a scalpel and DNA was extracted using the QIAamp DNA micro kit (Qiagen) according to the manufacturer's instructions. DNA concentration was measured using Qubit (Life Technologies) according to the manufacturer's instructions and 2 μg DNA from each sample was used for WES.

Exome libraries were created from template DNA and sequenced at the Wellcome Trust Sanger Institute. DNA was sheared to 100-400 bp on an ultrasonicator (Covaris) and purified with the QIAquick system (Qiagen). Fragmented DNA was end-repaired and re-purified. This was followed by addition of an A-tail and Minelute purification (Qiagen). Adapters were ligated to the DNA fragments with Quick T4 DNA ligase (Agilent) and purified with Ampure magnetic beads (Beckman Coulter). DNA was quantified on a BioAnalyser (Agilent) and specimens with less than 500 ng of librariedsample underwent a further 6 PCR cycles. Libraries were hybridised to biotynilated 120mer cRNA baits designed for exome capture (SureSelect, Agilent). Hybridised DNA was captured using streptavidin magnetic beads, purified, and sequenced on the HiSeq platform (Illumina).

Reads were aligned to the human genome and unmapped reads were dropped from analysis. Taking into account read position, orientation, and base quality, a naïve Bayesian

algorithm (CaVEMan) was used to estimate the posterior likelihood of each possible nucleotide at every position. The Pindel algorithm was used to analyse insertions and deletions. Where matched normal tissue was available, genomic variants were excluded. Where a library was successfully created for a tumour sample but not its matched normal, a normal sample from a different patient was used instead. SNVs were cross-referenced with the dbSNP database but not filtered on this basis. In order to enrich the dataset for high-confidence variants, a called variant was excluded if any of the following filters applied: *i*) Less than 1/3 mutant alleles were ≥25 base quality, *ii*) Coverage was less than 8 and no mutant alleles were found in the first 2/3 of a read, *iii*) More than 3% of mutant alleles that were ≥15 base quality were also found in the matched normal, *iv*) At least 2% of mutant alleles of base quality ≥20 were found in at least 2 unmatched normal samples, *v*) Mutant alleles were all on one direction of a read and only in the second half of the read. Second half of read contains the motif GGC[AT]G in sequenced orientation and the mean base quality of all bases after the motif was <20, *vi*) Mean mapping quality of the mutant allele reads was < 21, *vii*) The variant position falls within a simple repeat using the supplied normal, *viii*) Position falls within a centromeric repeat using the supplied normal, *ix*) Mutant reads were on one strand (permitted proportion on other strand: 4%), and mean mutant base quality was <21, *x*) More than 10% of reads covering the variant's position contained an indel according to mapping, *xi*) More than 80% of reads contain the mutant allele at the same read position, *xii*) The variant falls within a high sequencing depth region using the supplied bed file, *xiii*) The variant position could not be annotated against a transcript using the supplied bed file, *xiv*) The variant position has ≥3 mutant alleles present in at least 1% of unmatched normal samples in the unmatched VCF, *xv*) Coverage is ≥10 on both strands but the mutant allele is only present on one strand, and *xvi*) Tumour to normal sample mutant allele proportion is <0.2.

Silent mutations and those in non-coding regions were excluded. The damaging potential of mutations was assessed using PolyPhen-2 (Polymorphism Phenotyping v2 software), which predicts potential impact of an amino acid substitution based on protein structure and function. The PolyPhen-2 score ranges from 0.0 (tolerated) to 1.0 (deleterious). Variants with scores (0.0 to 0.15), (0.15 to 1.0) and (0.85 to 1.0) were predicted to be benign, probably damaging and possibly damaging respectively. Variants in known cancer genes in the census of the Catalogue of Somatic Mutations in Cancer (COSMIC) which were predicted to be "benign" were also included. Variants in recurrently mutated genes were

cross-referenced with COSMIC to determine if they are novel. Manual pathway analysis was carried out on these variants. High confidence SNVs and indels identified in tumour samples for which the patient's matched normal tissue were sequenced were subjected to gene functional annotation and functional classification clustering analyses using DAVID, with medium classification stringency and Bonferroni and Benjamini corrections.

A4.2 Beta-catenin and p53 staining

The WNT3A-expressing cell line HEK293 STF3A cells were cultured until 70% confluent and the conditioned media was used in a 50-50 mixture with fresh media. Induced U2932 and HBL-1 knockdown and control HEK923TF cells were seeded and cultured in STF3A-conditioned media for 24 h. Cytoplasmic and nuclear fractions were extracted from the cells using NE-PER Nuclear and Cytoplasmic extraction reagents (Thermo Scientific) following the manufacturer's protocol and tested for cytoplasmic and nuclear beta-catenin expression using western blot analyses.

Table A4.1 A list of DEPs altered in $HuT78_{VR}$.

Gene Symbol	Sum PEP Score	Q-value	Unique Peptides	$Log_2(HuT78_{VR}$ / HuT78)	Average $HuT78_{VR}$ / HuT78
MUC1	14.262	0	2	6.64	100
UNC119B	19.435	0	2	6.64	100
TUT1	55.744	0	7	6.64	100
RTN2	15.726	0	2	6.64	100
TPPP	18.115	0	2	6.64	100
CA2	23.903	0	3	6.64	100
ISG15	56.648	0	4	6.64	100
PCCA	38.646	0	8	6.64	100
EPHX1	37.191	0	9	6.64	100
CKB	301.781	0	18	6.64	100
ENO3	123.83	0	6	6.64	100
PTMS	5.676	0.001	2	6.64	100
MAOA	14.399	0	2	6.64	100
AHR	51.136	0	10	6.64	100
NUDT1	36.091	0	5	6.64	100
STXBP1	36.713	0	9	6.64	100
RIPK1	25.1	0	5	6.64	100
NAB2	21.183	0	6	6.64	100
FAM111B	39.514	0	9	6.64	100
KCTD12	36.895	0	7	6.64	100
REEP6	30.43	0	2	6.64	100
RPP25	12.204	0	2	6.64	100
WDR35	43.837	0	5	6.64	100
BLVRB	134.557	0	9	6.10	68.73
ITGA1	36.575	0	8	5.79	55.1655
UBE2T	28.293	0	9	5.76	54.167
EEF1A2	370.597	0	10	5.73	52.942
HEBP1	24.343	0	4	5.72	52.652
SFXN3	53.463	0	6	5.70	52.1465
PLBD2	33.974	0	6	5.70	51.8365
IFT27	22.977	0	3	5.69	51.7555
PRAF2	24.634	0	5	5.69	51.4915
DNAJC10	43.686	0	8	5.68	51.397
FOXK2	26.502	0	5	5.68	51.351
PGPEP1	44.259	0	3	5.68	51.262
FYTTD1	22.056	0	2	5.68	51.209
KDELC1	75.345	0	13	5.68	51.1785
TBPL1	35.218	0	6	5.68	51.174
GCAT	31.896	0	5	5.68	51.168
PXMP2	51.238	0	6	5.68	51.167

ATP6V0A1	32.396	0	6	5.68	51.142
PAFAH1B2	41.978	0	6	5.68	51.1275
CDIPT	57.473	0	5	5.67	51.079
KIFC1	71.149	0	10	5.67	51.047
NCEH1	18.229	0	4	5.67	51.0285
POLR3C	49.078	0	8	5.67	51.021
LGALS1	105.748	0	7	5.29	39.1805
LMNA	316.984	0	11	4.39	20.95
GSN	235.045	0	17	4.25	19.0885
HSPB1	171.164	0	16	4.04	16.488
PLEC	2490.401	0	228	3.45	10.951
SFN	144.396	0	11	3.37	10.332
PLEKHF1	21.978	0	4	3.28	9.7155
CRELD2	28.494	0	3	3.18	9.0675
GAMT	68.136	0	6	3.16	8.9675
FUCA1	93.994	0	9	3.14	8.824
TMEM205	51.523	0	4	3.08	8.44
PECR	88.542	0	11	2.73	6.6405
CKMT1A	68.833	0	9	2.54	5.8325
CPT1A	249.336	0	29	2.49	5.6235
CLGN	109.406	0	12	2.47	5.559
LPCAT3	56.946	0	9	2.43	5.3795
KRT81	35.532	0	5	2.43	5.372
VAT1	101.619	0	12	2.40	5.279
MVP	255.289	0	36	2.39	5.2425
CRYZ	102.885	0	11	2.38	5.2035
MAP1A	103.334	0	17	2.36	5.1385
SNAP29	53.648	0	7	2.21	4.6145
HSDL1	42.616	0	11	2.16	4.4695
CRIP1	6.247	0.001	2	2.15	4.4535
DHRS7	56.122	0	9	2.12	4.3345
LAMP1	37.599	0	5	2.11	4.326
STOM	182.185	0	14	2.06	4.1735
CYB5R1	48.546	0	8	1.97	3.9225
EBP	27.243	0	3	1.95	3.851
SUN2	293.591	0	28	1.94	3.838
MAPK3	186.504	0	12	1.90	3.721
TUBA4A	344.291	0	6	1.84	3.5795
DHCR24	119.716	0	15	1.83	3.546
PACSIN2	90.17	0	12	1.81	3.5145
SLC2A3	44.126	0	5	1.80	3.493
PMVK	86.346	0	11	1.80	3.4815
ZYX	173.45	0	3	1.77	3.415
NQO1	116.507	0	10	1.77	3.403
GANAB	435.771	0	2	1.77	3.4025

ETHE1	77.021	0	5	1.76	3.3825
TMX2	52.708	0	9	1.75	3.365
FAHD1	41.033	0	6	1.75	3.3625
VCL	569.386	0	53	1.71	3.271
C14orf1	34.165	0	5	1.71	3.2705
GALM	65.566	0	8	1.68	3.2125
ATOX1	22.257	0	3	1.67	3.18
LMCD1	66.194	0	11	1.66	3.1545
DGUOK	31.904	0	3	1.66	3.152
JMJD6	38.286	0	4	1.65	3.135
SLC25A1	65.631	0	8	1.64	3.123
SQLE	104.106	0	14	1.63	3.088
GNS	50.002	0	7	1.62	3.084
ARL3	74.813	0	11	1.62	3.065
GIPC1	43.65	0	8	1.60	3.0215
CTSA	65.929	0	7	1.59	3.007
LNPEP	227.471	0	28	1.55	2.9215
ACOT13	47.959	0	5	1.51	2.8385
PRDX5	118.072	0	13	1.50	2.835
AAK1	79.838	0	10	1.50	2.8315
MANBA	40.232	0	7	1.47	2.7685
PARP4	50.942	0	11	1.47	2.7655
FSCN1	107.19	0	16	1.46	2.7515
FLAD1	78.612	0	15	1.45	2.733
PRCP	47.054	0	6	1.45	2.726
NAA40	23.258	0	3	1.44	2.721
HSPB11	74.602	0	4	1.44	2.704
HSD17B10	329.014	0	18	1.43	2.699
FYB	58.317	0	8	1.42	2.6755
MTCH1	69.578	0	8	1.42	2.674
PGM2L1	111.002	0	22	1.42	2.6705
UBXN1	113.367	0	13	1.41	2.6525
ABHD11	54.868	0	9	1.38	2.602
CAMK2D	109.317	0	9	1.37	2.586
MBOAT7	53.487	0	8	1.37	2.5805
SCPEP1	62.543	0	8	1.36	2.569
PPME1	86.496	0	14	1.36	2.563
UBAC2	62.93	0	9	1.35	2.556
RTN3	27.25	0	2	1.35	2.5445
SDF2L1	70.153	0	6	1.33	2.5145
GSTK1	252.436	0	13	1.33	2.508
SEC22B	122.776	0	11	1.32	2.492
PEX3	64.976	0	10	1.32	2.49
PSAP	66	0	9	1.31	2.4835
ITGB1	40.614	0	6	1.30	2.4595

PDP1	45.143	0	8	1.29	2.447
HEXB	78.401	0	12	1.29	2.4385
THEM4	12.976	0	2	1.28	2.434
ARRB1	253.689	0	20	1.28	2.433
AAMDC	19.396	0	4	1.28	2.4215
GLO1	108.589	0	12	1.27	2.4085
MLEC	149.145	0	10	1.26	2.4025
PDPR	98.573	0	15	1.24	2.358
BLVRA	104.563	0	12	1.23	2.3535
NIT1	51.204	0	9	1.23	2.3425
CYB5R3	179.904	0	13	1.22	2.3305
PRKCSH	193.382	0	19	1.21	2.3165
ORMDL3	33.177	0	4	1.21	2.3165
SERPINB6	65.094	0	8	1.20	2.3045
MUT	115.779	0	19	1.20	2.292
ECHS1	177.604	0	14	1.20	2.2915
UBA1	861.872	0	55	1.19	2.2855
APMAP	119.36	0	13	1.18	2.2665
Uncharacterized	19.62	0	3	1.18	2.263
HSPA1B	601.626	0	29	1.17	2.257
CLPTM1	128.221	0	12	1.16	2.2415
TIGAR	71.715	0	9	1.16	2.2315
CDK5	97.296	0	11	1.15	2.2155
PIP4K2A	65.141	0	6	1.15	2.214
ACTN4	904.916	0	42	1.14	2.2095
ALDH6A1	71.96	0	13	1.12	2.1775
NADK2	50.308	0	8	1.12	2.172
HIBADH	138.39	0	11	1.12	2.1695
TUBB4A	494.821	0	3	1.12	2.1665
EMD	40.639	0	6	1.11	2.164
BCS1L	166.293	0	19	1.11	2.163
ACOT8	40.661	0	5	1.10	2.15
PSMB5	94.46	0	11	1.09	2.135
CDS2	71.382	0	7	1.09	2.128
PNP	352.458	0	23	1.09	2.1255
NT5DC3	59.911	0	7	1.09	2.1245
DNAJB6	80.151	0	8	1.07	2.1045
EEF1G	369.528	0	29	1.06	2.088
ARHGAP25	36.682	0	3	1.06	2.079
CDC37	144.451	0	15	1.04	2.0525
SLC25A20	45.12	0	10	1.03	2.049
PBDC1	32.923	0	8	-1.04	0.487
ACAT2	153.812	0	11	-1.05	0.4845
MMAB	60.425	0	6	-1.05	0.482
NME1-NME2	370.402	0	6	-1.09	0.47

PSMD10	98.365	0	8	-1.09	0.4695
HLA-A	132.404	0	6	-1.09	0.469
PPP6R1	176.929	0	18	-1.09	0.4685
ACSL4	186.245	0	24	-1.10	0.4665
NDUFA4	6.337	0.001	2	-1.11	0.463
NAA15	343.426	0	29	-1.12	0.4615
VBP1	127.883	0	9	-1.13	0.4585
IDH3A	111.812	0	11	-1.13	0.4555
GTF2I	355.412	0	42	-1.14	0.453
IAH1	61.108	0	6	-1.14	0.453
C1orf123	29.853	0	5	-1.14	0.4525
MRE11	87.293	0	16	-1.15	0.4515
PFDN4	30.904	0	3	-1.15	0.451
SRP9	16.808	0	4	-1.16	0.448
KDM3B	102.367	0	18	-1.16	0.446
UBE3A	65.958	0	12	-1.18	0.4415
SUB1	97.362	0	8	-1.18	0.441
IDH2	316.647	0	21	-1.18	0.44
THYN1	41.936	0	8	-1.18	0.44
NUBP1	12.127	0	3	-1.19	0.4395
GNAS	83.219	0	12	-1.19	0.438
SCAF4	93.381	0	6	-1.19	0.4375
SEPT6	205.187	0	14	-1.19	0.437
SRP14	42.525	0	5	-1.20	0.436
SEPT1	93.973	0	16	-1.20	0.4355
STK26	69.143	0	8	-1.21	0.433
KIAA0368	309.14	0	35	-1.21	0.4325
UBTF	123.544	0	17	-1.21	0.432
ARHGAP15	110.221	0	14	-1.21	0.431
SH3BGRL	71.481	0	7	-1.22	0.4295
CCDC58	68.034	0	5	-1.22	0.429
COA6	41.535	0	4	-1.22	0.428
CASP3	52.358	0	8	-1.23	0.4275
ABRACL	68.625	0	5	-1.23	0.4275
PRPS1	123.094	0	7	-1.23	0.4255
RAD21	274.048	0	23	-1.24	0.424
PRKRA	64.85	0	7	-1.25	0.421
PAK2	211.316	0	23	-1.25	0.4205
ACLY	531.273	0	50	-1.25	0.42
RCC2	221.542	0	25	-1.25	0.42
NKRF	61.495	0	13	-1.26	0.4185
HCFC1	269.157	0	35	-1.26	0.418
CYP51A1	53.825	0	10	-1.26	0.417
TM9SF3	49.08	0	9	-1.28	0.4125
DDX6	260.527	0	17	-1.29	0.4085

PRPS2	107.544	0	5	-1.29	0.408
WAS	65.625	0	13	-1.30	0.4075
FERMT2	64.003	0	8	-1.30	0.4075
MPI	66.644	0	7	-1.30	0.407
ANP32B	127.876	0	6	-1.30	0.4065
BPTF	184.382	0	31	-1.30	0.406
POLDIP3	74.494	0	10	-1.30	0.405
DDX50	219.086	0	20	-1.33	0.3975
GART	405.694	0	37	-1.33	0.397
GRK2	115.447	0	13	-1.33	0.397
DUT	113.405	0	9	-1.34	0.396
ARHGDIB	253.456	0	11	-1.34	0.3955
HPRT1	110.339	0	14	-1.34	0.395
RIOX2	29.834	0	5	-1.34	0.3945
IDH3G	58.836	0	8	-1.36	0.39
IFITM2	116.828	0	2	-1.36	0.3895
UBE2O	214.073	0	8	-1.37	0.388
NPEPPS	286.995	0	34	-1.37	0.386
DOCK2	409.829	0	57	-1.39	0.3825
FMR1	40.574	0	7	-1.39	0.382
SMARCC1	257.455	0	24	-1.39	0.382
CGGBP1	50.848	0	8	-1.41	0.377
EVL	238.468	0	17	-1.41	0.3755
HMGB3	109.573	0	9	-1.43	0.371
PDCL3	112.557	0	11	-1.43	0.371
TOP2B	753.927	0	60	-1.43	0.3705
PTPN2	74.882	0	11	-1.45	0.3665
CD247	42.316	0	6	-1.46	0.363
STAG2	257.165	0	26	-1.46	0.363
HLA-DRA	118.389	0	7	-1.47	0.361
STT3A	82.988	0	14	-1.47	0.3605
BDH1	84.939	0	11	-1.47	0.36
FABP5	182.351	0	11	-1.49	0.357
MBD3	79.159	0	9	-1.49	0.356
ITGB2	79.379	0	3	-1.50	0.3535
ADA	74.713	0	8	-1.51	0.3505
PSMB10	44.521	0	5	-1.51	0.3505
COASY	62.189	0	14	-1.51	0.35
PTRHD1	40.177	0	6	-1.51	0.35
RAB27A	69.078	0	10	-1.52	0.348
LIG3	134.323	0	20	-1.56	0.339
LYAR	150.447	0	15	-1.57	0.337
CD3G	10.746	0	2	-1.57	0.3365
DOCK8	393.271	0	58	-1.57	0.3365
CHCHD4	71.499	0	6	-1.60	0.331

PTPRC	154.248	0	28	-1.60	0.3305
MSI2	22.413	0	3	-1.60	0.33
EIF3J	54.72	0	8	-1.66	0.316
RAB9A	89.221	0	10	-1.69	0.311
HLA-DRB1	91.566	0	7	-1.71	0.306
S100A4	33.005	0	3	-1.71	0.305
ABT1	34.892	0	4	-1.76	0.295
PGM1	118.971	0	17	-1.76	0.2945
FMNL1	196.257	0	9	-1.79	0.289
ARID1B	75.334	0	15	-1.81	0.2845
TFRC	443.92	0	37	-1.83	0.282
SLC7A1	24.11	0	4	-1.83	0.281
CLASP2	132.476	0	18	-1.85	0.2775
GBP1	126.184	0	15	-1.85	0.2765
PML	89.105	0	18	-1.86	0.276
KMT2C	50.793	0	9	-1.89	0.269
ITGAL	129.704	0	22	-1.91	0.2665
MPP1	45.802	0	6	-1.97	0.255
SCO1	44.008	0	5	-1.98	0.2535
REXO4	24.435	0	3	-1.98	0.2535
CSTB	65.952	0	4	-1.98	0.253
SRPRA	67.57	0	12	-2.00	0.2505
PTPRA	41.57	0	7	-2.02	0.2465
ARHGEF2	250.852	0	23	-2.03	0.2455
VPS13C	184.653	0	29	-2.03	0.245
TXLNG	33.205	0	6	-2.06	0.24
BAP18	149.195	0	13	-2.10	0.234
FAM136A	46.916	0	5	-2.13	0.229
DCPS	93.212	0	11	-2.15	0.225
PARP14	117.645	0	17	-2.16	0.224
RTCA	41.722	0	7	-2.17	0.2215
ALG3	10.216	0	3	-2.18	0.2205
PM20D2	82.635	0	9	-2.25	0.21
CASP6	49.715	0	6	-2.30	0.203
PPIP5K2	69.231	0	5	-2.30	0.2025
METAP2	72.145	0	2	-2.33	0.1985
FERMT3	326.88	0	30	-2.40	0.1895
DTX3L	32.96	0	4	-2.47	0.1805
DOCK11	65.62	0	12	-2.56	0.1695
PYCARD	47.533	0	6	-2.57	0.1685
CREBBP	41.872	0	3	-2.59	0.166
GNPNAT1	36.184	0	7	-2.60	0.1655
TMEM164	6.732	0.001	2	-2.63	0.162
SPAG7	48.069	0	8	-2.74	0.15
FLNA	1396.571	0	109	-2.79	0.1445

SASH3	77.511	0	6	-2.82	0.142
UNC13D	242.969	0	23	-2.82	0.142
KDM4B	58.029	0	10	-2.85	0.139
COX11	29.886	0	3	-2.87	0.1365
FAS	67.783	0	6	-3.04	0.122
DENND1C	27.181	0	4	-3.09	0.1175
THY1	45.222	0	4	-3.10	0.117
FLNB	1429.939	0	109	-3.57	0.084
ADI1	49.146	0	8	-3.59	0.083
CTH	140.521	0	13	-3.69	0.0775
DCTD	78.316	0	8	-4.46	0.0455
ASS1	81.944	0	12	-4.88	0.034
ATP11C	73.495	0	12	-6.64	0.01
HLA-C	64.347	0	3	-6.64	0.01
LIN28B	30.96	0	7	-6.64	0.01
EPCAM	48.986	0	6	-6.64	0.01
IRF5	33.211	0	5	-6.64	0.01
ARHGAP27	29.783	0	5	-6.64	0.01
C12orf75	24.036	0	3	-6.64	0.01
STXBP3	34.121	0	6	-6.64	0.01
BIN1	75.797	0	8	-6.64	0.01
RPP14	13.396	0	3	-6.64	0.01
CSTA	16.173	0	2	-6.64	0.01
CTSH	23.835	0	3	-6.64	0.01
AK4	30.205	0	6	-6.64	0.01
COIL	24.268	0	6	-6.64	0.01
STAT5A	104.81	0	7	-6.64	0.01
BID	72.6	0	9	-6.64	0.01
GBE1	60.403	0	12	-6.64	0.01
APOBR	107.401	0	16	-6.64	0.01
GALNT2	17.947	0	3	-6.64	0.01
TARBP1	69.718	0	9	-6.64	0.01
ATR	56.265	0	9	-6.64	0.01
FLOT2	40.499	0	8	-6.64	0.01
PRPSAP1	63.476	0	7	-6.64	0.01
C9orf64	17.379	0	5	-6.64	0.01
QSOX2	36.372	0	6	-6.64	0.01
TRMT11	24.891	0	4	-6.64	0.01
WAPL	84.219	0	10	-6.64	0.01
CENPV	24.67	0	4	-6.64	0.01
PCGF5	25.707	0	2	-6.64	0.01
TRAPPC6B	11.893	0	3	-6.64	0.01
SLC35F2	24.512	0	3	-6.64	0.01
TMEM192	18.332	0	3	-6.64	0.01
PTPMT1	29.95	0	6	-6.64	0.01

TOPBP1	21.003	0	3	-6.64	0.01
HVCN1	17.807	0	3	-6.64	0.01
THOC3	34.331	0	5	-6.64	0.01
TMEM209	36.961	0	7	-6.64	0.01
PYM1	51.185	0	6	-6.64	0.01
CDK19	19.946	0	2	-6.64	0.01
UPF3B	13.407	0	3	-6.64	0.01
NHEJ1	31.559	0	5	-6.64	0.01
BRD7	27.333	0	5	-6.64	0.01
SIRT5	24.314	0	4	-6.64	0.01
USE1	30.106	0	5	-6.64	0.01
ZC3H7B	43.269	0	6	-6.64	0.01
ZMYND8	38.867	0	4	-6.64	0.01
GIT1	59.126	0	10	-6.64	0.01
UFC1	33.051	0	4	-6.64	0.01
HEBP2	25.368	0	4	-6.64	0.01
	Sum PEP Score: Protein score calculated as the sum of the negative logarithms of the posterior error probability (PEP) values of the connected peptide spectrum matches (PSMs)				

Table A4.2 A list of DDX3X variants in hematological malignancies reported in cBioPortal.

Protein Change	Mutation Type	Protein Change	Mutation Type
R528H	Missense_Mutation	M330K	Missense_Mutation
R534C	Missense_Mutation	M330K	Missense_Mutation
R534H	Missense_Mutation	M330K	Missense_Mutation
R534H	Missense_Mutation	A68V	Missense_Mutation
R534H	Missense_Mutation	R326C	Missense_Mutation
Y525H	Missense_Mutation	R37C	Missense_Mutation
S489*	Nonsense_Mutation	R475H	Missense_Mutation
Q309*	Nonsense_Mutation	R531H	Missense_Mutation
R46*	Nonsense_Mutation	M379I	Missense_Mutation
R46*	Nonsense_Mutation	M379I	Missense_Mutation
D354G	Missense_Mutation	I158V	Missense_Mutation
S24*	Nonsense_Mutation	N194S	Missense_Mutation
X439_splice	Splice_Site	Y200C	Missense_Mutation
X439_splice	Splice_Site	I211T	Missense_Mutation
E169Rfs*52	Frame_Shift_Del	L235P	Missense_Mutation
S456Ffs*40	Frame_Shift_Del	C317Y	Missense_Mutation
I214Tfs*7	Frame_Shift_Del	C317Y	Missense_Mutation
P568Cfs*5	Frame_Shift_Ins	D350G	Missense_Mutation
T369Nfs*14	Frame_Shift_Ins	D350E	Missense_Mutation
X590_splice	Splice_Site	V365D	Missense_Mutation
DDX3X-BCOR fusion	Fusion	I415T	Missense_Mutation
K418Sfs*15	Frame_Shift_Del	F487L	Missense_Mutation
K418Sfs*15	Frame_Shift_Del	F487L	Missense_Mutation
S429Kfs*29	Frame_Shift_Del	R488C	Missense_Mutation
Y53Tfs*168	Frame_Shift_Del	R488C	Missense_Mutation
T411Pfs*9	Frame_Shift_Del	S492G	Missense_Mutation
X342_splice	Splice_Site	A499T	Missense_Mutation
E180*	Nonsense_Mutation	R503G	Missense_Mutation
R263H	Missense_Mutation	F613L	Missense_Mutation
P267S	Missense_Mutation	D347V	Missense_Mutation
R603Q	Missense_Mutation	I507L	Missense_Mutation
R603Q	Missense_Mutation	L495V	Missense_Mutation
R603Q	Missense_Mutation	F487L	Missense_Mutation
R603Q	Missense_Mutation	A322V	Missense_Mutation
R475C	Missense_Mutation	K452E	Missense_Mutation
P568S	Missense_Mutation	D347H	Missense_Mutation
S410F	Missense_Mutation	S228F	Missense_Mutation
S410F	Missense_Mutation	P324Q	Missense_Mutation
S410F	Missense_Mutation	R333G	Missense_Mutation
I415V	Missense_Mutation		

Table A4.3 A list of STAT3 variants identified in exome sequencing of NKTCL and PTCL samples.

Gene.refgene	Ref	Alt	Func.refgene	ExonicFunc.refgene	AAChange.refgene	FATHMN
STAT3	C	T	exonic	missense SNV	R278H	T
STAT3	C	G	exonic	missense SNV	G618R	D
STAT3	T	A	exonic	missense SNV	N647I	D
STAT3	C	T	exonic	missense SNV	.D171N	T
STAT3	C	G	exonic	missense SNV	D427H	D
STAT3	T	C	exonic	missense SNV	H410R	D
STAT3	C	A	exonic	missense SNV	V667L	D
STAT3	C	T	exonic	missense SNV	D566N	D
STAT3	T	G	exonic	missense SNV	S614R	D
STAT3	G	A	exonic	missense SNV	P715L	D
STAT3	C	G	exonic	missense SNV	Q344H	D
STAT3	C	T	exonic	missense SNV	E696K	D
STAT3	C	T	exonic	missense SNV	E616K	D
STAT3	G	C	exonic	missense SNV	S614R	D
STAT3	T	A	exonic	missense SNV	Y640F	D
STAT3	C	A	exonic	missense SNV	D661Y	D
STAT3	C	T	exonic	missense SNV	D566N	D
STAT3	T	A	exonic	missense SNV	Y640F	D
STAT3	T	C	exonic	missense SNV	E616G	D
STAT3	T	A	exonic	missense SNV	N647I	D

Appendix 5

A5.1 STAT3 depletion enhances vorinostat sensitivity in HuT78 cells

We noticed that cells pre-treated with STAT3 GapmeR are more susceptible to apoptosis caused by vorinostat. We depleted expression of STAT3 in HuT78 cells using GapmeR and incubated with vorinostat (IC_{50} = 2 µM). We demonstrated using Annexin V/PI based flow cytometry analysis that 69% of STAT3 depleted HuT78 cells were in apoptotic stage compared to WT cells, which was 42%. This data clearly indicated that STAT3 depletion enhances vorinostat sensitivity in HuT78 cells.

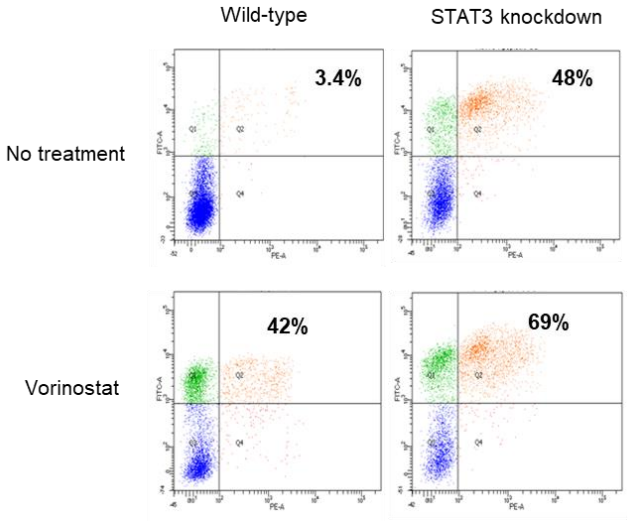

Figure A5.1 STAT3 inhibition increases sensitivity of HuT78 cells to vorinostat. Previously, it has been reported that STAT3 activation causes vorinostat resistance in cTCL cell lines such as STAT3. Here, we HuT78 cells were treated with STAT3 antisense GapmeR for period of 48 hr and were subsequently incubated in vorinostat containing medium for 24 hr. The cells were washed and staining with Annexin V/ Pi and examine for apoptosis using flow cytometry.

A5.2 DDX3Y, another isoform of DDX3 is rarely mutated in hematolymphoid malignancies

Using cBioPortal, we identified seven mutation in DDX3Y gene, however, none of them were oncogenic as predicted by OncoKB. This data suggests that DDX3Y may not play crucial role in progression of hematolymphoid malignancies.

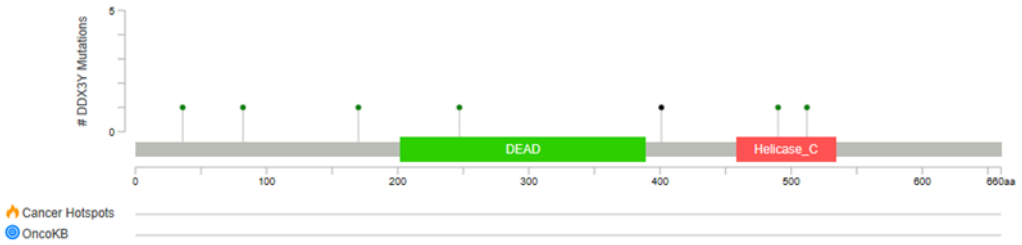

Figure A5.2 Mutational landscape of *DDX3Y* **(A)** To investigate the role of *DDX3Y* in hematolymphoid maliagncies, we used cBioPortal and OncoKB, to derive mutational variants of *DDX3Y* gene. Interestingly in 19,584 samples, only 7 variants were identified, however none of them were oncogenic.

A5.3 WNT signalling is not influenced in DDX3X depleted DLBCL cells

To investigate the effect of DDX3X depletion in DLBCL cells, we evaluated the nuclear translocation of β-catenin in DDX3X depleted cells. We showed that DDX3X depletion in U2932 and HBL-1 cells does influence cytoplasmic level of β-catenin. We used HEK293T cells are positive control.

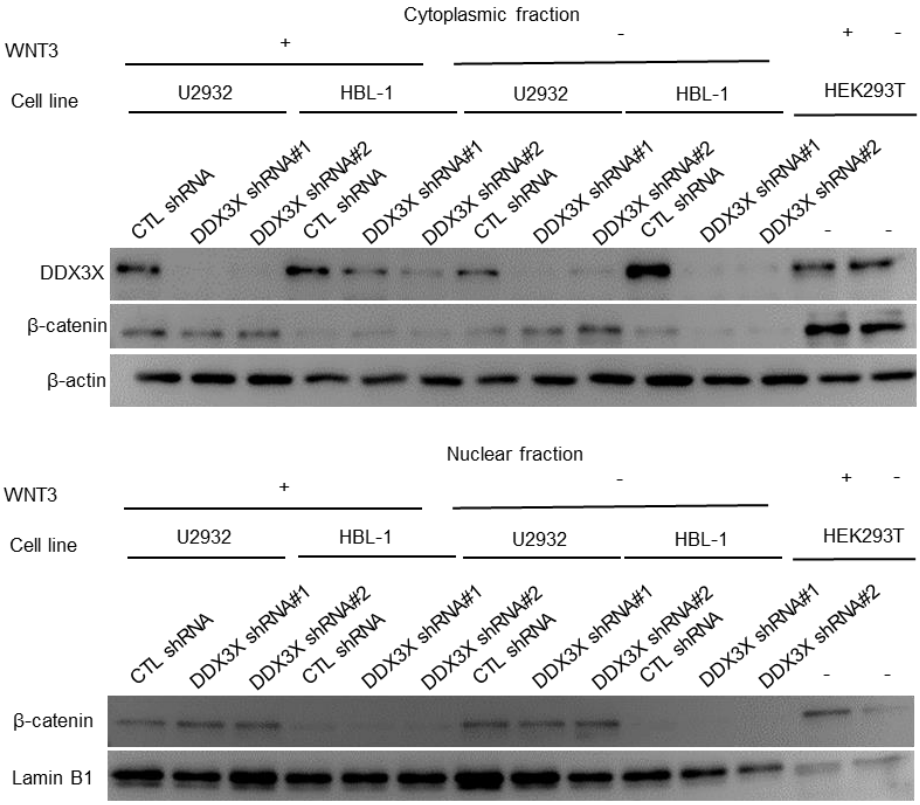

Figure A5.3 DDX3X does not influence WNT signaling. The WNT3A-expressing cell line HEK293 STF3A cells were cultured until 70% confluent and the conditioned media was used in a 50-50 mixture with fresh media. Induced U2932 and HBL-1 knockdown and control HEK293T cells were seeded and cultured in STF3A-conditioned media for 24 h. Cytoplasmic and nuclear fractions were extracted from the cells and tested for cytoplasmic and nuclear β-catenin expression using western blot analyses.

A5.4 epAON-mediated STAT3 depletion diminishes expression of survivin in HuT78 cells

To further, elucidate the mechanism of cell death in STAT3-epAOn treated cells, we evaluated levels of survivin expression, which is key anti apoptotic gene. We demonstrated that epAON mediated STAT3 depletion reduces the phosphorylated levels of STAT3 (Y705) and protein levels of survivin in HuT78 cells. It was evident that STAT3-epAON significantly decreased levels of pSTAT3 (Y05) and survivin.

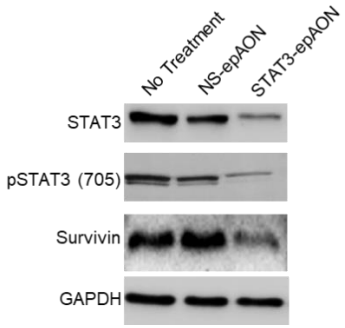

Figure A5.4 STAT3-epAON induces apoptosis through depletion of survivin in HuT78 cells. Previous reports suggest that STAT3 depletion induces apoptosis through down regulation of survivin. To demonstrate that STAT3-epAON HuT78 causes downregulation of phosphorylated STAT3 and survivin, we cell were treated with NS-epAON and STAT3-epAON for 96h and cell lysates were collected which ere immunoblotted with anti STAT3, anti pSTAT3 (Y705) and survivin.

A5.5 epAON molecules are safe

To evaluate the safety of epAON molecules, Twenty-five BALB/c mice were maintained Singapore Experimental Medicinal Centre, Singapore. Mice were categorized into five experimental groups: i) PBS ii) 5 mg/kg NS epAON iii) 25 mg/kg NS epAON iv) 5 mg/kg STAT3 epAON v) 25 mg/kg STAT3 epAON. Mice were administered with intervention through subcutaneous injection (200 µL) with dose regimen of 2 doses\ week for 2 weeks. The mice were monitored and were sacrificed after 15 days. Blood was collected at two time points i) before treatment (from venous sinus) and ii) after sacrifice (cardiac puncture). The organs were collected and froze in liquid nitrogen.

We noticed that no appreciable influence in the body-weight of mice upon epAON treatment (**Figure A5.5A**). We also demonstrated that administration of epAON does not influences serum levels of levels of aspartate aminotransferase (AST), alanine aminotransferase (ALT) and Creatine kinase (CK) in serum from mice treated epAON compared to PBS control (Figure A5.5 B, C, D). We also analysed the levels of IgG 1 of treated mice group. However, there were no significant changes in IgG 1levels (Figure A5.5 E). All experiments were performed according to the National Advisory Committee for Laboratory Animal Research guidelines (IACUC #2016/SHS/1252).

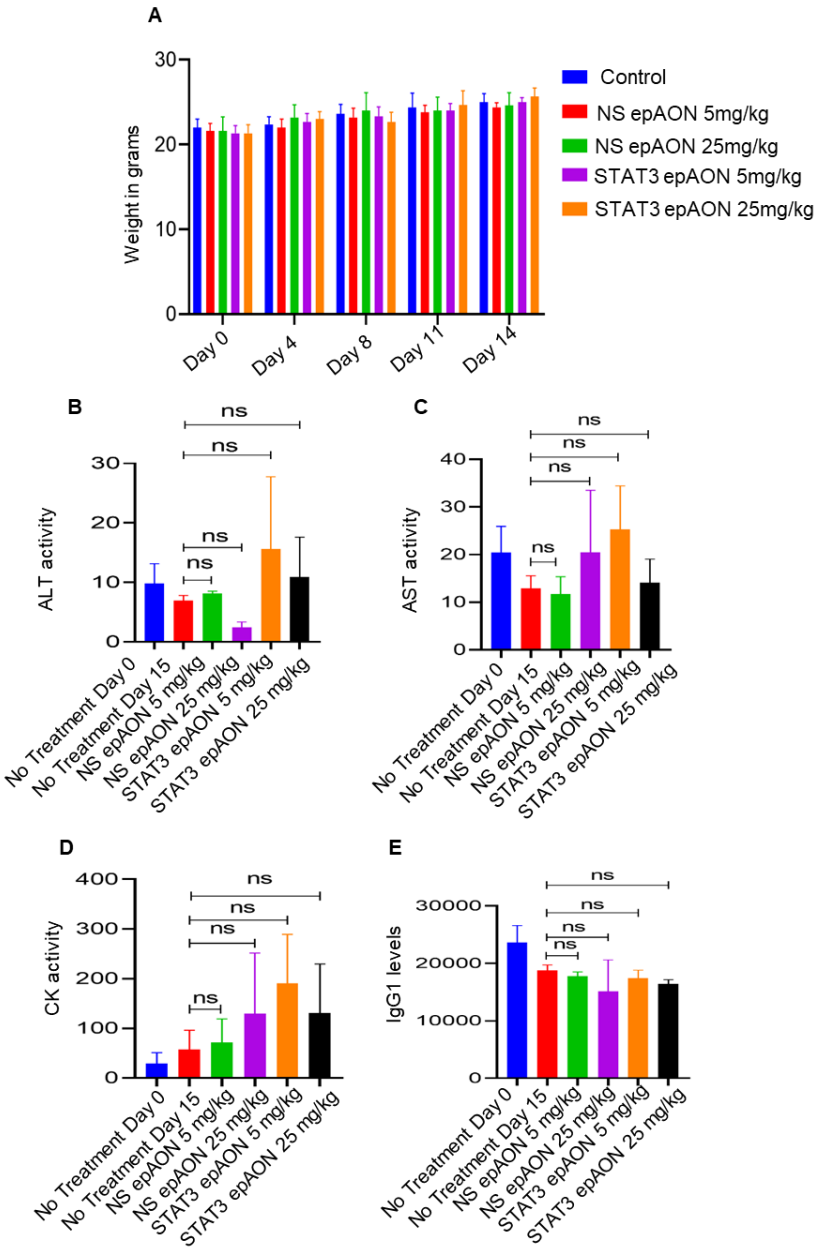

Figure A5.5 Assessment of toxicity of epAON. Mice were subcutaneously, injected with 5 mg/Kg and 25 mg/Kg non-targeting epAON 2 dose/week for 2 weeks. (**A**) The body-weight was monitored using weighing machine and data was presented as average of each treatment group. (**B, C**) Serum collected from treated mice groups were analysed for expression of alanine aminotransferase (ALT) and aspartate aminotransferase (AST) using kit-based assay. (**D**) Creatine kinase (CK) levels in serum were evaluated using kit-based assay. (**E**) IgG1 levels in serum of treated mice were analysed using ELISA test. (Mean± S.E.M.; ns, non-significant)

A5.6 *In vivo* distribution of epAON

To understand dissemination of epAON in body, we subcutaneously injected 5mg/kg FAM-epAON in BALB/C mouse. After 6 h, mouse was sacrificed and organs were collected. The organs were cryo-sectioned and stained (Fig. 5.12). It was observed that FAM-epAON was localised in liver, kidney, spleen but not in muscle and brain. It was inferred that epAON does not permeate blood -brain barrier.

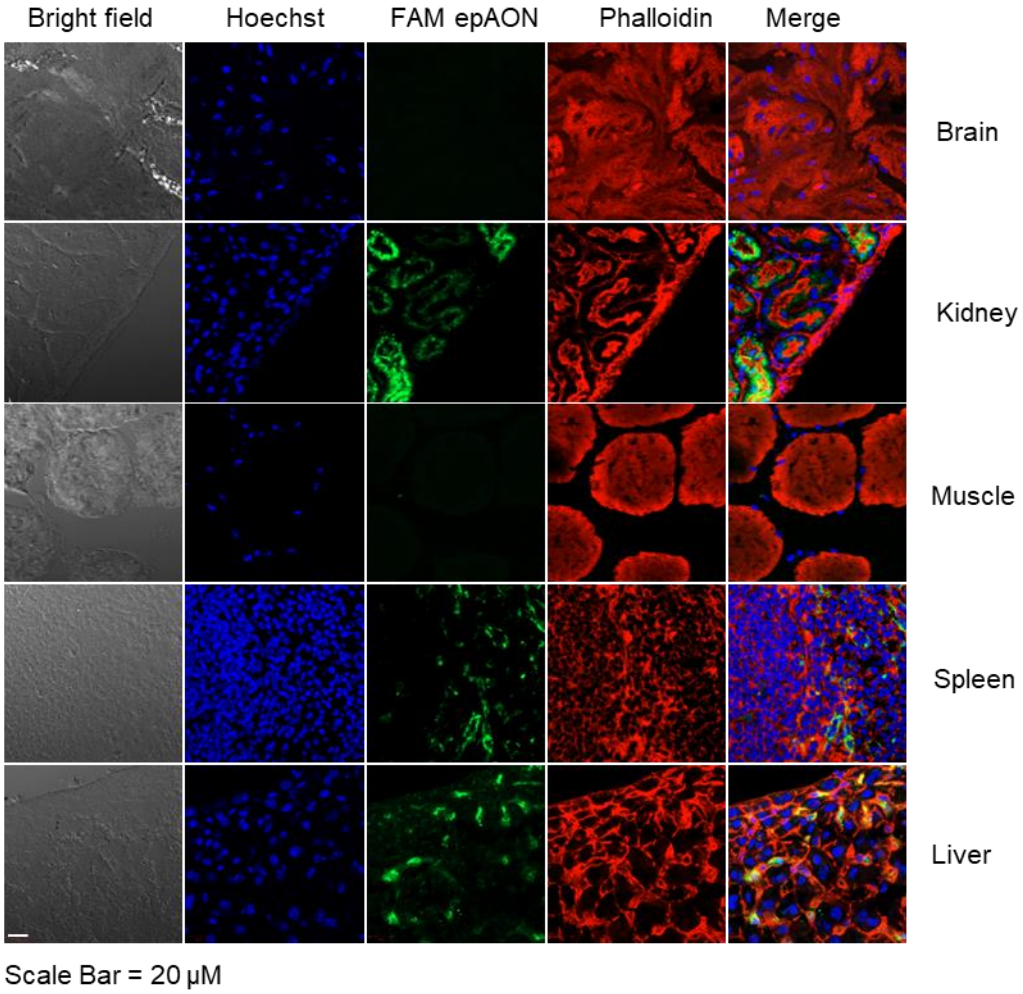

Figure A5.6 *In vivo* distribution of epAON. Mice were subcutaneously, injected with 5 mg/Kg non-targeting FAM-epAON (green) for 6 h. The tissues, such as brain, liver, kidney, spleen and skeleton were cryosectioned, fixed and counter-stained with Rhodamine-Phalloidin (to visualize cells, red) and Hoechst (to visualized nuclei, blue). The images were by confocal microscopy (40X).

A5.7 Vorinostat resistance of HuT78$_{VR}$ cells are reversible

To check whether reversibility of vorinostat resistance, we cultured HuT78$_{VR}$ cells in cell culture medium without vorinostat for period of one month. We found that IC_{50} of HuT78$_{VR}$ reverts to 2 µM from 36 µM. This clearly indicated that vorinostat resistance is reversible.

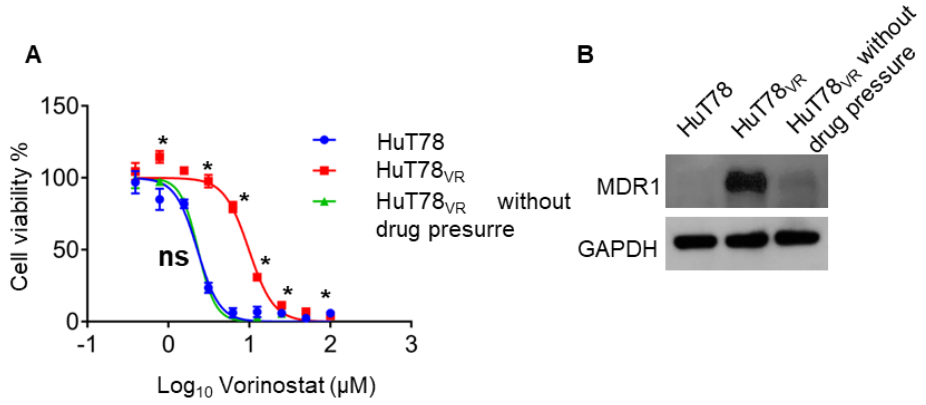

Figure A5.6 Acquired drug resistance is reversed upon incubation in absence of drug pressure. To check whether growing of HuT78$_{VR}$ in absence of drug pressure will reverse vorinostat resistance. (**A**)HuT78, HuT78$_{VR}$ and reversed HuT78$_{VR}$ (grown in normal medium) were treated with vorinostat and IC50 was calculated using GraphPad prism.(**B**) Cell lysates from HuT78, HuT78VR and HuT78VR (grown in normal medium) were collected and immunoblotted and probed for MDR1 and GAPDH. (ns non-significant, *p>0.01). These data suggested that vorinostat resistance mechanism in HuT78$_{VR}$ are reversible.